Digital Hologram Image Processing

by

Conor Mc Elhinney BSc.

NUI MAYNOOTH

Ollscoil na hÉireann Má Nuad

A thesis presented in fulfilment of the requirements for the Degree of

Doctor of Philosophy

Supervisor: Thomas J. Naughton

Department of Computer Science

Faculty of Science

National University of Ireland, Maynooth

Maynooth, Co.Kildare, Ireland

June, 2009

Acknowledgments

I would like to thank the digital holography group who I have worked with for the last couple of years. During my time in Maynooth I received a lot of support and help from my supervisor Thomas Naughton. Especially in the closing months of my Ph.D, this was greatly appreciated and will not be forgotten. Also thanks to Jonathan for helping keep me sane for the first couple of years and of course Bryan, Andrew, Lukas, John, Karen and Manos for pitching in whenever I needed a hand. I'd like to thank Enrique Tajahuerce and Bahram Javidi for use of their digital hologram data and also Yann Frauel and Betina Castro for helping us with our original digital hologram setup.

Of course I would not have got here without my family and friends, and I'm sure they won't ever let me forget it. I don't have room to name everyone who has helped me out over the years. So I'll just say a special thanks to a couple, thanks Claude, Aidan, Paddy and Owen.

This thesis has emanated from research conducted with the financial support of Science Foundation Ireland, Enterprise Ireland, and the Embark Initiative of the Irish Research Council for Science, Engineering, and Technology, under the National Development Plan.

Contents

List of Figures

List of Tables

List of Algorithms

Abstract

In this thesis we discuss and examine the contributions we have made to the field of digital hologram image processing. In particular, we will deal with the processing of numerical reconstructions of real-world three-dimensional macroscopic objects recorded by in-line digital holography. Our selection of in-line digital holography over off-axis digital holography is based primarily on resolution. There is evidence that an off-axis architecture requires approximately four times the resolution to record a hologram than an in-line architecture. The high resolution of holographic film means this is acceptable in optical holography. However, in digital holography the bandwidth of the recording medium is already severely limited and if we are to extract information from reconstructions we need the highest possible resolution which, if one cannot harness the functionality of accurately reconstructing phase, is achieved through using an in-line architecture. Two of the most significant problems encountered with reconstructions of in-line digital holograms include the small depth-of-field of each reconstruction and corruptive influence of the unwanted twin-image. This small depth-of-field makes it difficult to accurately process the numerical reconstructions and it is in this shortcoming that we will make our first three contributions: focusing algorithms, background and object segmentation algorithms and algorithms to create a single image where all object regions are in focus. Using a combination of our focusing algorithms and our background segmentation algorithm, we will make our fourth contribution: a rapid twin-image reduction algorithm for in-line digital holography. We believe that our techniques would be ap-

plicable to all digital holographic objects, in particular its relevant to objects where phase unwrapping is not an option. We demonstrate the usefulness of the algorithms for a range of macroscopic objects with varying texture and contrast.

Acronyms

2D	Two-dimensional
3D	Three-dimensional
CCD	Charged Coupled Device
DFF	Depth-From-Focus
DFRT	Discrete Fresnel transform
DFT	Discrete Fourier Transform
DH	Digital Hologram
DHIP	Digital Hologram Image Processing
DHM	Digital holographic Microscopy
DHs	Digital Holograms
DSP	Digital Signal Processing
EFI	Extended Focused Image
EM	Expectation Maximisation
FFM	Fourier Focus Measure
NRMS	Normalised root mean square
OB	Object Block
PTF	Propagation Transfer function
PSI	Phase-shifting interferometry
ROC	Receiver Operating Characteristic
SLM	Spatial Light Modulator

Chapter 1

Background and contributions

In this chapter we introduce the reader to the areas of holography, digital holography and digital hologram image processing (DHIP). We focus on the research that has been conducted that is relevant to this thesis. Our aim is to provide a general overview of the field and define holography, digital holography and DHIP. In this thesis we detail four contributions made to the area of DHIP. The first is in the field of focus detection of digital holographic reconstructions. Secondly we have developed segmentation algorithms for clustering regions from the same object together. Using focus information our third contribution creates an image where all of the objects are in-focus. Our final contribution is in the removal of the unwanted twin-image from in-line digital holograms (DHs). After introducing holography and digital holography we pay particular attention to the research conducted in these areas while detailing where there has been limited research, in which our contributions will be made.

1.1 Holography

Holography was invented by Dennis Gabor in 1948 [Gab48]. In his initial experiments, involving electron microscopy, an object was exposed to a radiation beam of strong coherence. The waves weakly scattered by the object interfered with the background wave on a photographic film to form an interference pattern, which was then recorded. Gabor showed how it was possible to reconstruct the original object wavefield by illuminating the recorded film with the original reference wave. However, an inherent artifact of the method is that the resultant image of the reconstructed object is marred by the presence of a twin-image. The twin-image problem was addressed by Leith and Upatnieks[LU62, LU63] who developed an off-axis recording setup which produced reconstructions free of the twin-image. Holography requires the use of photosensitive recording materials to record holograms which are costly financially and in terms of processing time as well as being inflexible.

Digital holography [GL67, BHG+74, YM80, OS87, SJ94, KAJ97, Kre05, SJ04a], refers to the science of using discrete electronic devices, such as charged coupled devices (CCDs) to record a hologram. In this case, reconstruction is performed numerically by simulating the propagation of the reference wave back to the plane of the object. One major advantage of digital holography over material holography is the convenience of using discrete signal processing techniques on the recorded signals [JT00, NFJT02, SJ04b, MMH+06a]. Digital holography has become feasible due to advances in megapixel CCD sensors with high spatial resolution and high dynamic range.

1.2 Background to Digital Holography

Digital holography is the science of recording a hologram on discrete electronic devices. This hologram is an interference pattern which is created from the interference between an object wave and a reference wave at the plane of the recording medium [Gab48, Har02]. A hologram contains both amplitude and phase information about the object(s) in the scene, this allows for the viewing of multiple perspectives and multiple depths [Har02]. The viewing of an optically recorded hologram is achieved through illumination of the film containing the interference pattern with the original reference wave. In digital holography a numerical function is applied to the DH which simulates the optical process of illuminating the hologram with the reference wave and produces an amplitude and phase image of the scene which can then be analysed or processed. This process is called numerical reconstruction. DHs can be reconstructed optically [GMH+08], through the use of spatial light modulators and the original reference wave but the work in this thesis is carried out on numerical reconstructions. Only holograms recorded on discrete electronic devices will be referred to as DHs in this thesis; we do not refer to the digitised reconstructions of optically recorded holograms [MAK04, Wat04, FTHH07] as DHs.

In-line holography refers to experimental setups that are similar to the original Gabor architecture. They require the reference wavefield to be traveling in the same direction and at the same angle as the object wavefield at the plane of the CCD. In Gabors original experiment the transmissive object was illuminated by the reference wave and the waves that were scattered by

the object interfered with the reference wave at the photographic film. This experimental setup is popular in particle holography. Another implementation of the in-line experimental setup involves splitting the illumination source into two waves. The first wave illuminates the object and becomes the object wave which propagates to the recording medium, while the second wave is the reference wave and propagates uninterfered to the recording medium. In general, a beam splitter is used to combine the object wave and the reference wave such that they are traveling in the same direction and at the same angle with respect to the recording medium. While these are two different experimental setups they are both called in-line as they have the same mathematical properties and are mathematically equivalent.

In macroscopic digital holography, one of the obstacles in off-axis digital holography is that the macroscopic objects have to be placed large distances away from the camera. For example using a camera with 2048^2 pixels of size 0.0074mm with a laser source of 632.8nm a 10mm^2 object needs to be placed at a minimum distance of 645mm and an object of size 100mm^2 needs to be placed a minimum distance of 2516mm away from the camera, these calculations are explained in Chapter 2.1. This is because a camera has a maximum recordable interference angle which is directly linked to the size of the object and the distance it is away from the camera. Using an in-line digital holography setup reduces the recording distances to 295mm and 762mm, respectively. However as will be discussed in Chapter 2 there are disadvantages to using an in-line setup.

The first example of digital signal processing (computers) and hologra-

phy combining was in 1967 [BL66] when binary holograms were computed and then printed onto materials for optical reconstruction. Goodman and Lawrence were the first to use a computer to reconstruct an optically recorded hologram [GL67]. It was not until 1974 that the first DH was recorded by Bruning et al. [BHG+74]. They used a 32×32 photodiode array to measure an interference pattern and used a computer to reconstruct the digitally recorded signal.

In the following years, the low spatial resolution of discrete electronic devices limited the research opportunities in digital holography. Research was conducted instead on computer generated holograms since the advantages of using computers to process reconstructions was evident. In 1979 Marie et al. [MBA79] addressed the twin-image problem for in-line digital holography using discrete signal processing. They reconstructed a simulated hologram to the focal plane of the unwanted twin-image. Then using a threshold operation on the reconstructions amplitude they segmented and removed that twin image from the reconstruction. This resulted in reconstructions with a suppressed twin-image.

In 1994 Schnars and Jüptner [SJ94, Sch94] recorded an off-axis DH and reconstructed it using a computer which demonstrated that the spatial resolution of discrete electronic devices had progressed to a sufficient level to make digital holography a practical science. They used a CCD with a pixel count of 1024×1024 and a pixel size of 6.8μm. They noted that digital holography was limited to the recording of small objects recorded at long distances. This was due to the spatial resolution of the CCDs available and

also their choice of an off-axis setup. The benefits and limitations of the main digital holography architectures is discussed in Chapter 2.

In 1997, Kreis and Jüptner [KJ97] demonstrated one of the primary benefits of digital holography. They digitally recorded a hologram and numerically suppressed the unwanted dc-term for off-axis holography. They demonstrated how it was possible to effectively suppress the dc-term through the subtraction of the average intensity which is roughly equivalent to high-pass filtering. Using a CCD with 2043×2024 pixels of size 9μm they experimentally validated their dc-term suppression and successfully demonstrated that post-suppression accurate phase can be recovered in areas previously corrupted by the dc-term.

In the same year Yamaguchi and Zhang [YZ97] developed a new form of in-line digital holography which has become known as phase-shift digital holography which belongs to the family of phase-shifting interferometry (PSI) [BHG+74] techniques. As in the optical case this method suffers from poor reconstructed image quality, due to the presence of the dc-terms and the out-of-focus twin-image that contaminates the reconstructed object image. While it is possible to remove the dc-terms and separate the twins with an off-axis recording setup, this increases the spatial resolution requirements, and limits the system significantly which is undesirable when one considers the already limited resolution of digital cameras. A hologram contains four terms: two dc-terms and two twin terms. All the information about the recorded scene is contained in just one of these twin terms with the other three terms being sources of noise and error in the reconstructed object im-

age. By applying a phase shift to the reference wave before recording a set of DHs, it is possible to recover the full complex field of the objects in the scene using linear equations. This results in a DH free of the dc-terms and the unwanted twin-term.

In Chapter 2 we discuss in detail digital holography, the different recording and reconstruction processes. Off-axis is the more popular choice for optical holography, this is because it spatially separates error terms inherent in DHs. However, this is achieved at the cost of resolution and with the resolution restrictions placed on digital holography by the recording mediums the higher resolution of in-line holography makes it a more attractive choice for digital holography. The advantages and disadvanatages of the two architectures is discussed in detail in Chapter 2.

1.3 Digital Hologram Image Processing

DHIP is a developing field where computer science and image processing knowledge can make its strongest contribution to digital holography. We define DHIP as the application of current and the development of novel image processing algorithms applied to DHs and in this thesis we focus on DHIP applied in the reconstruction domain. We are primarily interested in, although not limited to, the processing of the intensity from reconstructions. Phase information is by no means irrelevant to DHIP, it is of course integral to the reconstruction process [MNF+02, YYMY06]. In the macroscopic domain it has been shown to be very important in the compression of DHs [Sho06]. Phase information is also used to extract shape or deformation measurements.

Particularly in digital holographic microscopy (DHM) the unwrapped phase of a reconstruction contains information about the object shape.

DHs can be quite large in size, a 2048×2048 pixeled PSI DH can be as large as 65MBytes [Sho06]. As the spatial resolution of CCDs increase so does the size of the resultant hologram. A lot of research has been conducted in the area of compression for the purpose of efficient storage and transmission. There have been principally two approaches applied to the compression of holograms: compression at the hologram plane [NFJT02, NMJ03, NJ04, MY05, DS06a, DS06b, SNJ06b, SNJ06a, SNJ06c, SCK07] and compression at the reconstruction plane [DS07]. In the macroscopic domain, speckle noise is also a serious problem in reconstructions. This noise is inherent in any optical system using coherent light. However, the digital nature of DHs allows postprocessing of reconstructions to reduce speckle noise and improve the reconstructed image quality [BFRJ04, GSFP05, MHM+07]. Techniques have been applied to reconstructions of DHs and range from median filtering and neighbourhood averaging [GSFP05] of the intensity to the application of statistical based interpolation of the intensity [BFRJ04] and filtering in the Fourier domain of the complex reconstruction data [MHM+07]. The most relevant areas of DHIP to this thesis are in focus detection, segmentation and the extraction of information from a DHs reconstruction. It is in these areas that we make our first three contributions to digital holography. We now progress to discussing the research conducted in these areas in more detail.

1.3.1 Focus and Digital Holography

Imaging systems have a depth-of-focus with the majority having a finite depth-of-focus. The recorded image can either be in-focus or out-of-focus. The objects which lie within the depth-of-focus of the imaging system are in-focus (appearing sharp) while the objects which lie outside of the depth-of-focus of the system are out-of-focus (appearing blurred). While the development and application of focusing techniques in incoherent imaging has been well studied [Nay92, SCN93, Bov93, SC95, ST98], in an arbitrary 3D scene there exists no single definitive measure for finding the focal plane of a scene or finding the focal distance for a region within a scene.

To determine if an image is in-focus the accepted procedure is to either record a set of images with a dynamic scene or to record a set of images with a static scene where the focal plane of the camera is varied. A function, which is called a focus measure, is then applied to each image and the image which maximises (or minimises) this focus measure is taken as the in-focus image. Focus measures are also known as sharpness functions originating from the work of Muller et al. [MB74] where they were the first to apply a focus measure to an image to determine the most focused image, which they called an "image sharpness function". Modern focus measures are based on the assumption that edges are more defined in focused images and are therefore more sharp. This equates to an increase in the high spatial frequency energy in in-focus images. Numerous sharpness based focus measures have been developed [Bov93, KFZv06] and evaluated [SCN93, ST98, HJ07] for incoherent imaging which generally satisfy the following requirements:

independent of image content,

low computation complexity,

focus measure should have one peak,

there should be a large variation in returned value with respect to blurring and

robust to noise.

These critera require the input of an image block or the neighbourhood pixels around an image pixel to detect focus. However, the use of just the intensity value of one pixel in an image has been proposed as a focus measure [HK84]. The use of intensity has been mathematically proven as a sound focus measure but only in specific systems. They require microscopic systems that are telecentric [HK84] and also put requirements on the objects being examined. To use an individual intensity pixel, the objects must be pure amplitude or pure phase. Also any noise in the image will lead to an incorrect focus estimate. This is why neighbourhood pixel information is required for the vast majority of focus measures. We now proceed to a discussion on the research that has been conducted using focus measures in the field of digital holography.

Accurate determination of focus is essential to many applications of digital holography including phase unwrapping, object recognition, segmentation and depth estimation. An example of this is in DHM, to successfully unwrap the phase information from a DHs reconstruction one needs

to be at (or close to) the correct focal plane. While there are some examples of autofocusing in DHM [FCN+03] this is currently a manual operation and open to error. One of the main reasons why focus is an issue in digital holography is the small depth-of-focus of digital holographic reconstructions [FCN+03]. The depth-of-focus of a macroscopic digital holographic reconstruction is primarily determined by reconstruction distance and the reconstruction function used. For the majority of the DHs in this thesis the depth-of-focus is only in the order of 1mm for a given reconstruction. This is based on a wavelength of 632.8nm, a square pixel size of 7.4μm and camera dimensions of 2048×2048. A number of focus measures have been proposed and demonstrated [GK89, FCN+03, LU04, MWLJ04, DSCY06, ACYD08, LKB08, TIY08]. These employ focus measures such as self-entropy [GK89], phase changes [FCN+03], wavelet analysis [LU04, DJ07], grey level variance [ACYD08, MWLJ04, TIY08], integrated amplitude modulus [DSCY06], and Fourier-spectra based measures [LKB08] among others. Using these measures, applications such as the detection of the focal plane [FCN+03, LU04, DSCY06] in DHM and the measurement of 3D objects in digitised physical holograms [MWLJ04] have been demonstrated.

In 1980 focus detection was first applied to holography by Haussmann et al. [HL80], in the field of particle detection. They optically recorded their holograms which were recordings of fast moving gas bubbles in water. They optically reconstructed their holograms and used a 2D image scanner to record the intensity of the reconstructions. They determined that edges were the most reliable feature in their reconstructions for detecting focus. After

first applying filtering to their images they applied a focus measure which detected sharpness in the entire reconstruction. The reconstruction which maximised this function was considered the in-focus reconstruction.

Gillespie and King [GK89] proposed a focus measure for digital holography. They advocated the use of self-entropy as their focus measure. This was calculated on the phase of a DHs numerical reconstruction. They aimed to develop a function that could be used to autofocus the reconstructions of a DH. However, they used computer generated holograms in their experiments which did not suffer from speckle noise.

The first application of a focus measure to digital holography was performed by Murata and Yasuda [MY00] in 2000. They demonstrated that in particle holography when opaque particles are recorded, the intensity of the centre pixel of the particle is at a minimum at the focal plane. They experimented with simulated DHs of particles in a volume and were able to identify the depth of fifty particles in reconstructions from five different DHs with a 95-99% accuracy where the accuracy was dependent on the number of reconstructions used. The minimum or maximum intensity values are used in particle holography as a focus measure but are not generally applicable for focus detection as they rely on low noise and either fully opaque or transparent objects.

Yin et al. [YFB02] performed a survey of the application of four focus measures to digitised reconstructions of acoustic holograms. They selected gradient magnitude, modulus difference, modified Laplacian and grey level variance as their four focus measures. Using digitised reconstructions of an

optically recorded hologram of a prepared specimen they examined the output of these focus measures and determined that grey level variance achieved the best results. With an estimation of the point spread function of their experimental set-up they then applied spatial filtering to their reconstructions to reduce blurring and recover a focused image of the scene. In this work they assumed a linear relationship between the focus depth and the reconstruction depth.

Ferraro et al. [FCN+03] have proposed and demonstrated how to track the focal plane of a dynamic scene using the phase information of a DHs reconstruction in quasi-real-time. Their method requires knowledge of the focal plane of the first hologram and analyses the fringes in the phase information to determine the displacement of the object plane that has occurred since the previous hologram reconstruction. This allows them to track the objects focal plane. The correct identification of the object plane is required to successfully unwrap an objects phase. These microscopic displacements caused by a change in temperature or object movement in the $z-$direction can be enough to defocus the object and make unwrapping of the phase unsuccessful.

Liebling and Unser [LU04] developed Fresnelets, which are a new wavelet based numerical reconstruction method for DHs. Their holograms were recorded using DHM [CCD+02] and are free of speckle noise. In their work Fresnelets are evaluated as a focus measure compared to some popular image processing focus measures - such as the Laplacian of the reconstructed intensity and intensity squared - and it was found that Fresnelets outperformed

both image processing measures.

The first method for reconstructing a digital hologram at the in-focus plane using a depth-from-focus (DFF) technique was proposed by Ma et al. [MWLJ04], who used variance as their focus measure. DFF is an image processing approach for the estimation of surface shape in a scene using multiple independently focused images in the form of a depth map. DFF approaches estimate the focal plane of a digital hologram by maximizing a focus measure which is applied to the intensity of several 2D reconstructions where each reconstruction is at a different focal plane. Depth maps can be calculated using DFF approaches through computing a focus measure on the overlapping blocks of each reconstruction. The depth of each block is estimated by finding the reconstruction depth which maximizes the focus measure. DFF has been successfully applied to the segmentation of a DH into object and background [MMC+07a] and to create low-resolution depth maps of digitised physical holograms [MWLJ04].

Malkiel et al. [MAK04] processes sequences of digitised reconstructions of an optically reconstructed conventional hologram to create a depth map. The objects under examination are plankton. They have found that they can estimate the focal plane of object points by taking the maximum intensity value for each pixel over the volume of reconstructions. This allows them to create a depth map of the scene. This is the same focus measure approach proposed by Häusler and Körner [HK84] that assumes a near noiseless system. In their approach they heavily process their reconstructions to eliminate or suppress as much of the noise in the reconstructions. They are

able to successfully segment and autofocus the plankton objects encoded in their DHs using this technique.

Similar to the approach adopted by Ma, Thelen et al. [TBG+05] have applied grey level variance to the extraction of shape information from the digitised reconstructions of optically reconstructed holograms. By illuminating their scene with a speckle pattern they are ensuring that the maximum variance for each image block occurs at the in-focus plane. This increases the accuracy of their focus measure. They have successfully produced accurate high-resolution depth maps of human faces from the digitised reconstructions.

Dubois et al. [DSCY06] have conducted research in theoretically determining the best focus measure for microscopic scenes. They theorise and experimentally demonstrate that in a microscopic scene the integrated amplitude can be used to determine focus assuming that it is either a pure amplitude object or a pure phase object.

Burns et al. [BW07] have developed an algorithm for computing the focal plane of plankton in digitised reconstructions of optically reconstructed holograms. They advocate the use of the Tenegrad function, which is a variation of the energy of the image gradient.

The work of Dubois et al. [DSCY06] has been extended by Antkowiak et al. [ACYD08] in the field of DHM to create an extended focused image (EFI). Their focus measure of the integrated modulus of a reconstruction is applied to create an image of the microscopic scene where all the object points are in-focus. This allows for the detection and tracking of particles.

As we have identified, autofocusing is of great interest in various imag-

ing fields. Langehanenberg et al. [LKB08] have published a paper which overviews and reviews the current research in autofocusing applied to DHM. They review the application of focus measures to different types of objects, pure phase and pure amplitude, and discuss in detail some of the more important requirements of a focus measure. They propose the use of a Fourier-spectra based focus measure as the most reliable focus measure for DHM.

While the majority of research conducted in focus and digital holography has been in the microscopic domain there is still interest in the macroscopic domain. Tachiki et al. [TIY08] have worked on focus in a novel manner. They have determined that the area which requires attention is not in the analysis of data output after focus detection but in the assumption that the output plot from focus measures is unimodal. They have developed a group of processes that can be applied in the focus determination stage of the algorithm to help eliminate false positives and improve the accuracy of focus detection particularly in imaging systems with noise such as digital holography. They propose that the peak width in a focus plot is an important indicator in determining a focal plane and should be weighted similar to the location of the maximum peak. They have used grey level variance as their focus measure.

A novel focus measure which is not dependent on the detection of high frequencies has recently been proposed and experimentally validated in digital holography [YK08]. Yang et al. proposed a focus measure called the correlation coefficient for particle digital holography. They reconstruct a DH over a range of depths and sequence these reconstructions in a volume. They

then calculate the correlation between each successive reconstruction, the reconstruction that has the highest correlation with its neighbouring reconstructions is then assumed to the be the in-focus image.

What has been identified in the field of focus detection is that there is no individual focus measure that is applicable to all problem domains. The selection of a focus measure can be determined by, among other things, the type of imaging system being used and the amount of noise in the output images. While we use grey level variance as our focus measure we have intentionally developed all of our algorithms in a manner that variance can be replaced by any acceptable focus measure. This makes our algorithms transferable between the different domains of digital holography such as DHM and macroscopic digital holography. The science of focus, and the research we conducted in this field, is discussed and examined in detail in Chapter 3.

1.3.2 Segmentation and Digital Holography

Recently, several new approaches have been developed for the segmentation of hologram reconstructions into a compact representation of the useful information held in these reconstructed object images [Wat04, MAK04, GS04, ZC05, DJ06, MMC+07a, MHMN09]. These approaches have used phase information [GS04], intensity information [Wat04, MAK04, ZC05, MHNY06, MMC+07a], complex information [DJ06] and the estimated depth [MHMN09] to segment a reconstruction into object(s) and background. They can be further refined into approaches which segment using a single reconstruction [Wat04, MAK04, GS04, ZC05] or multiple reconstructions each at a

different depth [DJ06, JK05, JMYC05, JYMD06, MMC+07a, MHMN09]. Most of these methods have been developed for segmenting reconstructions containing microscopic objects, e.g. plankton.

Approaches to the segmentation of near 2D objects encoded in optically recorded particle holograms have been developed by Burns and Watson [BW07] and Malkiel et al. [MAK04]. Their segmentation algorithms are applied to the intensity of digitised reconstructions. Watson [BW07] segments plankton by thresholding the intensity of digitally enhanced digitised reconstructions where pixels with values above the threshold are classified as object and pixels below are classified as background. Malkiel et al. [MAK04] processes sequences of digitised reconstructions to create a depth map. The depth of every pixel is estimated by selecting the depth which results in the highest intensity in the digitised reconstruction. In both of these approaches the objects have a narraow depth-of-field which leaves a small number of focal planes per object when compared to macroscopic objects.

Active contour models have also been used for the segmentation of dynamic biological organisms recorded using DHM [DJ06]. Active contour models, also known as region snakes, are commonly used in the three-dimensional segmentation of medical images [BSS05, HFS03]. This approach has recently been applied to the segmentation of biological samples in single-exposure online holographic microscopic images [DJ06]. The active contour algorithm requires the manual selection of pixels, called seeds or nodes, belonging to target objects from an image. Segmentation is then achieved through application of a region-growing algorithm to each target object. The reconstructions

of these near 2D biological organisms are relatively free of speckle noise compared to reconstructions of macroscopic objects encoded in DHs [MMHN08].

1.3.3 Extraction of information from holograms

The first evidence in literature of information being extracted from reconstructions of holograms was in 1967. Thompson et al. [TWZ67] recorded holograms and anaylsed the resulting reconstructions that were displayed on a television monitor. They were able to count the number of particles in a hologram and obtain their size. This research was then continued by Haussmann et al. [HL80]. They optically recorded their holograms, which contained fast moving air bubbles in water, and used an Image Dissector Camera which performed a 2D scan of the reconstruction which they subsequently processed. They performed a number of operations on their reconstructions including focusing, particle counting, particle size estimation and particle depth estimation.

It is in the field of particle holography that the majority of research has been conducted in the extraction of information from holograms. We now discuss the research that we have identified as relevant to this thesis. In 1992 it was proposed by Onural and Özgen [OO92] that information could be extracted directly from the hologram without need for reconstruction using Wigner analysis. They applied their technique to digitised reconstructions of optically recorded holograms. Using this method it is possible to locate the position of objects in holograms. Using 1D Wigner analysis [HNM06] it is possible to determine the location of 1D objects by processing the hologram.

This is a very attractive processing technique as it extracts information directly from the hologram without the need for reconstructing or processing of multiple reconstructions. However, processing using 2D Wigner results in a 4D data and it is only recently that computing power has caught up to be able to process 2D objects.

Cuche et al. [CBD99, CMD99] demonstrated in 1999 how it was possible to extract the surface profile of objects using DHM. This is the first information extraction algorithm we are aware of that was performed on DHs rather than digitised reconstructions from optically recorded holograms. They demonstrated that in DHM the surface profile of an object can be extracted directly from the phase of the DH. This is true if the object does not too frequently produce phase variations higher than the wavelength of the original illumination source then the surface profile is directly encoded in the phase. If these phase variations exist and are less than twice the wavelength then phase unwrapping can be used to unambiguously reconstruct the surface profile, we call this the phase ambiguity problem. Also in 1999 Pedrini et al. [PFTS99] proposed an alternative shape measurement system for microscopic objects using DHs. They proposed the use of a digital holographic interferometry system. They recorded two DHs using different wavelengths and subsequently reconstructed. They demonstrated that the results of subtracting the phase of reconstructions of two DHs is a quantitative phase measurement of the object that after unwrapping results in the surface profile of the object. This dual wavelength digital holography is one of many digital holographic methods for extracting shape measurements from DHs.

Off-axis digital holography requires the object to be placed at large distances from the camera to maintain the sampling theorem. An alternative for off-axis digital holography was proposed by Pedrini et al. [PST99] in 1999. They asserted that by placing an aperture a small distance in front of the camera the spatial frequencies being recorded by the camera would be decreased to at least its maximum recordable interference angle (for that distance), this allows the recording of DHs of large objects much closer to the camera. They demonstrated the applicability of this technique by recording two DHs of a vibrating large plexiglass panel and measured the shape differences caused by vibrations from the resulting reconstructions. While in the paper this approach was only shown for vibration measurement it is applicable to deformation measurement and shape measurement.

Multiwavelength digital holography was invented to overcome the phase ambiguity problem. It is a technique that can measure the shape of an object through the combination of phase information from multiple DHs each recorded with a different wavelength. In 2000 Wagner et al. [WOS00] derived an algorithm which can be used to determine the minimum number of wavelengths required to extract the phase of an object which can be subsequently successfully unwrapped, due to a complete lack of phase ambiguities. This method extended the applications of multiwavelength digital holography through the efficient selection of the required wavelengths for the measurement of shape from objects using digital holography.

Another field which digital holography has been applied to is in the comparison of two near identical objects. The purpose is to detect physical

differences and defects. Osten et al. [OBu02] developed a new form of digital holography called "comparitive digital holography" which allows for the comparison of the shape of two objects. They first record a DH of the master object and then record a second DH of the same object after a load has been applied to it. The application of the load deforms the object and allows for the shape information about the object to be extracted. This is then called the mask of the master object. To compare the master object with any test object they record a DH of the test object, where the object wavefront illuminating the test object is the mask illuminated by the laser. A comparison of their technique to the shape measurement technique of dual-wavelength digital holography is presented. They confirm that they can detect small physical differences between two objects that are not easily discovered using alternative techniques such as dual-wavelength digital holography. This work has since been extended and improved [BOKJ06]. One of their improvements is the use of a spatial light modulator (SLM) to display the mask, and illuminate the test object. The use of an SLM gives computer control to the manipulation of the mask and allows for novel operations such as selective illumination of the test object.

The use of digital holography for shape and deformation measurement is widespread and in 2003, Kolenovicet al. [KOKL03] applied shape and deformation measurement to a new area, endoscopy. They designed and built a miniature digital holography endoscopic system for the purpose of three-dimensional shape and deformation measurement. In general, the majority of shape measurement extracted from DHs is 2.5D, as it is extracted from

only one individual perspective. To extract true 3D information from a DH, shape information needs to be extracted from at least two perspectives. This allows each (x, y), (horizontal, vertical), position in the shape map to have more than one (z), depth, value. If each (x, y) position can only have one (z) value then the shape information is only 2.5D. Kolenovic et al. [KOKL03] were able to extract true 3D information by illuminating the object under investigation from three different directions. Using an endoscopic digital holographic sensor with three illumination sources they performed deformation measurement. They illuminate the object and record a set of phase-shifted DHs for each of the three different illumination directions. Through applying an electrical current to the object they deform it and record a new set of phase-shifted DHs from the three directions. Phase maps can then be calculated through the subtraction of the phase values of the DHs before and after the deformation. These three phase maps are then unwrapped to obtain deformation information of the object from three different directions.

The automated extraction of information such as number of objects, size of objects and focal plane of objects is of great interest in particle holography. In this field they, until recently, do not record their holograms digitally but instead digitise the optically reconstructed holograms. This is due to the resolution increase acquired by using optical recording. Digital holography would be applicable to the recording of individual plankton but in the majority of particle holography the field of view is quite large compared the size of the objects being recorded in the scene, e.g. plankton. This limits the use of digital holography as a viable option, due to the large difference between ob-

ject size and field of view size. However, to extract information the optically reconstructed holograms are digitised and processed. These reconstructions are of much higher quality than those obtained by digital holography which after processing provides for more accurate information extraction. Malkiel et al. [MAK04] amongst others [HLR+00, Wat04, BW07] have demonstrated that analysis of digitised reconstructions can allow them access to information such as the focal plane of objects, the size of objects, the position of objects and the number of objects in the hologram.

The importance of the correct selection of reconstruction method was highlighted once more by Mann et al. [MYlK05], this time in the field of DHM. They compared three of the different reconstruction methods, angular spectrum, Huygens and the Fresnel transform. In the paper they demonstrated that for microscopy, the angular spectrum method returned the most accurate phase information and therefore the most accurate shape information.

While the majority of research in the extraction of information from holograms and DHs has focused on the extraction of shape and size information, it has been shown that through combining a vibrating object and digital holography new information can be extracted from sequences of DHs [FPO07]. Fu et al. [FPO07] in 2007 were able to extract the displacement, the velocity and the acceleration of a vibrating object from the reconstructions of a sequence of DHs.

1.4 Twin image removal and Digital Holography

After the invention of the laser, Leith and Upatnieks [LU63] proposed in 1963 a new experimental optical architecture that enables the complete separation of the unwanted twin-image term and the DC-term (or zero order term) from the wanted twin-image. In their method, the reference beam was incident on the hologram plane at some angle relative to the normal. In this way the twin-images were modulated on well-separated carrier spatial frequencies. The technique, called off-axis, significantly increased the bandwidth of the hologram which places a much greater requirement on the resolution of the recording material. Furthermore, the architecture imposes the need for numerous optical elements, in particular a beam splitter, which are not readily available in areas of holography using certain radiation sources. In these cases one must rely upon the initial Gabor architecture and the twin-image remains a detrimental and unavoidable source of noise that must be dealt with. Such is true in many cases including x-ray holography [TF96], gamma-ray holography [KK02] and electron holography [ARS05] which allow for improved crystallography and DNA imaging. For these reasons research needed to be conducted to remove the unwanted twin-image from in-line DHs. To date there is no definitive solution to this problem for all forms of in-line digital holography and it is in this area that we make our fourth and final contribution.

Despite the ready availability of optical elements the off-axis set-up still

poses a problem for digital holography. This is due to the increased bandwidth of the hologram. In digital holography, the pixelated recording cameras have resolutions an order of magnitude less than commercial photographic materials. Thus, the bandwidth is already severely limited and the use of an off-axis architecture will only serve to limit it further [XMA00, XPMA01]. However the off-axis approach has been implemented in microscopy [TKO99] and Cuche et al. [CMD00] proposed and experimentally validated the off-axis technique for real-time digital holographic recording. In this case, it is possible to digitally spatially filter the hologram to completely remove the DC-term and the unwanted twin-image.

Owing to the significance of the problem, twin-image elimination in in-line holography has received widespread attention since Gabors initial experiments. In 1951, soon after Gabors invention and many years before any off-axis architecture was developed, Bragg and Rogers [BR51] developed an innovative solution to the twin-image problem based on subtraction. In 1966, another twin-image reduction method was proposed by DeVelis et al. [DJT66] by recording in the far field of the object. When replayed in the far field the image of the object will appear but the unwanted twin-image will be so spread out that it appears as a DC-term and is therefore effectively removed. In 1968, Bryngdahl and Lohmann [BL68] developed a method to suppress the twin-image based on spatial filtering during both recording and replay.

The 1970s and 1980s saw the development of a new field of research for recovering the phase of a wavefield thereby negating any twin-image. These methods do not require interference and are collectively known under the

name of phase retrieval algorithms. They can be divided into two subsets; (i) deterministic [Tea83] and (ii) iterative [GS72, Fie78] phase retrieval. Despite the initial promise of phase retrieval algorithms, they have never managed to achieve results on a par with holographic methods. However there has been considerable interest in their usefulness in removing the twin-image for in-line holography [TBPN00, LS87, ZPOT03, LF07].

The first digital signal processing (DSP) technique for the removal of the twin-image [MBA79] appeared in 1979 but received little interest. Improved DSP based algorithms were developed some years later by Onural and Scott [OS87]. They described linear filtering operations to decode the information contained in the holograms.

In 1997 Yamaguchi and Zhang [YZ97, ZLG04] developed a new method for recording DHs free from the twin-image, known as phase shifting digital holography. This method used an in-line architecture, but required a number of separate interferograms to be captured. A phase shift is introduced to the reference beam between subsequent captures. These phase shifts are usually affected by rotation of a quarter and/or half wave plate or through the minute vibration of a mirror. Chen et al. [CLKC07] have presented a method that allows for the phase-shifting technique to be applied with an arbitrary phase shift and just two captures.

In relation to our twin-image algorithm, the most relevant two references are [PFFT98] and [DFFD05]. Pedrini et al. propose the first instance [PFFT98] of spatial filtering the reconstruction planes of DHs. This involves cutting out the wanted digitally reconstructed image from its sur-

rounding pixels. However, this area still contained considerable noise from the unwanted twin-image. In [CMD00] traditional spatial filtering in the Fourier domain was applied to an off-axis digital holography. Denis et al. have proposed a novel method [DFFD05] of spatially filtering the reconstruction domain and it is this method that we build on in this thesis. It was shown that by cutting out the reconstructed focused unwanted twin and returning to the plane of the wanted twin-image by numerical propagation one could free oneself of the unwanted noise. Their method was proposed only in the area of particle holography and the removal of the twin-images is a manual operation.

Throughout this introduction we have paid little attention to the DC-term, i.e. the intensity terms that appear as a by-product of the in-line holographic process. In some cases this artifact is far noisier than the unwanted twin. Many of the twin-reduction and twin-removal methods reviewed above will remove this term in addition to removing the unwanted twin. However, a number of methods have been developed in the literature to remove this term alone to augment those methods that do not. These methods are based on spatial filtering of the hologram [KJ97], subtracting stochastically different holograms [DMS03], phase-shifting [LKN00] and by subtracting the numerically generated intensity of the object and reference waves from the digital holography. For the results in this thesis we employ the spatial filtering method outlined in [KJ97] as well as simply subtracting a previous recording of the reference beam intensity.

1.5 Publications

In this section we list the publications of the author to date. These publications can be categorised as making contributions to the following areas:

Digital hologram image processing

1. Focus detection and depth estimation [AMHN08, HMF+06, MMS+05, MHA+08, MHAN09, MHAN08, MHBN08, MHMN07, MHMN09, MHMN08, MHN07, MHN08a, MHN08b, MHN08c, MMH+09, MMH+06c, MMH+06d, MMN+05, MMC+07b, MMHN08]

2. Segmentation [AMHN08, HMF+06, MMS+05, MHA+08, MHAN09, MHAN08, MHBN08, MHMN07, MHMN09, MHMN08, MHN07, MHN08b, MHN08c, MMH+09, MMH+06c, MMH+06d, MMC+07a, MMC+07b, MMHN08]

3. Speckle reduction [MMM+06, MMM+05a, MMS+05]

4. Compression [MSNJ04a, MSNJ04b]

Digital holography

Display [GMH+08]

Scene reconstruction [HMF+06, HMM+06, MMH+06a, MMH+06b, MMS+05, MHBN08, MMM+05b]

Error-term removal [MHA+08, MHAN09, MHAN08, MMH+09]

Theory [AMHN08, HMM+06, KHMN08, MMH+06a, MMH+06b, MHA+08, MHAN09, MHAN08, MMH+09]

The following is an ordered list of the publications of the author:

International journal publications

1. J. Maycock, **C.P. Mc Elhinney**, B.M. Hennelly, T.J. Naughton, J.B. Mc Donald, and B. Javidi. "Reconstruction of partially occluded objects encoded in three-dimensional scenes by using digital holograms", *Applied Optics*, **45**, pp. 2975-2985, May, 2006.

2. **C.P. Mc Elhinney**, J.B. Mc Donald, A. Castro, Y. Frauel, B. Javidi, and T.J. Naughton. "Depth-independent segmentation of macroscopic three-dimensional objects encoded in single perspectives of digital holograms", *Optics Letters*, **32**, pp.1229-1231, April, 2007.

3. U. Gopinathan, D.S. Monaghan, B.M. Hennelly, **C.P. Mc Elhinney**, D.P. Kelly, J.B. McDonald, T.J. Naughton, and J.T. Sheridan. "A projection system for real world three dimensional objects using spatial light modulators", *Journal of Display Technology*,**4**, pp.254-261, 2008.

4. **C.P. Mc Elhinney**, B.M. Hennelly, and T.J. Naughton. "Extended focused imaging for digital holograms of macroscopic three-dimensional objects", *Applied Optics* **47**, pp.D71-D79, July 2008.

Journal in submission

1. **C.P. Mc Elhinney**, B.M. Hennelly, J.B. Mc Donald, and T.J. Naughton " Multiple object segmentation in macroscopic three-dimensional scenes from a single perspective using digital holography", In submission to Applied Optics.

Journals in preparation

1. **C.P. Mc Elhinney**, B.M. Hennelly, L. Ahrenberg, and T.J. Naughton "Rapid twin-image removal through inverse aperture segmentation in inline digital holograms", in preparation.

2. **C.P. Mc Elhinney**, B.M. Hennelly, L. Ahrenberg, J. Maycock, T. Kreis, J. McDonald, and T.J. Naughton "Automated detection and subsequent removal of the twin-image through digital processing for in-line digital holography", in preparation.

Book Chapters

1. **C.P. Mc Elhinney**, B.M. Hennelly, T.J. Naughton, and B. Javidi "Extraction of three-dimensional information from reconstructions of in-line digital holograms", *Three-dimensional Imaging, Visualization and Display*, Springer October 2008.

Invited conference papers

1. J. Maycock, **C.P.Mc Elhinney**, A.E. Shortt, T.J. Naughton, J.B. McDonald, B.M. Hennelly, U. Gopinathan, D.S. Monaghan, J.T. Sheridan, and B. Javidi. "Holographic image processing of three-dimensional objects", *Proc. SPIE Optics East, Boston, USA*, **6016**, 23^{rd}-26^{th} October, 2005.

2. **C.P. Mc Elhinney**, B.M. Hennelly, and T.J. Naughton, "Image processing of real-world three-dimensional objects sensed with digital holography," *Advanced Laser Technologies - ALT'07, Levi, Finland*, 3^{rd}-7^{th} September, 2007.

3. **C.P. Mc Elhinney**, B.M. Hennelly, L. Ahrenberg, and T.J. Naughton "Automated twin-image removal from in-line digital holograms", Euro American Workshop on Information Optics, Annecy, France, 1^{st}-5^{th} June, 2008.

International Conference papers

1. **C.P. Mc Elhinney**, A.E. Shortt, T.J. Naughton, and B. Javidi. " Blockwise discrete Fourier transform analysis of DH data of three-dimensional objects", *Proc. SPIE, Colorado, USA*, **5557**, 2^{nd}-6^{th} August 2004.

2. **C.P. Mc Elhinney**, A.E. Shortt, T.J. Naughton, and B. Javidi. " Discrete Fourier transform quantisation tables for digital holograms of three-dimensional objects", *Proc. of Irish Machine Vision and Image Processing Conference, Dublin, Ireland*, 1^{st}-3^{rd} September 2004.

3. **C.P. Mc Elhinney**, J. Maycock, J.B. McDonald, T.J. Naughton, and B. Javidi. "Three-dimensional scene reconstruction using digital holograms", *Proc. SPIE – Opto-Ireland: Imaging and Vision, Dublin, Ireland* , **5823**, 4^{th}-6^{th} April, 2005.

4. **C.P. Mc Elhinney**, J. Maycock, T.J. Naughton, J.B. McDonald, and B. Javidi. "Extraction of three-dimensional shape information from a DH", *Proc. SPIE, San Diego, USA*, **5908**, 31^{st} July-4^{th} August 2005.

5. J. Maycock, **C.P. Mc Elhinney**, J.B. McDonald, T.J. Naughton, and B. Javidi "Independent Component Analysis Applied to Digital Holograms of Three-Dimensional Objects",*Proc. SPIE, San Diego, USA*,

5908,31st July-4th August 2005.

6. J. Maycock, **C.P. Mc Elhinney**, J.B. McDonald, T.J. Naughton, B.M. Hennelly and B. Javidi. "Speckle reduction in digital holography using Independent Component Analysis", *Proc. of SPIE Photonics Europe, Strasbourg, France*, **6187**, 3rd-7th April 2006.

7. J. Maycock, **C.P. Mc Elhinney**, B.M. Hennelly, J.B. McDonald, T.J. Naughton, and B. Javidi. "Reconstruction of partially occluded objects using digital holograms", *Proc. of SPIE Photonics Europe, Strasbourg, France*, **6187**, 3rd-7th April 2006.

8. B.M. Hennelly, **C.P. Mc Elhinney**, Y. Frauel, T.J. Naughton, and J.B. McDonald. "Superposition of digital holograms", *Workshop on Information Optics, Toledo, Spain*, 5th-7th June 2006.

9. B.M. Hennelly, J. Maycock, **C.P. Mc Elhinney**, T.J. Naughton, J.B. McDonald and B. Javidi, "Analysis of partially occluded objects encoded in digital holograms using the Wigner distribution function," *Proc. of SPIE, San Diego, USA*, **6311**, 13th-17th August 2006.

10. **C.P. Mc Elhinney**, J. Maycock, B.M. Hennelly, T.J. Naughton, J.B. McDonald, and B. Javidi. "Extraction and reconstruction of shape in-

formation from a DH of three-dimensional objects", *Proc. of Irish Machine Vision and Image Processing Conference, Dublin, Ireland*, 30^{th} August-1^{st} September 2006.

11. **C.P. Mc Elhinney**, J. Maycock, B.M. Hennelly, T.J. Naughton, J.B. McDonald, and B. Javidi. "Extraction of shape information from three-dimensional objects encoded in a DH" *ICO Topical Meeting on Optoinformatics/Information Photonics 2006, St. Petersburg, Russia*, 4^{th}-7^{th} September 2006.

12. **C.P. Mc Elhinney**, A. Castro, Y. Frauel, J.B. Mc Donald, B. Javidi, and T.J. Naughton. "Segmentation of three-dimensional objects from background in digital holograms", *Irish Machine Vision and Image Processing Conference, Maynooth, Ireland*, 5^{th}-7^{th} September 2007.

13. **C.P. Mc Elhinney**, B.M. Hennelly, J.B. Mc Donald, and T.J. Naughton. "Segmentation of macroscopic objects from digital holograms using focus and shape information", *Photonics Ireland Conference, Galway, Ireland*, 24^{th}-26^{th} September 2007.

14. **C.P. Mc Elhinney**, B.M. Hennelly, J.B. Mc Donald, and T.J. Naughton. "Segmentation of macroscopic object digital holographic reconstructions using extracted depth information", *Photonics Europe Confer-*

ence, Strasbourg, France, 7^{th}-11^{th} April 2008.

15. **C.P. Mc Elhinney**, B.M. Hennelly, and T.J. Naughton. "Focused image creation algorithms for digital holograms of macroscopic three-dimensional objects", *Digital Holography and Three-Dimensional Imaging, Tampa Bay, Florida, USA*, 17^{th}-19^{th} March 2008.

16. **C.P. Mc Elhinney**, B.M. Hennelly, and T.J. Naughton. "Focused Image creation approaches for macroscopic objects encoded in digital holograms", *Photonics Europe Conference, Strasbourg, France*, 7^{th}-11^{th} April 2008.

17. K.M. Molony, **C.P. Mc Elhinney**, B.M. Hennelly, and T.J. Naughton "Segmentation of three-dimensional scenes encoded in digital holograms", *Optics and Photonics, SPIE, San Diego, USA*, 10^{th}-14^{th} August 2008.

18. **C.P. Mc Elhinney**, B.M. Hennelly, L. Ahrenberg, and T.J. Naughton, "Twin-image reduction via segmented removal of the twin-image," *Optics and Photonics, SPIE, San Diego, USA*, 10^{th}-14^{th} August 2008.

19. D.P. Kelly, B.M. Hennelly, **C.P. Mc Elhinney**, and T.J. Naughton, "A Practical Guide to Digital Holography and Generalized Sampling," *Optics*

and Photonics, SPIE, San Diego, USA, 10^{th}-14^{th} August 2008.

20. L. Ahrenberg, **C.P. Mc Elhinney**, B.M. Hennelly, and T.J. Naughton, "Parallel approaches to reconstruction and noise reduction in digital holography", *ICO Topical Meeting on Optoinformatics/Information Photonics 2008, St. Petersburg, Russia*, 15^{th}-18^{th} September 2008.

1.6 Contributions of the thesis

In this thesis we detail, primarily, four contributions we have made to the field of DHIP. Until recently the extraction of information from DH reconstructions has been mostly limited to digitised reconstructions of optically recorded holograms and DHs of microscopic objects. We have developed image processing algorithms applicable to the reconstructions of DHs encoding three dimensional macroscopic objects. These reconstructions contain speckle which is viewed as noise by all current information extraction algorithms.

Our first contribution is the development of focus detection algorithms for digital holography. Many tasks require the accurate detection of focus either for an entire image or for regions within the image. We have developed a fast autofocus algorithm which takes as input a DH and outputs the estimated focal plane for the object(s) encoded in the DH. This autofocus algorithm has been optimised for digital holography by incorporating a stop condition

dependent on the depth-of-focus of the numerical reconstruction function. This algorithm, on average, determines the focal plane of an input DH in 14 iterations. We have also developed a DFF algorithm which takes a volume of reconstructions as input and outputs a maximum focus map and a depth map. We show how these outputs can be used to segment digital holographic reconstructions.

Through taking the maximum focus map output from our DFF algorithm we demonstrate our background segmentation algorithm. Our first segmentation algorithm segments a DH into object and background. This is a novel technique for performing segmentation of macroscopic three-dimensional objects. A block size and a threshold value are the two inputs that our algorithm requires. Varying these inputs can improve or reduce the accuracy of our technique. We recommend a general block size for use with all DHs although the threshold value is specific to each DH. A non-trivial extension to this segmentation work is our depth segmentation algorithm which segments a digital holographic scene into independent objects or object regions using a depth map. This depth information is calculated using our DFF algorithm and is applied to the same reconstruction volume used to segment the scene into object and background. This novel technique is experimentally verified using scenes containing multiple objects, including scenes with varying textures. The approach relies on the manual selection of areas (called modes) from a histogram of the depth information. These segmentation algorithms are our second contribution to the DHIP field.

A disadvantage of holographic reconstructions is the limited depth-of-

focus. When a DH is reconstructed, a distance value d is input as a parameter to the reconstruction algorithm. The depth-of-focus range for a reconstruction using the Fresnel approximation is in the order of a millimeter. For our third contribution we demonstrate our technique for creating an in-focus image of the macroscopic objects encoded in a DH. This EFI is created by combining numerical reconstructions with depth information extracted using our DFF algorithm. We have successfully created EFIs for scenes containing multiple and single objects and containing low and high contrast objects and have demonstrated an increase to the depth-of-focus of our system from 0.5mm to 56mm.

Our final contribution is a novel three stage solution to the twin-image problem. Given an in-line DH as input our algorithm only requires a single manual step. We detail how to calculate the spatial extent of the wanted twin-image at the unwanted twin-images focal plane. Our twin-image removal approach relies on our autofocus algorithm and our background segmentation algorithm. We provide experimental results of in-line DHs free of the twin-image. We have also implemented this algorithm using stream programming allowing us to calculate reconstructions of size 8192×8192 in 3.4 seconds and DHs free of the twin-image in under 9 seconds.

1.7 Outline of the thesis

Chapter 2 discusses the science of digital holography and goes into detail about its practical implementation. We start with the first stage of any digital holographic process, the recording stage. We detail the different recording

architectures available and compare their strengths and weaknesses. Furthermore, we proceed to the second stage of a digital holographic process, the different methods for identifying and removing of the error-terms inherent in DHs. In this section of the chapter we introduce PSI, which is the primary in-line digital holographic architecture used to record the holograms in this thesis. We then examine the PSI theory and detail the PSI proof. The last section in this chapter examines the third stage of the digital holographic process, the reconstruction stage. There are multiple reconstruction algorithms available for DHs [HS05], we detail the two used in this thesis and reason which applications the different algorithms are applicable to.

In Chapter 3 we detail how we evaluated the applicability of our selected focus measure, variance. We then discuss multiple algorithms we have developed which take a focus measure and a DH as input. The first algorithm is a novel rapid autofocus algorithm which calculates the focal plane of the centred object in a DH in, on average, 14 iterations. We then discuss in detail our DFF algorithm which calculates a depth map and a maximum focus map from a volume of digital holographic reconstructions. These outputs of DFF are the foundation of the experimental results discussed in Chapters 4,5 and 6. We conclude the chapter by discussing the limitations of the algorithms and how they can be implemented in general to all forms of digital holography.

Our segmentation algorithms and their applications are discussed in Chapter 4. We first introduce a technique for segmenting a DHs reconstruction into object and background in Chapter 4.1. This is achieved through the

application of our DFF algorithm and the subsequent thresholding of the maximum focus map. We demonstrate how the segmentation is successful for a range of DHs encoding real-world 3D objects of varying texture and contrast. Our hypothesis that applying the segmentation process to a volume of reconstructions is more successful than its application to an individual reconstruction is then examined. In Chapter 4.1.5 we demonstrate how our segmentation process can be applied to synthetic digital holographic scene creation, through the segmentation of the full objects wavefront and the digital superposition of multiple segmented objects to create a new synthetic DH. We demonstrate that the 3D information in the original DHs is retained in the new synthetic DH by displaying reconstructions which display the properties of parallax and numerical focusing in the new synthetic DH. We discuss the first (to our knowledge) technique for segmenting a real-world reflective macroscopic scene, recorded by digital holography, into independent objects and object regions using depth information in Chapter 4.2. In the first of three stages, the degree of focus is estimated at each point in the reconstruction volume. In the second stage, a DFF algorithm is used to calculate a depth map of the scene and to segment the scene from the background. In the third stage, a depth segmentation algorithm is applied to the depth map, and different object regions are identified and segmented. We then conclude the chapter with a discussion of the advantages and disadvantages of the proposed algorithms and techniques.

In Chapter 5 we present a method for creating EFIs from sets of digital holographic reconstructions of macroscopic objects. We first create a depth

map using our DFF technique. We then combine the depth map and the intensity information from a volume of reconstructions to create an EFI. We discuss a method for creating an EFI in a short length of time using a non-overlapping block approach and a method for creating a qualitatively more accurate EFI using an overlapping block approach. We also demonstrate EFIs created on both low and high-contrast scenes, and discuss the advantages and disadvantages of the techniques. We present a sequential discussion of our different EFI creation approaches. This includes experimental results of EFIs created from DHs encoding real-world 3D objects. We then finish the chapter by drawing conclusions about the benefits and limitations of the different EFI creation algorithms.

Our twin-image removal algorithm is examined in Chapter 6. We discuss for the first time the relative spreading of the unwanted twin-image and the wanted twin-image and how one might manage this spreading in the numerical reconstruction. We discuss the implementation of a rapid twin-image removal approach which requires only one manual thresholding step. As part of our new approach we automatically determine the depth using a novel autofocus algorithm optimised for digital holography. Once determined, this depth allows us to calculate the padding required to ensure that none of the wanted twin-image's energy is wrapped in the reconstruction window, which can then be removed in the segmentation process. The segmentation is performed using our DFF algorithm and a manual thresholding step. We provide experimental results of our twin-image removal process created from DHs encoding real-world 3D objects and compares it to PSI DHs of the same

objects. Some conclusions are drawn about the benefits and limitations of our algorithm and we briefly discuss future improvements.

In Chapter 7 we summarise the novel techniques presented in this thesis along with their results. We discuss the limitations to the current techniques and briefly offer some insight into methods to overcome these limitations. We then discuss how we are currently improving these algorithms and addressing their highlighted limitations. We present our progress in this continuing work in Chapter 8.

Chapter 2

Introduction to Digital Holography

Standard photography uses a lens to focus light diffracted from a scene onto a photographic film, or CCD, which records a focused image. This scene is illuminated using incoherent light. Incoherent light is a wavefront of light containing different phases and possibly different wavelengths. (i.e. sunlight). Light is diffracted from an object in the scene and this wavefront propagates towards the recording medium. In general for recording a hologram we split the laser beam into an object beam and a reference beam. The object beam illuminates the object, and the diffracted object wavefront propagates a distance d to the recording medium[Gab48, Cau79, LU62, LU63, LU64, Goo05, Kre05]. The recording media are holographic film in the case of optical holography, and a CCD in the case of digital holography. The reference beam propagates uninterfered to the recording medium,

where it interferes with the diffracted object beam. This interference pattern is then recorded, and is called an interferogram or a hologram. It is the interference of the reference beam with the diffracted object wavefront (which has an unknown amplitude and phase) that produces an intensity pattern containing the objects amplitude and phase information. The hologram allows the viewing of different perspectives of the scene by tilting the holographic film or changing the inputs to the numerical reconstruction algorithm in digital holography. To reconstruct an optical hologram, the film is illuminated using the reference beam that was used to record the hologram. This creates a real image at a distance d and a virtual image at a distance $-d$ from the film. A DH can be reconstructed using a discretised version of the Fresnel-Kirchoff integral[OS87]. The Fresnel-Kirchoff integral models the propagation of light. Given a wavefront and a distance d, it approximates the wavefront after propagation of the distance d.

In this chapter we deal with the three stages of digital holography. In Sect. 2.1 we discuss digital holographic recording and detail the two main architectures used, in-line and off-axis. We discuss the recording constraints of both architectures and discuss their relevant advantages and disadvantages. Section 2.2 deals with the main error terms which are inherent in the recorded DH. A brief discussion of the approaches for removing these error sources from holograms recorded using the two architectures will follow. The final section of this chapter discusses the third stage of digital holography, the reconstruction stage. We introduce the two reconstruction functions used in this thesis and demonstrate their relative advantages and limitations. The

3D information contained within a DH is visible in the reconstruction plane in two ways. The first is through numerical focusing, reconstructing at different distances away from the CCD. Secondly in perspective information, DHs can be reconstructed from different perspectives and we display this information and briefly discuss how to reconstruct from different perspectives. Speckle noise in the reconstruction plane can be suppressed and we demonstrate the visual impact of our selected speckle reduction technique.

2.1 Hologram recording

The recording of a hologram does not differ much from the recording of a photograph. In Fig. 2.1 the two are displayed. In both cases, the object (or scene) needs to be illuminated and then the diffracted wavefront from the object propagates to a recording medium where it is recorded as an image. In photography the illumination source is generally incoherent light such as the sun or a flash, and in most cases there is a lens or alternatively a pinholeplaced in front of the film to focus the light and create a focused image of the object/scene. In holography the illumination source is, in general, coherent. There are two other differences between a simple photograph and a hologram recording. The first is that another light source illumintates the recording medium. This is called the reference wavefront and is also coherent. These two waves, object and reference, come from the same source, are split in the experimental setup and must be mutually coherent. At the recording medium the interference between the object and reference wavefronts is recorded and this interference pattern is a hologram. The second difference is that, in

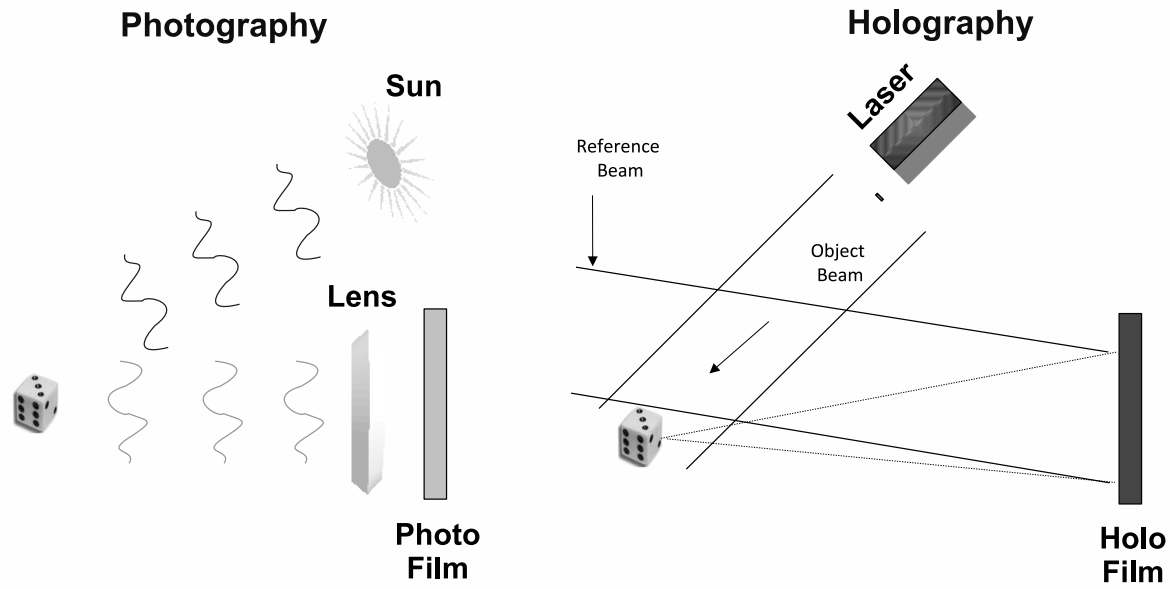

Figure 2.1: Recording of a photograph and a hologram.

general, a lens is not needed in a holographic system. This is because a hologram is not an image of the object/scene but is a representation of the object wavefront. It contains 3D information about the object/scene and this information can be reconstructed (optically or numerically).

DH relies on the ability to record an interference pattern, which requires one to use coherent light. Coherence can be thought of as the ability of light waves to interfere [Kre05]. There are two types of coherence: temporal and spatial. It is difficult to observe visible interference with sunlight. One primary reason is that it contains many wavelengths (it has a broad frequency spectrum) which results in it having low temporal coherence. A monochromatic light source such as a sodium lamp would be highly temporally coherent but would have low spatial coherence because the phases between different parts of the wavefront are uncorrelated. For macroscopic objects with large 3D dimensions we need a specific light source which is sufficiently spatially coherent (and by default temporally coherent) such as a laser. When we correlate a wavefront with itself at different time steps we are examining its temporal coherence. In a Michelson interferometer a coherent light source is split into two beams that then propagate to the detector. These two beams have the same path length to the detector propagate. The temporal coherence of the light source can be tested by modifying the path length of one of the beams and observing whether an interference pattern is recorded. Also, when we attempt to correlate different parts of the wavefront in one plane we are examining the wavefronts spatial coherence. The spatial coherence of a beam is tested using Young's double aperture experiment. An

opaque screen is placed in front of a light source and a detector is placed behind the opaque screen. The screen has two small slits and if the beam is coherent an interference pattern will be observed at the detector.

To understand what a hologram actually contains we now provide a mathematical description of what is recorded. We define the reference wavefront as,

$$R_{\Delta\phi}(x,y) = A_{R_{\Delta\phi}}(x,y)\exp\{i[\phi_{R_{\Delta\phi}}(x,y) + \Delta\phi]\}, \tag{2.1}$$

where $\Delta\phi$ is an arbitrary phase shift in the reference wavefront and the object wavefront is defined as,

$$O(x,y) = A_O(x,y)\exp\{i[\phi_O(x,y)]\}. \tag{2.2}$$

Where $A(x,y)$ is a wavefronts amplitude, $\phi(x,y)$ is a wavefronts phase. The interference pattern $H(x,y)$ that is incident at the recording medium can be represented as a superposition of these waves

$$H(x,y) = O(x,y) + R_{\Delta\phi}(x,y). \tag{2.3}$$

We now describe what is recorded when a CCD is used as the recording medium and how this is different from the recording of any photograph. A CCD can only record intensity and if you were to record the object wavefront on its own you would just record the intensity of Eq. (2.2) which is $A_O(x,y)^2$ and if you were to record the reference wavefront on its own, you would

record $A_{R_{\Delta\phi}}(x,y)^2$. If you were to just add these two recordings together you would have $A_O(x,y)^2 + A_{R_{\Delta\phi}}(x,y)^2$ which is an image where the only object wavefront information is its amplitude squared. In short, you would have less than a standard photograph as you wouldn't even have a focused image of the object. Since a CCD can only record intensity, how is it that a hologram contains the object wavefront (more than just intensity)? Well, if you let the object beam and reference beam interfere at the CCD plane what you record is

$$H_{\Delta\phi}(x,y) = |O(x,y,0) + R_{\Delta\phi}(x,y,0)|^2. \tag{2.4}$$

In this case you are getting an intensity reading after the superposition of the object wavefront and the reference wavefront, not before. When you expand this equation you find that the recorded hologram is defined by

$$I(x,y) = O^2(x,y) + R^2_{\Delta\phi}(x,y) + O^*(x,y)R_{\Delta\phi}(x,y) + O(x,y)R^*_{\Delta\phi}(x,y), \tag{2.5}$$

where $*$ is the complex conjugate. In this format it is easy to explain the three components of a hologram. We have the dc-terms, $O^2(x,y)$ and $R^2_{\Delta\phi}(x,y)$, which are corruptive error sources. We have the real image $O^*(x,y)R_{\Delta\phi}(x,y)$ and the virtual image $O(x,y)R^*_{\Delta\phi}(x,y)$ which combined are called the twin images. Only one of the twin-images is required to reconstruct a hologram. By taking one of these twin-images and multiplying it by the original reference wavefront (or its conjugate depending on which twin is selected) we are able to propagate the object wavefront. This is numerical propagation and

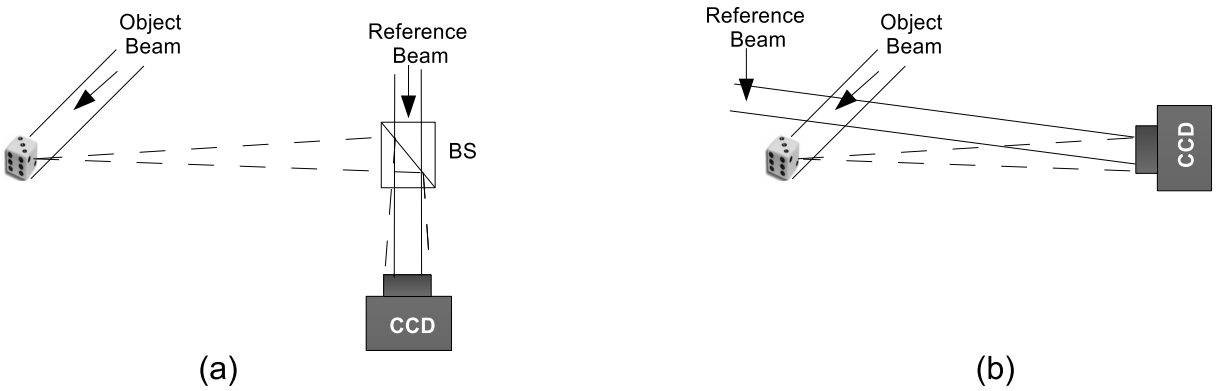

Figure 2.2: Digital hologram recording: (a) in-line configuration, (b) off-axis configuration. BS: beam splitter.

is discussed in more detail in Sect. 2.3. However, if the second twin-image is not removed before propagation it can manifest as another corruptive error source. This equation can also be written as

$$\begin{aligned} H_{\Delta\phi}(x,y) &= |O(x,y,0) + R_{\Delta\phi}(x,y,0)|^2 \\ &= A_O^2(x,y) + A_{R_{\Delta\phi}}^2(x,y) + 2A_O(x,y)A_{R_{\Delta\phi}}(x,y) \\ &\quad \times \cos[\phi_O(x,y) - \phi_{R_{\Delta\phi}}(x,y) - \Delta\phi], \end{aligned} \tag{2.6}$$

and within this equation is information about both the objects amplitude $A_O(x,y)$ and the objects phase $\phi_O(x,y)$. We will use this form of the equation to anaylse the theory of PSI in Chapter 2.2.1

2.1.1 Architectures

There are two forms of digital holographic recording: in-line and off-axis. In this thesis we focus on macroscopic reflective digital holography. In an in-line setup, shown in Fig. 2.2(a), the reference beam and the diffracted

object beam are both at the same angle with respect to the CCD. In an off-axis setup, shown in Fig. 2.2(b), the reference beam is at a different angle with respect to the CCD than that of the diffracted object wavefront. The popularity of off-axis digital holography over in-line digital holography has been based on the host of computationally simple approaches for removing these error sources [KJ97, KJ04, SJ94, PKI+00, CMD00, ZLG04, SJ04a, Kre05, ZLG04]. It is only recently that in-line digital holography is developing methods for dealing with these error sources (particularly the twin-image problem). The in-line setup has many advantages over an off-axis setup including; a less developed speckle noise and a more efficient use of the CCD bandwidth[XMA00] and is our preference.

In-line

In-line holography refers to the form of holography where the object is centred on the optical axis of the recording medium and the reference beam is incident on the recording medium at a 0° angle as shown in Fig. 2.3. The 1D geometry of which is shown in Fig. 2.4. It is important to obey the sampling theorem when recording a DH, as a DH is just a discretisation of a continuous signal [XMA00, Kre05, PL08]. We start our analysis of in-line sampling with the geometry of an in-line system. Our analysis is carried out in one-dimension without loss of generality. What we are looking to find out is, for a given object what is the distance, $d_{in-line}$, it needs to be placed at away from the CCD to obey the sampling theorem. The sampling theorem states that the sampling rate must be higher than the Nyquist rate to successfully

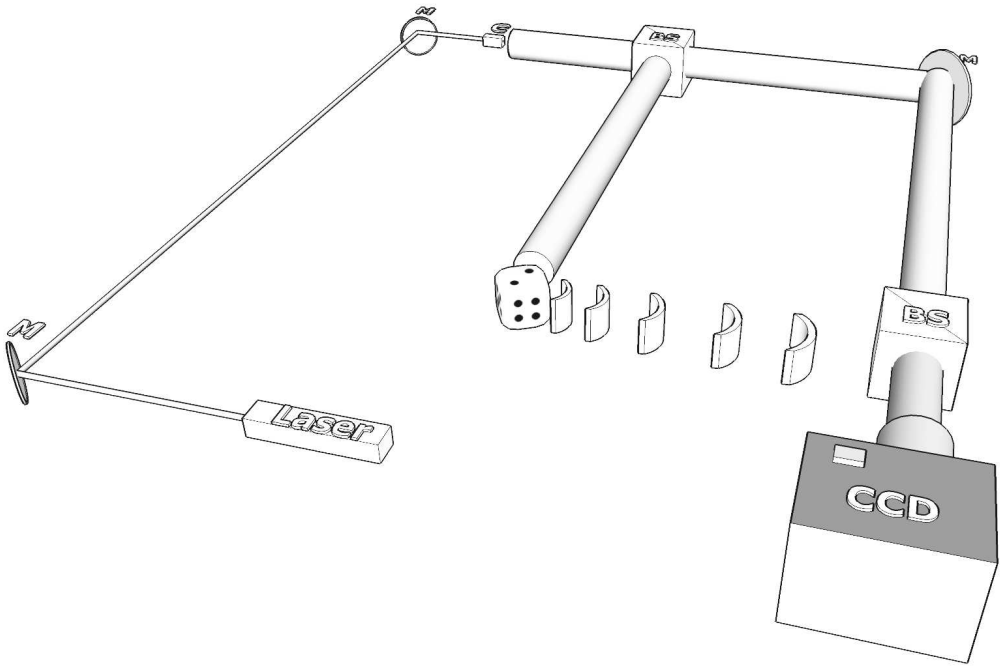

Figure 2.3: In-line setup, M: mirror, C: collimator and BS: beam splitter.

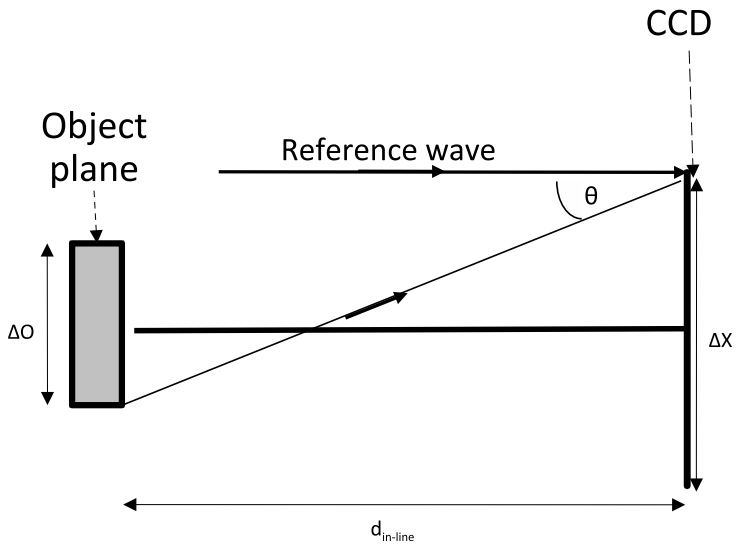

Figure 2.4: In-line setup, θ is the maximum interference angle, ΔO is the spatial extent of the object and ΔX is the spatial extent of the CCD.

recover the original signal. In Fig. 2.4, θ is the maximum interference angle allowed between the reference wave direction and the object wave direction, for in-line digital holography, to avoid aliasing. According to the sampling theorem, in order to record the signal successfully there must be at least 2 pixels per interference fringe. Given a CCD with a spatial extent ΔX and N_x pixels, we can calculate the spatial resolution of a pixel as $\delta\xi = \frac{\Delta X}{N_x}$. The sampling theorem states that

$$2\delta\xi < \Delta p \tag{2.7}$$

where Δp is the size of a fringe period and can be calculated with

$$\Delta p = \frac{\lambda}{2\sin[\frac{\theta}{2}]}, \tag{2.8}$$

where λ is the wavelength of the light. We are assuming that the fringes are formed from the interference of two plane waves - the reference wavefront at an angle of 0° and the most extreme object angular plane wave at an angle θ. Therefore,

$$2\delta\xi < \frac{\lambda}{2\sin[\frac{\theta}{2}]}. \tag{2.9}$$

We can further simplify this equation with the approximation $\sin\theta \approx \tan\theta \approx \theta$, due to our knowledge that θ will remain small, to

$$2\delta\xi < \frac{\lambda}{\theta}, \tag{2.10}$$

and use this equation to approximate θ as

$$\theta < \frac{\lambda}{2\delta\xi}. \tag{2.11}$$

We can also represent θ in terms of $d_{in-line}$ using the geometry of Fig. 2.4 with

$$\tan\theta = \frac{\frac{\Delta X}{2} + \frac{\Delta O}{2}}{d_{in-line}} \tag{2.12}$$

and again due to our knowledge that θ will remain small we can substitute this into Eq. (2.11) to obtain

$$\frac{\frac{\Delta X}{2} + \frac{\Delta O}{2}}{d_{in-line}} < \frac{\lambda}{2\delta\xi}. \tag{2.13}$$

We can then resolve this equation with respect to $d_{in-line}$ to come up with an equation for the minimum distance an object of size ΔO needs to be placed away from the CCD with

$$d_{in-line} > \frac{\delta\xi(\Delta O + \Delta X)}{\lambda}. \tag{2.14}$$

Another property of the in-line configuration is that the dc-terms and twin-images are all in the same spatial and spatial frequency location. This allows for efficient use of the CCD pixels as all the pixels in the reconstruction plane are capable of being used to contain object information. There is a negative side however, the reconstructions from in-line holograms are corrupted by these terms and the twin-image has always been hard to remove in in-line digital holography.

Off-Axis

Off-axis holography gets its name from the fact that the reference wave and the object wave interfere at the CCD at an offset angle, as shown in Fig. 2.5. The changes to the recording geometry are highlighted in Fig. 2.6. These changes impact on the required distance that the object needs to be placed at to maintain the sampling theory. The first change to the recording geometry compared to the in-line system is that the object is offset from the optical axis of the CCD, a distance of a. This introduces an offset angle $\theta_{off-axis}$ which must be

$$\theta_{off-axis} >= \sin^{-1}(3K\lambda), \tag{2.15}$$

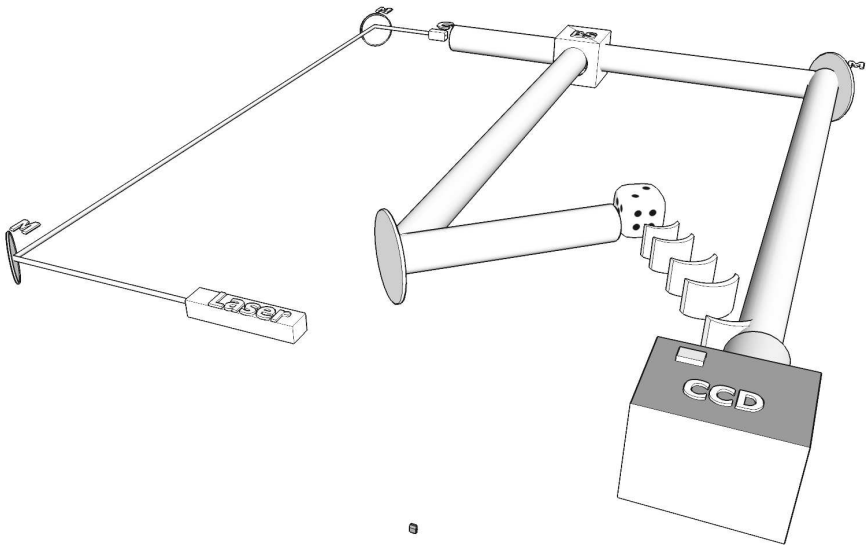

Figure 2.5: Off-axis setup, M: mirror, C: collimator and BS: beam splitter.

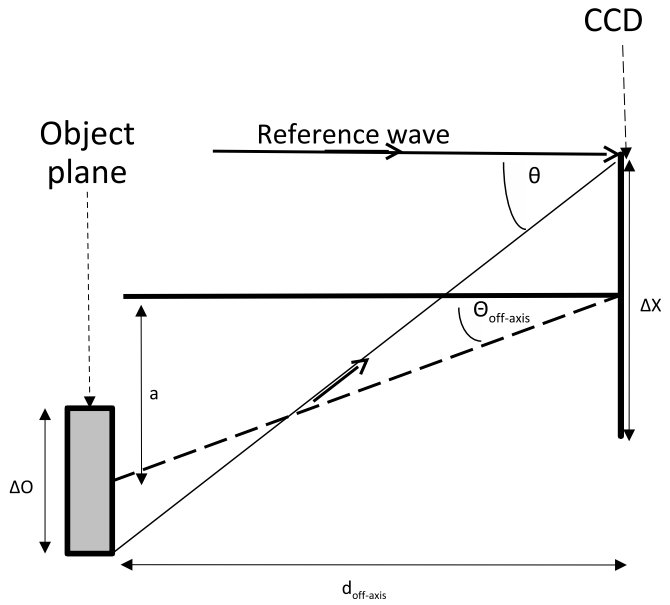

Figure 2.6: Off-axis setup, θ is the maximum interference angle, $\theta_{off-axis}$ is the offset angle with respect to the optical axis, a is the offset distance, ΔO is the spatial extent of the object and ΔX is the spatial extent of the CCD.

where K is the highest spatial frequency of the object [Goo05]. This is required so that the error sources in the hologram are separated in the spatial and spatial frequency domain. This angle can be approximated, for small values of $\theta_{off-axis}$ with [XMA00]

$$\theta_{off-axis} \approx \frac{3\Delta O}{2D} \tag{2.16}$$

where D is the distance the object is placed away from the CCD, in our example $D = d_{off-axis}$. Now $d_{off-axis}$ can be expressed as [XMA00]

$$d_{off-axis} > \frac{\delta\xi(\Delta X + \Delta O + 2a)}{\lambda} \tag{2.17}$$

where from Fig. 2.6 and Eq. (2.16)

$$\begin{aligned} \tan\theta_{off-axis} &= \frac{a}{d_{off-axis}} && (2.18)\\ a &= \theta_{off-axis} \times d_{off-axis} && (2.19)\\ &= \frac{3\Delta O}{2d_{off-axis}} \times d_{off-axis} && (2.20)\\ &= \frac{3\Delta O}{2}. && (2.21) \end{aligned}$$

By substituting this into Eq. (2.17) we obtain our final representation of $d_{off-axis}$ as

$$d_{off-axis} > \frac{\delta\xi(\Delta X + 4\Delta O)}{\lambda}. \tag{2.22}$$

The condition set by Eq. (2.15) is one of the most important for off-axis digital holography. It allows for the spatial frequency separation of the twin-

images and dc-term at the CCD plane, which in turn enables for their easy removal using spatial filtering. This again does have a negative impact on the reconstructions though. In the reconstructions, the dc-term is in the centre the real image is in-focus but at an angle related to the offset angle, and the virtual image is out-of-focus at the inverse offset angle. The optimal recording occurs when the three orders do not overlap in the reconstruction plane [PL08]. It has been demonstrated that the dc-term is twice the width of either of the twins in the reconstruction plane. This means that, in general, only about one quarter of the pixels of the CCD at the reconstruction plane can contain object information [PL08]. This is quite inefficient especially when compared to the in-line reconstructions, the pixel efficiency in the off-axis architecture is sacrificed for the ease of the removal of the error terms.

2.1.2 Recording Constraints

When recording a DH there are two main recording constraints dependent on the architecture, the first is the objects placement in the z-direction (its distance from the CCD). The second is its positioning in relation to the CCD. We have shown how to calculate the minimum distance an object needs to be placed for both in-line, Eq. (2.14), and off-axis, Eq. (2.22). We now show what practical impact this constraint has on DH recording. Given our current experimental setup, a CCD with 2048×2048 pixels of size $7.4\mu m$ and a 632.8nm laser source, we have plotted the size of the object to be recorded as a function of the minimum recording distance, for both architectures, in Fig. 2.7. What is evident from Eq. (2.14) and Eq. (2.22) and the figure is

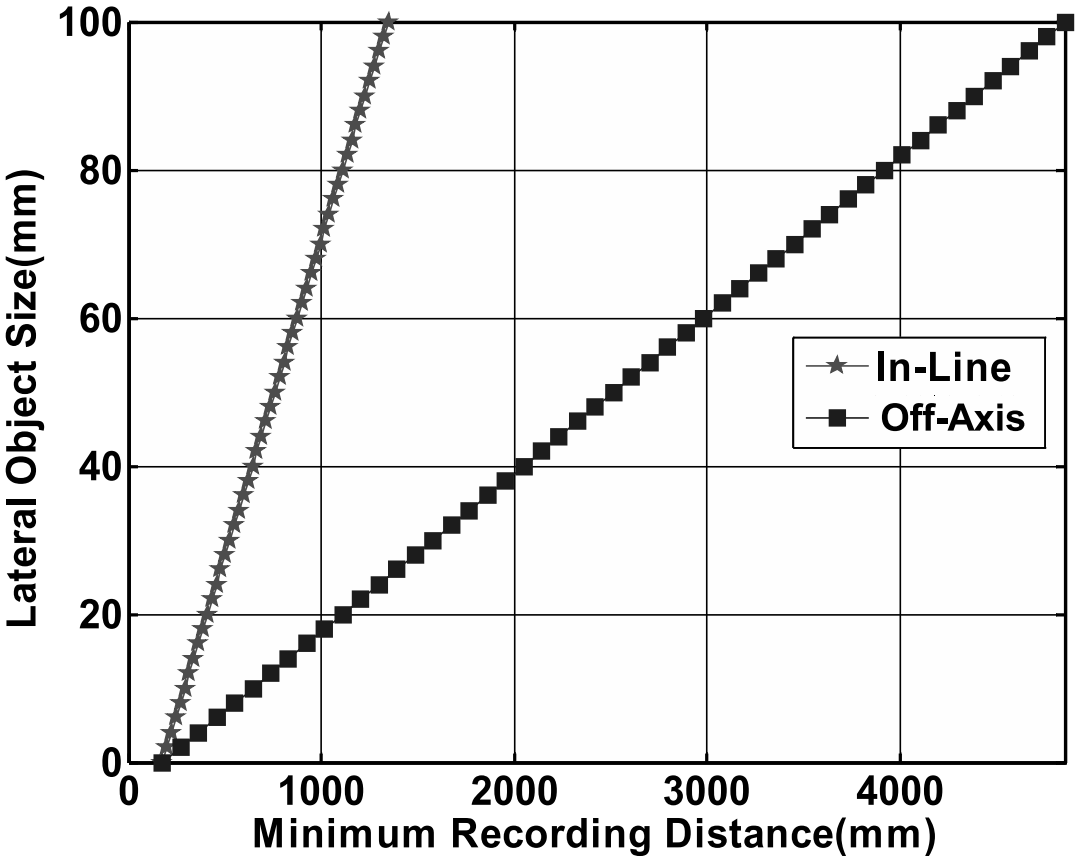

Figure 2.7: Plot of object size as a function of minimum recording distance for in-line and off-axis holographic setups.

that the slope for both architectures minimum recording distance is linear. However, the slope for an in-line setup is equal to $\frac{\delta\xi}{\lambda}$ while for an off-axis setup the slope is 4 times larger at $\frac{4\delta\xi}{\lambda}$ [XMA00, PL08]. This translates to the following equality for the same object

$$d_{off-axis} = \frac{3\Delta O \times \delta\xi}{\lambda} \times d_{in-line}. \tag{2.23}$$

This is quite a significant difference between the recording setups.

The second recording constraint to consider is object placement. This is quite simple in the in-line case. To use the pixels of the CCD most efficiently and to record the highest possible spatial frequencies of the object, its centre should be placed on the optical axis of the experimental setup. For the off-axis case the object placement is dependent, primarily, on the object size which allows for the calculation of the offset angle with Eq. (2.15).

From our discussion of the recording architectures, it is apparent that in-line offers higher resolution and for the object to be placed closer to the CCD. These are both desirable properties. However, error-term removal in off-axis is a much simpler process and to date more successful. Also an in-line experimental setup is more difficult to practically implement and calibrate, due to the requirement that the reference and object wavefront must both be at a 0° angle with respect to the CCD.

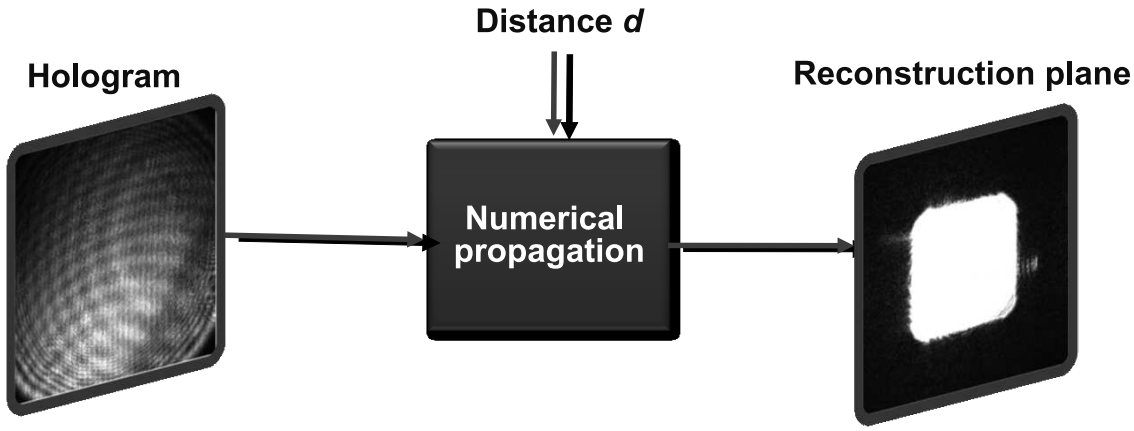

Figure 2.8: Numerical reconstruction of an in-line DH displaying the dc-term.

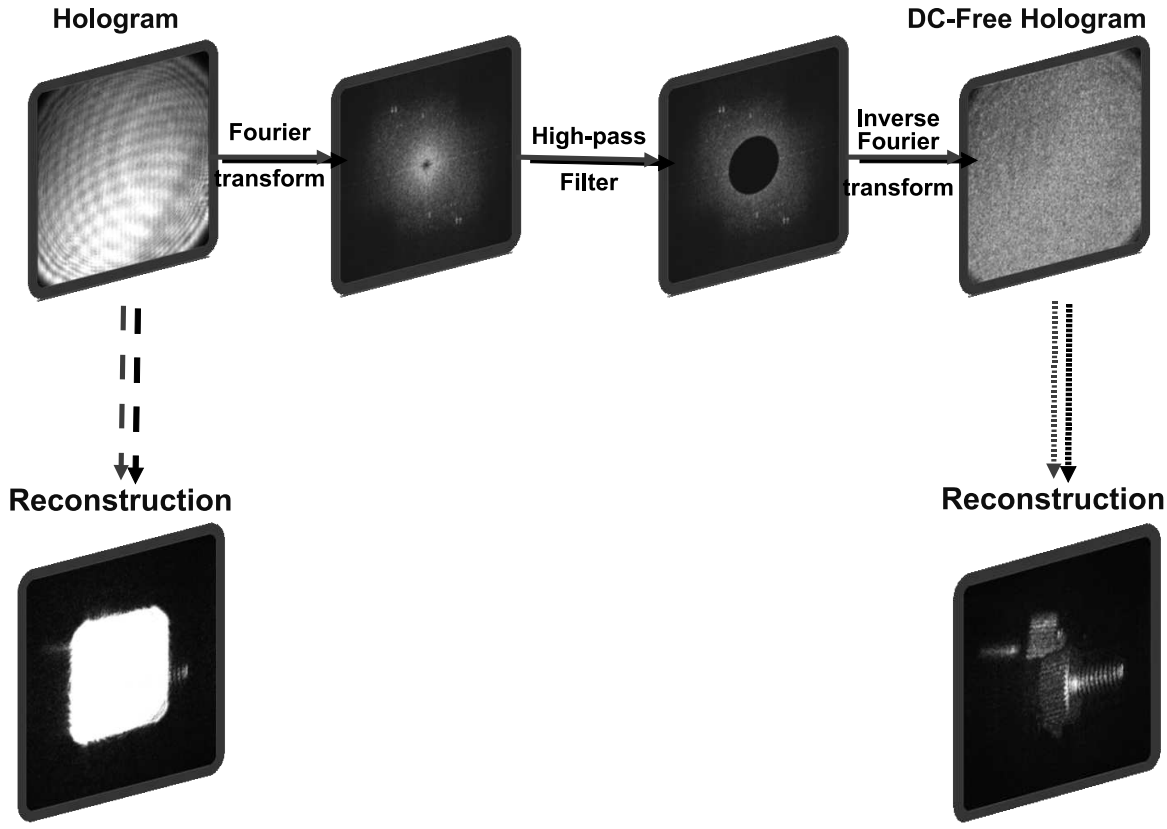

Figure 2.9: DC-term removal for digital holography.

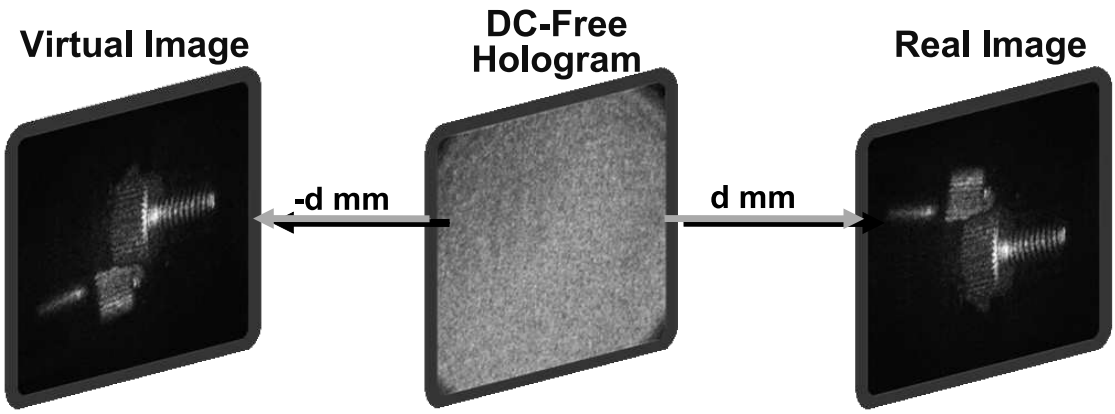

Figure 2.10: Numerical reconstruction of an in-line DH displaying the twin-images.

2.2 Error-terms

We now consider some of the error sources associated with digital holography. The two error terms in a hologram were identified in Eq. (2.5), these were the dc-term and the virtual image (the unwanted twin image). The dc-term is the summation of the intensity of the reference wavefront and the intensity of the object wavefront and dominates the low-frequencies in the spatial frequency domain of the hologram. The impact of the dc-term on a reconstruction is shown in Fig. 2.8 where the object has been occluded by the high intensity of the dc-term. There are two common methods that are used to suppress the dc-term for both in-line and off-axis DHs. The first method involves recording the object and reference wavefronts intensity separate to the recording of the hologram. Once these have been recorded it is possible to just subtract these from the original hologram to leave only the real and virtual images in the hologram, as $I(x,y) - O^2(x,y) - R^2_{\Delta\phi}(x,y) =$

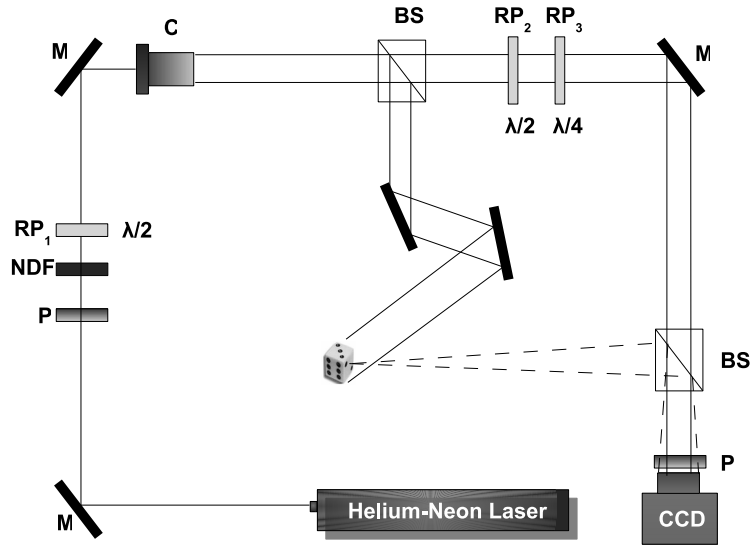

Figure 2.11: Experimental setup for PSI: P, polarizer; NDF, neutral density filter; C, collimator; BE, beam expander; BS, beam splitter; RP, retardation plate; M, mirror.

$O(x,y)R^*_{\Delta\phi}(x,y) + O^*(x,y)R_{\Delta\phi}(x,y)$. This requires the object to be static for the duration of all recordings which is not preferable as it restricts the range of recordable objects. Also the successful recording of the intensity of the object wavefront is object dependent and not generally applicable. This process can be simplified to just the subtraction of the reference wavefronts intensity [SJ04a, DJ06]. Another method is to high-pass filter the hologram, removing the low frequencies, which is where the dc-term is located. This process is displayed in Fig. 2.9 where the new filtered hologram $I'(x,y)$ is defined by

$$I'(x,y) = F^{-1}(F(I(x,y)) \times circ(x,y)), \tag{2.24}$$

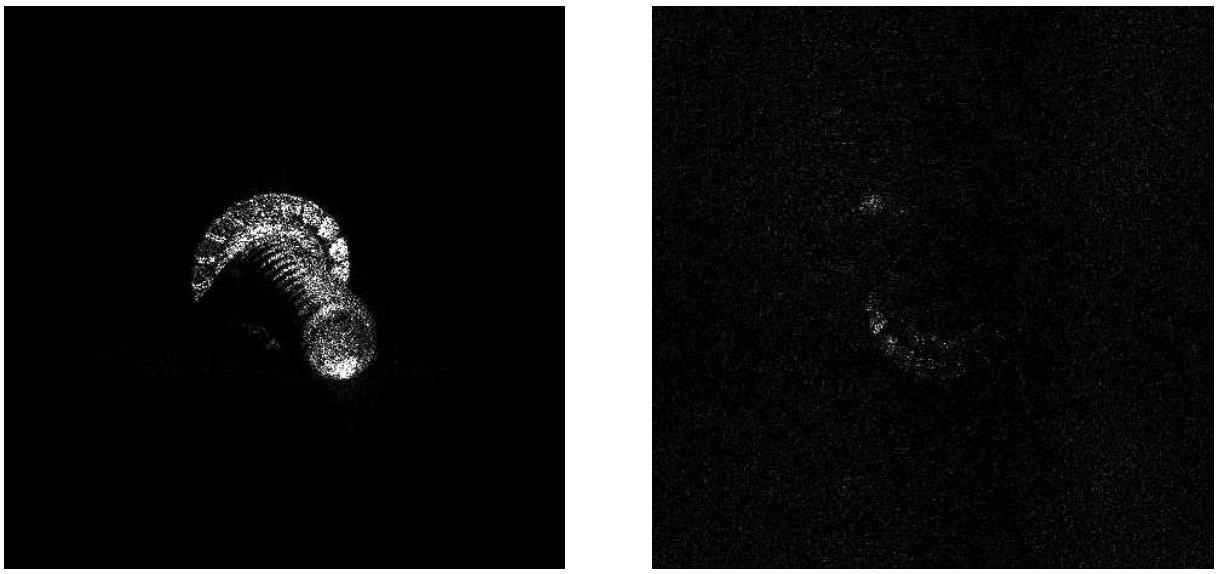

Figure 2.12: Numerical reconstruction from a PSI DH recorded by Tajahuerce [JT00, MHBN08], (a) real image and (b) virtual image (contrast is the same for both images).

where $circ(x, y)$ is another image where there is a circular occlusion at its centre. The object is now visible in the reconstruction of the new filtered hologram. There are many ways of suppressing the dc-term but most attempt to suppress the low-frequencies at the hologram plane [Kre05].

In in-line digital holography, the twin-images both lie on the optical axis, which results in the corruption of the reconstruction of one twin by the out-of-focus energy of the other twin. They are also held within the same area in the spatial frequency domain, so simple spatial filtering will not remove either one. A reconstruction of both of the real and virtual image is shown in Fig. 2.10. As explained in Chapter 1.4 twin-image removal and suppression is a complicated and well researched area, and there is no individually accepted method for removing the twin-image for in-line digital holography. We have developed a novel method which segments and removes the unwanted twin from an in-line DH at its focal plane which is dealt with in Chapter 6. There already exists some techniques for dealing with the twin-image in in-line digital holography [YZ97, LBV99]. The most popular of these is PSI which requires the recording of multiple independent holograms. This produces in-line DHs free of the dc-term and unwanted twin-image but requires a static scene to record the holograms. This is the technique we employ to record our DHs and is explained in detail in the next section. In off-axis digital holography removing the twin-image is generally trivial, this is because the real and virtual image are separated in the spatial frequency domain and one or the other can be removed through band-pass filtering. Also if the DH is recorded with a sufficiently large offset angle then, as stated by Kreis [Kre05],

"One must admit that this twin image elimination is of pure cosmetic nature because the twin images must be well separated, but then they do not conflict with each other."

2.2.1 PSI error suppression

PSI (Phase-shifting interferometry) [YZ97] is a digital holographic technique that calculates in-line holograms free of the twin-image and dc-term although it requires multiple recordings. A set of DHs are recorded where a specific phase shift has been introduced into the reference wavefront before each recording. Our PSI setup is displayed in Fig. 2.11. In our system, a linearly polarised Helium-Neon (632.8 nm) laser beam is expanded and collimated, and then split into object and reference waves. The object wave illuminates an object placed at a distance d (selected based on Eq. (2.14)). Our CCD camera has 2048×2032 pixels of size 7.4μm in both dimensions.

PSI Theory

To calculate a hologram using a PSI setup, multiple interferograms with different phase shifts need to be recorded. Different techniques exist for the creation of holograms using different numbers of interferograms and different phase shifts [Kre05]. We employ the four frame PSI algorithm first proposed

for digital holography by Yamaguchi et al. [YZ97], which requires the recording of four DHs with phase shifts in the reference beam of $[0°, 90°, 180°, 270°]$.

PSI assumes that the amplitude of the reference wavefronts is a constant, $\forall\Delta\phi : A^2_{R_{\Delta\phi}}(x,y) = 1$. It also assumes that the phase is constant and the the initial phase can be given a value of zero, $\phi_{R_0}(x,y) = 0$. This is because the reference beam should be a plane wave and the phase shift should not affect the reference wavefronts original phase and amplitude. Taking this information we can now rewrite Eqn. (2.6) as

$$\begin{aligned} H_{\Delta\phi}(x,y) &= A^2_O(x,y) + 1^2 + 2A_O(x,y)(1)\cos[\phi_O(x,y) - 0 - \Delta\phi] \\ &= A^2_O(x,y) + 1 + 2A_O(x,y)\cos[\phi_O(x,y) - \Delta\phi]. \end{aligned} \tag{2.25}$$

For simplicity we define $P_{\Delta\phi}$ to be

$$P_{\Delta\phi}(x,y) = \cos[\phi_O(x,y) - \Delta\phi] \tag{2.26}$$

therefore,

$$H_{\Delta\phi}(x,y) = A^2_O(x,y) + 1 + 2A_O(x,y)P_{\Delta\phi}(x,y). \tag{2.27}$$

The amplitude of the object wavefront, $A_O(x,y)$, is calculated using four interferograms with phase shifts of $\Delta\phi = 0, \frac{\pi}{2}, \pi, \frac{3\pi}{2}$

$$A_O(x,y) = \frac{1}{4}\sqrt{|H_0(x,y) - H_\pi(x,y)|^2 + |H_{\frac{\pi}{2}}(x,y) - H_{\frac{3\pi}{2}}(x,y)|^2}. \tag{2.28}$$

We recover the phase of the object wavefront, $\phi_O(x,y)$, with the same holo-

grams

$$\phi_O(x,y) = \arctan\left\{\frac{H_{\frac{\pi}{2}}(x,y) - H_{\frac{3\pi}{2}}(x,y)}{H_0(x,y) - H_\pi(x,y)}\right\}. \tag{2.29}$$

We can simplify these equations by defining α and β as

$$\alpha = H_0(x,y) - H_\pi(x,y) \tag{2.30}$$

$$\beta = H_{\frac{\pi}{2}}(x,y) - H_{\frac{3\pi}{2}}(x,y) \tag{2.31}$$

and substituting these into Eq.(2.28) and (2.29) to obtain

$$A_O(x,y) = \frac{1}{4}\sqrt{|\alpha|^2 + |\beta|^2} \tag{2.32}$$

$$\phi_O(x,y) = \arctan\left\{\frac{\beta}{\alpha}\right\}, \tag{2.33}$$

PSI Proof

To prove that these equations return the correct amplitude and phase we first need to solve α and β

$$\begin{aligned} \alpha &= H_0(x,y) - H_\pi(x,y) \\ &= [A_O^2(x,y) + 1 + 2A_O(x,y)P_O] - [A_O^2(x,y) + 1 + 2A_O(x,y)P_\pi] \\ &= 2A_O(x,y)[(P_O - P_\pi) \end{aligned} \tag{2.34}$$

$$\begin{aligned}\beta &= H_{\frac{\pi}{2}}(x,y) - H_{\frac{3\pi}{2}}(x,y) \\ &= [A_O^2(x,y) + 1 + 2A_O(x,y)P_{\frac{\pi}{2}}] - [A_O^2(x,y) + 1 + 2A_O(x,y)P_{\frac{3\pi}{2}}] \\ &= 2A_O(x,y)(P_{\frac{\pi}{2}} - P_{\frac{3\pi}{2}}).\end{aligned} \tag{2.35}$$

Using the cosine sum formula

$$\cos[A - B] = \cos[A]\cos[B] + \sin[A]\sin[B] \tag{2.36}$$

and

X	0	$\frac{\pi}{2}$	π	$\frac{3\pi}{/2}$
cos[X]	1	0	-1	0
sin[X]	0	1	0	-1

we are able to simplify all $P_{\Delta\phi}$ to

$$\begin{aligned} P_O &= \cos[\phi_O(x,y)], & P_\pi &= \cos[\phi_O(x,y)]\cos[\pi] \\ & & & \quad + \sin[\phi_O(x,y)]\sin[\pi] \\ & & &= -\cos[\phi_O(x,y)] \\ P_{\frac{\pi}{2}} &= \cos[\phi_O(x,y)]\cos[\tfrac{\pi}{2}] & P_{\frac{3\pi}{2}} &= \cos[\phi_O(x,y)]\cos[\tfrac{3\pi}{2}] \\ & \quad + \sin[\phi_O(x,y)]\sin[\tfrac{\pi}{2}], & & \quad + \sin[\phi_O(x,y)]\sin[\tfrac{3\pi}{2}] \\ &= \sin[\phi_O(x,y)], & &= -\sin[\phi_O(x,y)]. \end{aligned} \tag{2.37}$$

We substitute the resulting $P_{\Delta\phi}$ into Eqn. (2.34) and Eqn. (2.35) giving us

$$\begin{aligned} \alpha &= 2A_O(x,y)\{\cos[\phi_O(x,y)] + \cos[\phi_O(x,y)]\}, \\ &= 4A_O(x,y)\cos[\phi_O(x,y)] \\ \beta &= 2A_O(x,y)\{\sin[\phi_O(x,y)] + \sin[\phi_O(x,y)]\}, \\ &= 4A_O(x,y)\sin[\phi_O(x,y)] \end{aligned} \tag{2.38}$$

Using these reduced α and β terms we are able to show that

$$|\alpha|^2 + |\beta|^2 = 16A_O^2(x,y)\cos^2[\phi_O(x,y)] + 16A_O^2(x,y)\sin^2[\phi_O(x,y)] \tag{2.39}$$

$$= 16A_O^2(x,y)\{\cos^2[\phi_O(x,y)] + \sin^2[\phi_O(x,y)]\}, \tag{2.40}$$

$$= 16A_O^2(x,y). \tag{2.41}$$

Substituting this into Eqn. (2.28) we can show

$$A_O(x,y) = \frac{1}{4}\sqrt{16A_O^2(x,y)} \tag{2.42}$$

$$= A_O(x,y). \tag{2.43}$$

$$\tag{2.44}$$

Proving that, by assuming that the reference wavefronts amplitude and phase are constant, we are able to calculate the object wavefronts amplitude. Using the α and β from Equation (2.38) we get

$$\frac{\beta}{\alpha} = \frac{4A_O(x,y)\sin[\phi_O(x,y)]}{4A_O(x,y)\cos[\phi_O(x,y)]} \tag{2.45}$$

$$= \frac{\sin[\phi_O(x,y)]}{\cos[\phi_O(x,y)]} \tag{2.46}$$

and substituting this into Eqn. (2.29) we get

$$\phi_O(x,y) = \arctan\left\{\frac{\sin[\phi_O(x,y)]}{\cos[\phi_O(x,y)]}\right\} \tag{2.47}$$

which also verifies that (if the amplitude and phase of the reference wavefront are constant) we are able to recover the object wavefronts phase.

In Fig. 2.12 we display two reconstructions from a PSI DH. The first reconstruction is shown in Fig. 2.12(a) and is a reconstruction at a distance d from the hologram displaying the in-focus real image. Figure 2.12(b) shows where the in-focus virtual image should be located, a reconstruction distance of $-d$, but in this case it is hard to make out. This is because it has been suppressed by the recording of four holograms and the PSI algorithm. In our experience PSI does not, in practice, completely remove the dc-term and the unwanted twin-image but suppress' both sufficiently such that the DHs reconstructions are of high quality.

2.3 Hologram reconstructing

To understand how a hologram is viewed (reconstructed), we find it useful to compare this process to the more common photographic process. In Fig. 2.13 the optical reconstruction process for a hologram and a photograph is displayed. To view the image that is recorded onto the photographic film, you need to illuminate the film with incoherent light. For holography the process can be thought of as the same, to view (reconstruct) the hologram the film needs to be illuminated by the original source, a laser. To reconstruct a DH,

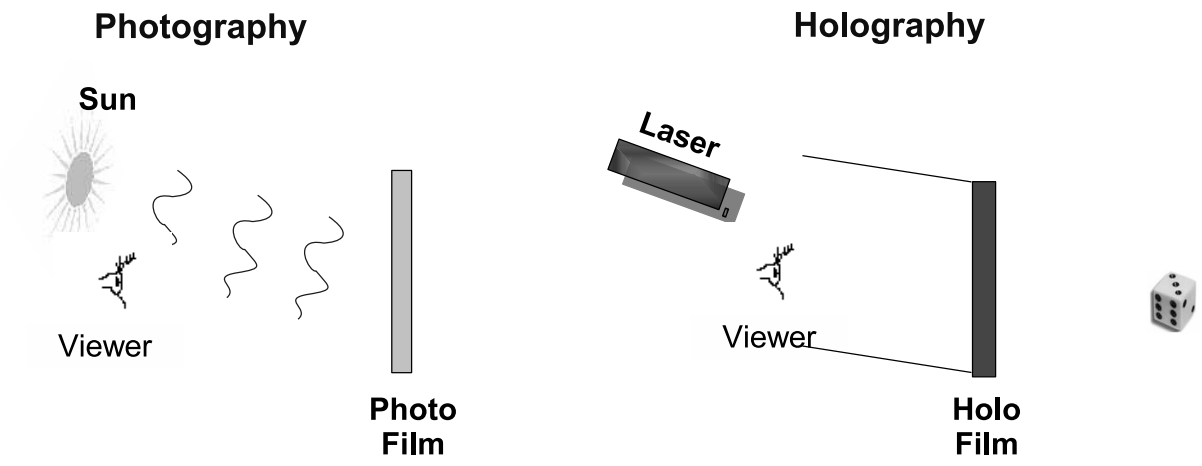

Figure 2.13: Optical reconstruction of a photograph and a hologram.

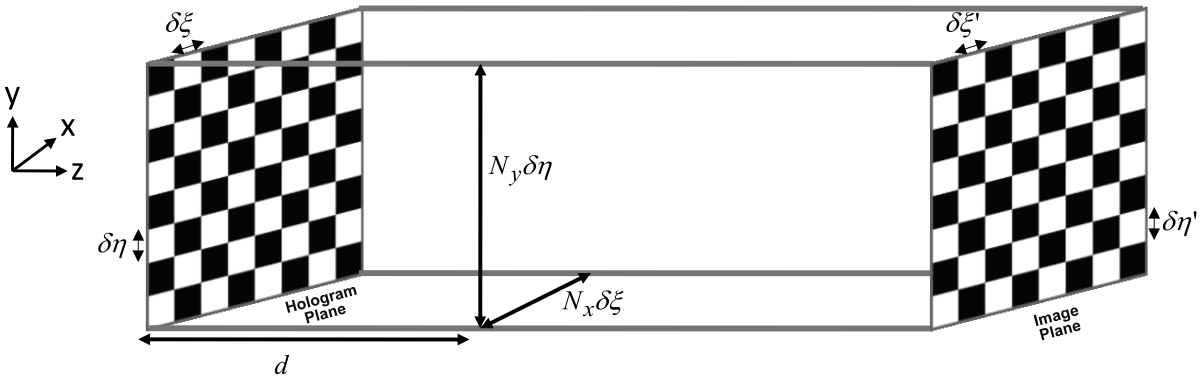

Figure 2.14: Geometry of the propagation transfer function.

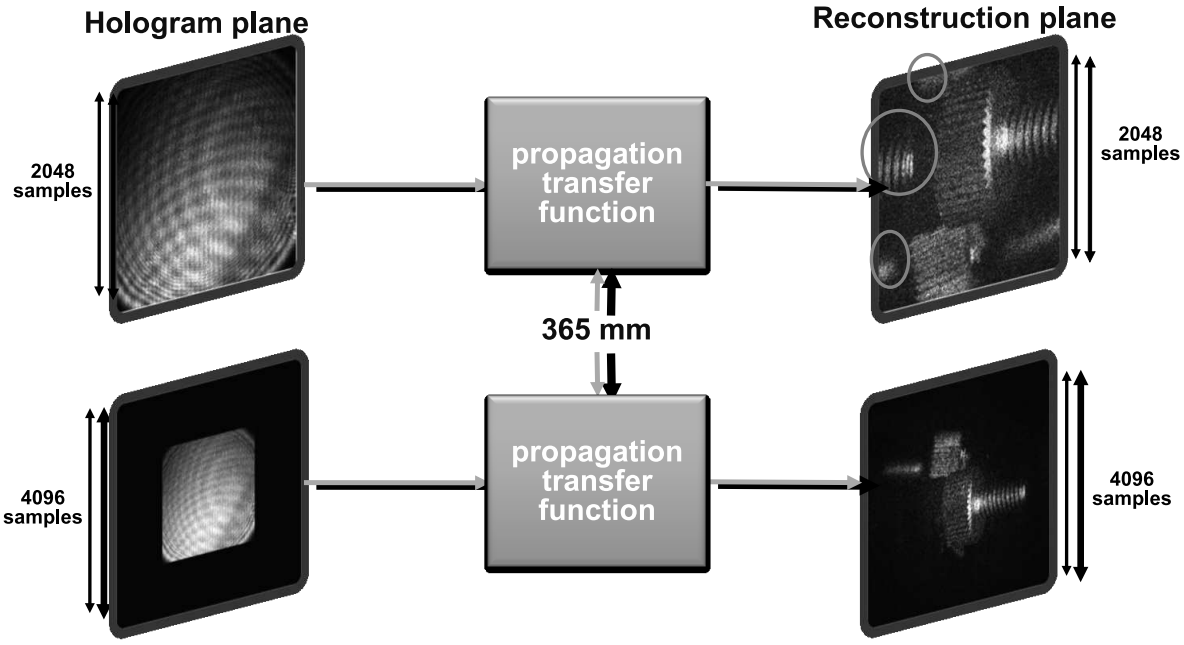

Figure 2.15: Numerical reconstruction with the propagation transfer function.

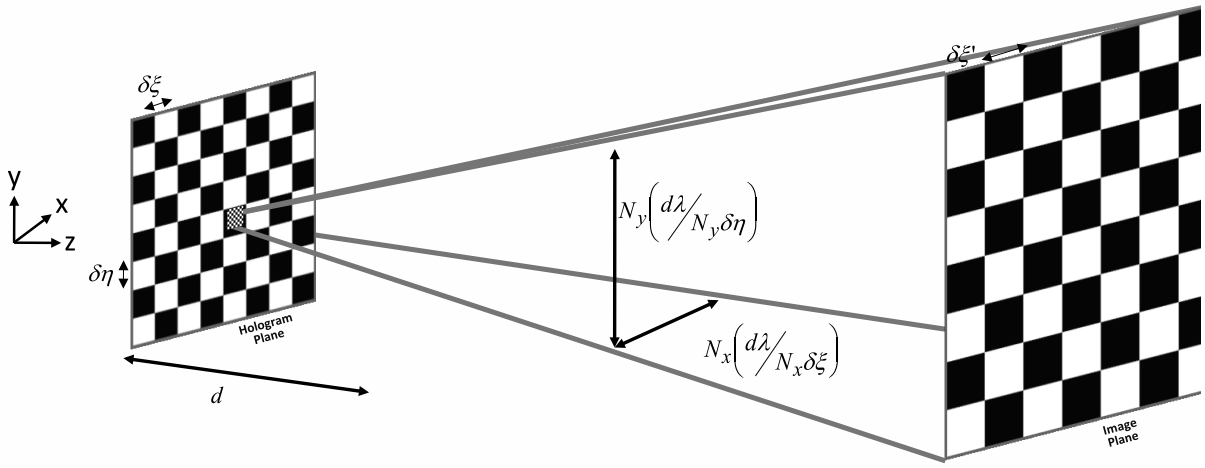

Figure 2.16: Geometry of the discrete Fresnel transform.

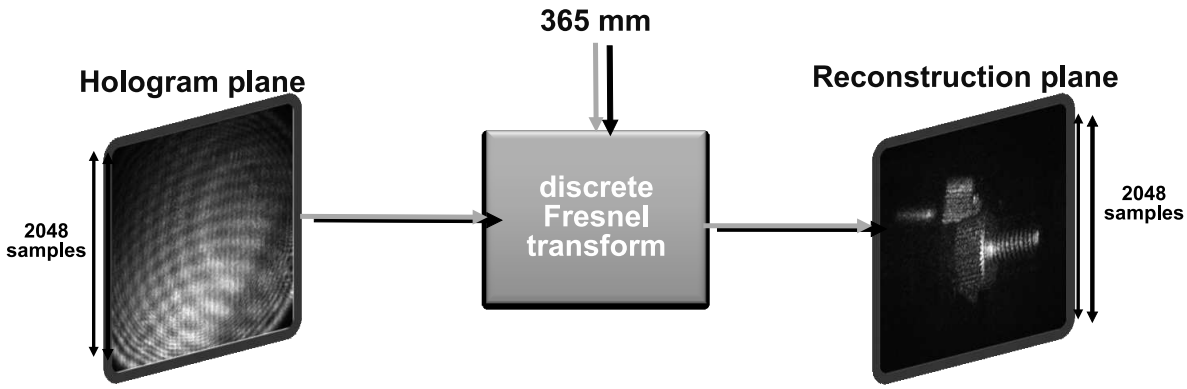

Figure 2.17: Numerical reconstruction with the discrete Fresnel transform.

we follow the same process. We first create a numerical representation of the original reference wave and through the Fresnel transform we simulate the propagation of the DH containing the object wavefront information illuminated by this numerical reference wave to an arbitrary plane a distance d away. We now have a representation of the amplitude and phase of the object wavefront at the plane d away from the hologram that can be later viewed or processed.

In this thesis we employ two reconstruction functions: the PTF calculated with Eq. (A.32) and the DFRT calculated with Eq. (A.23), as discussed in Appendix A. The geometry of the PTF reconstruction function is shown in Fig. 2.14. The PTF simulates a reference wave which leads to a constant pixel size at all depths. In other words, the physical size of a pixel at the hologram plane is the same as the physical size of a pixel in any of the possible reconstruction planes, $\forall d : \delta\xi = \delta\xi', \delta\eta = \delta\eta'$. Due to this constant pixel size and the fact that a Fresnel transform is a lossless transform, the main advantage of the PTF over the DFRT is evident, that it is reversible. If you

propagate a hologram any distance d, take the result and propagate this a distance $-d$ you would be left with the original hologram. This makes the PTF very useful for processing DHs as you can go to a specific plane, remove/add/modify and then reverse propagate back to the original hologram plane. This is also the source of the PTF's main limitation as displayed in Fig. 2.14 and 2.15. The field-of-view of PTF reconstructions is equal to the number of reconstructed pixels, N_x and N_y, multiplied by the pixel size, $\delta\xi$ and $\delta\eta$. Due to the use of the DFT in the reconstruction function (with finite support and its conservation of energy), objects with a larger dimension than $(N_x\delta\xi) \times (N_y\delta\eta)$ will be wrapped within the reconstruction. This is visible in Fig. 2.15 where in the reconstruction using 2048 samples there are a number of parts of the bolts objects which have been wrapped in the reconstruction. To overcome this, the hologram needs to be padded before propagation. This artificially increases N_x and N_y which in turn increases the reconstructed field-of-view [FCA+04, FNC+04, JFH+05, ACN+05]. This allows us to reconstruct objects larger than the original CCD, as is apparent in the reconstruction using 4096 samples in Fig. 2.15. However, padding the hologram comes at the severe cost of computation time.

The geometry of the DFRT reconstruction function is shown in Fig. 2.16. The DFRT differs from the PTF in that the pixel size in the image plane is a function of the pixel size in the hologram plane, the reconstruction distance and the wavelength of the light. If $d > \frac{N_x\delta\xi}{\lambda}$ then $\delta\xi' > \delta\xi$ and the reconstructed image displays a larger field of view than the PTF function. This is both an advantage and a limitation. Firstly it means that the DFRT

is not easily reversible. While there is no loss of energy in the propagation from the hologram plane to the image plane a distance d away, the change in pixel size means that you cannot just reverse propagate a distance $-d$ to get back the original hologram. This change in pixel size is also an advantage as it allows for the reconstruction of large fields-of-view with the original $N_x \times N_y$ sized hologram. This is displayed in Fig. 2.17 where using only the original 2048×2048 samples, we can now reconstruct the bolts object free of wrapping. This is a major advantage over the PTF, as it can significantly decrease computation time, particularly if from one hologram a set of different reconstructions needs to be processed. Unless otherwise stated all numerical reconstructions in this thesis have been reconstucted using the DFRT.

DHs contain 3D information and as we have already mentioned, to extract this information from DHs containing macroscopic objects sets of reconstructions need to processed. To be more exact, a set of reconstructions where each reconstruction is at a different depth needs to be processed. Then another set of reconstrucions, this time from a different perspective, needs to be processed and the data from these two sets can then contain 3D information. The information from either one of the sets of reconstructions contains only 2.5D information. In Fig. 2.18 we demonstrate the impact of numerical focusing. The DH encodes two bolts, located at approximately 355mm from the CCD. We have reconstructed this DH at four different depths: 345mm where everything is out-of-focus, 360mm where the front bolt is in-focus, 370mm where the back bolt is in-focus, and 380mm where everything is out-of-focus again. This is achieved through varying the d value in Eq. (A.23).

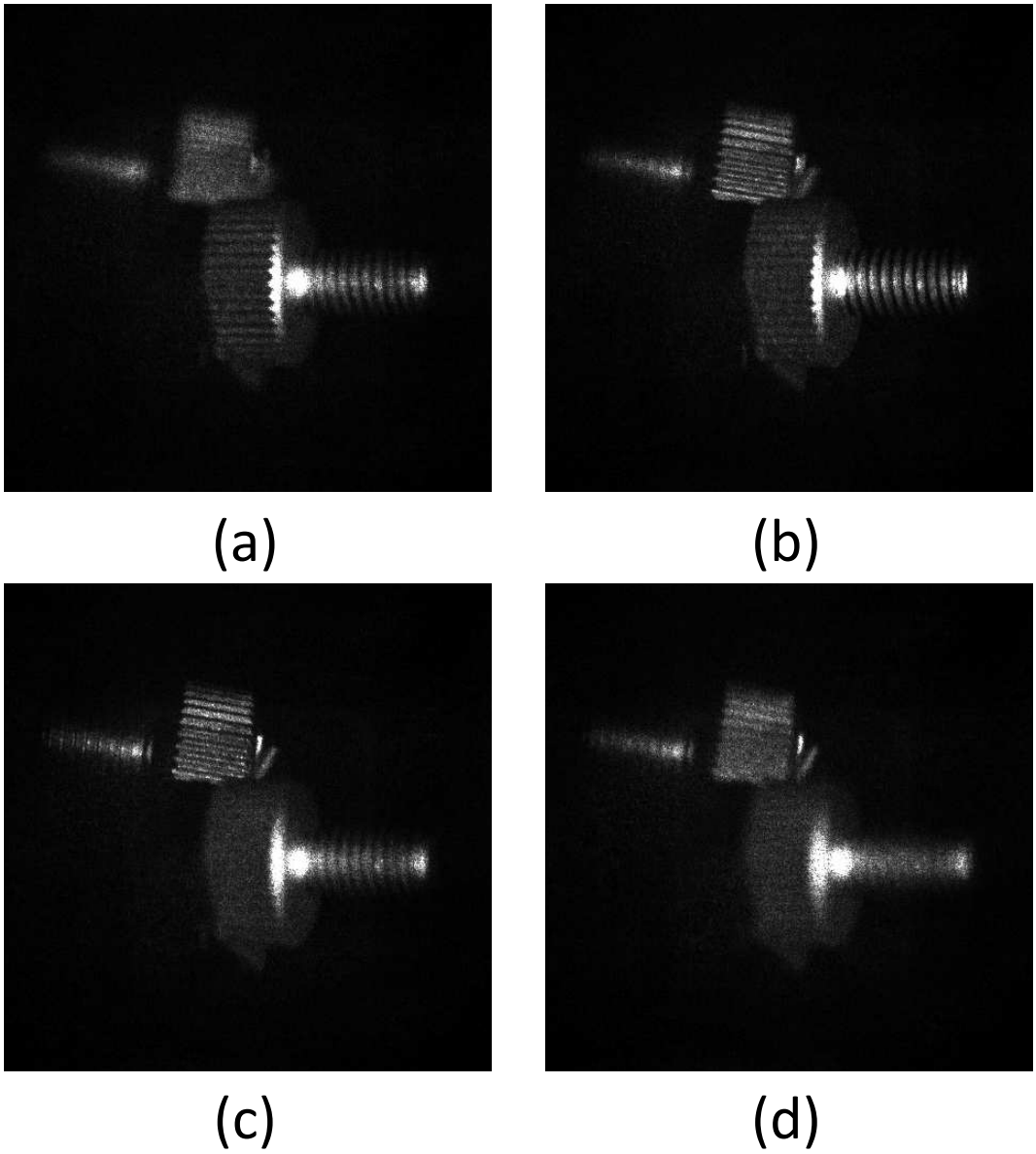

Figure 2.18: Numerical reconstruction with the discrete Fresnel transform at four different depths, (a) 345mm, (b) 360mm, (c) 370mm and (d) 380mm.

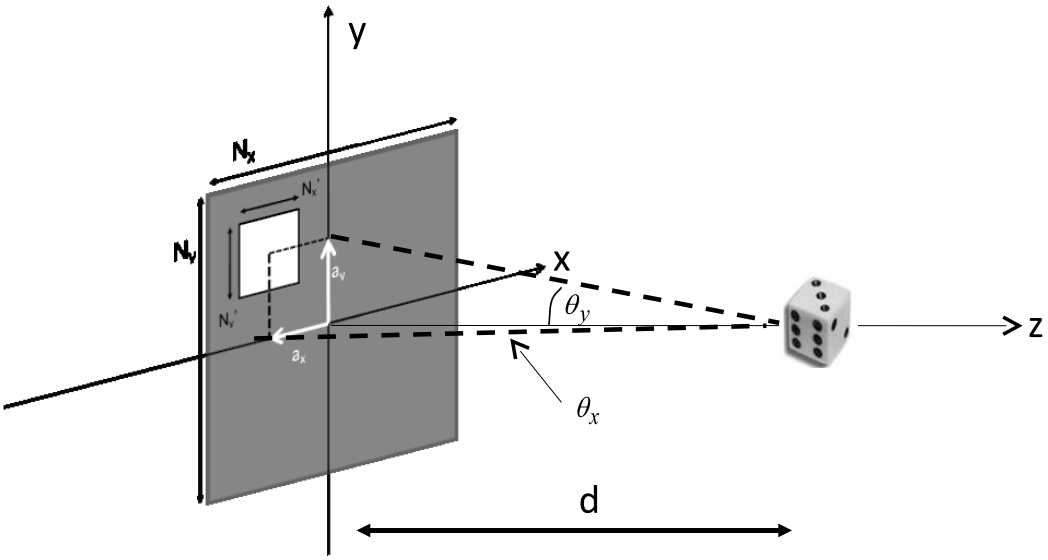

Figure 2.19: Geometry of numerically reconstructing a DH from a perspective not centred on the optical axis.

To understand how to reconstruct a perspective other than the primary perspective (along the optical axis), we need to think about optical holograms and take a look at the reconstruction geometry, as shown in Fig. 2.13 and Fig. 2.19 respectively. Reconstructing a DH at a distance d is analogous to viewing an optical hologram along the optical axis and focusing with your eye to a distance d. To view a new perspective, you would move your head to the new position, then centre your view to a point on the optical axis a distance d away and finally focus at the distance d. Numerically reconstructing a perspective attempts to simulate this and is shown in Fig. 2.19. Taking our $N_x \times N_y$ sized DH we first select a window sized $N_x^{'} \times N_y^{'}$ where $N_x^{'} < N_x$ and $N_y^{'} < N_y$. We then select the window of pixels from the original hologram whose centre is offset from the optical axis a_x pixels in the x-direction and

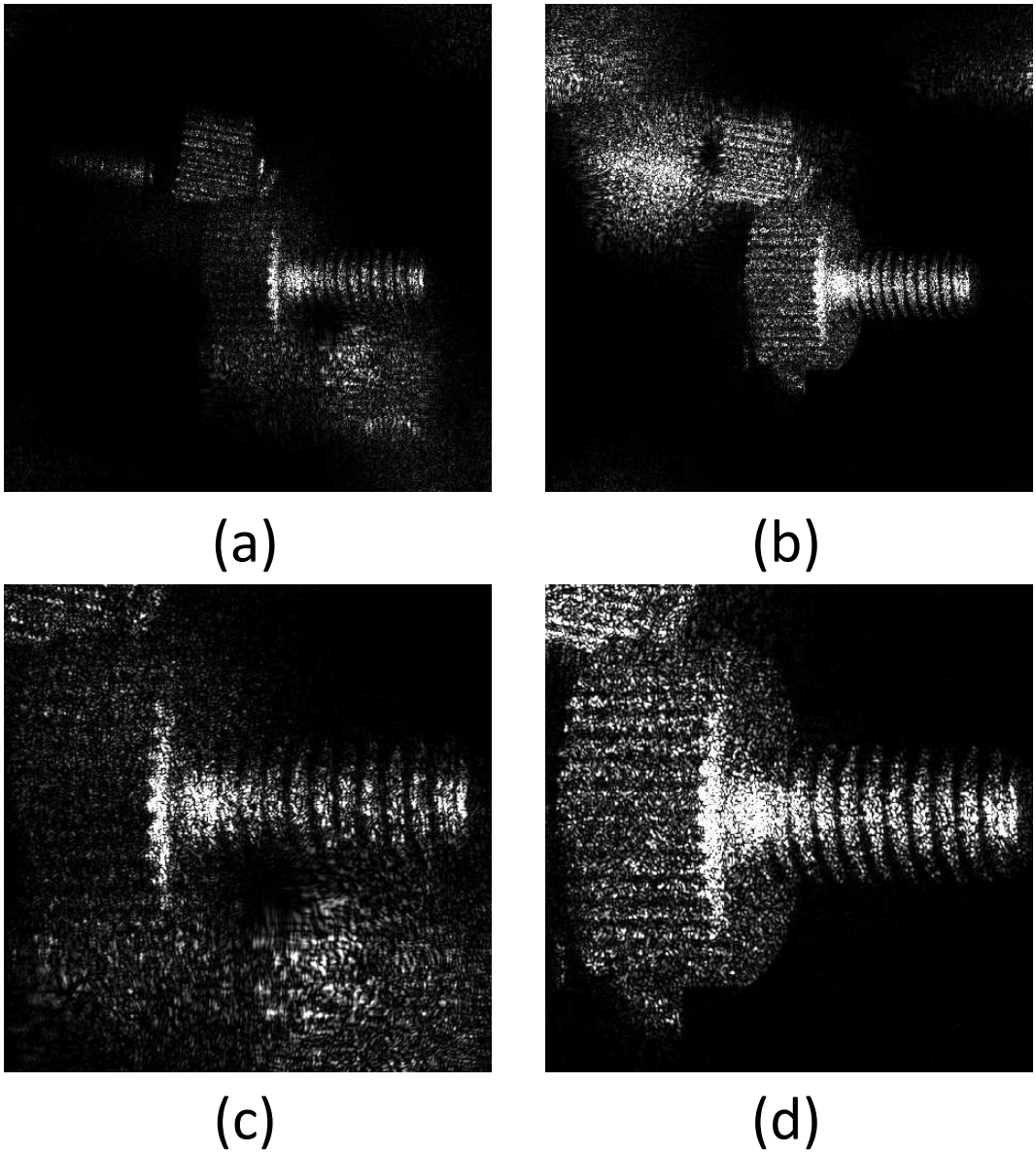

Figure 2.20: Numerical reconstruction of a DH from two perspectives, (a) top-left perspective, (b) bottom-right perspective and zoomed in reconstructions centred on front bolt (c-d).

a_y in the y-direction which is equivalent to moving your head in the optical case. This window is then centred in a new hologram of zeros sized $N_x \times N_y$. The quality of the reconstructed perspective is determined by the quality of the original hologram recording and then by the size of the window. The smaller $N_x^{'}$ and $N_y^{'}$ are the worse the visual quality. We next have to re-centre our view back to the optical axis, this is achieved through inputting (a_x, a_y) to the linear phase shift of the reconstruction function. Finally we input our reconstruction distance d to numerically focus. This results in a reconstruction from a new perspective which is centred on the optical axis. To calculate the change in perspective achieved we need to return to the geometry of Fig. 2.19. We can see that the changes in perspective are the angles made by the x-axis with the z-axis and by the y-axis with the z-axis and are easily calculable with

$$\theta_x = \tan^{-1}\left(\frac{a_x}{d}\right) \qquad \text{and} \qquad \theta_y = \tan^{-1}\left(\frac{a_y}{d}\right) \tag{2.48}$$

There is a theoretical limit placed on θ_x and θ_y for a DH which is dependent on the pixel size of the CCD [Kre05]. For the CCD's available today, this ranges from around 2° to 4°. We have reconstructed the two bolts object DH from two different perspectives in Fig. 2.20. We used a window of size 400×400 for both reconstructions. For the reconstruction in Fig. 2.20(a) we set $a_x = -700$ and $a_y = 700$, and for the reconstruction in Fig. 2.20(b) we set $a_x = 700$ and $a_y = -700$. This equates to views from the top-left perspective and the bottom-right perspective respectively. It also corresponds to angular shift of 0.8° in both the x- and y-direction. This is not a large change in

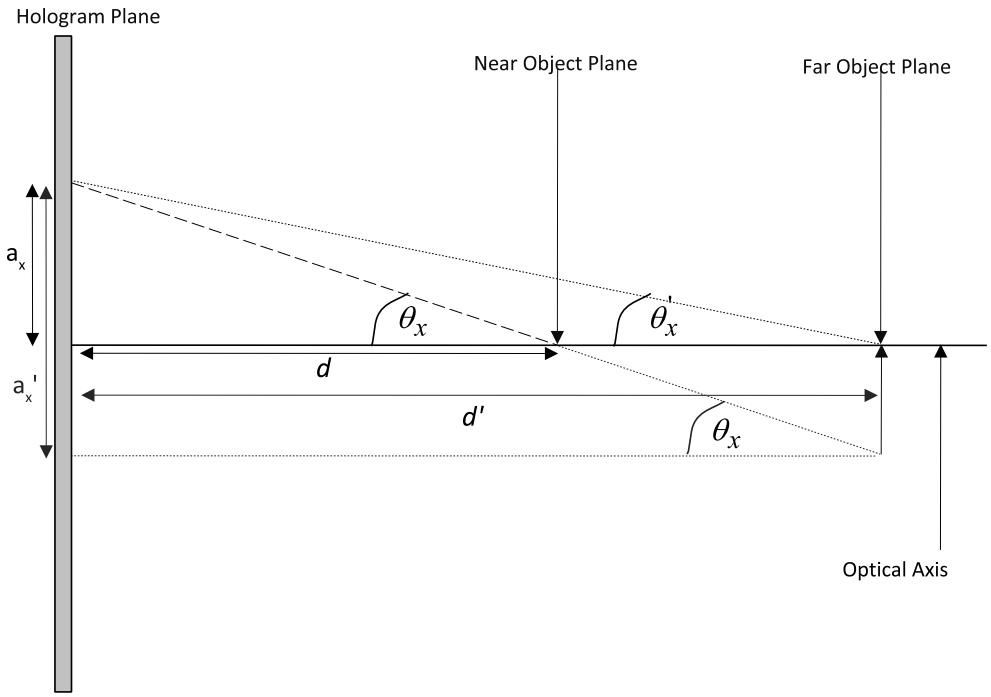

Figure 2.21: Geometry for maintaining the same perspective at two different reconstruction distances.

perspective and is hard to see the difference between the reconstructions, for this reason we have zoomed in on the front bolt in Fig. 2.20(c) and (d). It is also apparent from this figure that the visual quality of the reconstructions has been negatively affected by the relatively small window size.

From the equations in Eq. (2.48), it is apparent that the angle the reconstruction it is viewed at depends on the distance of propagation. If you were to take two reconstructions using the same $N_x^{'}, N_y^{'}, a_x$ and a_y values but changed the d value in the second reconstruction you would get a reconstruction at a different perspective (θ_x and θ_y would be different in the second reconstruction). To be able to compare or process two reconstructions from

the same perspective we need to keep θ_x and θ_y constant for all reconstruction distances. This is described in one-dimension in Fig. 2.21, where we have shown two reconstructions at distances d and $d^{'}$ respectively. The first reconstruction comes from inputting a_x and d into the Fresnel transform resulting in $\theta_x = \frac{a_x}{d}$, while the second reconstruction comes from inputting a_x and $d^{'}$ into the Fresnel transform giving us $\theta_x^{'} = \frac{a_x}{d}$. Since in the second reconstruction we are focusing on the optical axis at distance $d^{'}$, the perspective is not the same as the first reconstructions. Therefore, we need to modify what we input into the Fresnel transform to maintain the same perspective in both reconstructions. This is achieved through keeping the perspective fixed on a point a distance d along the optical axis rather than at a point a distance $d^{'}$ along the optical axis in the second reconstruction. We input $d^{'}$ and $a_x^{'}$ into the Fresnel transform instead of $d^{'}$ and a_x where $a_x^{'}$ is calculated by

$$\tan\theta = \frac{a_x^{'}}{d^{'}} \tag{2.49}$$

$$a_x^{'} = \tan\theta \times d^{'}. \tag{2.50}$$

All coherent imaging systems contain speckle, this is because speckle is created when coherent light illuminates an optically rough surface. The size of the speckle in the $x-$direction and $y-$direction can be calculated with knowledge of the experimental setup. It has been shown to increase with the reconstruction distance [Kre05] and exhibit itself as noise in the reconstructions. This is why speckle noise is a problem for macroscopic digital holography, the large distance the object needs to be placed at away from the CCD (large when compared to microscopic digital holography) allows

the speckle the time to evolve and become a corruptive noise visible in the reconstructions.

Speckle reduction algorithms attempt to increase the visual quality of reconstructions through the suppression of speckle noise. The increase in visual quality usually comes at the expense of image detail (the resolvable resolution in the reconstruction after application of speckle reduction). We have selected the discrete Fourier filtering technique developed by Maycock et al. [MHM+07] as our speckle reduction technique for four reasons. The first is that they have shown that it outperforms both mean and median filtering which are common easy methods from noise suppression in standard image processing. Secondly their function can use different sized filters, a smaller filter suppress' more speckle but at the cost of resolution while a larger filter maintains resolution but at the cost of speckle reduction. They also quantitatively determined the exact impact their technique has on resolution for the different filter sizes using a resolution chart. Finally and more importantly, they can quantify the amount of speckle reduction that will occur through the application of the filter. This allows us to know in advance the impact of applying the discrete Fourier filter. We have selected a filter of 512×512 for application to DHs of size 2048×2048 in this thesis as it results in a speckle index of nearly 0.25 (a speckle index of 1 means no speckle reduction) and a resolution of $\frac{1}{2}$. The results of speckle reduction are shown in Fig. 2.22 where the reconstructions before speckle reduction are shown in (a) and (c) and the speckle reduced reconstructions are shown in (b) and (d) respectively.

This concludes our introduction to digital holography. We have discussed

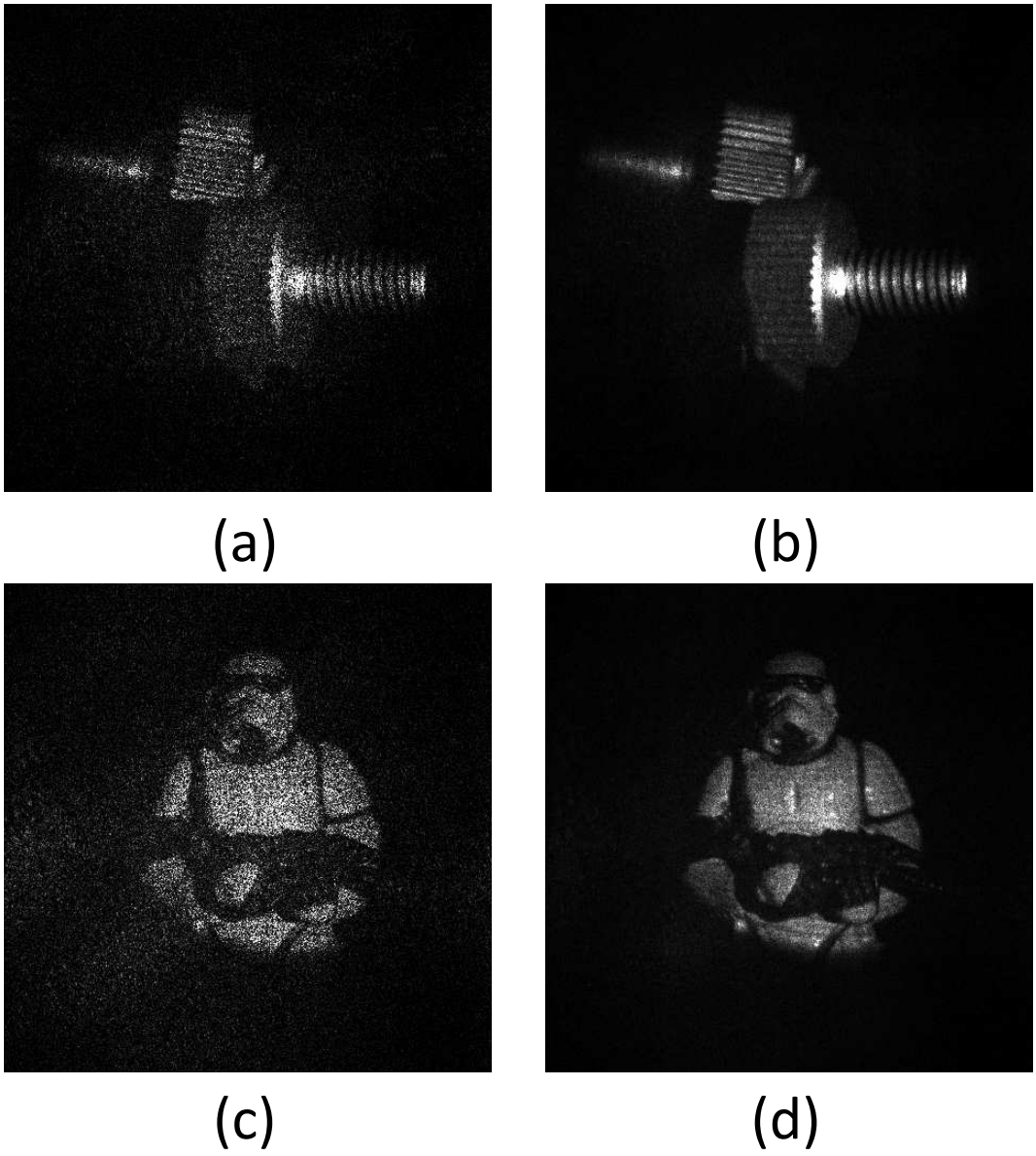

Figure 2.22: Numerical reconstruction with the discrete Fresnel transform of two bolts object (a) without speckle reduction, (c) with speckle reduction and of a stormtrooper object (b) without speckle reduction and (d) with speckle reduction.

in detail the recording of DHs, the inherent error terms and the reconstructing of DHs. In the next chapter we deal with focusing and digital holographic reconstructions. We discuss the theory of focus detection and its application to hologram reconstructions. We then progress to our work in automatically focusing a region within a reconstruction.

Chapter 3

Developing automatic focusing in digital holography

All imaging systems generally have a finite depth-of-focus. The image can either be in-focus or out-of-focus. The objects which lie within the depth-of-focus of the imaging system are in-focus (appearing sharp) while the objects which lie outside of the depth-of-focus of the system are out-of-focus (appearing blurred). Focus measures are functions which have been developed to determine the relative level of focus of sets of images. The accepted image property maximised by these functions is the high spatial frequency energy of the image [SCN93], which is most accurately computed with the Fourier transform [Goo05]. High spatial frequencies equate to edges in 2D images while low spatial frequencies equate to image detail. For this reason we create a simple example to demonstrate focus detection on an image containing

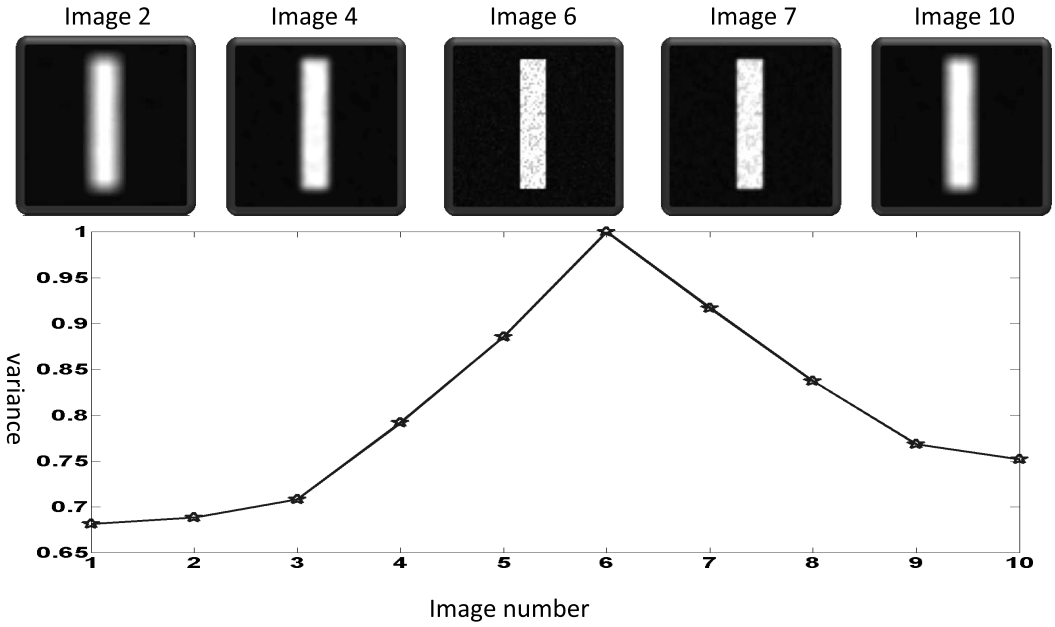

Figure 3.1: Focus detection on a set of images containing one edge.

a single edge. We select variance as our focus measure calculated with

$$V(I_z) = \frac{1}{n^2} \sum_{i=1}^{n} \sum_{j=1}^{n} \left[I_z(i,j) - \overline{I_z} \right]^2 \tag{3.1}$$

where I_z is an image or image region, of size $n \times n$, indexed by pixel locations i and j and where $\overline{I_z}$ is the arithmetic mean of I_z calculated by

$$\overline{I_z(i,j)} = \frac{1}{n^2} \sum_{x=1}^{n} \sum_{y=1}^{n} I_z(x,y). \tag{3.2}$$

$V(I_z)$ is a 1D vector containing a focus value for each image, or image region, I_z. The I_z which returns the highest variance value is selected as the most in-focus image. We calculate $V(I_z)$ on a set of ten images containing an

individual edge blurred to different degrees. We start by calculating our initial sharp image and placing it in the centre of our set of ten images

$$I_6 = \text{rand}(81) \times 0.1 \tag{3.3}$$

where rand(81) creates an 81×81 sized block of random numbers between 0 and 1. This gives the background a random texture and we multiply by 0.1 to maintain a low intensity in the background. To add an edge we set the pixels $I_6(x, y)$ to one where $x = [10, ..., 70]$ and $y = [35, ..., 46]$. Finally we add multiplicative noise (speckle noise) with

$$I_6 = I_6 + (n \times I_6), \tag{3.4}$$

where n is uniformly distributed noise with mean of 0 and variance of 0.04. We now have an image containing an edge, a textured background and speckle noise. To create our defocused images, $I_{1-5,7-10}$, we convolve I_6 with a 9×9 2D Gaussian with varying standard deviations. We select convolution with a Gaussian as this is an accepted simple model for defocus [FP03]. A selection of the edge images is shown in Fig. 3.1. To detect the most in-focus image, we apply Eq. (3.1) to I_z where $z = [1, ..., 10]$. A plot of the returned variance values for all ten images is displayed in Fig. 3.1. It is clear from this plot that I_6 returns the highest variance value and is determined as the most in-focus image. We demonstrate in more detail the use of variance for the detection of focus in digital holography in the next section.

In this chapter we review the work we have completed on developing

automatic focusing for digital holography and we detail how we can use focus detection to extract depth information from a hologram. Section 3.1 details our initial investigation into focus detection and digital holography. We evaluate the applicability of variance as a focus measure by comparing it to a known function for calculating spatial frequency, the Fourier transform. The Fibonacci search [Fer60] with an optimised termination condition for digital holography is employed in our autofocus system described in Sect. 3.2. We discuss its implementation and demonstrate how it efficiently estimates the correct focal plane for a DH even in large search ranges. In Sect. 3.3, we discuss in detail how to extract depth information from a DH using our DFF algorithm. Our DFF algorithm takes a number of inputs and we demonstrate the impact of each input and advise, where possible, what values to choose. Finally we end the chapter in Sect. 3.4 with an overview and discussion of our work on automatic focus detection.

3.1 Evaluation of focus measures

We now proceed to compare two focus measures variance and a measure based on the Fourier transform which accurately calculates the high spatial frequency content of an image block. The Fourier transform of an image has been proven to be a sound focus measure [SCN93] but is computationally expensive compared to the alternatives. The two-dimensional Fourier transform can be calculated with Eq. (A.21). To compute our Fourier focus measure (FFM) using only the high spatial frequency we set the centre

$M \times M$ pixels in $F(k,l)$ to be zero, equivalent to a high-pass filter, and sum

$$\mathrm{FFM}(I_z) = \sum_{k=0}^{N-1} \sum_{l=0}^{N-1} \mid (F(k,l)) \mid . \tag{3.5}$$

$FFM(I_z)$ is therefore a focus value for the image, or image region, I_z. Variance is a popular focus measure because it satisfies all the requirements identified for good focus measures in Chapter 1.3.1 particularly, compared to the FFM, computational complexity. It has been proven to be a sound focus measure [SCN93] but, to the authors knowledge, its application to digitally recorded holograms where speckle noise reduces the effectiveness of focus measures has not been evaluated. While the FFM more accurately measures the spatial frequencies in an image, the time taken to calculate the FFM places it at a disadvantage when compared to variance. In this section we quantify the increase in computation time required to use the FFM as a focus measure and we demonstrate that variance returns qualitatively accurate results.

To evaluate the performance of variance as a focus measure compared with the FFM we compare the estimated depth values returned by both measures and the computation time required on two DHs containing a high and low contrast object. The first hologram contains two bolts positioned approximately 15mm apart and the second hologram contains a Lego block. We selected two 81×81 object blocks, one on the two bolts object (OB_1) and one on the Lego block (OB_2). We qualitatively determined the in-focus planes for these blocks to be 356.2mm and 298mm respectively. A numerical reconstruction of the the DHs with OB_1 and OB_2 highlighted is displayed in

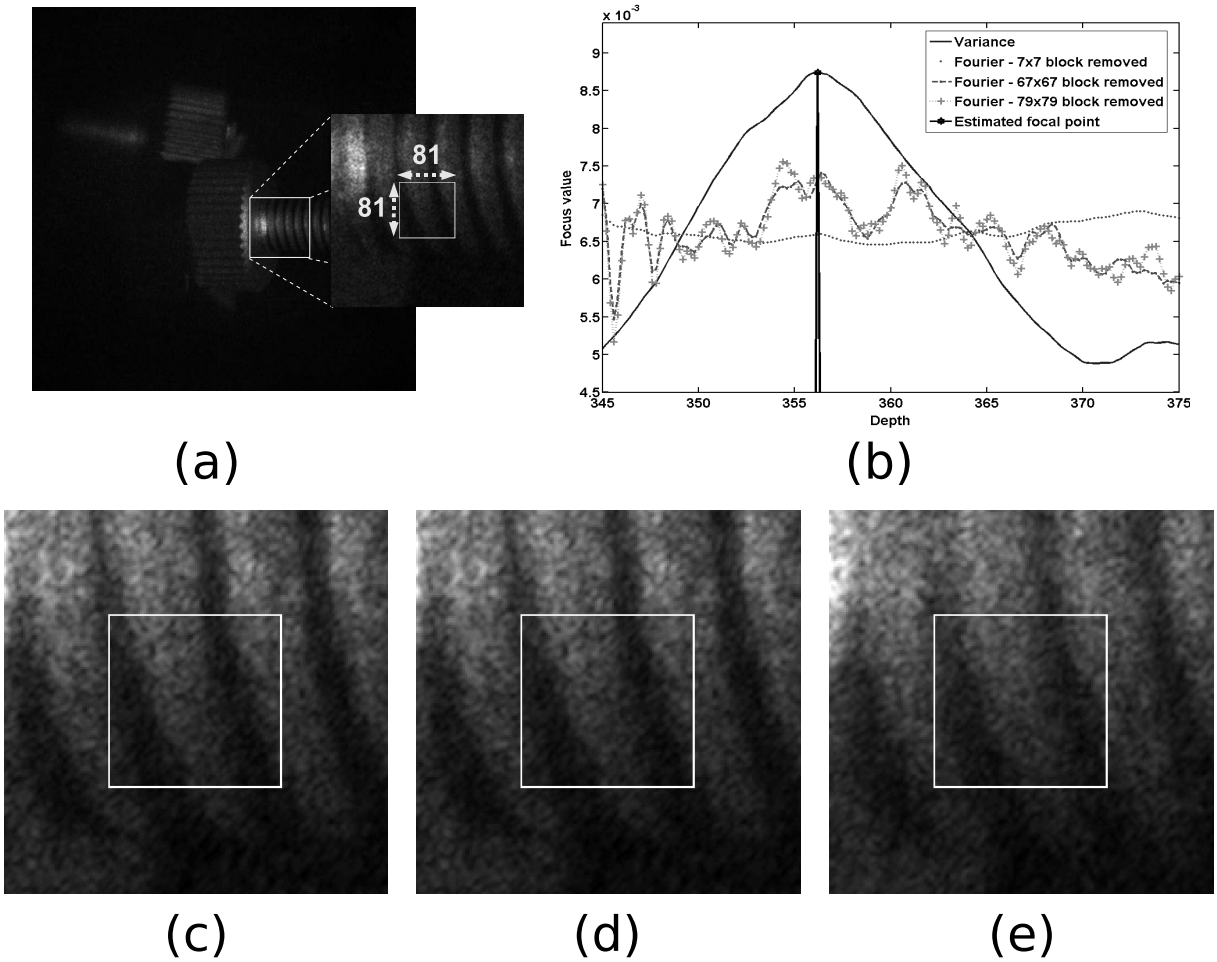

Figure 3.2: Two bolts object DH: (a) numerical reconstruction with OB_1 highlighted, (b) focus measure plots for OB_1, (c) zoomed in numerical reconstruction of OB_1 at depth estimated by variance, (d) zoomed in numerical reconstruction of OB_1 at depth estimated by FFM, (e) zoomed in numerical reconstruction of OB_1 at depth 5mm away from estimated focal plane.

Fig. 3.2(a) and Fig. 3.3(a). We numerically reconstruct each DH over a range of depths and apply discrete Fourier filtering [MHM+07] to reduce speckle. We then calculate variance and the FFM on both object blocks for each reconstruction in the range. By varying the size of the $M \times M$ block to be removed from $F(k,l)$ prior to the calculation of FFM(OB_1) and FFM(OB_2), we can determine which block size returns more accurate results. We removed block sizes ranging from 7×7 up to 79×79 from the Fourier transform of OB_1 and OB_2. In Fig. 3.2(b) and Fig. 3.3(b) we plot the variance focus measure and selected FFM's applied to OB_1 and OB_2 as a function of depth. It is apparent that by only removing a small block, or too large a block, in the Fourier transform the FFMs estimation of depth is negatively affected. A small $M \times M$ block saturates the focus measure calculation with low spatial frequencies while a large $M \times M$ block suppress' all but the highest spatial frequencies. We found that for $M \times M$ block sizes in the range of 31×31 up to 75×75, the estimated depth is never more than 0.2mm away from our qualitatively estimated depth. Using multiple DHs we qualitatively selected 67×67 as the best block size to remove for use with the FFM calculated on an 81×81 object block. It is evident from the focus measure plots that variance returns a unimodal curve, while the FFM has multiple local maxima.

We also investigate the length of time required to calculate both of the focus measures. We selected seven blocks, each of a different size, from a DH reconstruction and calculate, and time, variance on the block ten thousand times. We then carry out the same experiment using the FFM as the focus measure. The average time for both focus measures is shown in Table. 6.1,

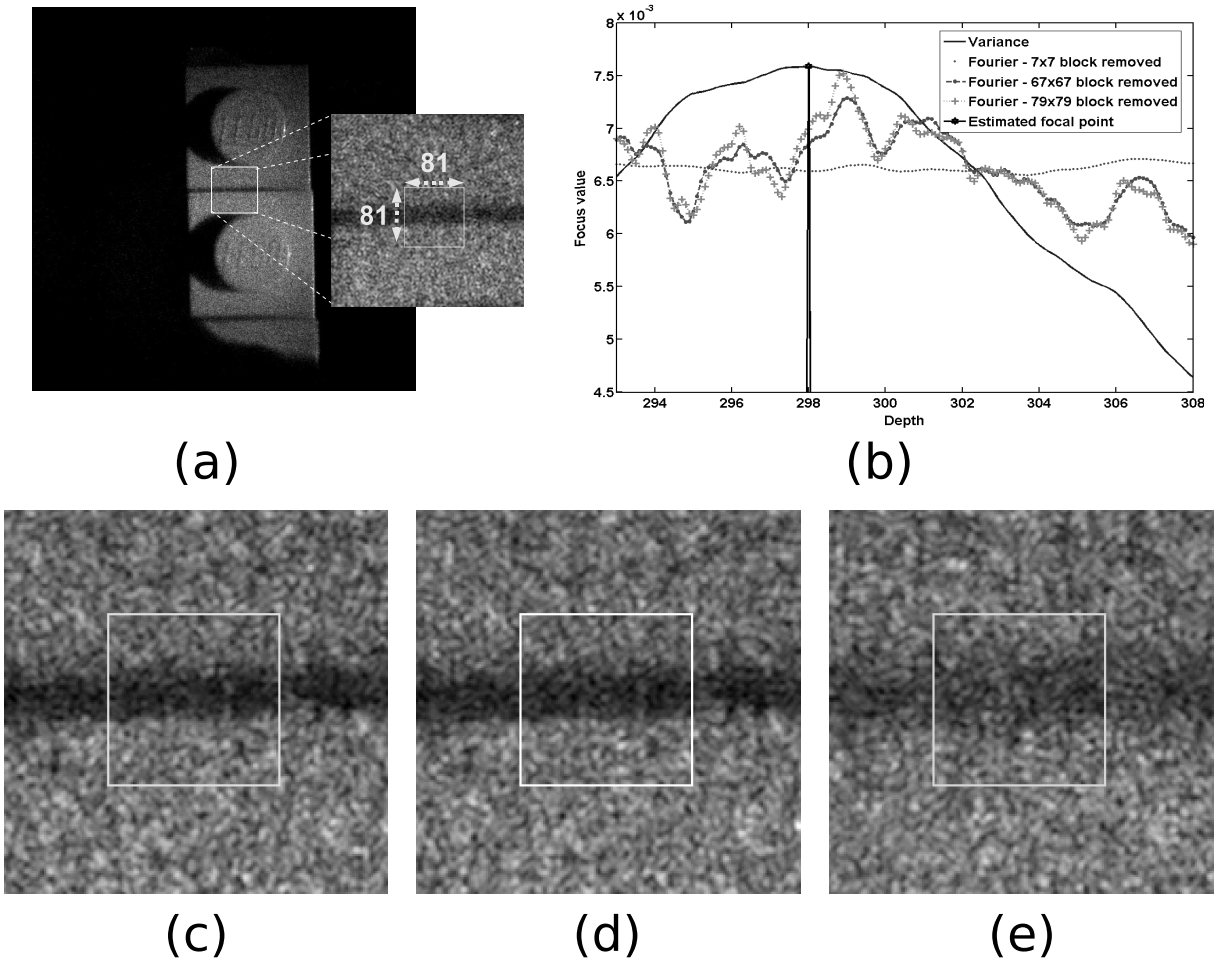

Figure 3.3: Lego block object DH: (a) numerical reconstruction with OB_1 highlighted, (b) focus measure plots for OB_1, (c) zoomed in numerical reconstruction of OB_1 at depth estimated by variance, (d) zoomed in numerical reconstruction of OB_1 at depth estimated by FFM, (e) zoomed in numerical reconstruction of OB_1 at depth 5mm away from estimated focal plane.

Table 3.1: Focus measure computation time (seconds)

Block Size	Variance	FFM
21×21	0.000069	0.000425
41×41	0.000099	0.001205
51×61	0.000145	0.002317
81×81	0.000211	0.002425
101×101	0.000295	0.005964
121×121	0.000398	0.006998
141×141	0.000528	0.016544

which demonstrates a 12:1 ratio in computation time for the FFM compared to variance for the block size of 81×81.

In this section, we have shown why variance may be considered a better focus measure than the FFM due to its lower computational complexity and unimodal focus plots. We originally selected variance as it has been successfully employed as a focus measure in many imaging systems and we have demonstrated it is applicable to digital holography.

3.2 Autofocus

A simple autofocus system for digital holography involves taking a set of numerical reconstructions, where each reconstruction is at a different depth, and applying a focus measure to them. The reconstruction which returns the maximum focus value will be taken as the in-focus reconstruction. We first take a DH and select a range of depths to reconstruct over, in this example our two bolts DH and $z = [345, 345.2, 345.4, ..., 379.8, 379.8, 380]$. By applying Eq. (3.1) to all of the reconstuctions, we are able to estimate

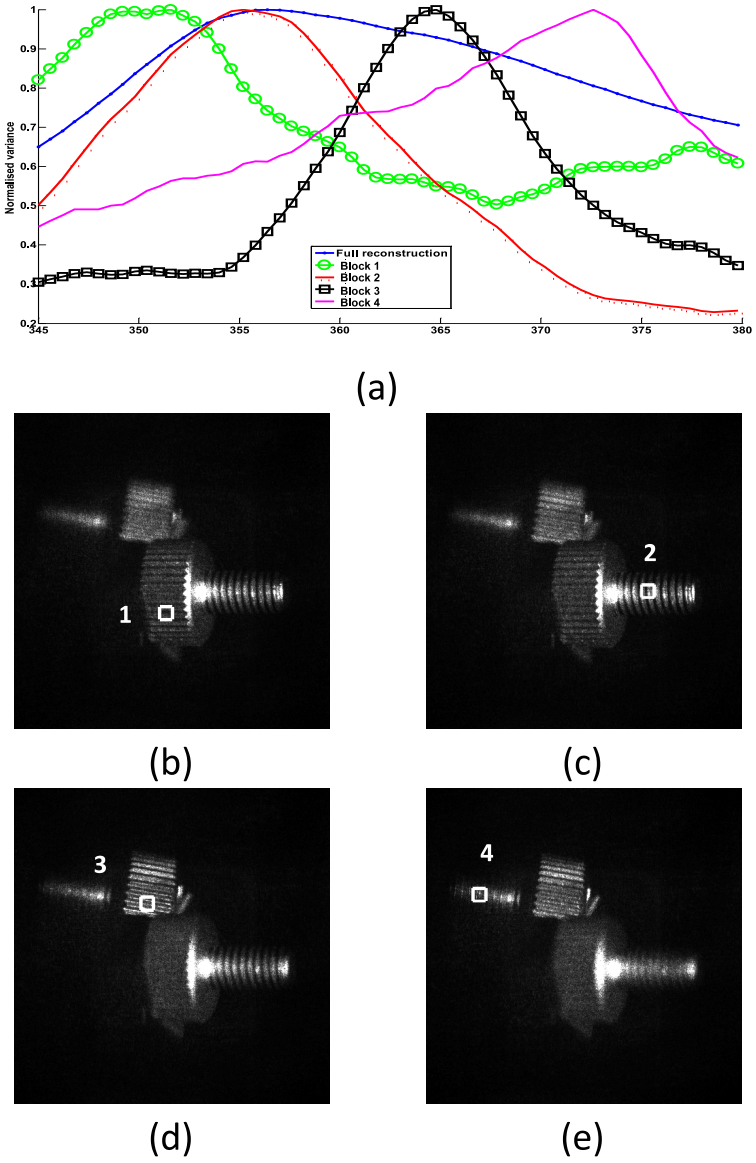

Figure 3.4: Autofocusing four object blocks in a two bolts object DH: (a) variance plot for the full reconstruction and the four object blocks, (b) numerical reconstruction at the estimated depth for object block 1, (c) numerical reconstruction at the estimated depth for object block 2, (b) numerical reconstruction at the estimated depth for object block 3, (b) numerical reconstruction at the estimated depth for object block 4.

the focal plane of the DH. The focus values for this simple linear search are plotted in Fig. 3.4. The returned value of 356.4mm equates to the qualitively determined focal plane of the threads of the front bolt. To demonstrate the impact of selecting different image regions, we select four (81×81) object blocks, one on the threads, and head, of the front and back bolt, these blocks are highlighted in Fig. 3.4(b-e). We plot the focus values for the four object blocks in Fig. 3.4(a), and the numerical reconstructions in Fig. 3.4(b-e) are at the estimated focal planes for object blocks 1-4 respectively. What is evident from the sharp reconstructions in this figure is that variance correctly identified the focal plane for the four object blocks.

A linear search such as the one we implemented is slow. Also, considering a focus measure should be unimodal a linear search is an inefficient search. We have implemented an intelligent autofocus function using the Fibonacci search [Fer60] and variance as the focus measure. However, we note that our algorithm is not reliant on variance and will work with any focus measure. This is important for cases in which variance is not a good focus measure, i.e. pure phase objects [LKB08]. Our search function assumes that the plot of focus values for a reconstruction as a function of distance is unimodal and that the maximum focus value is at the reconstruction distance where the objects image is in-focus. This is the same assumption made for all focus detection algorithms [SCN93]. We chose the Fibonacci search as it has been shown to outperform other search functions such as the fixed stepsize search (a linear search), the iterative search and the variable stepsize search [Bat00]. Our algorithm is detailed in Alg. 3.1.

The Fibonacci search is similar to a binary search, given a search range it iteratively samples the search space, using the golden ratio and Fibonacci numbers, comparing two samples in an attempt to find the global maximum value and iterating until the termination condition is breached. Typically the Fibonacci search requires a relative definition of accuracy. This is the termination condition as it determines the maximum number of iterations in the Fibonacci search. We have created our own optimised termination condition for digital holography to take account of the depth-of-focus of the reconstructions. At any iteration, the Fibonacci search compares two reconstructions at distances d_1 and d_2, the termination condition is breached if $\text{dof}^{j}_{d_1} > \text{dof}^{i}_{d_2}$ (from Eq. (A.31) or (A.33)). This is when the focal range of the two reconstructions overlap and there is redundant focus information. We employ the DFRT (Eq. (A.23)) in our autofocus algorithm to reconstruct our DHs and using Eq. (A.31) we can create Alg. 3.2, which is the function that terminates our Fibonacci search.

To experimentally validate the Fibonacci search we apply Alg. 3.1 and Alg. 3.2 to DHs of real world objects. For this example we use single capture DHs, which we call interferograms, which have had the dc-term suppressed but still contain the unwanted twin-image. The reconstructions from these DHs are noisier than reconstructions from our PSI DHs due to the presence of the unwanted twin-image. Our use of this type of DH is solely to illustrate the applicability of our autofocus algorithm to Stage 1 of our twin-image removal algorithm, see Chapter 6. We reconstruct our DHs and calculate our focus measure on the centre 400×400 pixels of the intensity. In Fig. 3.5 we display

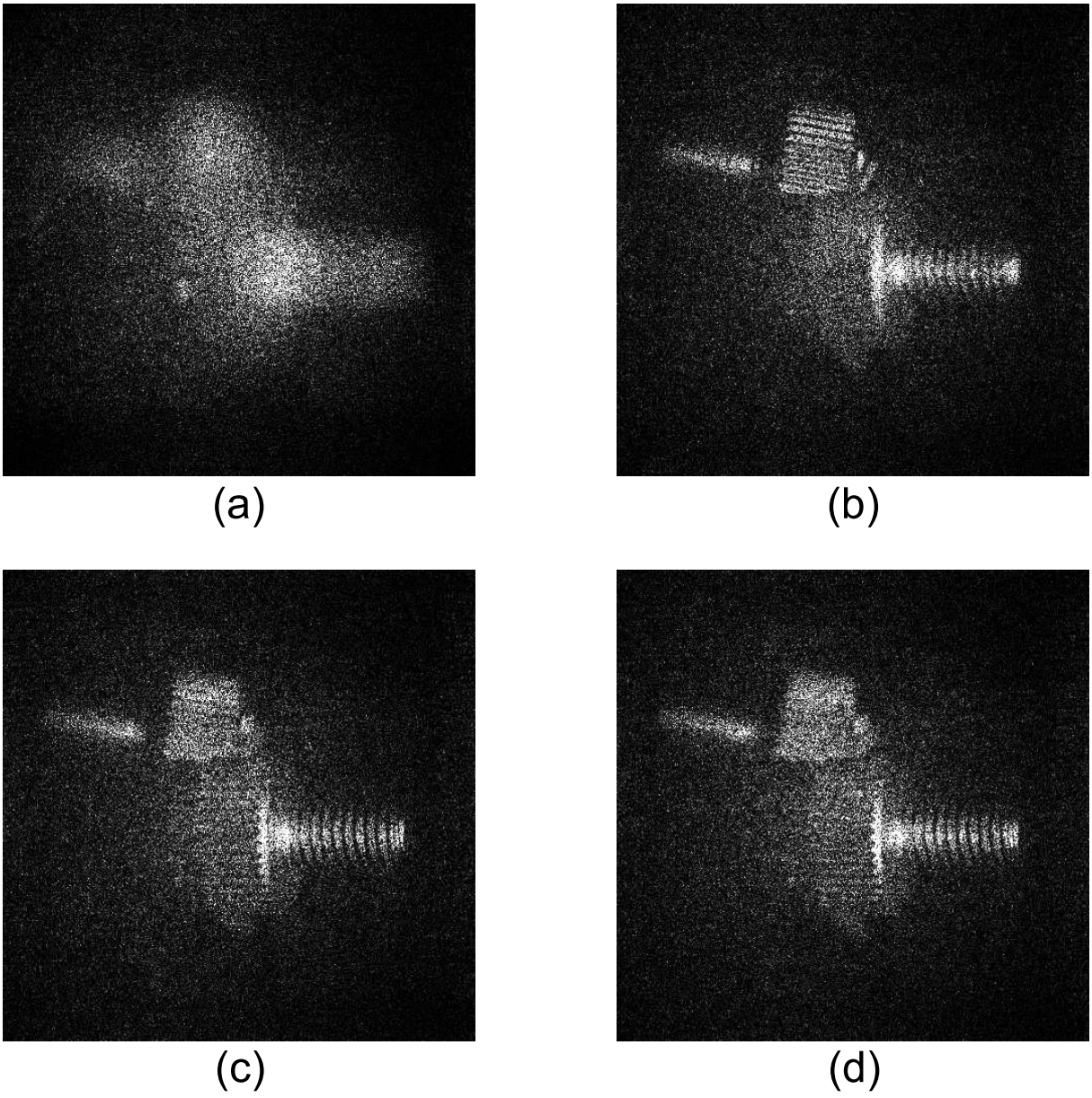

Figure 3.5: Fibonacci search focus estimates, numerical reconstruction at estimate after (a) iteration 1, (b) iteration 2, (c) iteration 7 and (d) final iteration.

Data: A starting depth s. An ending depth e. The maximum number of iterations I. A function F which computes a focus value for a given depth.

Result: The in-focus depth D of the hologram.

$M = I + 2$;
$d_1 = s + \frac{F_{M-2}}{F_M}(s - e)$;
$d_1 = e - \frac{F_{M-2}}{F_M}(s - e)$;
$f_1 =$F(d_1);
$f_2 =$F(d_2);
while DOF(d_1,d_2) $\bigwedge$ M ≥ 3 **do**
    if $f_1 < f_2$ **then**
        $D = d_2$; $s = d_1$; $d_1 = d_2$; $f_1 = f_2$;
        $d_2 = e - \frac{F_{M-2}}{F_M}(e - s)$;
        $f_2 =$F(d_2);
    else
        $D = d_1$; $e = d_2$; $d_2 = d_1$; $f_2 = f_1$;
        $d_1 = s + \frac{F_{M-2}}{F_M}(e - s)$;
        $f_1 =$F(d_1);
    $M = M - 1$;

Algorithm 3.1: Fibonacci autofocus algorithm for digital holography using the DOF function defined in Alg. 3.2.

four of the depth estimates from the autofocus algorithm applied to the two bolt object DH. In the interests of speed we have not applied any speckle reduction to the reconstructions. Figure 3.5 (a) and (b) shows a numerical reconstruction at the estimated depth after the first and second iterations. It is clear that after a very short estimation period the algorithm has already found the focal plane of the back bolt. The reconstructions from the depth estimates after the seventh and final iterations are displayed in Fig. 3.5(c) and (d) respectively. These demonstrate qualitatively the effectiveness of the

Data: Two depths d_1 and d_2.
Result: A true if the distance between d_1 and d_2 is greater than the combined depth-of-focus of the depths, a false otherwise.

$\mathrm{df}_1 = d_1 / \left(1 - \frac{d_1 \lambda}{N^2 \delta \xi^2}\right)$;
$\mathrm{df}_2 = d_2 / \left(1 + \frac{d_2 \lambda}{N^2 \delta \xi^2}\right)$;
if $\mathrm{df}_2 \geq \mathrm{df}_1$ **then**
    result $= true$;
else
    result $= false$;

Algorithm 3.2: DOF: optimised termination condition for Fibonacci search on digital holograms.

search to accurately determine focus.

The complete process of using the Fibonacci search is displayed graphically in Fig. 3.6(a). In this figure the first 8 iterations are highlighted on the curve representing the fixed stepsize search using 930 reconstructions. Both search strategies used reconstructions at depths ranging between 170mm and 1000mm. Assuming the DH is recorded in accordance with sampling theory and a square object, these distances allow for objects ranging from a minimum size of 0.1mm up to a maximum size of 70mm for our experimental setup, calculated with

$$\Delta O = \frac{d\lambda}{\delta \xi} - \Delta X, \tag{3.6}$$

where ΔO is the object size, d is the reconstruction distance, λ is the wavelength of the illumination source, δxi is the square pixel size and ΔX is the CCD size. The success of our autofocus algorithm to find the correct focal plane in such a large search space demonstrates the effectiveness of our

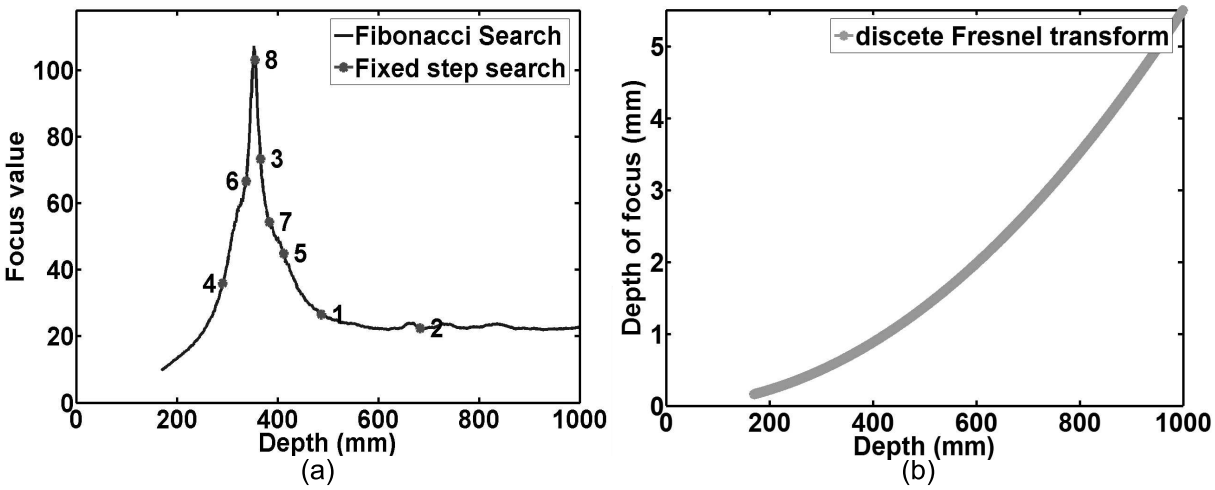

Figure 3.6: Autofocus search, (a) fibonacci search compared to fixed stepsize search, (b) depth-of-focus for the discrete Fresnel transform.

search. In Fig. 3.6(b) we display the depth-of-focus as a function of distance for the discrete Fresnel transform for these distances.

We also apply the Fibonacci search to a second DH containing a Lego object. In Fig. 3.7 we display a reconstruction of the estimated focal plane using the Fibonacci search applied to the Lego DH and the previous two bolt DH. We also show a plot of the Fibonacci search versus the fixed stepsize search below each reconstruction. Experiments using both these DHs required a maximum of 14 iterations to arrive at the correct focal plane, which is noticeably fast considering the large input search space of 970mm. The depth estimates per iteration for both of these DHs are shown in Table 3.2. These results show that the Fibonacci search can be successfully applied to reconstructions from DHs.

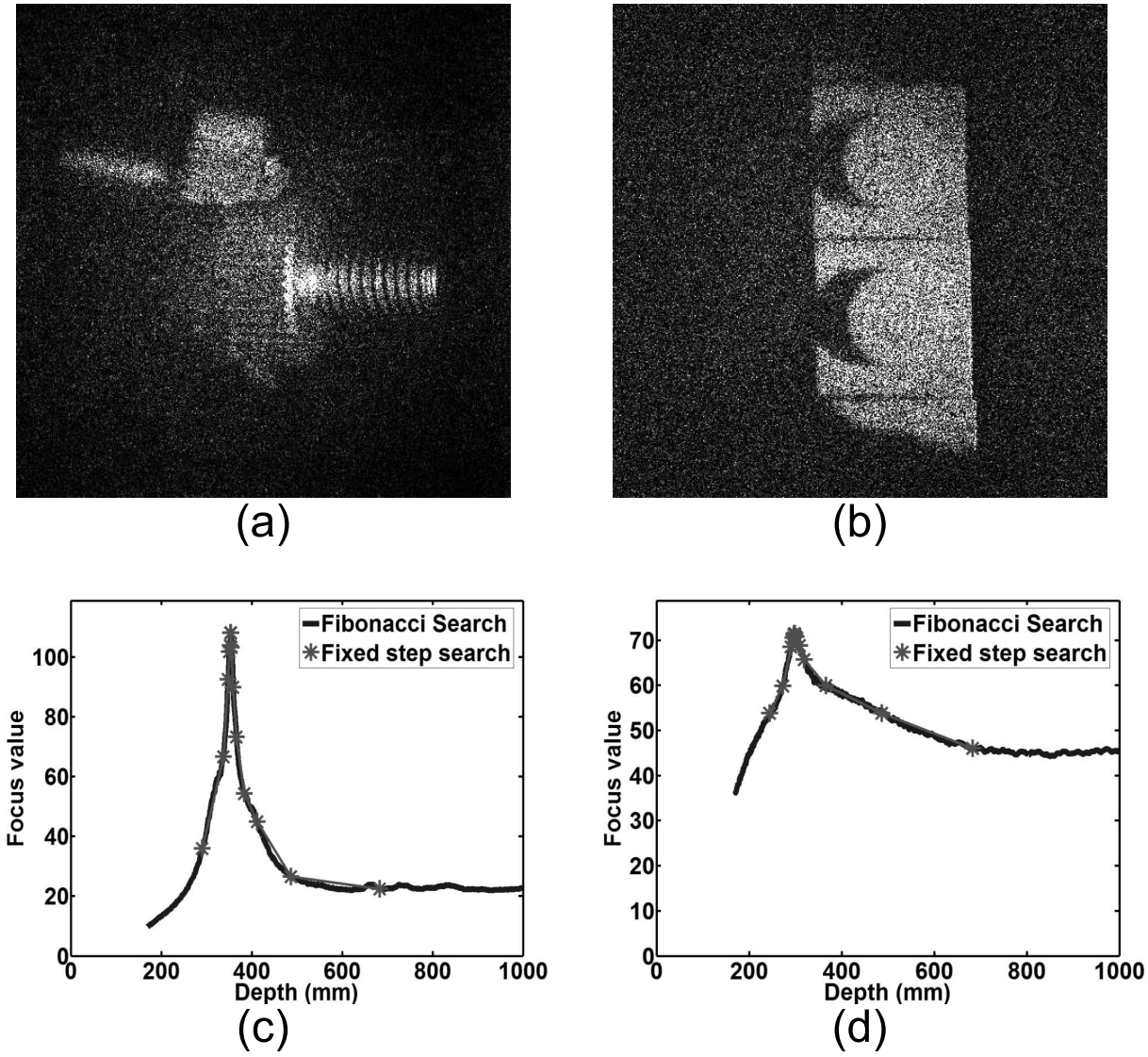

Figure 3.7: Autofocus results, numerical reconstructions at estimated in-focus depth of (a) two bolt object, (b) Lego object and (c-d) focus plot of focus values as a function of depth for objects (a-c).

Table 3.2: Autofocus iteration depth estimation

Iteration	Two bolts DH (mm)	Lego DH (mm)
1	487.03	487.03
2	365.94	365.94
3	365.94	291.10
4	365.94	291.10
5	365.94	291.10
6	365.94	291.10
7	355.02	302.02
8	355.02	302.02
9	355.02	297.84
10	352.44	297.84
11	352.44	297.84
12	353.42	297.84
13	353.42	298.45
14	—	298.45

3.3 Depth-from-focus

Depth-from-focus (DFF) is an image processing approach for the estimation of surface shape in a scene using multiple independently focused images. DFF approaches estimate the focal plane of a DH by maximizing a focus measure which is applied to the intensity of several 2D reconstructions where each reconstruction is at a different focal plane. Depth maps can be calculated using DFF approaches through calculating a focus measure on blocks in each reconstruction. The depth of each block is estimated by finding the reconstruction depth which returns the maximum focus value for that block. DFF is used in many applications ranging from autofocus [TKN04, SCN93], video surveillance [MR94], robotics [NATG96, NATG97] and shape recovery of 3D surfaces [EL91, EL93, Bov93, DW88, SC95, NN90, Nay92].

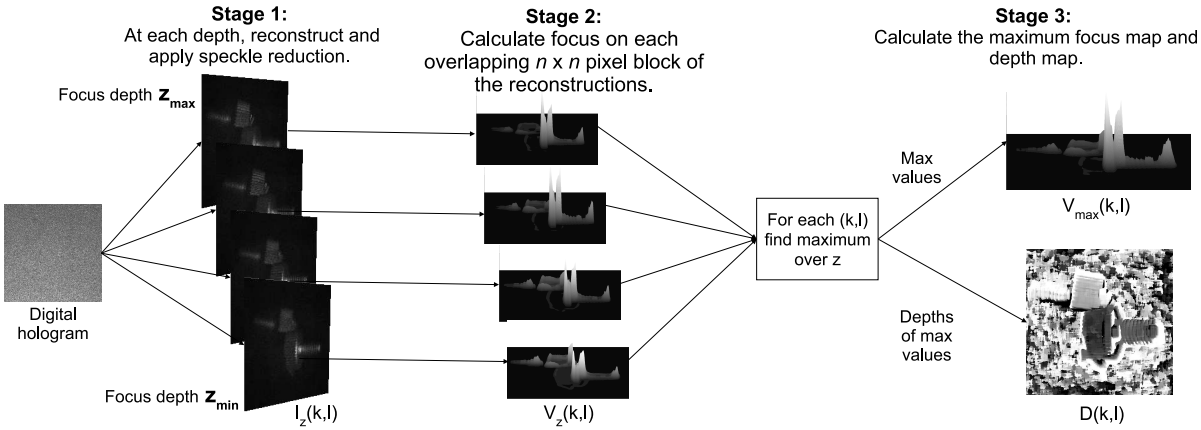

Figure 3.8: Depth-from-focus process, Step 1: numerically reconstruct over a range of depths, Step 2: block process each reconstruction using variance, Step 3: calculate depth map.

3.3.1 DFF algorithm

Ma et al. [MWLJ04] first proposed a DFF algorithm applied to digitised physical holograms for the recovery of shape information. By calculating variance on non-overlapping blocks from reconstructions of a DH at different depths they recovered depth information from a lower-resolution version of the sensed object. Variance is calculated on the intensity of each reconstruction, $I_z(x, y) = |U_z(x, y)|^2$, where $I_z(x, y)$ is of size $M \times N$ pixels. Our algorithm requires five input parameters: a DH, a block size $n \times n$, a start depth $z_{\min}$, an increment z_{step} and an end depth $z_{\max}$. The initial reconstruction depth z is set to the starting depth, $z = z_{\min}$. The algorithm involves the following three steps as illustrated in Fig. 3.8:

Step 1: The input DH is reconstructed at depth z and a speckle reduction technique can be applied. Speckle reduction is an optional part of the process

where the speckle reduction technique to be used is chosen by the user. The output reconstructions intensity is stored in $I_z(x, y)$.

Step 2: We then calculate a focus value for each pixel by calculating variance on $n \times n$ pixel overlapping blocks approximately centred on each pixel, and address each block with (k, l) where $k \in [0, (M-1)], l \in [0, (N-1)]$. Variance of each overlapping block at each depth z is calculated with function $V_z : \mathbb{R}^{n \times n} \rightarrow \mathbb{R}^+$ defined by

$$V_z(k,l) = \frac{1}{n^2} \sum_{x=k-\lfloor \frac{n-1}{2} \rfloor}^{k+\lceil \frac{n-1}{2} \rceil} \sum_{y=l-\lfloor \frac{n-1}{2} \rfloor}^{l+\lceil \frac{n-1}{2} \rceil} \left[I_z(x,y) - \overline{I_z(k,l)} \right]^2, \tag{3.7}$$

$V_z(k, l)$ is therefore a volume storing a 2D variance image for each depth z and $\overline{I_z(k,l)}$ is defined as

$$\overline{I_z(k,l)} = \frac{1}{n^2} \sum_{x=k-\lfloor \frac{n-1}{2} \rfloor}^{k+\lceil \frac{n-1}{2} \rceil} \sum_{y=l-\lfloor \frac{n-1}{2} \rfloor}^{l+\lceil \frac{n-1}{2} \rceil} I_z(x,y). \tag{3.8}$$

For the non-overlapping algorithm the volume is calculated with

$$V_z^{\text{no}}(r,s) = \frac{1}{n^2} \sum_{x=rn}^{rn+n-1} \sum_{y=sn}^{sn+n-1} [I_z(x,y) - \overline{I_z(rn + \lfloor \frac{n-1}{2} \rfloor, sn + \lfloor \frac{n-1}{2} \rfloor)}] \tag{3.9}$$

where $r \in [0, 1, ...\lfloor (M-1)/n \rfloor], s \in [0, 1, ...\lfloor (N-1)/n \rfloor]$. We iterate this step by incrementing z by a value of z_{step} until $z > z_{\text{max}}$.

Step 3: The next step is to calculate the depth map and the maximum focus map. The maximum focus map is calculated by finding the maximum focus

value in the variance volume for each pixel with

$$V_{\max}(k,l) = \max_{z}\left[V_z(k,l)\right], \tag{3.10}$$

$$V^{\mathrm{NO}}_{\max}(r,s) = \max_{z}\left[V^{\mathrm{NO}}_{z}(r,s)\right]. \tag{3.11}$$

where $V_{\max}(k,l)$ is the maximum focus map for the overlapping case and $V^{\mathrm{NO}}_{\max}(r,s)$ is the maximum focus map for the non-overlapping case. The depth where this maximum occurs is then stored in the depth maps which are calculated with

$$D_{z_{\mathrm{step}}}(k,l) = \min\{d : V_d(k,l) = V_{\max}(k,l)\}, \tag{3.12}$$

$$D^{\mathrm{NO}}_{z_{\mathrm{step}}}(r,s) = \min\{d : V^{\mathrm{NO}}_{d}(r,ls) = V^{\mathrm{NO}}_{\max}(r,s)\}, \tag{3.13}$$

$$\tag{3.14}$$

where $\min\{\cdot\}$ returns the minimum element of a set, $D_{z_{\mathrm{step}}}(k,l)$ is the depth map for the overlapping case and $D^{\mathrm{NO}}_{z_{\mathrm{step}}}(r,s)$ is the depth map for the non-overlapping case.

3.3.2 Block size

In Fig. 3.9 and Fig. 3.10 we demonstrate the impact block size has on the output depth maps. To determine the depth of a block in the reconstruction volume using a focus measure, there needs to be enough object information contained in the block. Assuming there is enough object information in the block, there is also a trade off between larger block sizes and smaller block

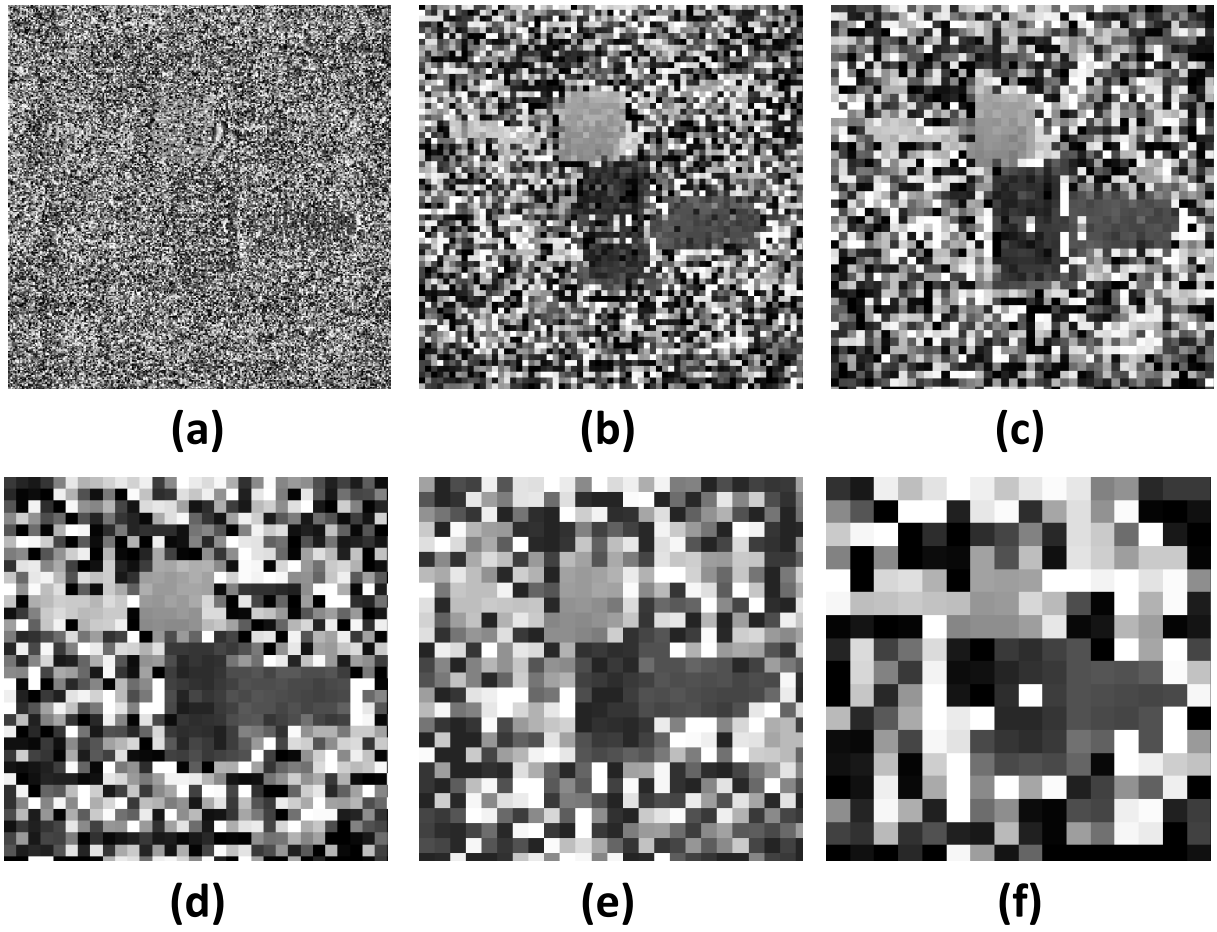

Figure 3.9: Two bolts object hologram non-overlapping DFF: depth maps created with a (a) 7×7 block size, (b) 31×31 block size, (c) 43×43 block size, (d) 63×63 block size, (e) 81×81 block size and (f) a 121×121 block size.

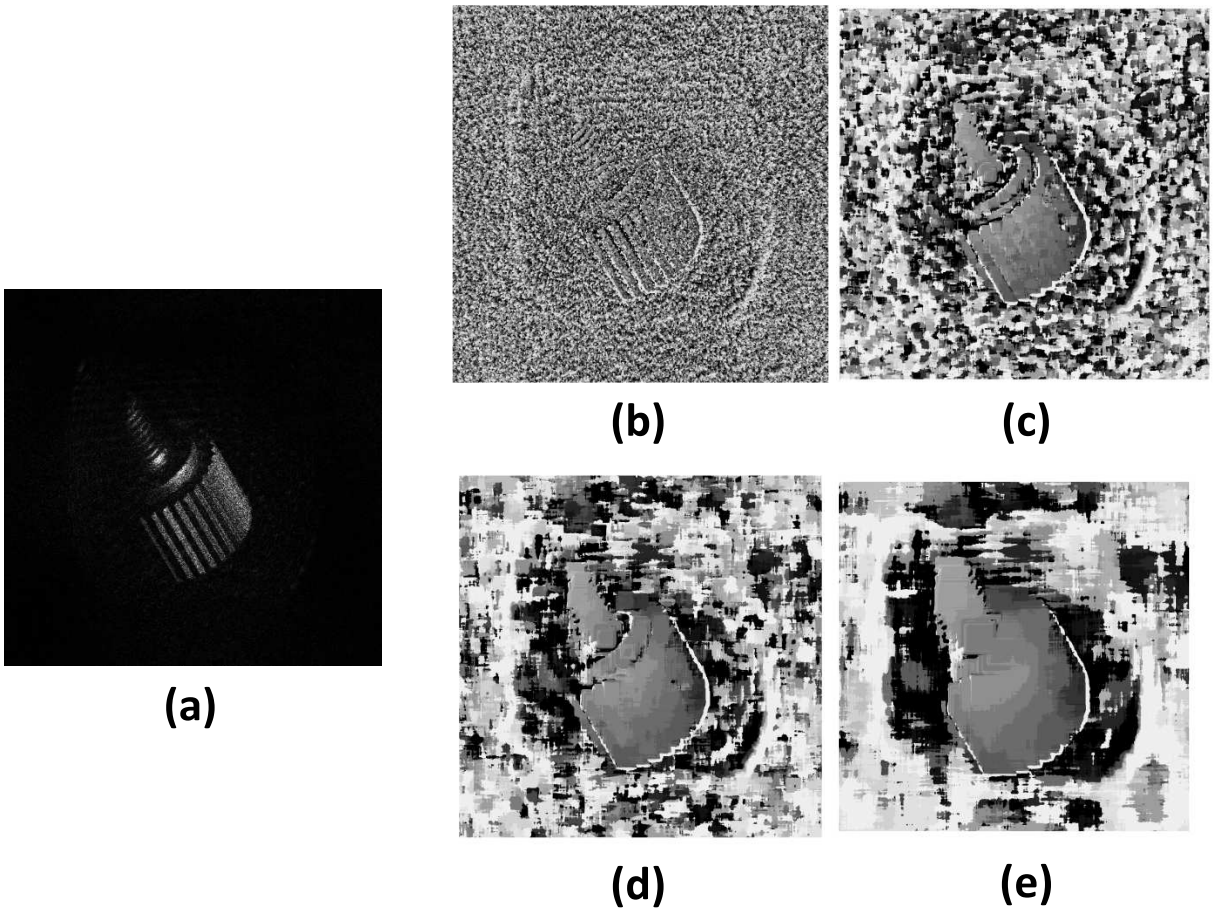

Figure 3.10: Bolt object hologram overlapping DFF: (a) numerical reconstruction, depth maps created with a (b) 7×7 block size, (c) 43×43 block size, (d) 81×81 block size and a 121×121 block size.

sizes. The larger block sizes give a good estimate of the global shape of the object at the expense of fine object features. However, the smaller block sizes identify the finer object features but have high error in the estimate of the global object shape. While using a large block size is potentially acceptable in the overlapping case, Fig. 3.10(e), the loss of resolution in the non-overlapping case, Fig. 3.9(f), is too great to make the depth map usable for most applications. For our macroscopic objects we have identified a block size of 63×63 for the non-overlapping case and a block size of 81×81 for the overlapping case to provide a good trade-off between fine object features and global shape. The reason for the difference between the block sizes of the two approaches is purely the image resolution, there is a 25% increase in image resolution between depth maps created using a 63×63 block size over a 81×81 block size and the non-overlapping algorithm. It is worth noting that this block size is dependent on the size of the reconstructions, the 81×81 block size is recommended for 2048×2048 sized reconstructions. If the reconstructions are a factor of n smaller or larger than 2048, the selected block size should be the same factor n of 81.

3.3.3 Overlapping versus non-overlapping

The length of time our DFF approach takes is dependent on three factors: the number of reconstructions used, the block size input and whether the non-overlapping, Eq. (3.9), or overlapping, Eq. (3.7), algorithm is used. To calculate a single $V_z(k,l)$ using a block size of 7×7 requires 9 minutes on a P4 3GHz PC, while calculating $V_z(k,l)$ with our recommended 81×81 block size

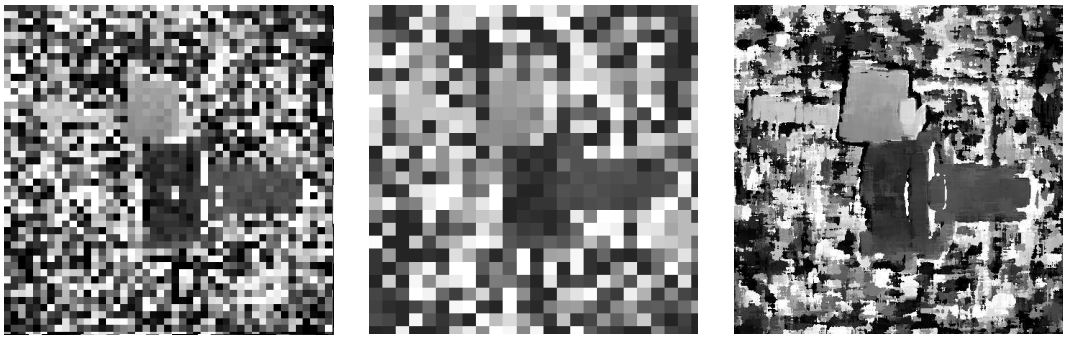

Figure 3.11: Depth maps created using 151 reconstructions, the (a) non-overlapping algorithm (with a 63×63 block size), (b) non-overlapping algorithm (with a 81×81 block size) or the (c) overlapping algorithm (with a 81×81 block size).

requires 25 minutes. This is in stark contrast to the one minute processing time required to calculate $V_z^{\mathrm{NO}}(r,s)$ for an 81×81 block size. This translates to a running time of 62 hours to calculate $\mathrm{D}_{0.2}(k,l)$ with 151 reconstructions and only 2.5 hours to calculate $\mathrm{D}_{0.2}^{\mathrm{NO}}(r,s)$ with the same number of reconstructions. Considering the lengthy processing time difference, is there any need to calculate $\mathrm{D}_{0.2}(k,l)$, instead of just $D_{0.2}^{NO}(r,s)$?

We compare two $\mathrm{D}_{0.2}(k,l)$'s and a $\mathrm{D}_{0.2}^{\mathrm{NO}}(r,s)$ in Fig. 3.11. These were created using the two bolts object DH, 151 reconstructions and a block size of 81×81 for the overlapping example and a block size of 63×63 and 81×81 for the non-overlapping examples. We display two non-overlapping examples as they both return qualitively good depth maps. A set of depth maps using the non-overlapping algorithm and different block sizes are displayed in Fig. 3.9 for a more thorough comparison. It is demonstrated in Chapter 4.1 how $\mathrm{D}_{0.2}(k,l)$ can be used to segment the object(s) from the background, and

in Chapter 4.2 how it can be used to perform depth segmentation. The low resolution of $\mathrm{D}_{0.2}^{\mathrm{NO}}(r,s)$ would not allow for accurate background segmentation, especially if the shape of the object boundary is complex and not easily identifiable in low resolution. However, there is enough depth information in $\mathrm{D}_{0.2}^{\mathrm{NO}}(r,s)$ to allow us to create an extended focused image as is shown in Chapter 5.1. In general we recommend applying the overlapping algorithm to the DH but realise that it is computationally expensive, we are currently researching methods to improve the speed of the algorithm through the use of the Fibonacci search in the step 2 of the DFF algorithm.

3.3.4 Speckle reduction

As discussed in Chapter 2.3 speckle is a source of noise in numerical reconstructions of macroscopic objects. It is a multiplicative source of noise which manifests itself as both low and high spatial frequencies. Due to its multiplicative nature, simple mean, median or gaussian filtering is not as successful as it is for additive noise. For this reason speckle reduction algorithms have been developed specifically for digital holography [BFRJ04, GSFP05, MHM+07]. We select discrete Fourier filtering [MHM+07] with a block size of 512×512 as our speckle reduction technique, this equates to a reduction in resolution by $\frac{1}{2}$ in the reconstructions and a speckle index of 0.25. While the visual quality of the reconstructions are better after speckle reduction, an examination into whether the resolution loss caused by the speckle reduction would hamper our DFF algorithm needs to be carried out. We create two $D_{0.2}^{\mathrm{NO}}(r,s)$ using a block size of 41×41, $z_{\min} = 345\text{mm}$ and $z_{\max} = 380\text{mm}$

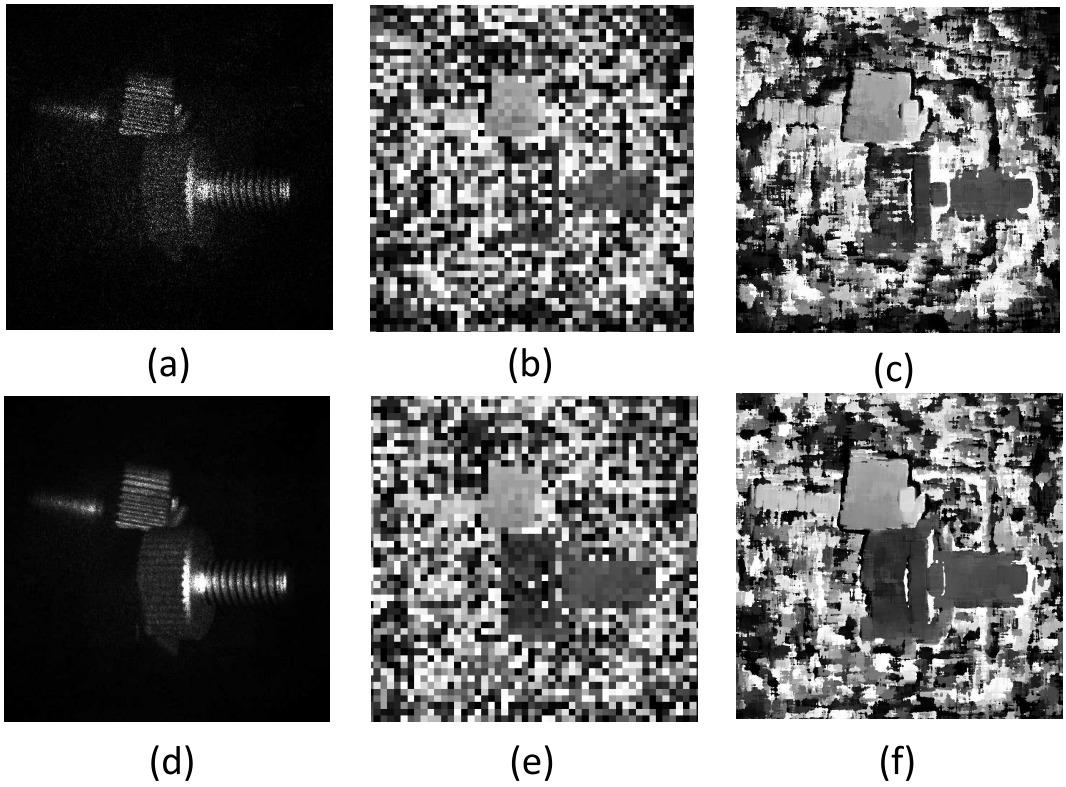

Figure 3.12: Numerical reconstruction (a) without speckle reduction (b) corresponding non-overlapping and (c) overlapping depth maps. Numerical reconstruction (d) with speckle reduction, (e) corresponding non-overlapping and (f) overlapping depth maps.

from our two bolts object DH and two $D_{0.2}(r,s)$ using a block size of 81×81. The first $D_{0.2}^{\mathrm{NO}}(r,s)$ is created with reconstructions where no speckle reduction has been applied, the second $D_{0.2}^{\mathrm{NO}}(r,s)$ is created with reconstructions after discrete Fourier filtering has been applied. We wanted to investigate if there is less or more noise in the depth map post speckle reduction. The most extreme noise in depth maps is pure white or pure black pixels in regions we know to be object pixels. Pure white or pure black pixels equate to depth estimates of $z_{\min}$ or $z_{\max}$. Since these values are initially chosen so that the object is out-of-focus at $z_{\min}$ then comes into focus and then is completely defocused at $z_{\max}$, an object pixel with an estimated depth of $z_{\min}$ or $z_{\max}$ is incorrect. We display a reconstruction before speckle reduction in Fig. 3.12(a) along with the corresponding $D_{0.2}^{\mathrm{NO}}(r,s)$ in Fig. 3.12(b) and the $D_{0.2}(k,l)$ in Fig. 3.12(c). The numerical reconstruction after speckle reduction is shown in Fig. 3.12(d), the non-overlapping depth map is shown in Fig. 3.12(e) and the overlapping depth map in Fig. 3.12(f). It is evident in both the non-overlapping and the overlapping case that the depth maps created using numerical reconstructions where speckle reduction is applied have less noise, this is particularly obvious when looking at the front bolt region.

3.3.5 Reconstruction interval

The final DFF input parameter to discuss is z_{step}, the reconstuction interval. This interval has a large impact on both the total time of DFF and of the quality of the output $\mathrm{D}_{z_{\mathrm{step}}}(k,l)$. Theoretically the z-resolution of our DFF

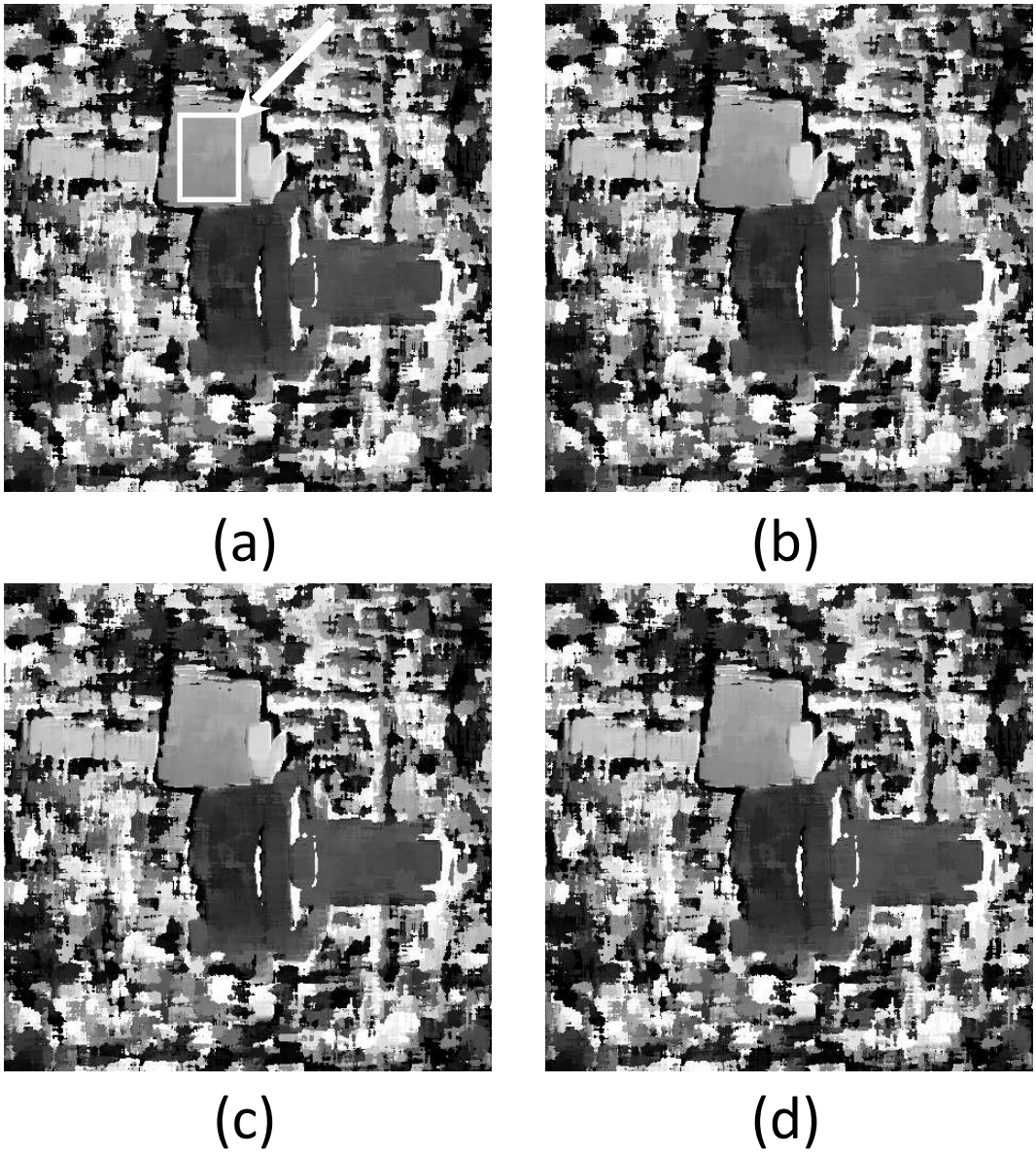

Figure 3.13: Depth maps created using four different intervals (a) $D_{0.1}$(k,l) (with highlighted object block OB), (b) $D_{0.2}$(k,l), (c) $D_{0.5}$(k,l) and (d) D_1(k,l).

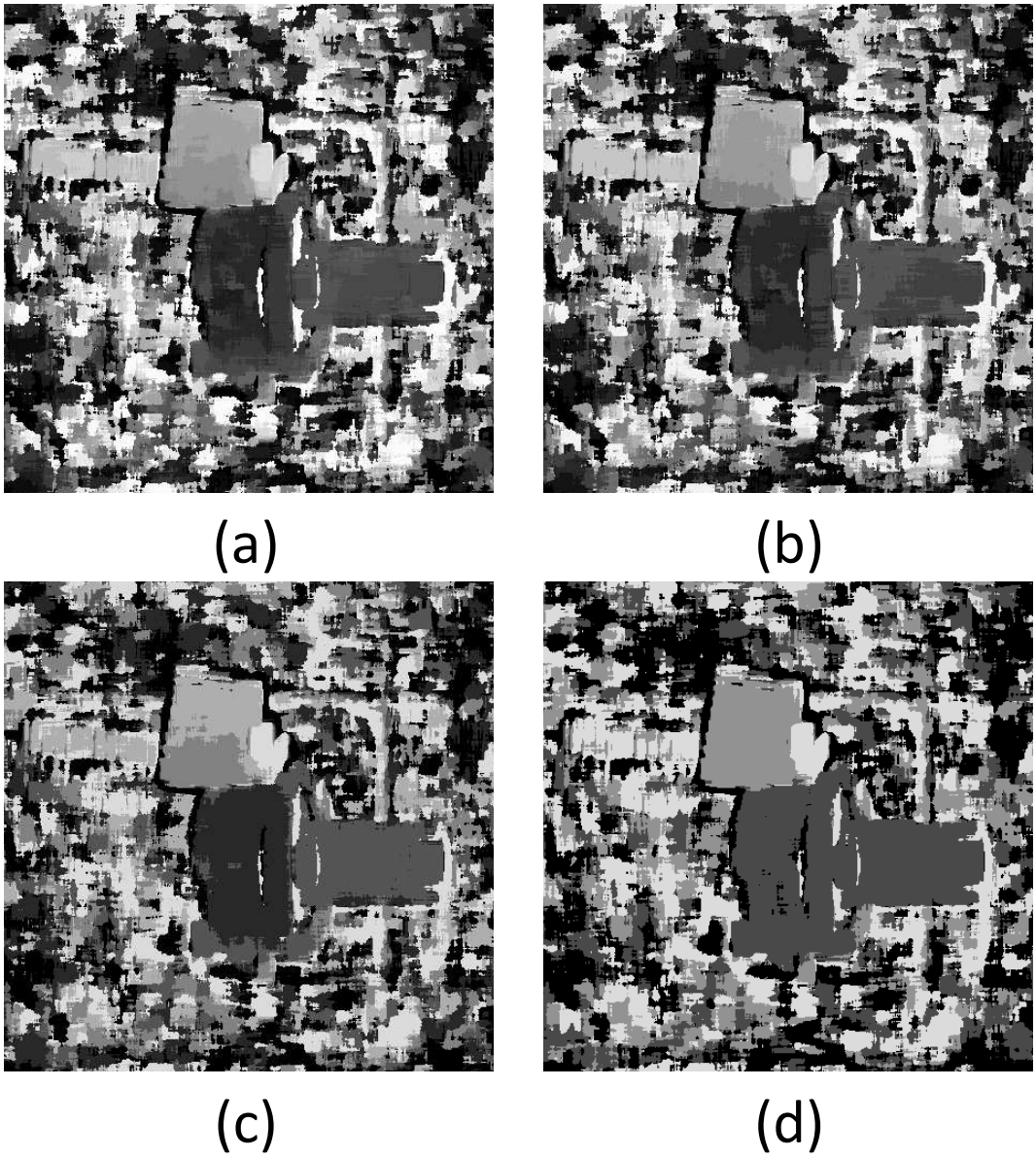

Figure 3.14: Depth maps created using four different intervals (a) D_2(k,l) (with highlighted object block OB), (b) D_3(k,l), (c) D_6(k,l) and (d) D_{10}(k,l).

algorithm is limited by the depth-of-focus of the numerical reconstuction function. Using a reconstruction interval where $z_{\text{step}} = \text{dof}^{j}_{z_{min}}$ (where $\text{dof}^{j}_{z_{min}}$ is calculated from Eq. (A.31), the depth-of-focus calculation for the DFRT) should produce the depth map with the highest z-resolution. By setting z_{step} in this way, we ensure that the focus range in two successive reconstructions does not overlap and that we are not processing redundant focus information.

To demonstrate the impact of the reconstruction interval we select our two bolts object DH and calculate $\text{dof}^{i}_{z_{min}}$ as 0.2mm and create eight depth maps: $\text{D}_{0.1}(k,l)$, $\text{D}_{0.2}(k,l)$, $\text{D}_{0.5}(k,l)$, $\text{D}_{1}(k,l)$, $\text{D}_{2}(k,l)$, $\text{D}_{3}(k,l)$, $\text{D}_{6}(k,l)$ and $\text{D}_{10}(k,l)$ where $z_{\text{min}} = 345\text{mm}$, $z_{\text{max}} = 380\text{mm}$ and a block size of 81×81. The resulting depth maps are displayed in Fig. 3.13 and Fig. 3.14. We expect there to be virtually no difference between $\text{D}_{0.1}(k,l)$ and $\text{D}_{0.2}(k,l)$. While the difference between $\text{D}_{0.1}(k,l)$ and $\text{D}_{10}(k,l)$ is apparent from Fig. 3.13(a) and 3.14(d), it is difficult to tell if there is any difference between any of the depth maps displayed in Fig. 3.13. For this reason we select an object block, OB, on the head of the back bolt (which is highlighted in Fig. 3.13(a)) from all of the eight depth maps. We display OB in pseudo 3D, from the perspective of the arrow in Fig. 3.13(a), for all of the depth maps in Fig. 3.15 and 3.16. Visually there is no difference between the plots in Fig. 3.15(a) and (b) and this is verified by the standard deviation of their difference which is only 0.0765mm. However, there is a visible difference between Fig. 3.15(b) and (c) where the curvature of OB has become more discretised with more planes evident in Fig. 3.15(c). This is surprising as the interval has only changed from 0.2mm to 0.5mm, in this case the standard deviation of their difference

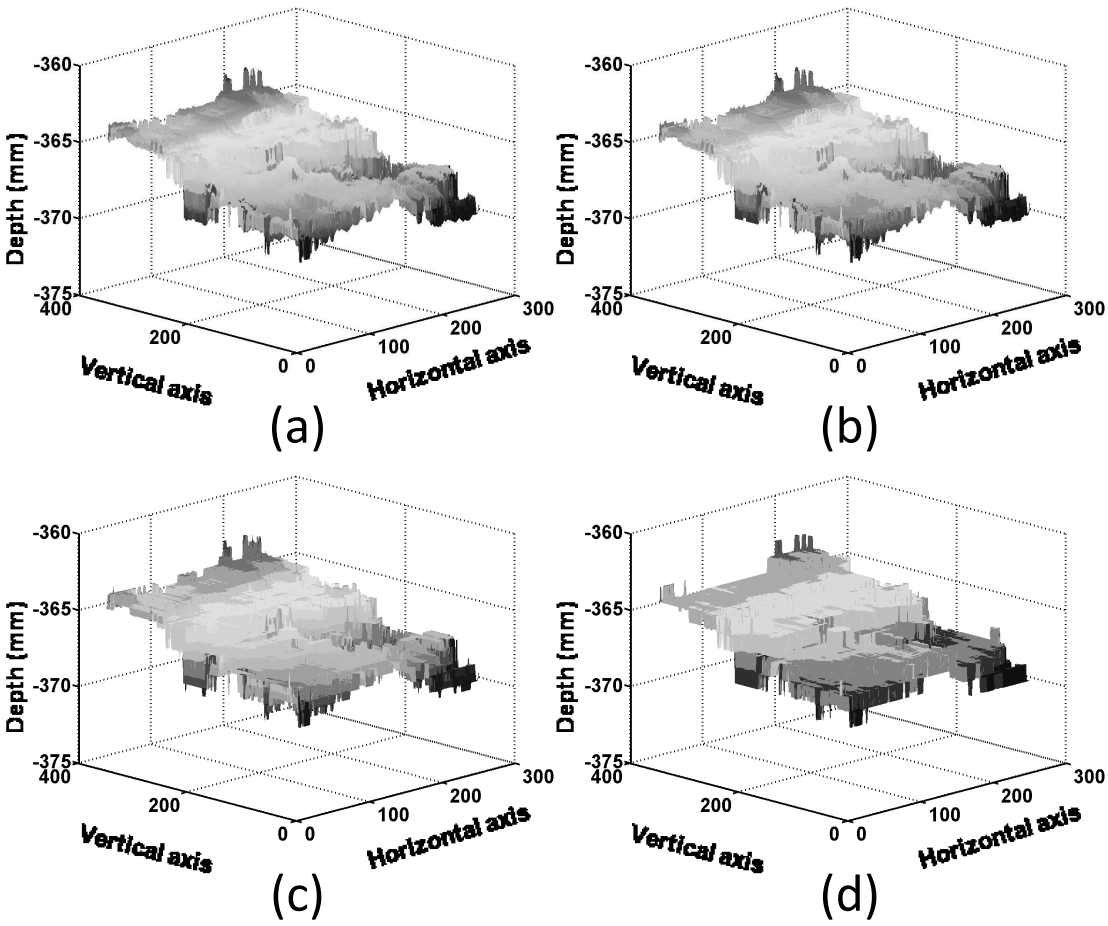

Figure 3.15: Pseudo 3D plot of OB from depth maps (a) $D_{0.1}$(k,l), (b) $D_{0.2}$(k,l), (c) $D_{0.5}$(k,l) and (d) D_1(k,l).

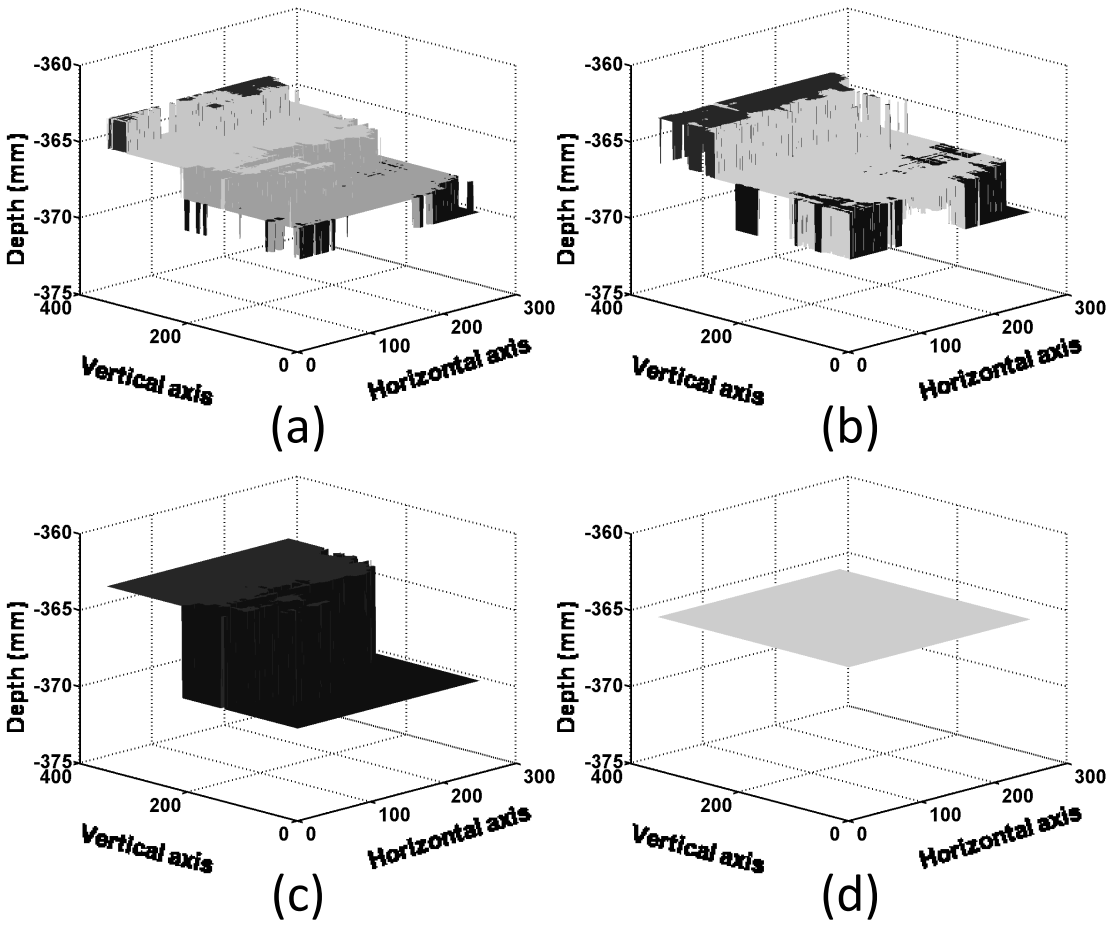

Figure 3.16: Pseudo 3D plot of OB from depth maps (a) D_2(k,l), (b) D_3(k,l), (c) D_6(k,l) and (d) D_{10}(k,l).

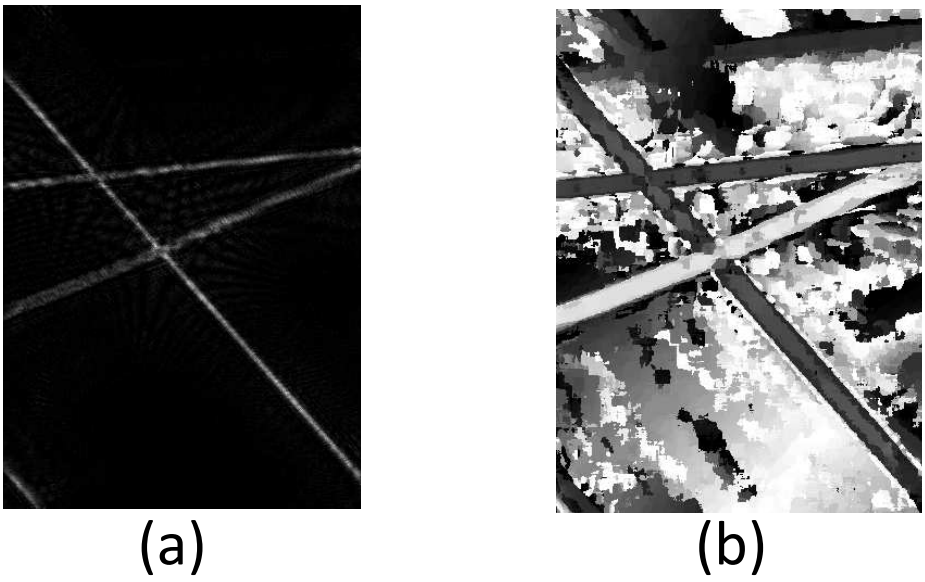

Figure 3.17: Hairs object DH, (a) numerical reconstruction and (b) D_1(k,l).

is 0.1692mm. OB for all eight depth maps is displayed in Fig. 3.15 and 3.16. We demonstrate the impact this subtle reconstruction interval difference can have on depth segementation in Chapter 4.2.

3.3.6 Depth map examples

In this section we display a subset of the depth maps created from our DHs and give the parameters input to our DFF algorithm:

Figure 3.17: Hairs object DH:

- $z_{\text{min}} = 220\text{mm}$
- $z_{\text{step}} = 1\text{mm}$
- $z_{\text{max}} = 320\text{mm}$

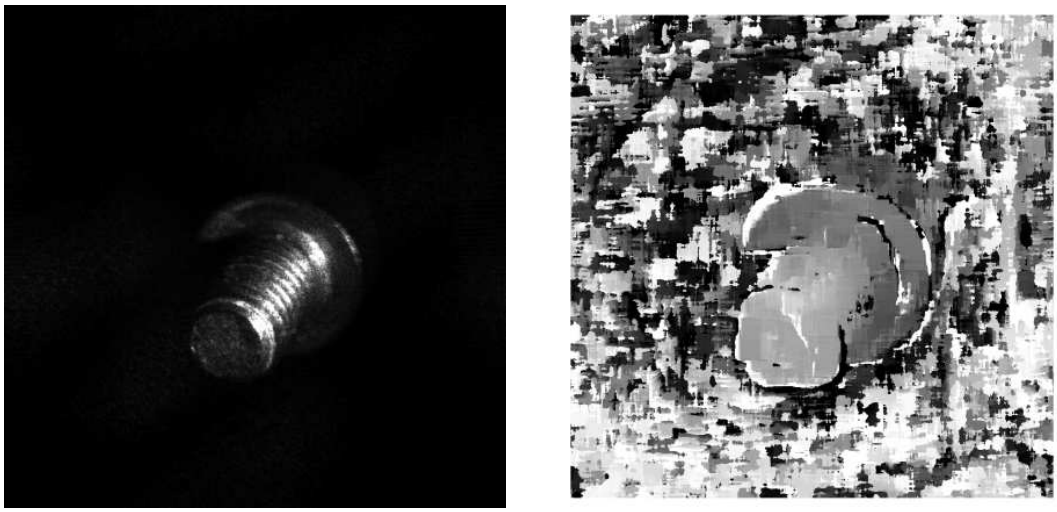

Figure 3.18: Large bolt object DH, (a) numerical reconstruction and (b) $D_{0.5}$(k,l).

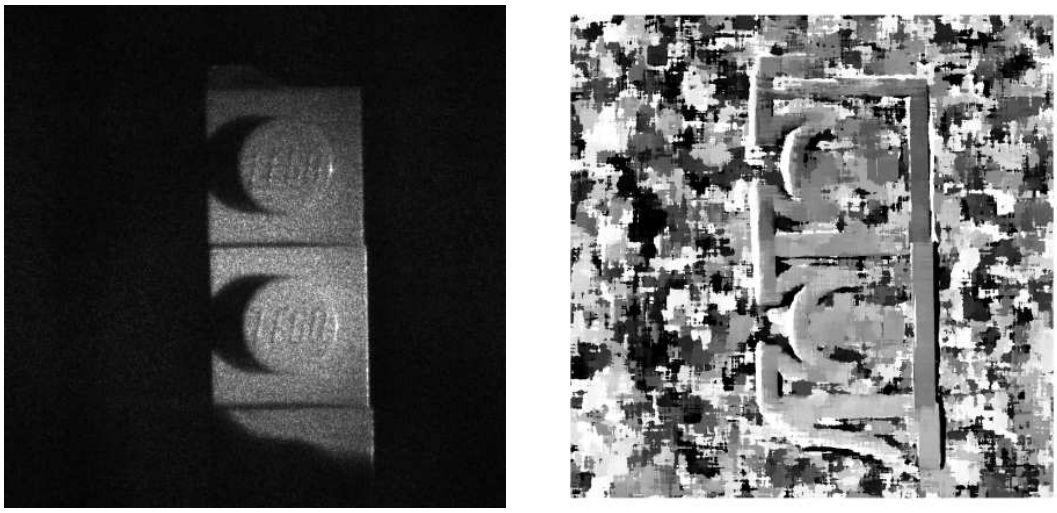

Figure 3.19: Lego object DH, (a) numerical reconstruction and (b) $D_{0.5}$(k,l).

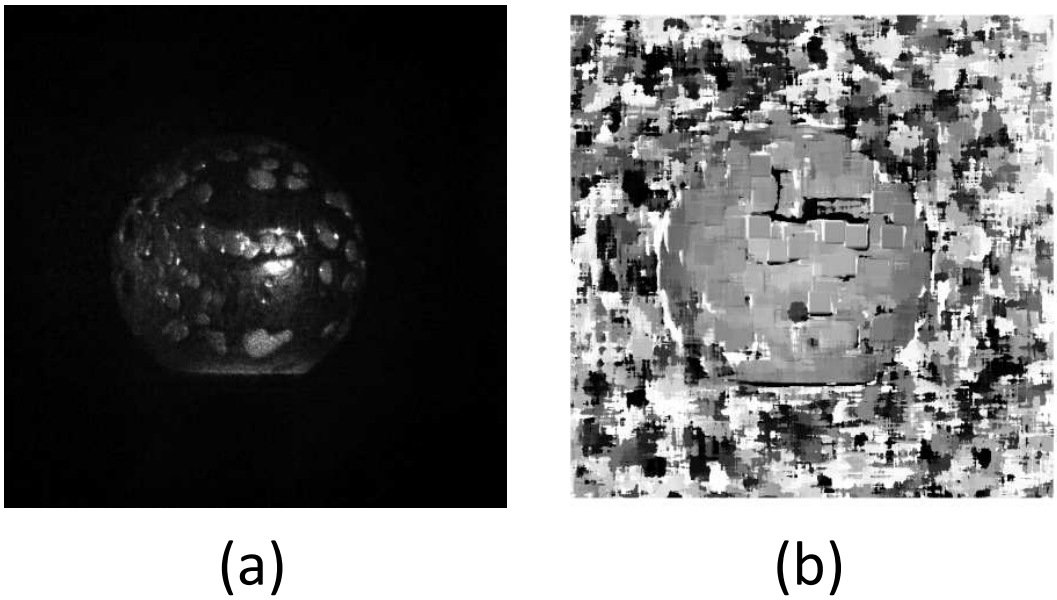

Figure 3.20: Marble object DH, (a) numerical reconstruction and (b) $D_{0.5}$(k,l).

- $n \times n = 81 \times 81$
- $M \times N = 3000 \times 2048$.

Figure 3.18: Large bolt object DH:

- $z_{\text{min}} = 320\text{mm}$
- $z_{\text{step}} = 0.5\text{mm}$
- $z_{\text{max}} = 350\text{mm}$
- $n \times n = 81 \times 81$
- $M \times N = 2048 \times 2048$.

Figure 3.19: Lego object DH:

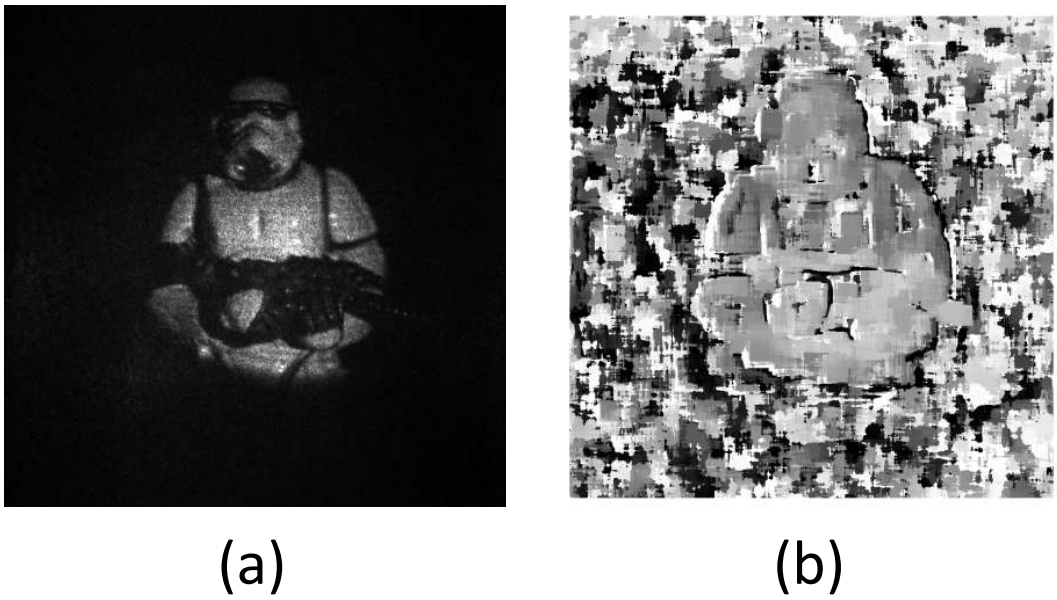

Figure 3.21: Stormtrooper object DH, (a) numerical reconstruction and (b) $D_{0.5}$(k,l).

- $z_{\text{min}} = 290\text{mm}$
- $z_{\text{step}} = 0.5\text{mm}$
- $z_{\text{max}} = 310\text{mm}$
- $n \times n = 81 \times 81$
- $M \times N = 2048 \times 2048$.

Figure 3.20: Marble object DH:

- $z_{\text{min}} = 355\text{mm}$
- $z_{\text{step}} = 0.5\text{mm}$
- $z_{\text{max}} = 380\text{mm}$
- $n \times n = 81 \times 81$

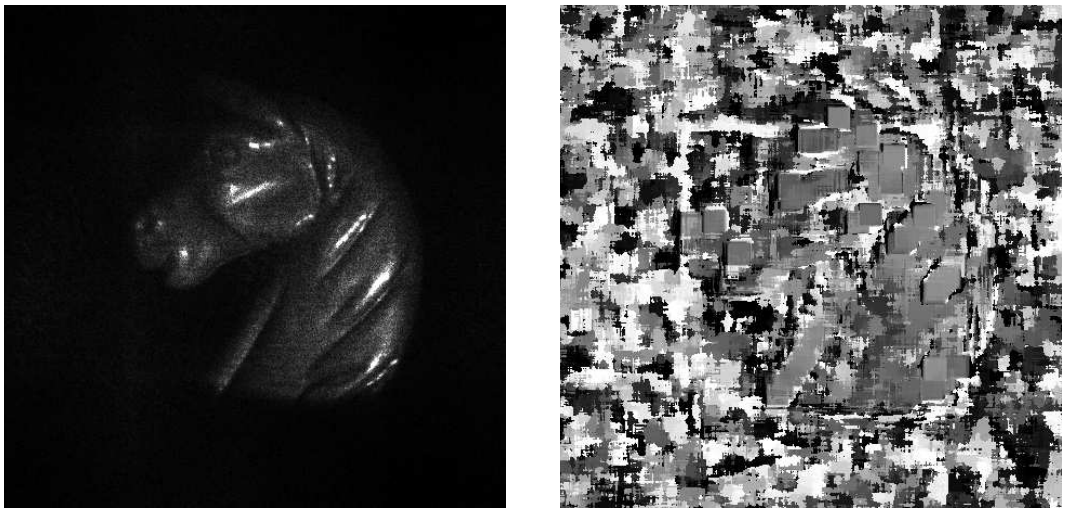

Figure 3.22: Knight object DH, (a) numerical reconstruction and (b) $D_{0.5}$(k,l).

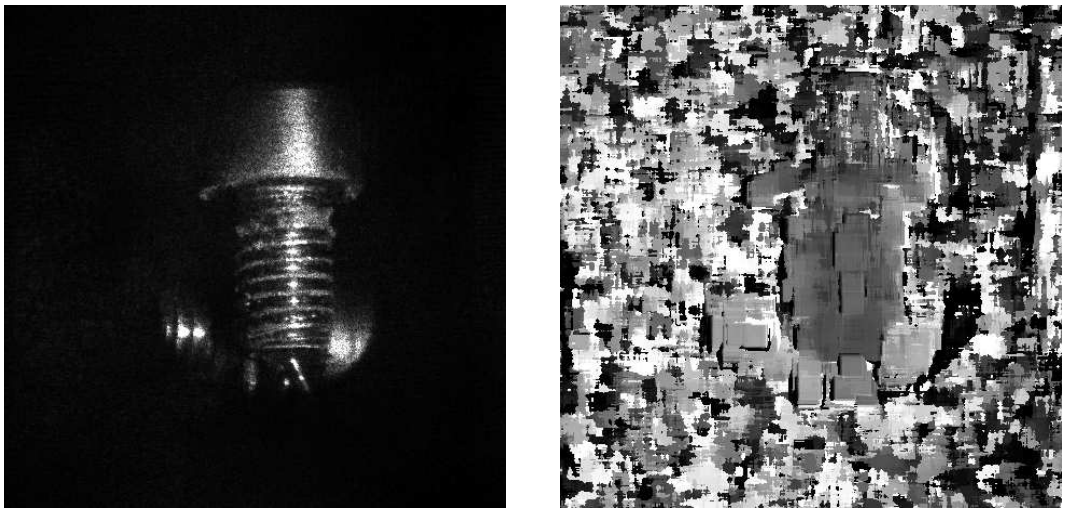

Figure 3.23: Bolts object DH, (a) numerical reconstruction and (b) $D_{0.5}$(k,l).

- $M \times N = 2048 \times 2048$.

Figure 3.21: Stormtrooper object DH:

- $z_{\text{min}} = 355\text{mm}$
- $z_{\text{step}} = 0.5\text{mm}$
- $z_{\text{max}} = 380\text{mm}$
- $n \times n = 81 \times 81$
- $M \times N = 2048 \times 2048$.

Figure 3.22: Knight object DH:

- $z_{\text{min}} = 360\text{mm}$
- $z_{\text{step}} = 0.5\text{mm}$
- $z_{\text{max}} = 380\text{mm}$
- $n \times n = 81 \times 81$
- $M \times N = 2048 \times 2048$.

Figure 3.23: Bolts object DH:

- $z_{\text{min}} = 355\text{mm}$
- $z_{\text{step}} = 0.5\text{mm}$
- $z_{\text{max}} = 380\text{mm}$
- $n \times n = 81 \times 81$
- $M \times N = 2048 \times 2048$.

3.4 Discussion

In this chapter we have discussed the application of focus detection in digital holography. We first carried out an evaluation of variance as a focus measure, and tested its applicability to digital holography. Since focus measures attempt to find the image containing the most high spatial frequencies, we compared variance to a focus measure based on the Fourier transform. Variance successfully focused reconstructions at the correct plane and produced a unimodal curve in a time significantly faster than the Fourier based measure. These desirable focus measure properties and its success in the detection of focus in other imaging systems led us to select variance as our focus measure.

Variance is implemented in a simple linear search autofocus system for digital holography. Our Fibonacci search autofocus algorithm is discussed in detail and we outlined our optimised termination condition for digital holography. We evaluated the applicability of this search algorithm using two test object DHs and demonstrated that it successfully estimated the focal plane of both DHs in at most 14 iterations given a relatively large search range of 970mm. Finally we described in detail our DFF shape extraction algorithm. The different input parameters and their impact on the outputs of DFF were heavily discussed.

Chapter 4

Application of focus information to the segmentation of digital holograms

In this chapter we demonstrate how the focus and depth information returned by our DFF algorithm can be used to segment a DH, first into background and object(s) and then into independent objects or object regions. The background segmentation of numerical reconstructions is performed using the maximum focus map and is detailed in the next section. The background segmentation process is based on the maximum focus map output by DFF, which means it computes a segmentation mask using multiple reconstructions. This is computationally expensive and in Sect. 4.1.3 segmenting using

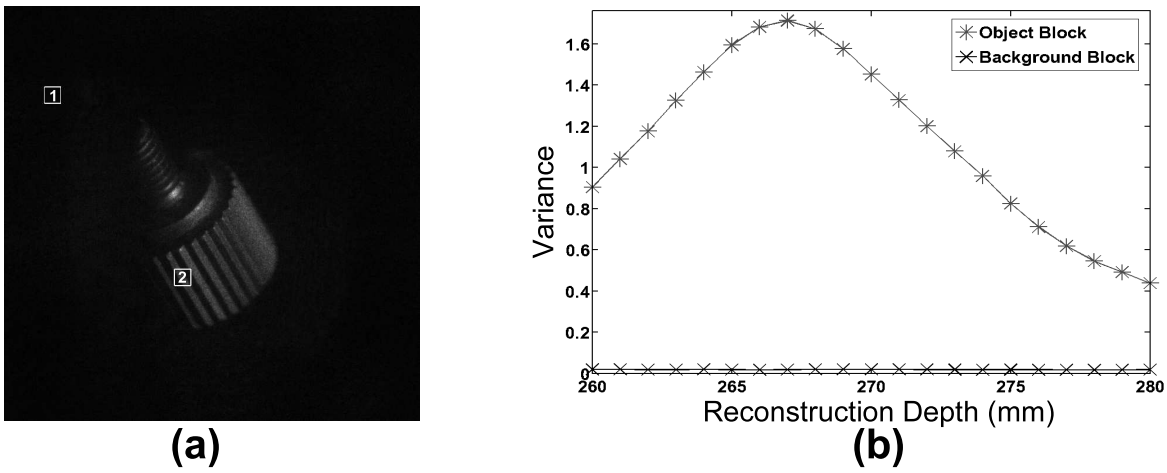

Figure 4.1: Screw object digital holography: (a) numerical reconstruction, (b) variance plot for background and object regions.

our multiple reconstruction DFF approach is shown to be advantageous compared to segmenting an individual reconstruction. We use the segmentation mask output from background segmentation to create a segmented depth map which is the required input for our depth segmentation algorithm. Section 4.2 deals with the application of our depth segmentation process for the purpose of segmenting a reconstruction into independent objects or object regions. The algorithm identifies the homogeneous regions within a depth map and uses these to segment the scene. Regions are then manually selected from unprocessed histograms of the depth maps to isolate the scene segments. The results obtained from scenes containing multiple-objects and objects with varying textures are presented.

4.1 Background segmentation

Using our DFF algorithm we calculate the maximum focus map $V_{\max}(k,l)$ using Eq.(3.10). A location with high variance indicates the nearby presence of an object whereas a low maximum variance indicates a background region. To perform background segmentation a threshold τ is chosen and $V_{\max}$ is transformed as

$$\text{SMask}(k,l) = \begin{cases} 1, & \text{if } V_{\max}(k,l) \geq \tau \\ 0, & \text{if } V_{\max}(k,l) < \tau, \end{cases} \tag{4.1}$$

where 0 denotes a background pixel and 1 denotes an object pixel. The binary image SMask(k,l) is our segmentation mask. Finally, we apply a mathematical morphology erosion operation (with neighbourhood $\lceil n/2 \rceil \times \lceil n/2 \rceil$) to SMask$(k,l)$ to shrink the boundaries of the object; our use of overlapping blocks uniformly enlarges the mask.

We verify our background segmentation technique using DHs of real-world objects. The first object (screw) is 1 cm^3 and is positioned approximately 268 mm from the camera. We input $z_{min} = 260$mm, $z_{step} = 1$mm, $z_{max} = 280$mm and $n \times n = 81 \times 81$ into our DFF algorithm to obtain $V_{\max}(k,l)$. A reconstruction of the screw object is shown in Fig. 4.1(a), where we highlight two manually seletected 81×81 pixel blocks labeled 1 and 2 indicating example background and object regions, respectively. Plots of variance calculated on these blocks over the full z range of 21 mm are shown in Fig. 4.1(b). It can be seen that the variance of the background

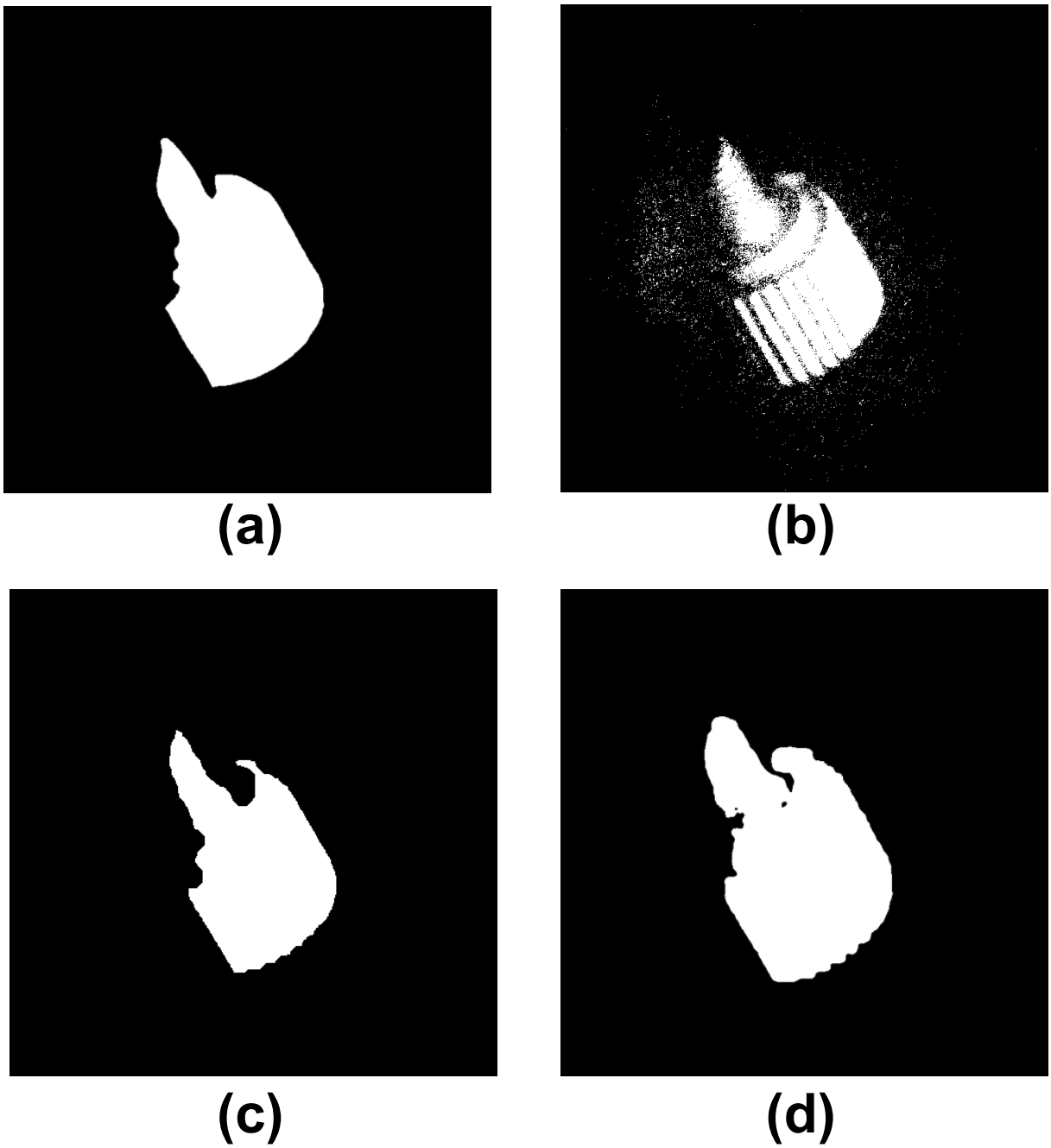

Figure 4.2: Segmentation of screw object digital holography: (a) manual, (b) EM approach, (c) single reconstruction approach (d) our DFF approach.

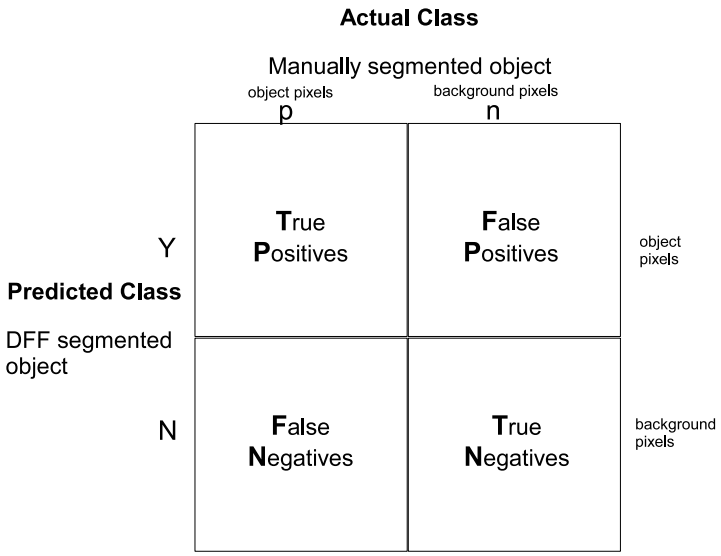

Figure 4.3: Confusion matrix.

block is 10^{-2} lower than that for the object block for this hologram. We found background blocks to have a significantly low variance value compared to that of object blocks. We believe this is primarily due to the dark nature of our background and the fact that the background area should contain only blurred data and therefore have a relatively low variance. This allows us to choose the appropriate normalised values of $\tau = 0.02$ for the screw object DH to segment object from background.

In Fig. 4.2 we compare our results with a ground-truth case where each pixel is manually classified as background or object, and also with the well-known and robust intensity-based segmentation technique expectation-maximization (EM) [FP03]. The shallow focal range of the screw object DH allows for a comparison between our method and this 2D technique. We use receiver operating characteristic (ROC) analysis [Faw06] to display the relative tradeoff

between the true positive rate and the false negative rate of our classifiers. In this form of analysis a pixel by pixel comparison is made between a manually created segmentation mask (the actual class as shown in Fig. 4.2(a)) and a segmentation mask created algorithmically (the predicted class as shown in Fig. 4.2(b-d)). Each pixel can then be assigned one of four labels: true positive, false positive, true negative and false negative. These labels are determined with the confusion matrix which is shown in Fig. 4.3. For example, if pixel (x,y) in the actual class is an object pixel and the corresponding (x,y) pixel in the predicted class is an object pixel then (x,y) is labeled as a true positive and the total number of true positives is incremented by one. If the (x,y) pixel in the predicted class is a background pixel then it is labeled as a false negative and the total number of false negatives is incremented. In this analysis the input $n \times n$ block size to DFF is the variable in our choice of classifier. We estimate the true positive rate of a classifier as

$$\text{tp rate} \simeq \frac{\text{True Positives}}{\text{Total number of positives}} \tag{4.2}$$

and the false positive rate as

$$\text{fp rate} \simeq \frac{\text{False Positives}}{\text{Total number of negatives}}. \tag{4.3}$$

A tp rate of 1 means every object pixel has been correctly identified and a fp rate of 0 means every background pixel has been correctly identified. A segmentation mask containing all 1's input as the predicted class would result in a tp rate of 1, which is obviously not a perfect segmentation mask.

Conversely, a segmentation mask containing all 0's would result in a fp rate of 0. This is why we need to combine the tp rate and the fp rate to determine the accuracy of any segmentation mask. It is also important to note that a segmentation mask that results in a tp rate that is equal to the fp rate is no better than segmentation mask created using random guesses. Classification results are plotted on orthogonal axes defined by tp rate and fp rate, allowing us to choose the block size $n \times n$ that best maximizes the tp rate while simultaneously minimizing the fp rate. For the screw object DH, we used a set of nine different block sizes, ranging from $n \times n = 7 \times 7$ to $n \times n = 151 \times 151$.

The ROC curve this set of classifiers generates can be seen in Fig. 4.4(a) with the top left area of the plot displayed in Fig. 4.4(b) for clarity. As desired, all points are located far from the random guess classifier performance. It is clear from these graphs that a small block size classifies background pixels perfectly at the expense of object pixels, and a large block size classifies object pixels at the expense of background pixels. Our compromise between background/object segmentation is to minimise the distance between the points in ROC space and the point (0,1), since we regard false positives and false negatives as being equally undesirable. We chose the block size of 81×81 pixels which has a tp rate of 91.96% and a fp rate of 0.7%. Using this block size, we created the segmentation mask shown in Fig. 4.2(d). By comparison, EM achieved a good fp rate of 1% but a relatively poor tp rate of 80%. The segmentation mask created by EM is shown in Fig. 4.2(b). To demonstrate that segmenting using multiple reconstructions outperforms a single reconstruction we take $V_{268}(k, l)$ calculated using an 81×81 block size

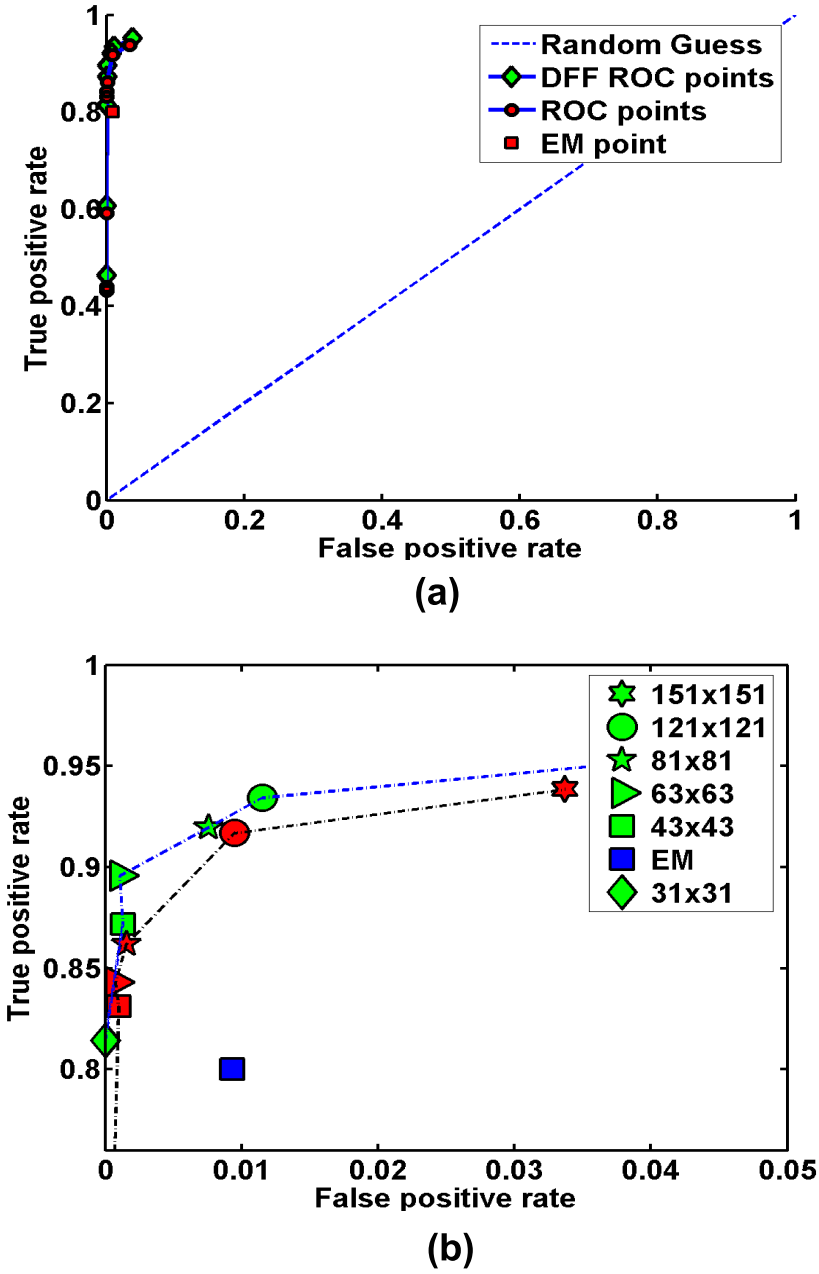

Figure 4.4: ROC graph for object segmentation using different block sizes where red labels equate to segmentation applied to one depth plane and green labels to multiple depth planes.

and input it into Eq. (4.1). We use the same τ value of 0.02 to threshold and create SMask(k, l), this is shown in Fig. 4.2(c). The tp rate and fp rate this produces are plotted in Fig. 4.4(b), the single reconstruction segmentation mask achieves a tp rate of 78% and an fp rate of 0%. From these findings it is clear that the multiple reconstruction approach outperforms the single reconstruction approach.

4.1.1 Erosion operator

Erosion is a mathematical morphological image processing operator which given a binary image and a structuring element returns a new image. This function shrinks any boundary pixels, both internal and external boundaries, dependent on the size and shape of the structuring element. In general, the structuring element is a simple 2D shape such as a circle, a diamond or a square. We apply erosion to SMask(k, l) to shrink the boundaries as they will be uniformly enlarged through the application of neighbourhood processing in our DFF algorithm. In Fig. 4.5 we demonstrate the impact of erosion to SMask(k, l). We select a circle structuring element whose diameter is $\frac{n}{2}$ where this is the same n used in the DFF algorithm for the block size. Figure 4.5(a) displays SMask(k, l) pre-erosion, and Fig. 4.5(b) displays the final SMask(k, l) after application of erosion. The impact of erosion is most apparent in the segmented reconstructions, which are shown in Fig. 4.5 (c) and (d). There is a very obvious border or halo around the object in the segmented reconstruction before erosion has been applied, while the borders of SMask(k, l) are tight to the boundary of the object in Fig. 4.5(d).

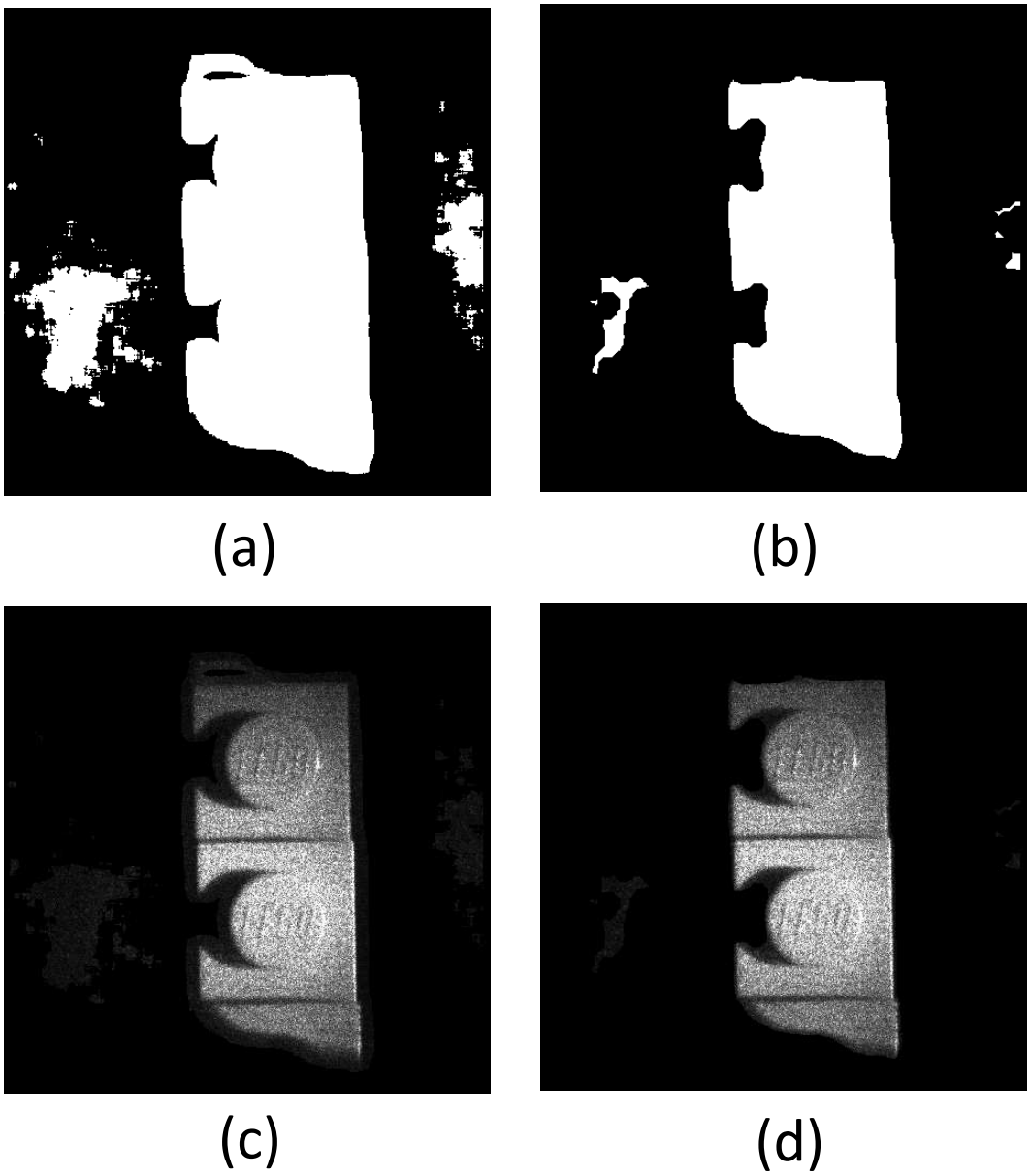

Figure 4.5: Effect of erosion operator, (a) SMask(k, l) before erosion and (b) after erosion and the segmented reconstructions (c) before erosion and (d) after erosion.

4.1.2 Threshold variation

The selection of τ, the threshold value, is currently a manual operation. A slight variation of this threshold can have a dramatic impact on the returned SMask(k,l). In Fig. 4.5(b), the final SMask(k,l) for the Lego object DH is displayed. This is created using a τ of 0.2005 applied to the normalised $V_{\max}(k,l)$. We demonstrate the impact the threshold has on SMask(k,l) through modifying τ by just 1%. First we set τ to be 0.1905, as displayed in Fig. 4.6(a) and (c), and then we set τ to be 0.2105 as shown in Fig. 4.6(b) and (d). By varying τ by such a small amount we achieve quite a dramatic change in the form of over and some under segmentation. We have found for the objects we have recorded that $0.1 \geq \tau \leq 0.3$.

4.1.3 Multiple reconstructions versus individual reconstruction

It is our assertion that using multiple reconstructions provides a more accurate segmentation mask than one created using an individual reconstruction. To verify this we were provided with a DH of 3 hairs recorded using digital holography and a microscopic objective [MMHN08]. In the reconstruction process the front focal plane containing two hairs is located at 249mm and the back focal plane containing the other hair is located at 306mm. A reconstruction at these planes with the sharp images of the hairs is shown in Fig. 4.7(a) and (b). We then calculate two focus maps, $V_{249}(k,l)$ and $V_{306}(k,l)$ and by applying Eq. (4.1) and $\tau = 0.3$ to these focus maps we obtain two segmentation masks. These segmentation masks are displayed in

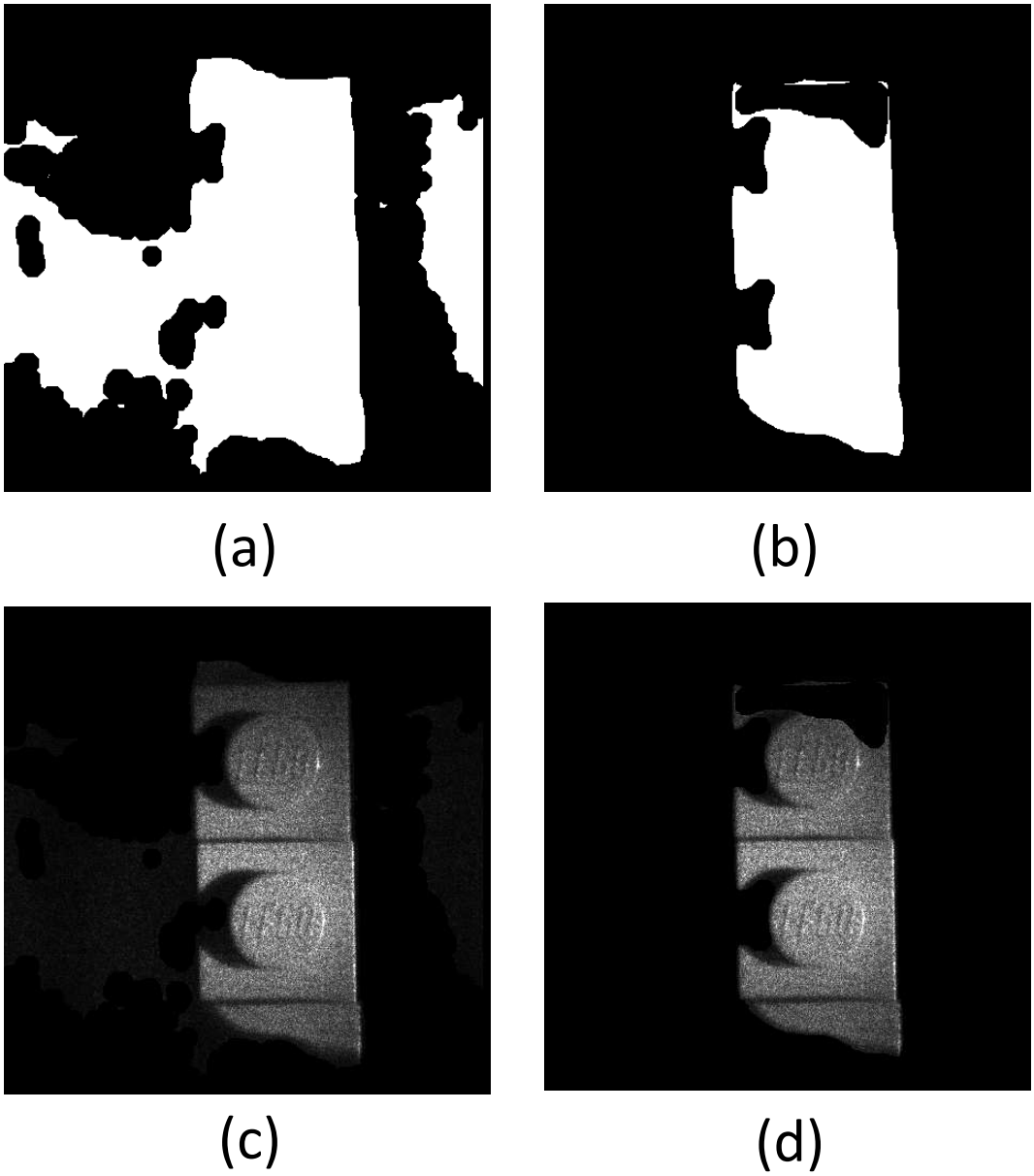

Figure 4.6: Effect of varying threshold on SMask(k, l) by 1% (a) too low and (b) too high and the respective segmented reconstructions in (c) and (d).

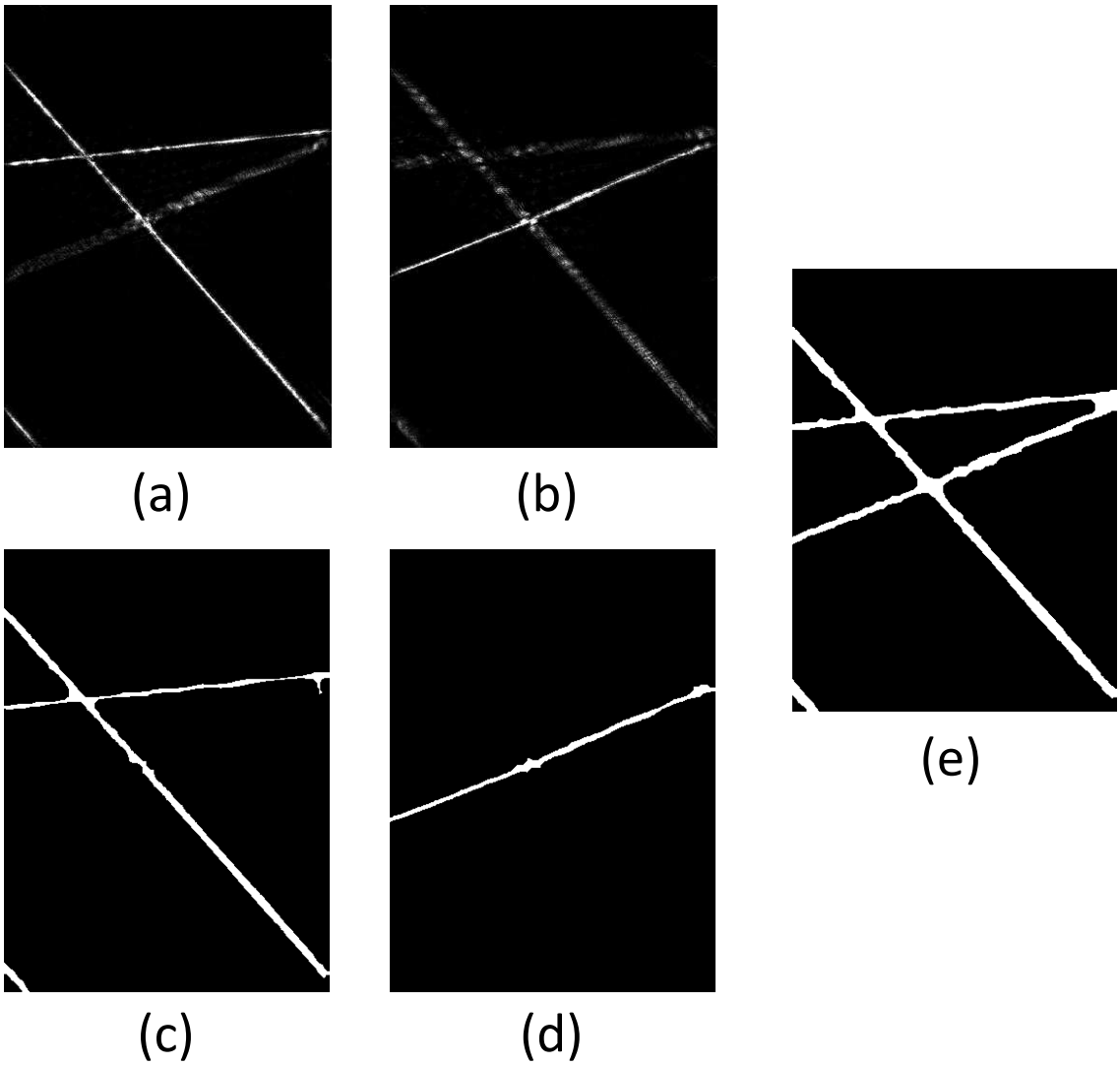

Figure 4.7: Hairs object, numerical reconstruction at (a) front focal plane, (b) back focal plane, segmentation masks created using only (c) front focal plane, (d) back focal plane and (e) using 100 reconstructions.

Fig. 4.7(c) and (d), what is apparent is that only the in-focus sharp hairs in each reconstruction have been segmented as desired. To obtain a segmentation mask for all of the hairs in the DH we need to apply our DFF algorithm. To achieve this we input: $z_{\text{min}} = 220\text{mm}$, $z_{\text{step}} = 1\text{mm}$, $z_{\text{max}} = 320\text{mm}$ and $n \times n = 81 \times 81$. The resulting $V_{\text{max}}(k, l)$ is then thresholded with $\tau = 0.3$ to obtain $\text{SMask}(k, l)$ as shown in Fig. 4.7(e). In this case we successfully segment all three hairs which demonstrates the improvement obtained by using multiple reconstructions over individual reconstructions.

4.1.4 Background segmentation examples

In this section we display a subset of the segmentation masks created from our DHs and DFF process displayed in Chapter3.3 and give the threshold parameter input to Eq. (4.1):

Figure 4.8: Knight object DH:

- $\tau = 0.12$.

Figure 4.9: Marble object DH:

- $\tau = 0.105$.

Figure 4.10: Bolts object DH:

- $\tau = 0.1$.

Figure 4.11: Two bolts object DH:

- $\tau = 0.1245$.

Figure 4.8: Segmentation of knight object DH: (a) numerical reconstruction, (b) segmentation mask obtained, (c) segmented reconstruction.

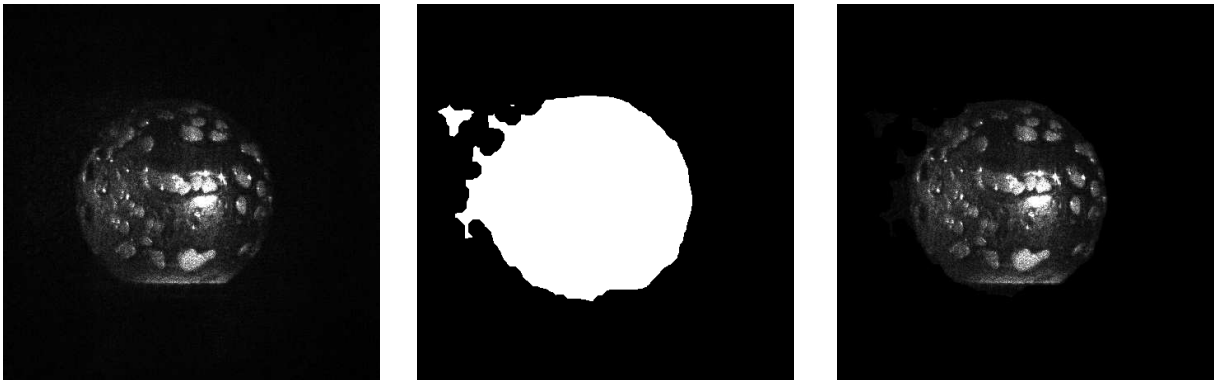

Figure 4.9: Segmentation of marble object DH: (a) numerical reconstruction, (b) segmentation mask obtained, (c) segmented reconstruction.

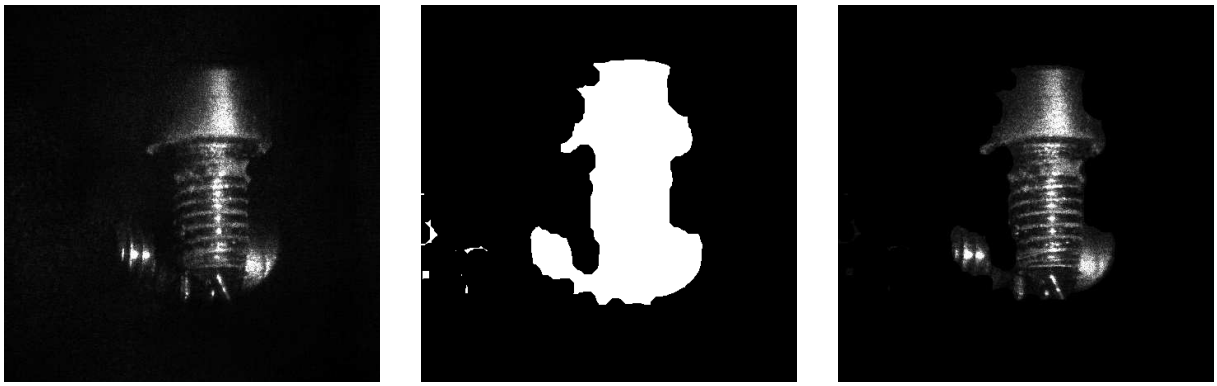

Figure 4.10: Segmentation of a two bolts object DH: (a) numerical reconstruction, (b) segmentation mask obtained, (c) segmented reconstruction.

4.1.5 Synthetic digital holographic scene creation

We call a synthetic DH one which contains objects that were not in the original recording. These can be either computer generated or real-world objects. To create a synthetic DH, we take a DH and propagate to the in-focus plane of the object we want to add to the new synthetic hologram. We remove the object by segmenting its complex distribution. We then add this complex distribution to the synthetic DH, we repeat this for the desired number of objects or digital holograms. We take the output synthetic DH and propagate back to the original hologram plane. We need to employ the PTF, Eq. (A.32), reconstruction method as our propagation to and from the hologram plane which requires a reciprocal function. We employ our background segmentation process to calculate $\mathrm{SMask}(k, l)$ and then segment

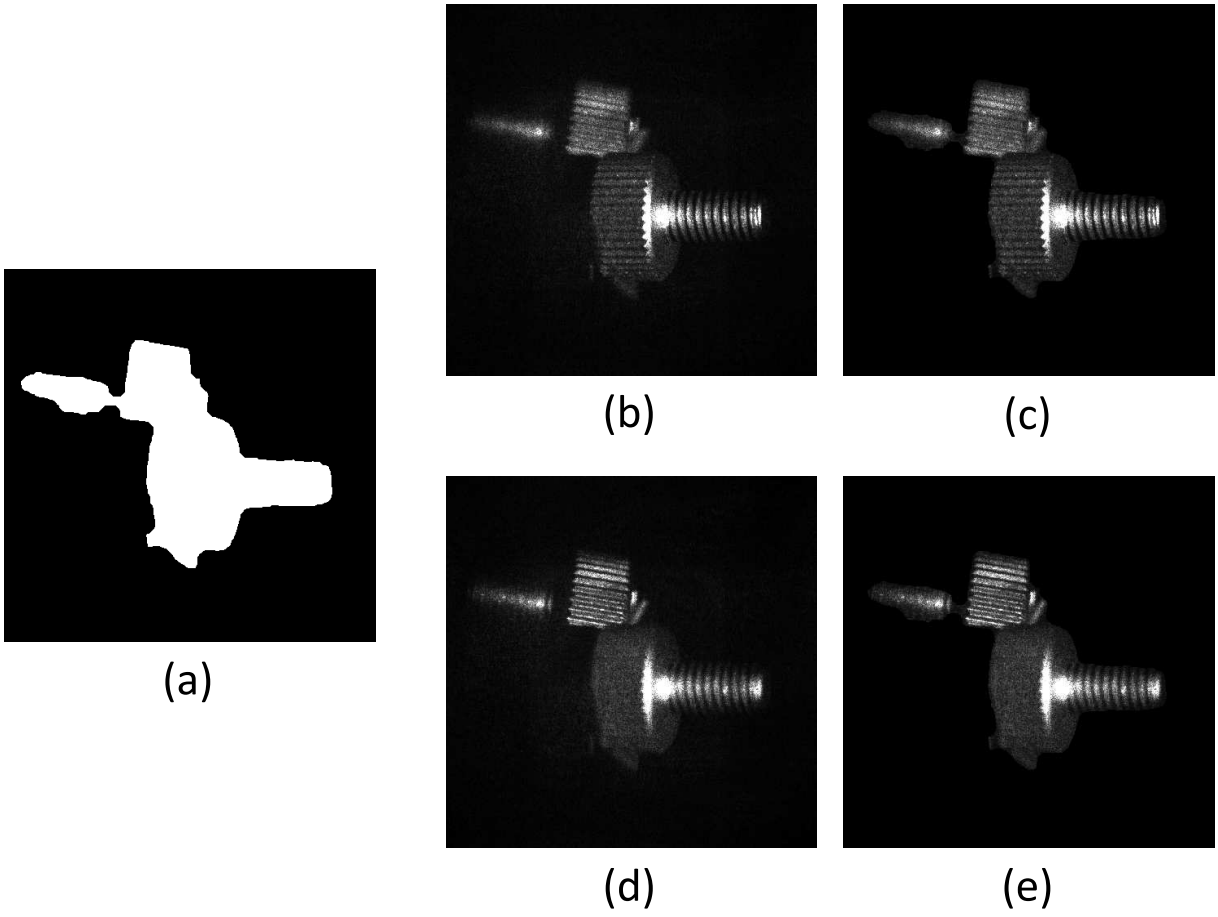

Figure 4.11: Segmentation of a two bolts object DH: (a) segmentation mask obtained, (b) numerical reconstruction at front object focal plane, (c) segmented reconstruction at front object focal plane, (d) numerical reconstruction at back object focal plane and (e) segmented reconstruction at back object focal plane.

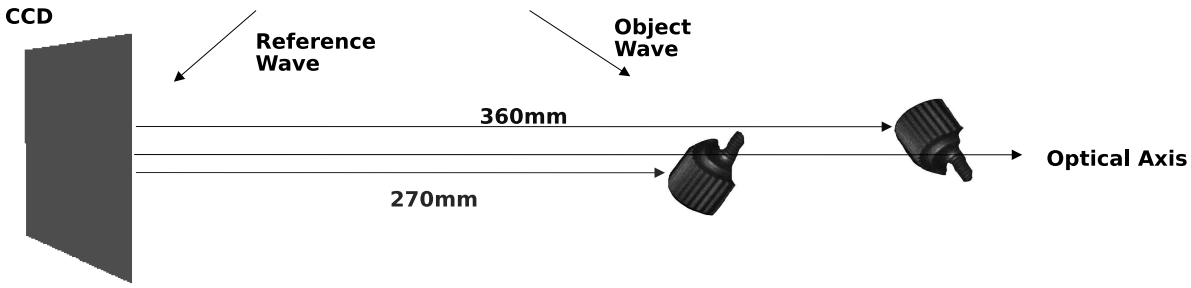

Figure 4.12: Simulated experimental set-up for the superposed hologram, with an second object superposed a distance of 90mm from the original object.

the full complex wavefront to create our segmented object $S_z(k,l)$ with

$$S_z(k,l) = \text{SMask}(k,l) \cdot U_z(k,l), \tag{4.4}$$

where the reconstruction distance z is calculated with our autofocus algorithm. Our synthetic digital hologram is initialised with all zeros to begin with and is stored in $U_z^{\text{synth}}(k,l)$. In Fig.4.12 the simulated experimental set-up is illustrated. To demonstrate this process we take our screw object DH and its SMask(k,l) as shown in Fig. 4.2(a), and calculate $S_{270}(k,l)$. We then take $S_{270}(k,l)$, rotate it 180°, and centre it in the new synthetic DH $U_{360}^{\text{synth}}(k,l)$. The second object is superposed into the scene by propagating -90mm to $U_{270}^{\text{synth}}(k,l)$ and adding the original unrotated $S_{270}(k,l)$, in this case we only add complex values from $S_{270}(k,l)$ that do not equal zero. We propagate back to the hologram plane $U_0^{\text{synth}}(k,l)$ and have a synthetic DH containing two objects that were not in the original DH.

To demonstrate the 3D information in our synthetic DH we calculate four reconstructions from two perspectives at the near object plane and the

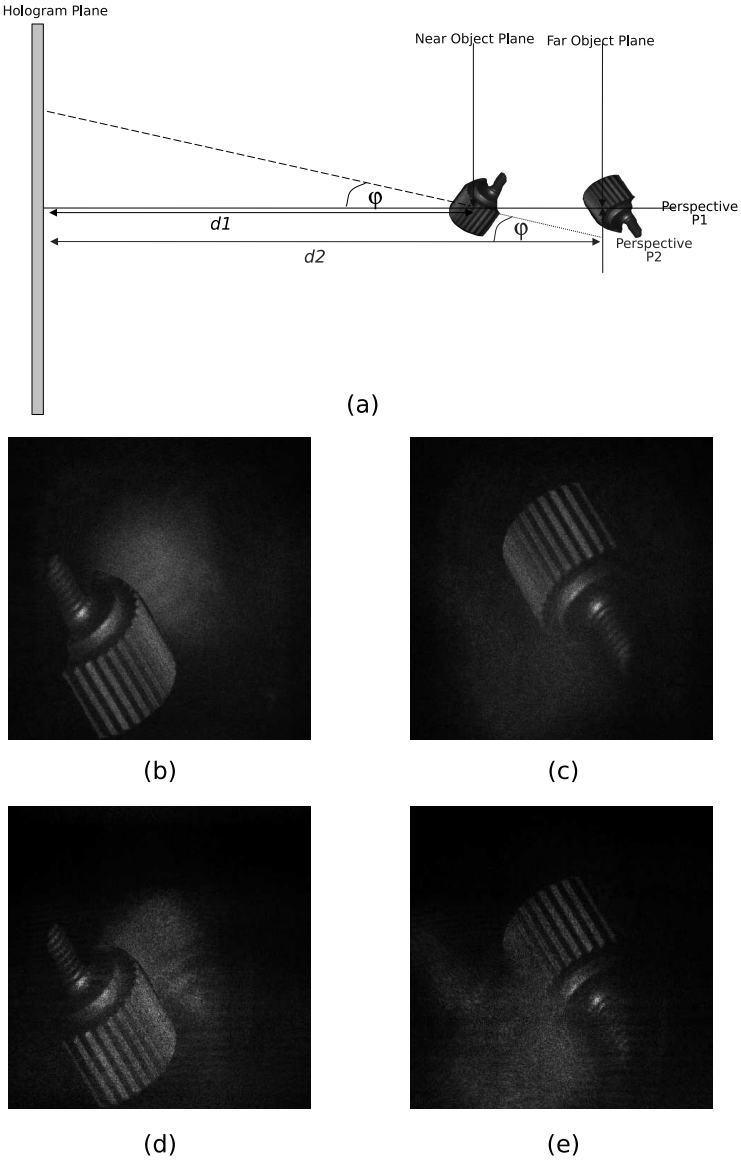

Figure 4.13: Superposed digital holography: (a) diagram showing perspectives P1, along the optical axis, and P2, from above the optical axis, (b) near plane reconstruction at depth d1 from perspective P1, (c) far plane reconstruction at depth d2 from perspective P1, (d) near plane reconstruction at depth d1 from perspective P2, and (e) far plane reconstruction at depth d2 from perspective P2.

far object plane. We selected the perspective from the optical axis, P1, and one from above the optical axis focused on the near object plane, P2, as shown in Fig.4.13(a). This equates to change in viewing angle of 0.7°. Reconstructions from perspective P1 are shown in Fig.4.13(b) and (c) while reconstructions from perspective P2 are shown in Fig.4.13(d) and (e). As can be seen when comparing the reconstructions from perspective P1 and P2, both objects change orientation but there is also an observable parallax between the reconstructions caused by the change of angular position and physical position of the far object. This allows us to construct synthetic holograms of real scenes, or combine real and computer generated holograms to create overlays. The synthesised result can be used in three-dimensional display systems the same way as traditional computer generated holograms, for instance using spatial light modulators as described in [[Luc97, SCS05]].

4.2 Depth Segmentation

Our full segmentation algorithm can be considered a three stage process as displayed in Fig. 4.14. The first stage is our DFF algorithm, see Chapter 3.3, the second stage is our background segmentation algorithm, see Chapter 4.1, and the final stage is our depth segmentation algorithm which is dealt with in this section. We combine $D_{z_{\text{step}}}(k,l)$ from the DFF process with $\text{SMask}(k,l)$ from the background segmentation process to create a segmented depth map $\text{DMap}_{z_{\text{step}}}(k,l)$ using

$$\text{DMap}_{z_{\text{step}}}(k,l) = D_{z_{\text{step}}}(k,l) \cdot \text{SMask}(k,l). \tag{4.5}$$

The depth segmentation algorithm is itself a four step process where the different object regions are identified by isolating homogenous clusters in the depth map. One input argument, the number of segments s with which to partition $\mathrm{DMap}_{z_{\mathrm{step}}}(k,l)$, is required.

Step 1: A histogram of the depth values in $\mathrm{DMap}_{z_{\mathrm{step}}}(k,l)$ is created. The s non-overlapping histogram modes with the largest area in this 1D function are identified. The depth values marking the start and end of each histogram mode i are recorded as s^i_{start} and s^i_{end}, respectively.

Step 2: We now create our depth segmentation mask, $\mathrm{DMask}(k,l)$, where each pixel in $\mathrm{DMask}(k,l)$ is labeled with a segment index, e.g 0 for background, 1 for segment 1, 2 for segment 2 and so on. For each selected histogram mode i, and for each pixel (k,l), the pixel in $\mathrm{DMask}(k,l)$ is assigned integer i if the value in $\mathrm{DMap}_{z_{\mathrm{step}}}(k,l)$ is within the range of the histogram mode i. $\mathrm{DMask}(k,l)$ is therefore defined as

$$\mathrm{DMask}(k,l) = \begin{cases} i, & \text{if } s^i_{\mathrm{start}} \geq \mathrm{DMap}_{z_{\mathrm{step}}}(k,l) > s^i_{\mathrm{end}} \\ 0, & \text{otherwise.} \end{cases} \quad . \tag{4.6}$$

Step 3: Step 3 is an optional step which can be used to increase the accuracy of the final depth segmentation mask. For each segment index in $\mathrm{DMask}(k,l)$ we calculate the total number of connected regions and their respective areas. One pixel is connected to another if their edges or corners touch. A connected region is a unique set of pixels with the same label and the area is the total number of pixels in the connected region. For all connected regions if their

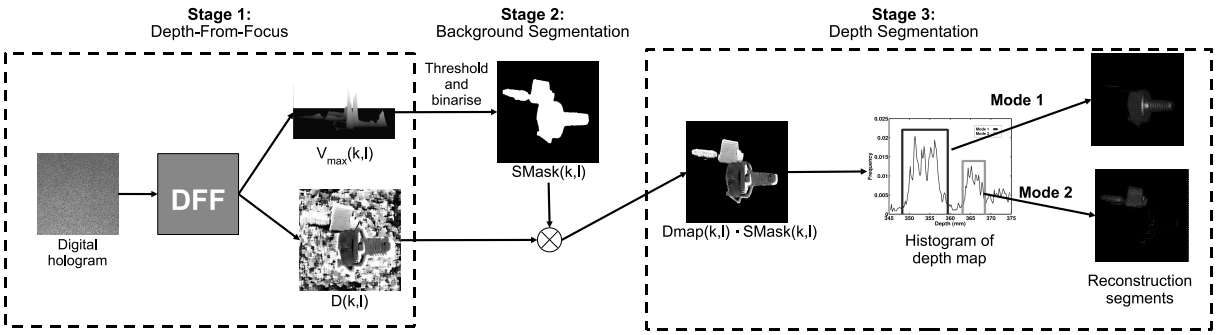

Figure 4.14: Three stage segmentation process, stage 1: depth-from-focus, stage 2: background segmentation and stage 3: depth segmentation.

area is below a threshold value υ we designate its pixels as unlabeled by setting them equal to zero and move onto Step 4.

Step 4: It is possible that not all of the object pixels in $\text{DMap}_{z_{\text{step}}}(k,l)$ are labeled in $\text{DMask}(k,l)$ during Step 2 or some have been unlabeled during Step 3. In this final step we label these final object pixels in $\text{DMask}(k,l)$ by assiging them a segment index. We make this decision based on the pixels proximity to a segment, we label the pixels with the index of the segment which has the closest boundary. The output of this algorithm is the segmented image $\text{DMask}(k,l)$ where every identified object pixel has been labeled.

For the experimental results in this chapter, for Step 2, we qualitatively select a histogram's modes by identifying the clustered regions within the histogram plot. These histogram modes are the basis of our depth segmentation technique. Although for this chapter we chose the modes manually, an automated method of partitioning the modes could be based on compression techniques [SNJ07] or probabilistic histogram segmentation [FP03]. In Step

3 we choose a threshold of $\upsilon = 20000$, therefore we unlabel any objects which have an area of less than 0.5% of the pixel area of the full reconstruction. This is a reasonably small area and for our DHs equates to allowing object with a square size of greater than 2mm^2.

Our first scene is the two bolts object DH. A reconstruction of the front bolt's and the back bolt's focal plane are shown in Fig. 4.15(a) and (b) respectively. In the first stage we use a sequence of one hundred and seventy six depths with an interval of 0.2mm between successive depths. We input $z_{min} = 345\text{mm}$, $z_{step} = 0.2\text{mm}$, $z_{max} = 380\text{mm}$ and $n \times n = 81 \times 81$ to our DFF algorithm. In this section we demonstrate the impact of this interval on the depth segmentation process. In the second stage, we combine $\text{SMask}(k, l)$, Fig. 4.15(c), with $\text{D}_{0.2}(k, l)$ to create $\text{DMap}_{0.2}(k, l)$, Fig. 4.15(d). Two obvious segments in the scene were observed: the front bolt and the back bolt. This led to the selection of $s = 2$ as the input into the third stage of our segmentation technique. The histogram of $\text{DMap}_{0.2}(k, l)$ along with the highlighted boundaries of the two selected modes is shown in Fig. 4.16.

4.2.1 Small object removal

We demonstrate the advantage of the optional Step 3 in our algorithm in Fig. 4.17. In Fig. 4.17(a) and (b) we display the output $\text{DMask}(k, l)$ from Step 2 and the unlabeled pixels, respectively. If we skip Step 3 the final output $\text{DMask}(k, l)$ obtained from our algorithm is shown in Fig. 4.17(c), while if we remove the small objects as detailed in Step 3 the final output $\text{DMask}(k, l)$ obtained is much improved as shown in Fig. 4.17(d). We can

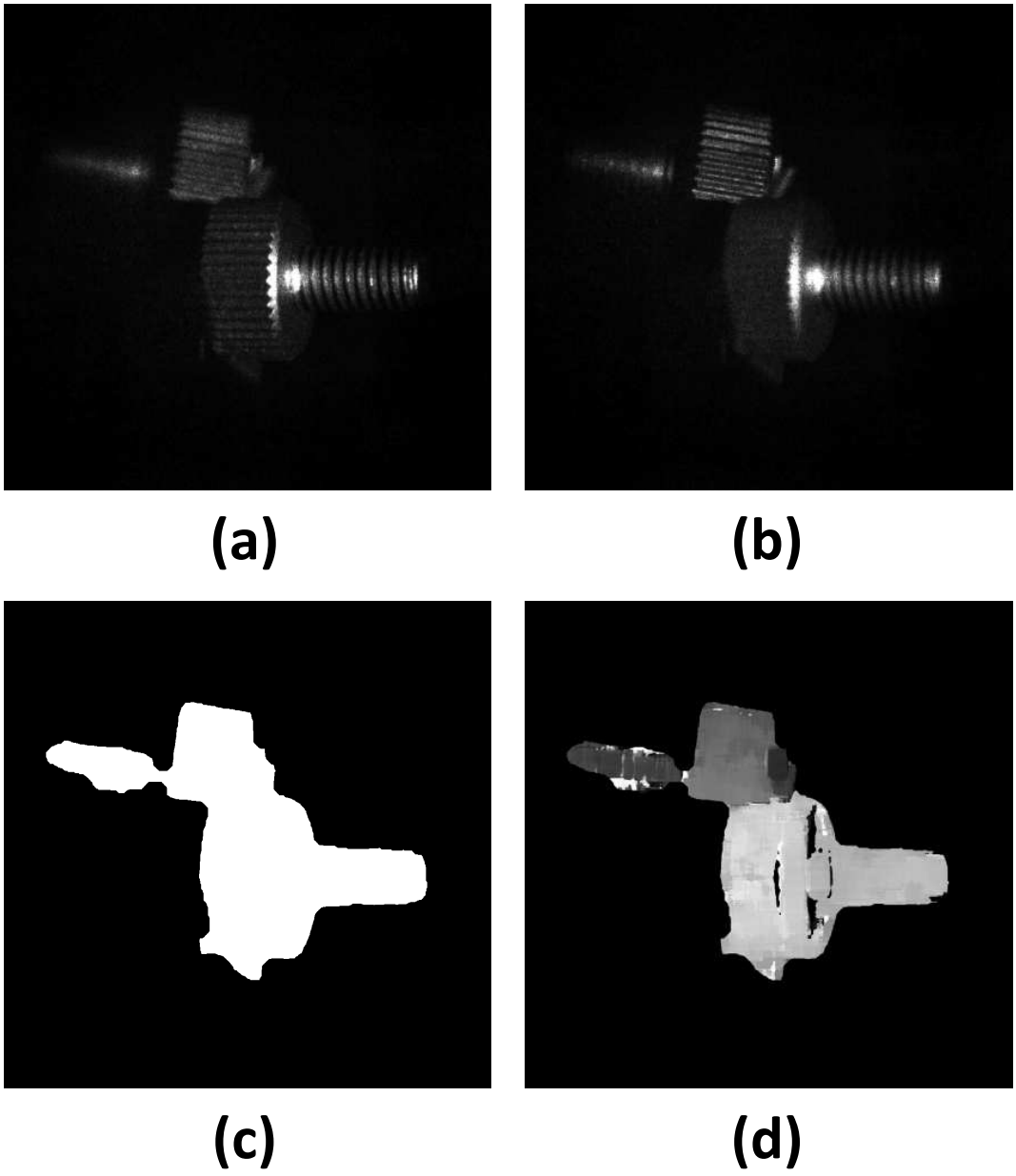

Figure 4.15: Two bolts object hologram: (a) numerical reconstruction at the front of the scene, (b) numerical reconstruction at the back of the scene, (c) background segmentation mask, (d) segmented depth map.

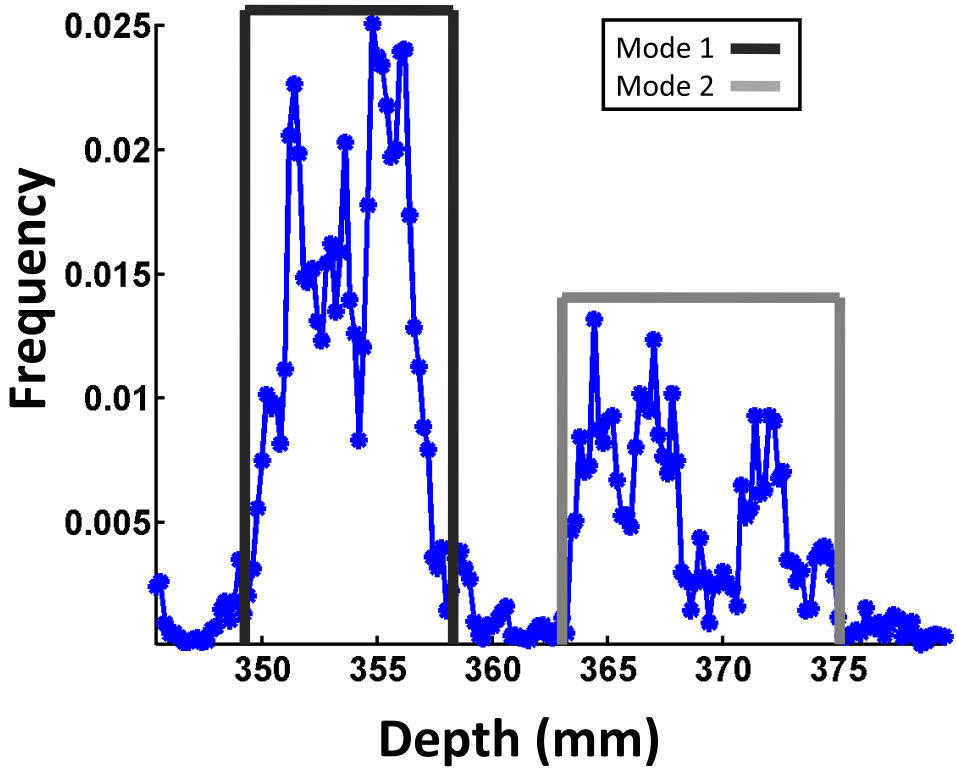

Figure 4.16: Histogram of two bolts object hologram's depth map.

calculate the focal plane of each segment i by averaging the depth value of every pixel in $\text{DMap}_{0.2}(k,l)$ which corresponds to a pixel in DMask with a value of i. A reconstruction of the first segment region at its calculated focal plane is shown in Fig. 4.17(e) and a reconstruction of the second segment region at its focal plane is shown in Fig. 4.17(f). In this figure we show that without Step 3 there are some small object regions which were incorrectly segmented. By applying Step 3 we can associate these with the correct segment index.

4.2.2 Varying desired number of segments

Our algorithm is not limited to the segmentation of individual objects but can also segment one object into different segments based on depth information. We input the same two bolts object into our full segmentation algorithm with one change, we input $s = 4$, in this case we identify four segments in the scene: the head of the front bolt, the threads of the front bolt, the head of the back bolt and the threads of the back bolt. The results of this experiment are displayed in Fig. 4.18 where the output depth segmentation mask is displayed in Fig. 4.18(a). The segmented reconstructions for segments 1-4 are displayed in Fig. 4.18(b),(c),(d) and (e), respectively. DMask and the segmented reconstructions illustrate that multiple objects can be automatically segmented from a digital holographic scene using depth information.

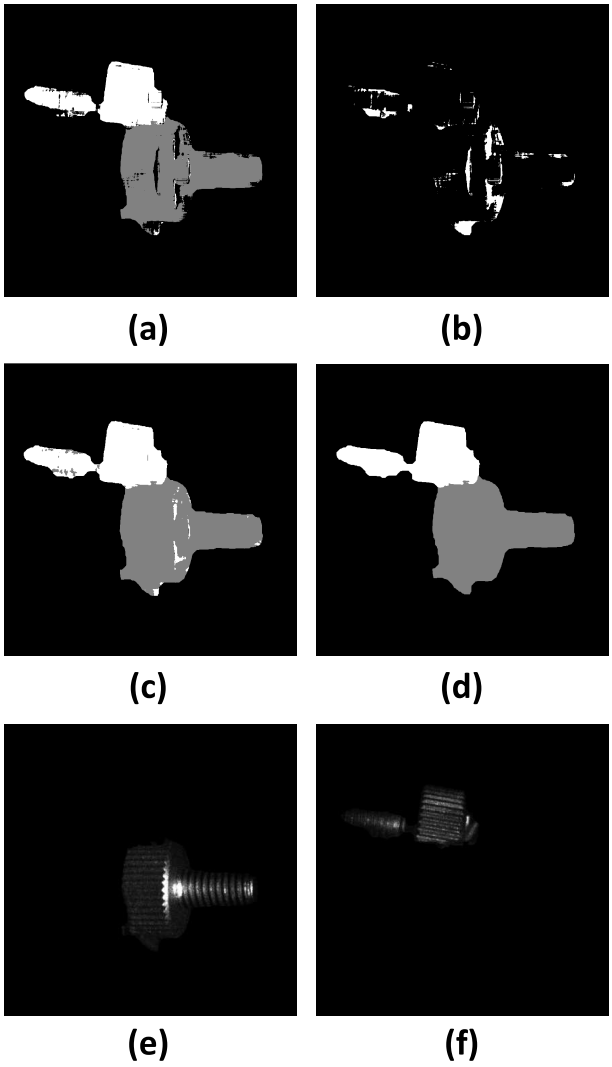

Figure 4.17: Depth Segmentation of two bolts object hologram: (a) depth segmentation mask after stage 2, (b) unlabeled pixels, (c) depth segmentation mask without small object removal, (d) depth segmentation mask with small object removal and segmented reconstructions of two bolts object hologram: (e) in-focus reconstruction of segment 1, (f) in-focus reconstructoins of segment 2.

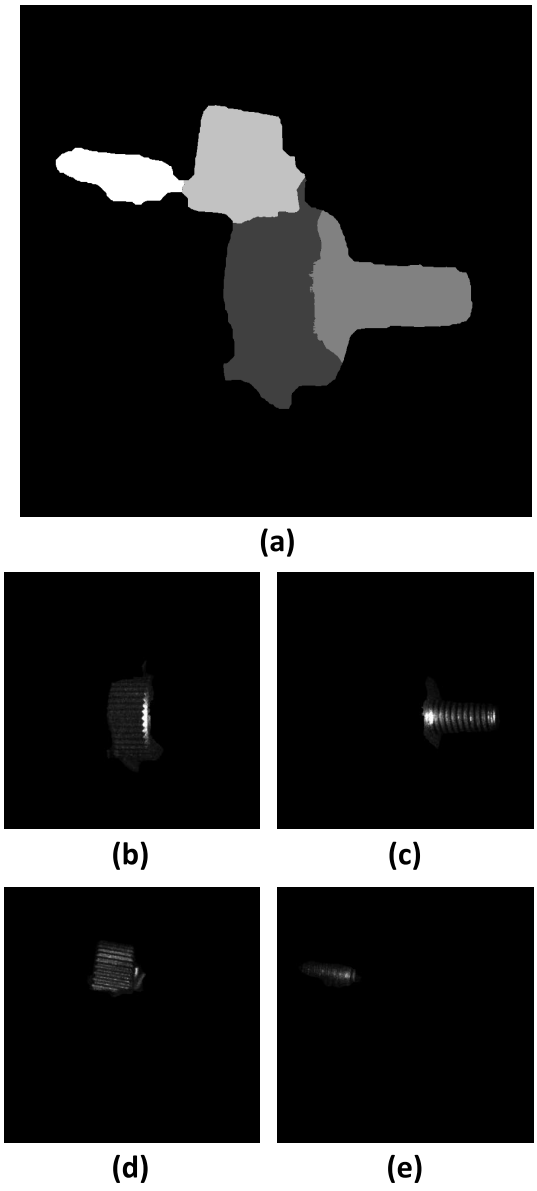

Figure 4.18: Two bolts object hologram segmented into four regions: (a) depth segmentation mask, (b) in-focus reconstruction of segment 1, (c) in-focus reconstruction of segment 2, (d) in-focus reconstruction of segment 3, (e) in-focus reconstruction of segment 4.

4.2.3 Reconstruction interval and depth segmentation

At this point we can demonstrate the impact z_{step} has on the depth segmentation process. We create four depth segmentation masks using the following z_{step} values: 0.1mm, 0.2mm, 0.5mm and 1mm. These depth maps are shown in Fig. 3.13 in Chapter. 3. The resulting depth segmentation masks are shown in Fig. 4.19. As discussed in Chapter 3.3.5, there should be no difference between the segmentation masks created using an interval of 0.1mm and 0.2mm because each reconstruction in both cases is within the depth-of-focus of the next reconstruction in the volume. However, the segmentation should be less successful when the interval is greater than the maximum depth-of-focus of the reconstructions, which is 0.4mm. Our results are in agreement with the theory, as can be seen from the incorrect segmentation of the head of the front bolt in Fig. 4.19(c-d). These segmented depth maps demonstrate that selecting the reconstruction interval for each hologram based on the minimum depth-of-focus of the reconstruction volume returns the best results.

4.2.4 Depth Segmentation examples

In this section we display a subset of the depth segmentation masks created from our DHs give the experimental parameters relevant to depth segmentation:

Figure 4.20: Lego object DH:

- $\upsilon = 20000$.
- $s = 3$.

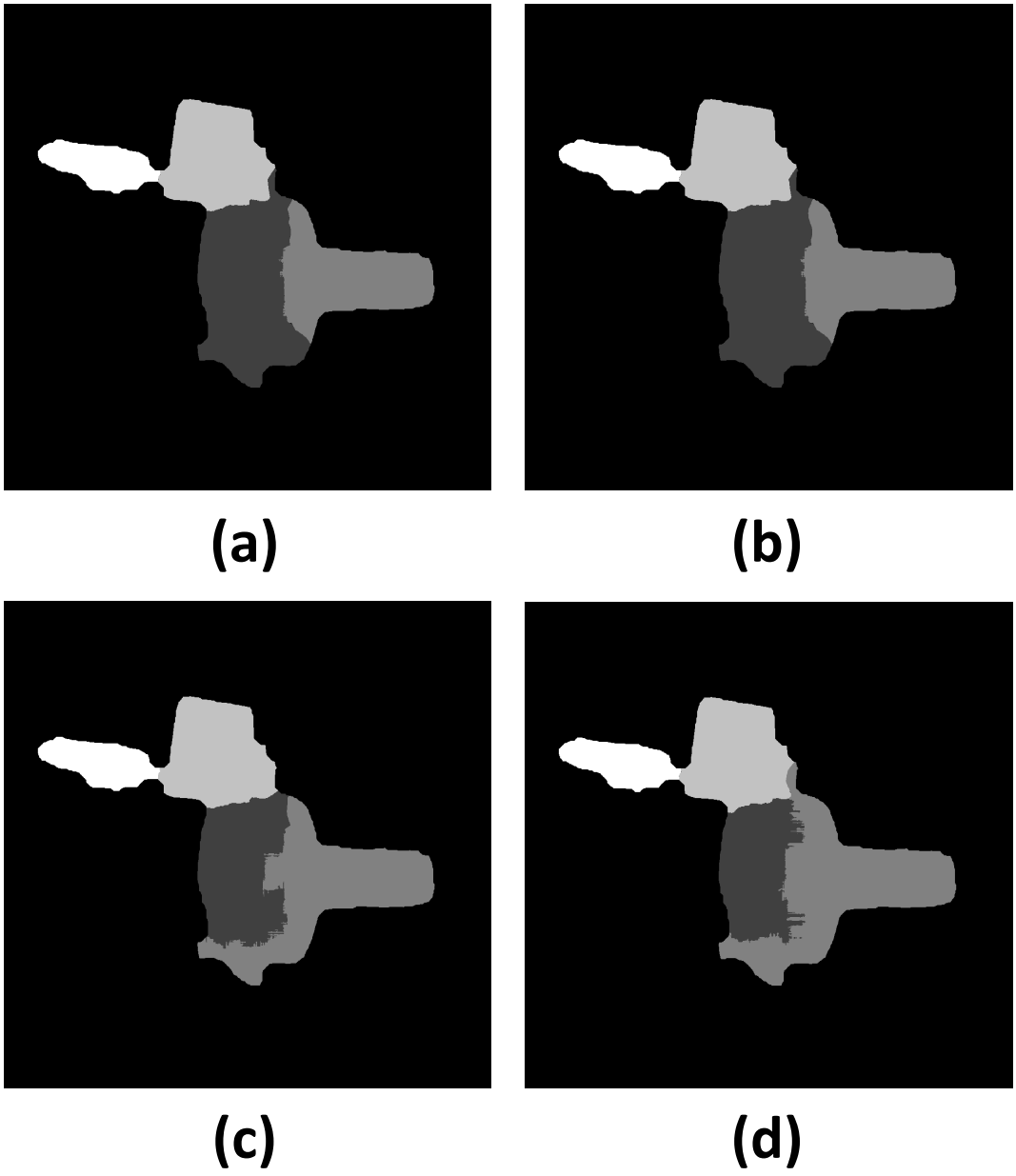

Figure 4.19: Two bolts object hologram depth segmentation masks using reconstruction volumes with an interval of : (a) 0.1mm, (b) 0.2mm, (c) 0.5mm and (d) 1mm.

Figure 4.21: Marble object DH:

- $\upsilon = 20000$.
- $s = 2$.

Figure 4.22: Bolts object DH:

- $\upsilon = 20000$.
- $s = 2$.

4.3 Discussion

We expect our background segmentation method will be successful for all macroscopic objects recorded by digital holography except pure phase objects. For microscopic objects it is expected that a phase-unwrapping based approach would be best. The accuracy of our approach is limited by an appropriate choice of block size and threshold value. We believe that the depth segmentation technique demonstrated in this chapter will be successful in segmenting digital holographic scenes containing macroscopic objects. The interval between successive reconstructions in the DFF process impacts the final segmented depth map. We have shown the impact of incorrectly selecting an interval and recommend selecting an interval equal to the minimum depth-of-focus of the reconstruction volume input to the DFF process. Our technique would not be successful for scenes containing pure phase objects. Also in microscopic scenes, we advise using a phase unwrapping approach

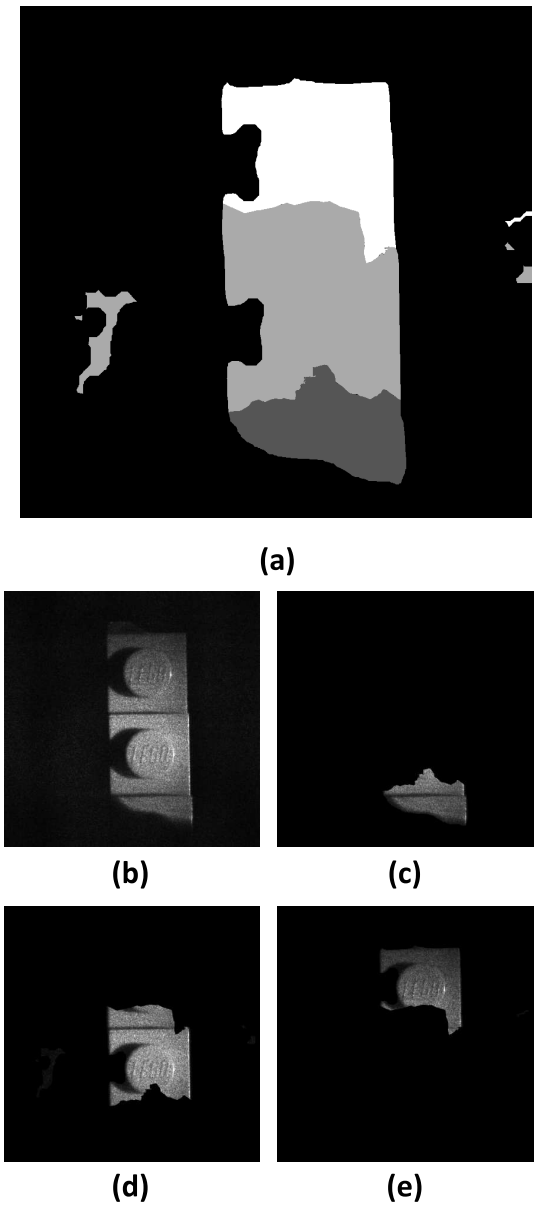

Figure 4.20: Lego object hologram segmented into three regions: (a) depth segmentation mask, (b) in-focus reconstruction of full object, (c) in-focus reconstruction of segment 1, (d) in-focus reconstruction of segment 2, (e) in-focus reconstruction of segment 3.

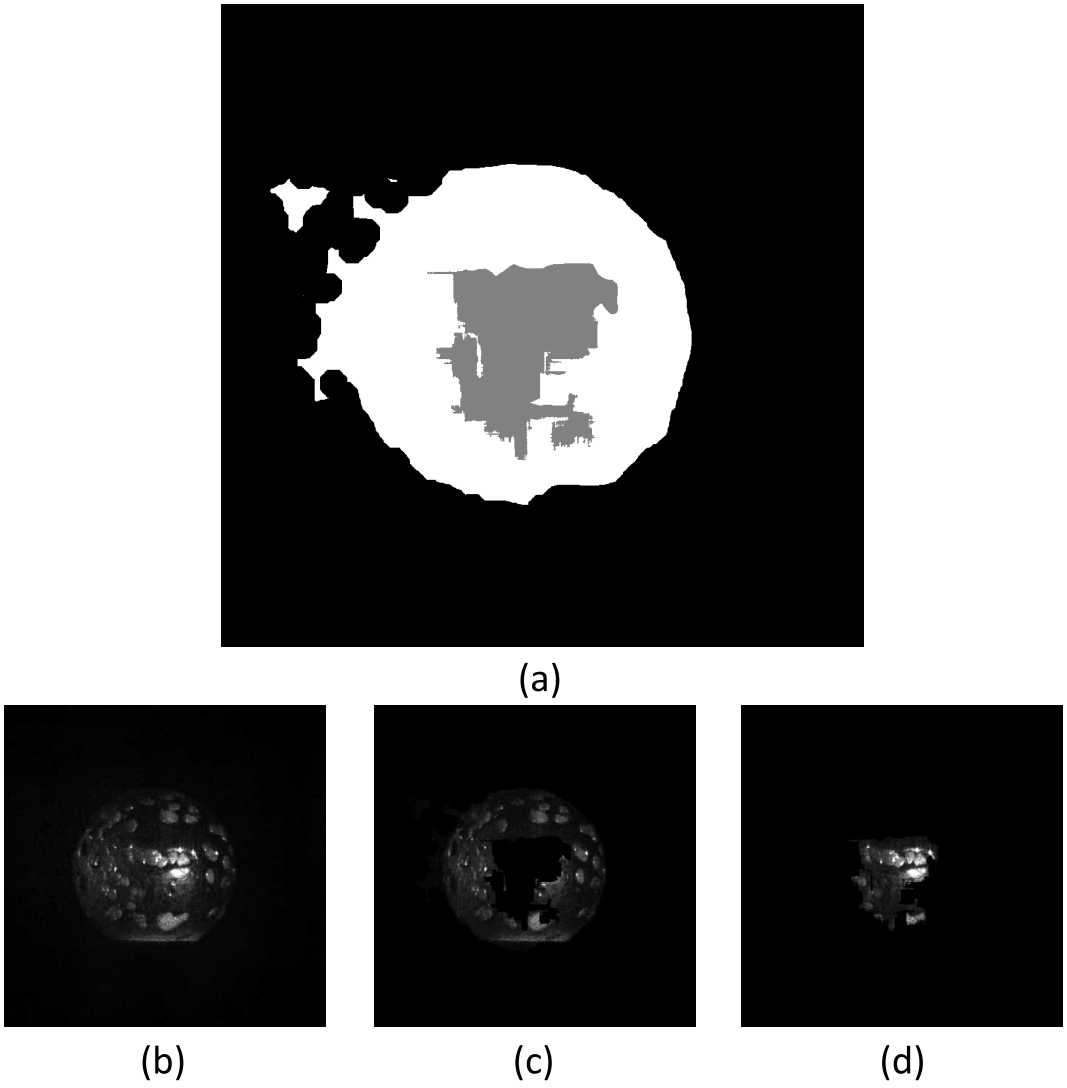

Figure 4.21: Marble object hologram segmented into three regions: (a) depth segmentation mask, (b) in-focus reconstruction of full object, (c) in-focus reconstruction of segment 1 and (d) in-focus reconstruction of segment 2.

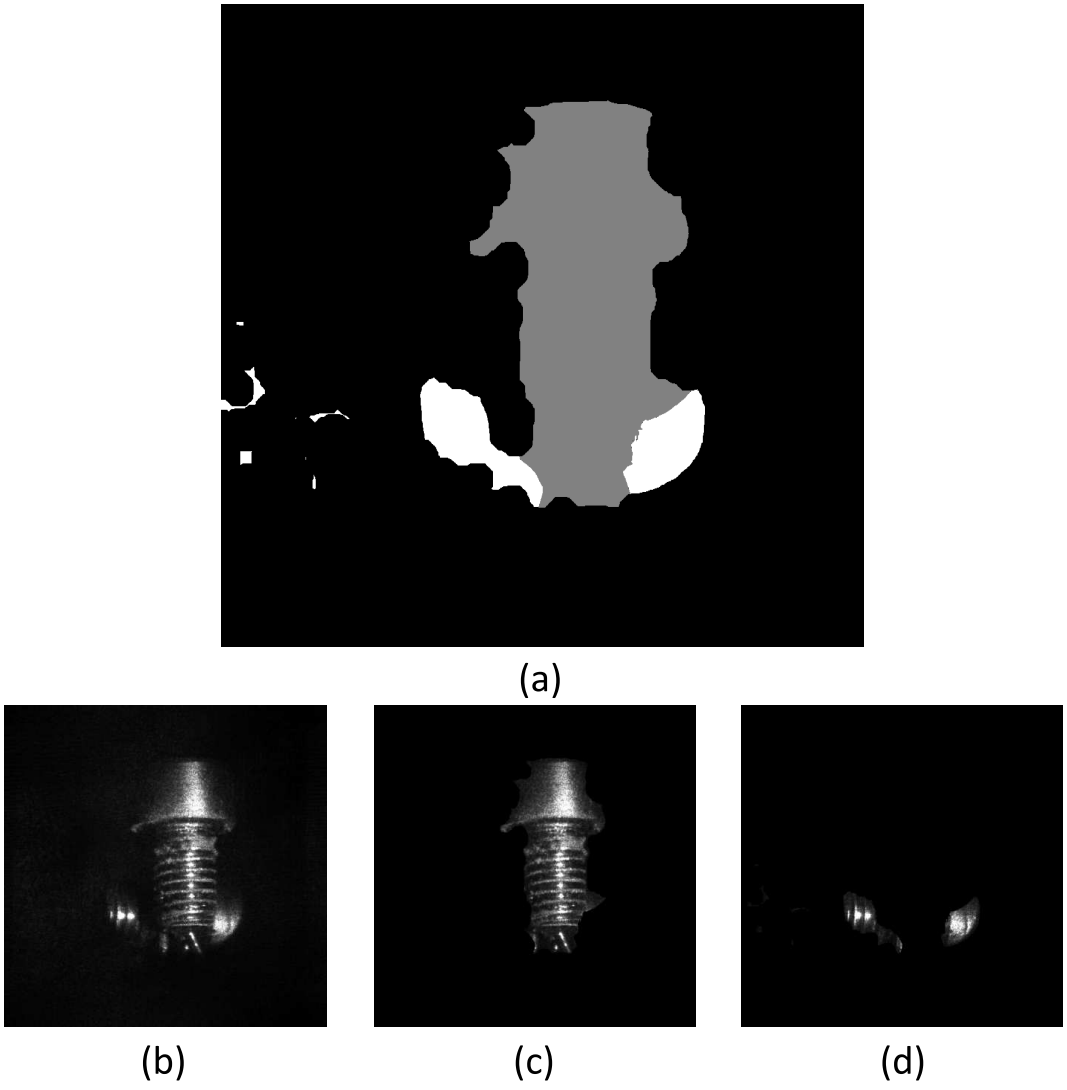

Figure 4.22: Bolts object hologram segmented into three regions: (a) depth segmentation mask, (b) in-focus reconstruction of full object, (c) in-focus reconstruction of segment 1 and (d) in-focus reconstruction of segment 2.

for the creation of the depth maps[FCN+03]. Our depth segmentation approach requires the selection of modes from a histogram of the depth map. We have demonstrated that the algorithm is more accurate with scenes' containing high contrast objects but it is still successful with scenes' containing low contrast objects. We recommend illuminating scene's containing objects with no texture or low contrast objects with a speckle pattern to increase the accuracy of the approach.

Chapter 5

Extended Focused Imaging

All optical systems have a calculable depth-of-field. One of the primary advantages in holographic systems is the large depth-of-field. However, each holographic reconstruction has a limited depth-of-field. This is in contrast to traditional optical systems where the system's depth-of-field translates directly to the viewable depth-of-field in the output image. When a DH is reconstructed, a distance value d is input as a parameter to the reconstruction algorithm. The depth-of-focus range for a reconstruction using the Fresnel approximation is in the order of a millimeter. For complex 3D scenes, scenes containing multiple objects or containing multiple object features located at different depths, this leads to reconstructions with large blurred regions. We are interested in the creation of an image with an extended depth-of-field [PK83], which we are calling an extended focus image (EFI) [FGA+05], from sets of digital holographic reconstructions where the full scene is in-focus. To do this we must be able to identify when certain

object regions are in-focus at a given depth. This effectively necessitates the development of a shape extraction technique for macroscopic objects encoded in DHs [MWLJ04, MMC+07a]. An EFI technique has been previously developed for microscopic objects recorded using digital holography [FGA+05], but the shape extraction technique they employ is not applicable to our macroscopic objects primarily due to the corruptive effect of speckle noise which is not present in digital holographic microscopy. In 2008 another extended focused image technique was developed based on reconstructing tilted planes [JH08]. An object that was titled with respect to the CCD would have parts out-of-focus in a standard numerical reconstruction. However, by reconstructing tilted planes an image with the object in-focus could be obtained. The drawback of this approach is that it reconstructs one titled plane and objects generally do not lie upon one plane.

In this chapter we begin by introducing our first EFI creation algorithm, the non-overlapping approach, in Sect. 5.1. The primary advantage of this approach is speed but this is at the expense of visual quality. We detail how the parameters of our DFF algorithm can be modified to create a qualitively good EFI in a relatively fast time. Our next EFI creation algorithm is the overlapping approach which uses the higher resolution depth maps as input, as described in Sect. 5.2. It is more time consuming but produces more qualitively accurate EFIs. Also the higher resolution allows us to develop a second algorithm in the overlapping approach which uses the extra depth information for error suppression.

5.1 Non-Overlapping

By using the non-overlapping DFF algorithm, low resolution depth maps can be created. Through combining a depth map, $D^{\mathrm{NO}}_{z_{\mathrm{step}}}(r,s)$, with numerical reconstructions, $I_z(k,l)$, of the DH we can create EFIs. For each pixel in $D_{z_{\mathrm{step}}}(r,s)$, an $n \times n$ pixel block of intensity values is mapped to the non-overlapping-case EFI with

$$\mathrm{EFI}_{\mathrm{NO}}(k,l) = I_{D^{\mathrm{NO}}_{z_{\mathrm{step}}}(r,s)}(k,l), \tag{5.1}$$

where $r = \lfloor k/n \rfloor, s = \lfloor l/n \rfloor$, where the notation $I_{D^{\mathrm{NO}}_{z_{\mathrm{step}}}(r,s)}(k,l)$ denotes the real-valued intensity value at lateral coordinates (k,l) and depth $D^{\mathrm{NO}}_{z_{\mathrm{step}}}(r,s)$ in the reconstruction volume, where $k \in [0,1,\ldots,M'], l \in [0,1,\ldots,N']$, and where $M' = n\lfloor M/n \rfloor, N' = n\lfloor N/n \rfloor$ (for the nonoverlapping case only, the $M' \times N'$ pixel dimensions of the EFI will be smaller than the the original reconstructions if n does not divide M,N). We proceed to examine two parameters in the DFF algorithm and their impact on $\mathrm{EFI}_{\mathrm{NO}}(k,l)$. The first is the reconstruction interval z_{step}.

5.1.1 Reconstruction Interval

In Fig. 5.1 two numerical reconstructions, from the front focal plane and back focal plane of the DH, are displayed alongside two $\mathrm{EFI}_{\mathrm{NO}}(k,l)$ reconstructions. The objects in this DH have a depth-of-focus of approximately 20mm. We created two $\mathrm{EFI}_{\mathrm{NO}}(k,l)$s, one from a $D^{\mathrm{NO}}_{0.2}(r,s)$ and one from a $D^{\mathrm{NO}}_{2.8}(r,s)$ where $n \times n = 81 \times 81$, $z_{\mathrm{min}} = 350\mathrm{mm}$ and $z_{\mathrm{max}} = 380\mathrm{mm}$. This results

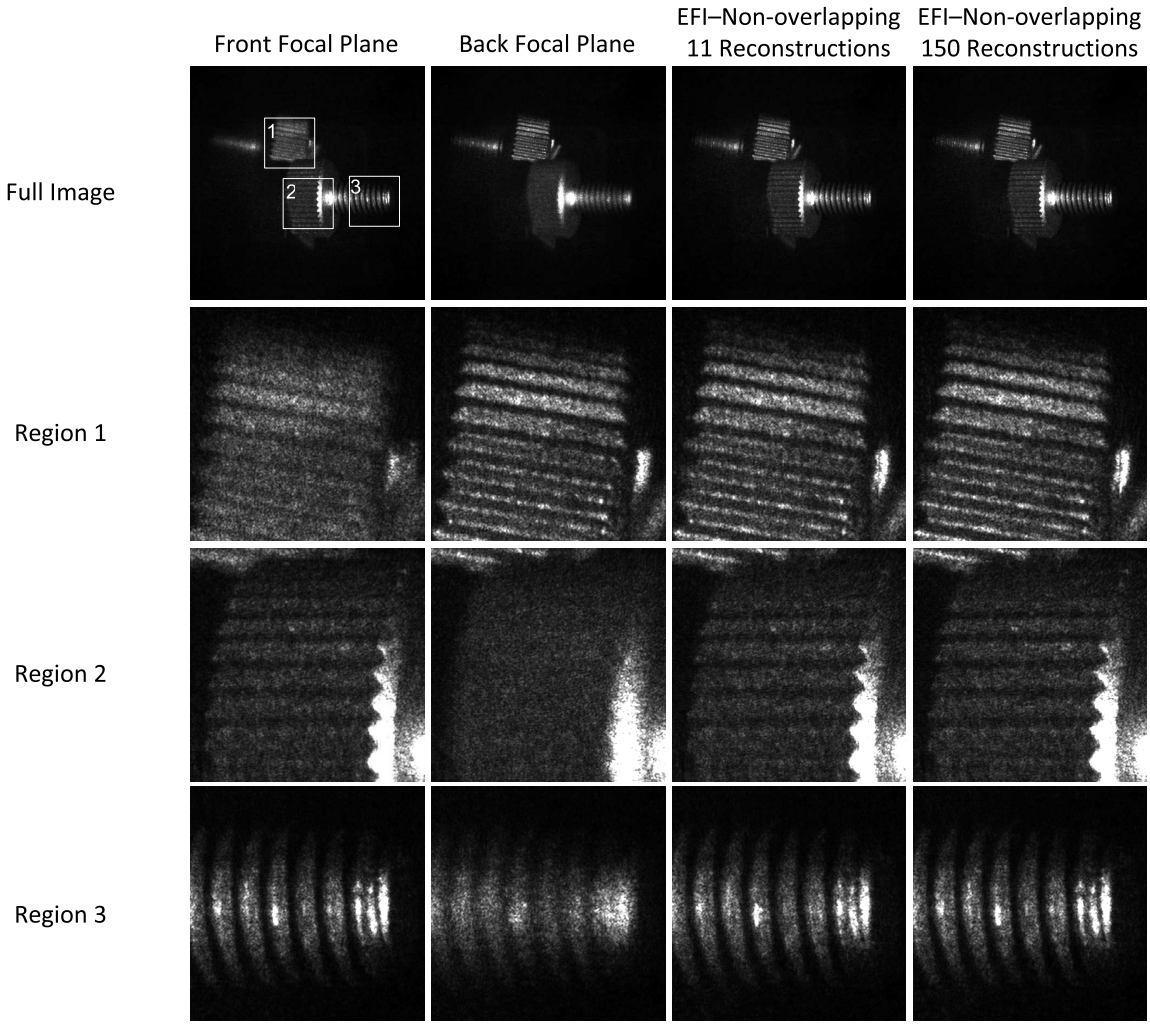

Figure 5.1: Two bolts object DH, reconstructions and the non-overlapping approach EFIs.

in an $\mathrm{EFI}_{\mathrm{NO}}(k,l)$ containing intensity information from 151 reconstructions, $D_{0.2}^{\mathrm{NO}}(r,s)$, and 11 reconstructions, $D_{2.8}^{\mathrm{NO}}(r,s)$. We have already shown that a greater number of reconstructions results in a more accurate depth map and should therefore result in a more accurate EFI, see Chapter 3.3.5. To compare these two $\mathrm{EFI}_{\mathrm{NO}}(k,l)$ reconstructions we selected three object regions which are labelled in Fig. 5.1: two on the front bolt object and one on the back bolt object. The numerical reconstructions in Fig. 5.1 illustrate the limited depth-of-field of a digital holographic reconstruction, while the output $\mathrm{EFI}_{\mathrm{NO}}(k,l)$ demonstrates how our technique can overcome this limitation to create images where all object regions are in-focus. To demonstrate the full impact of z_{step} we need to compare accuracy as a function of computation time. We vary z_{step} to create multiple $\mathrm{EFI}_{\mathrm{NO}}(k,l)$s from the same reconstruction volume and compare them to our qualitive best $\mathrm{EFI}_{\mathrm{NO}}(k,l)$ created from $D_{0.2}^{\mathrm{NO}}(r,s)$.

5.1.2 Computation time

Due to the large size of DHs the DFF algorithm, and consequently the EFI creation, is computationally intensive. On a P4 3GHz PC the creation of the $\mathrm{EFI}_{\mathrm{NO}}(k,l)$ using 151 reconstructions takes almost 2.5 hours. We investigated the impact of reducing the number of reconstruction on the output EFI for a set of DHs. By taking the $\mathrm{EFI}_{\mathrm{NO}}(k,l)$ created using a large number of reconstructions (151) as our best EFI, we compared the $\mathrm{EFI}_{\mathrm{NO}}(k,l)$ created using different numbers of reconstructions on two criteria: running time and normalised root-mean-square error (NRMS) error [Fie97]. Plots of

running time and NRMS error as a function of the number of reconstructions used in the $\text{EFI}_{\text{NO}}(k,l)$ creation are shown in Fig 5.2. The jumps in error value in Fig. 5.2 occur when our sampling of the reconstruction space does not include the depth for some of the large object regions. This leads to a depth with incorrect estimates of depths in object regions, causing blurring in the resulting $\text{EFI}_{\text{NO}}(k,l)$ and an increase in error. For some scenes, it can happen that a lower sampling of depths will include more exact depths at which object regions are located. In a short period of time, less than ten minutes, an $\text{EFI}_{\text{NO}}(k,l)$ using only eleven reconstructions can be created with an error of 17.5% when compared to our qualitative best EFI. A visual comparison of the two non-overlapping EFIs is displayed in Fig. 5.1. Both of the $\text{EFI}_{\text{NO}}(k,l)$ reconstructions produce images of the scene where both objects are in-focus. They also both struggle to select the correct blocks for the wires protruding from the head of the back bolt of the front bolt as shown in the row of region 1 images in Fig. 5.1. These EFIs can be improved on through the use of the overlapping DFF algorithm to create higher resolution depth maps prior to the calculation of an EFI.

5.1.3 Block Size

In Chapter 3.3.2 and 4.1, we discussed the impact that block size has on depth maps and our DHIP algorithms. In this section we compare $\text{EFI}_{\text{NO}}(k,l)$s created with different block sizes to demonstrate that our selection of 81×81 block size for the non-overlapping algorithm is valid. We use the following six block sizes: 7×7, 31×31, 43×43, 63×63, 81×81 and 121×121.

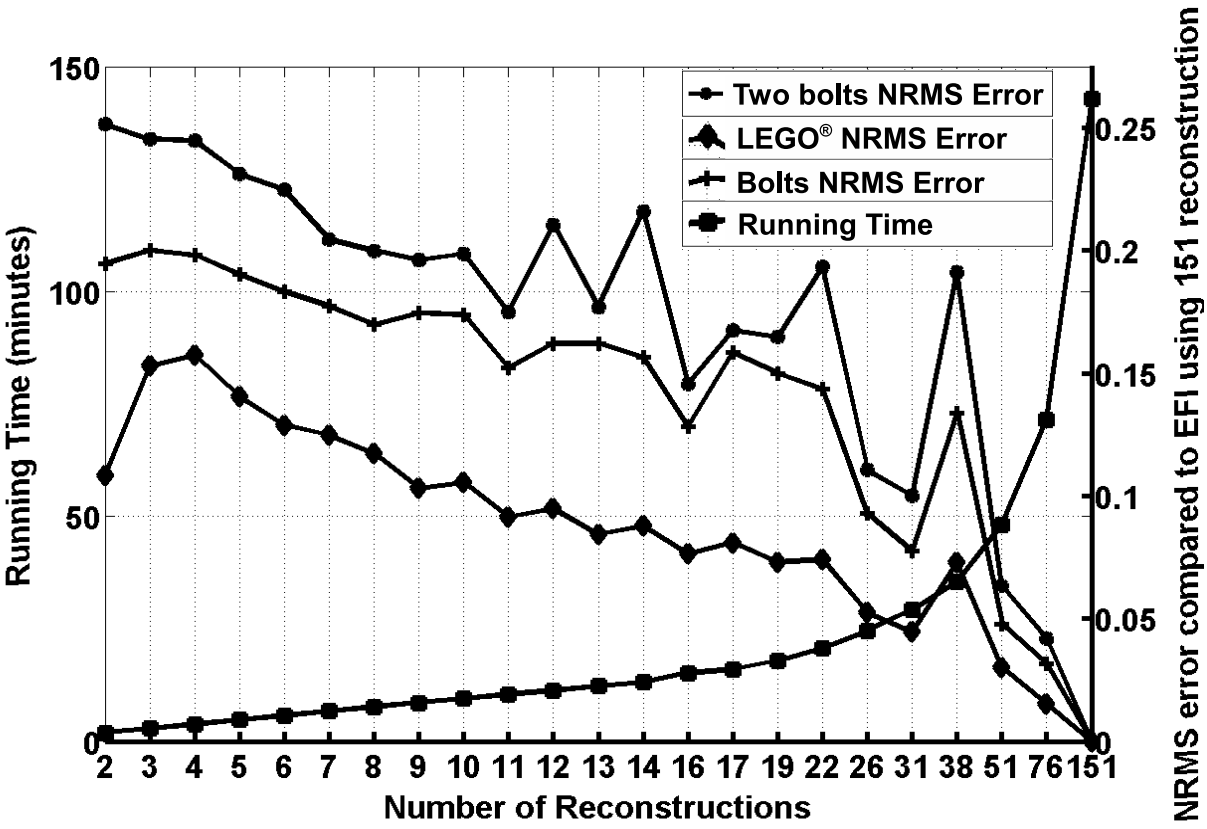

Figure 5.2: Accuracy and timing plot for the non-overlapping approach EFIs created using increasing numbers of reconstructions.

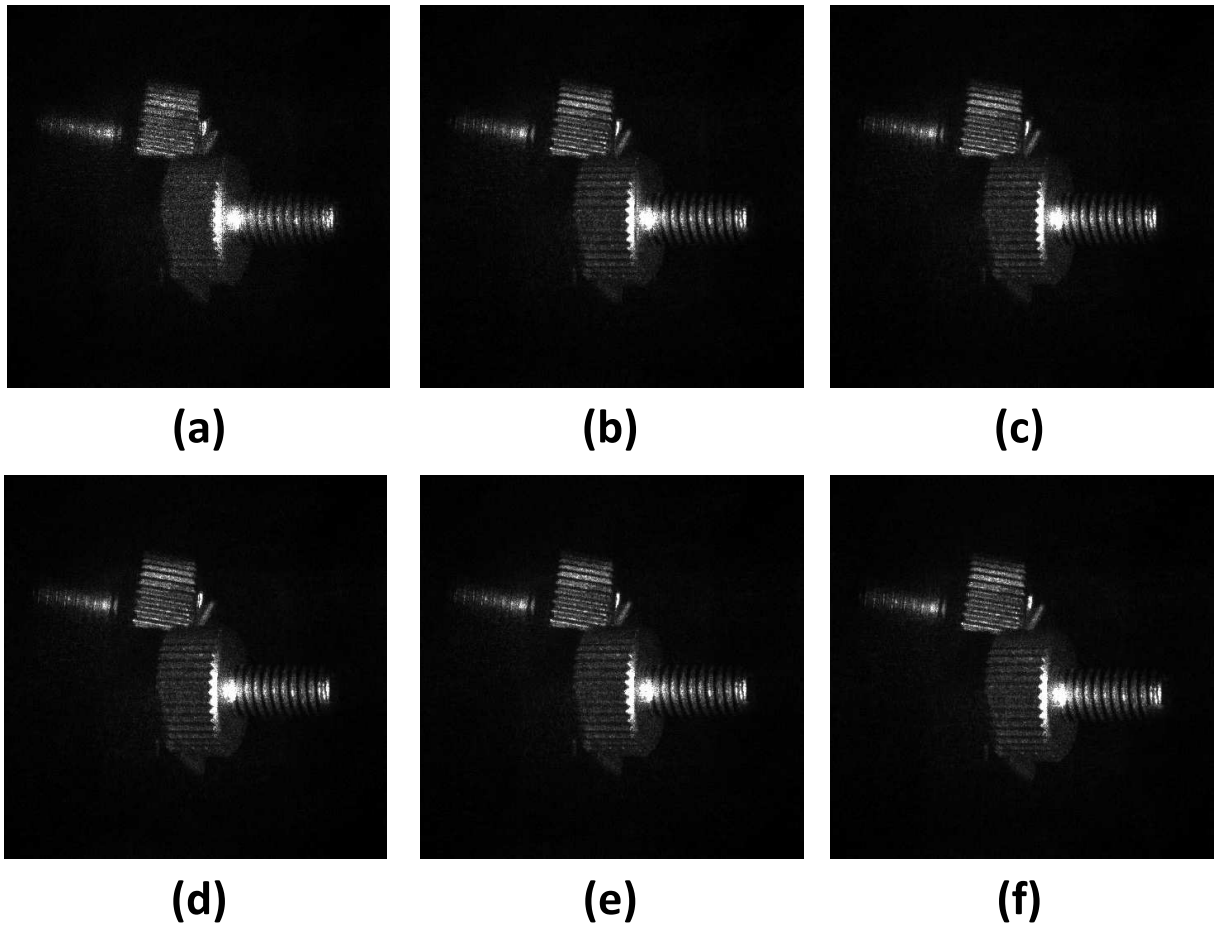

Figure 5.3: Two bolts object DH, $\mathrm{EFI}_{\mathrm{NO}}(k,l)$'s created with a block size of (a) 7×7, (b) 31×31, (c) 43×43, (d) 63×63, (e) 81×81 and (e) 121×121.

These result in the depth maps displayed in Fig. 3.9 and the $\mathrm{EFI}_{\mathrm{NO}}(k,l)$s displayed in Fig. 5.3. From this figure the only $\mathrm{EFI}_{\mathrm{NO}}(k,l)$ where the objects are obviously not in-focus is the one created with the 7×7 block size. This is unsurprising as at such a small block size there is not a lot of information in the blocks to accurately determine focus. It demonstrates the this block size is too small to estimate depth. However, the other block sizes all seem to produce focused images. We select four of the block sizes and display them along with the three zoomed in regions in Fig. 5.4 to illustrate any differences. There is obvious artifacting in regions 1 and 2 of the 43×43 case but apart from this the other three EFIs are comparable. We select the 81×81 block size for two main reasons, the first is that a depth map created from this block size has no obvious errors (unlike the one spike in the 121×121 case) and also we have shown that the 81×81 block size produces very good results in the overlapping case. We now progress to the discussion of the overlapping EFI creation algorithms which produce EFIs from higher resolution depth maps.

5.2 Overlapping

We have developed two approaches for creating EFIs from depth maps calculated using the overlapping DFF algorithm. The pointwise approach produces a sharp EFI but does not attempt to compensate for any errors in $D_{z_{\mathrm{step}}}(k,l)$ which can occur for a number of reasons including poor object illumination or speckle noise. Our neighbourhood approach applies smoothing based on the $n \times n$ block size used to create $D_{z_{\mathrm{step}}}(k,l)$. The overlapping

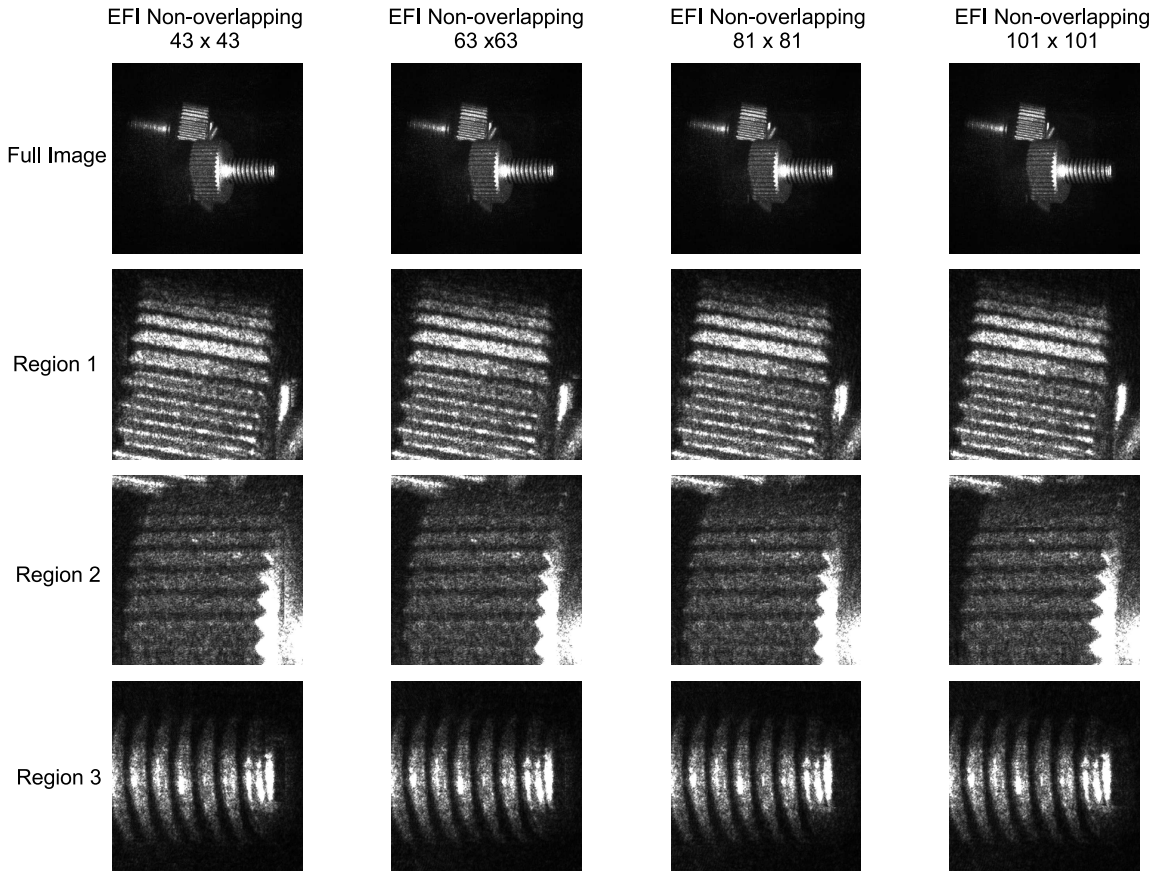

Figure 5.4: Two bolts object DH, comparison of $\mathrm{EFI}_{\mathrm{NO}}(k,l)$'s created using different block sizes.

algorithm takes, on average, 25 minutes to process an individual reconstruction compared to less than one minute for the non-overlapping algorithm (for the 81×81 block size). However, the overlapping approach returns a high resolution $D_{z_{\text{step}}}(k,l)$ allowing for a higher quality EFI.

5.2.1 Pointwise approach

To calculate the pointwise EFI, $\text{EFI}_\text{P}(k,l)$, we take the depth for each pixel from $D_{z_{\text{step}}}(k,l)$ and store the intensity value of the corresponding pixel from $I_z(k,l)$ for that depth in $\text{EFI}_\text{P}(k,l)$. We calculate $\text{EFI}_\text{P}(k,l)$ with the following function

$$\text{EFI}_\text{P}(k,l) = I_{D_{z_{\text{step}}}(k,l)}(k,l) \tag{5.2}$$

where $k \in [0,(M-1)], l \in [0,(N-1)]$.

5.2.2 Neighbourhood approach

We have also developed a second approach for creating EFIs from depth maps created using the overlapping DFF algorithm. This uses the $n \times n$ block size input to DFF to smooth potential errors about a neighbourhood. For each pixel (k,l) in $D_{z_{\text{step}}}(k,l)$ we take the $n \times n$ pixels, centred around (k,l), from $I_z(k,l)$ and store them in the neighbourhood EFI, $\text{EFI}_\text{N}(k,l)$. This has the effect of reducing the impact of blocks whose depth was incorrectly estimated by summing intensity values for each pixel around a neighbourhood. We

calculate $\mathrm{EFI_N}(k,l)$ with

$$\mathrm{EFI_N}(k,l) = \frac{1}{n^2} \sum_{r=k-\lfloor \frac{n-1}{2} \rfloor}^{k+\lceil \frac{n-1}{2} \rceil} \sum_{s=l-\lfloor \frac{n-1}{2} \rfloor}^{l+\lceil \frac{n-1}{2} \rceil} I_{D_{z_{\mathrm{step}}}(k+(r-k),l+(s-l))}(r,s), \tag{5.3}$$

where $k \in [0,(M-1)]$,$l \in [0,(N-1)]$.

A comparison of the two overlapping approaches, $\mathrm{EFI_P}(k,l)$ and $\mathrm{EFI_N}(k,l)$, and the two $\mathrm{EFI_{NO}}(k,l)$ reconstructions, detailed in Sect. 5.1, is displayed in Fig. 5.5. There are not many noticeable differences between the images in this figure so we display region 1 for the four EFIs in Fig. 5.6. In this figure there is some artifacting in both non-overlapping EFIs where the wires are at the back of the two bolts object, this is not the case in the overlapping case.

The difference between the pointwise and neighbourhood approach is, in general, subtle. If a depth map is low in error then the main visual impact of the neighbourhood approach is its negative affect on image sharpness when compared to the pointwise approach. To demonstrate its advantages we need to take a less accurate depth map than $D_{0.2}(k,l)$. We can achieve this through manipulation of z_{step} in our DFF process (increasing the reconstruction interval). We demonstrate this in Fig. 5.7 where we compare an $\mathrm{EFI_P}(k,l)$ with an $\mathrm{EFI_N}(k,l)$ created using $D_5(k,l)$. Using the reconstruction interval of 5mm causes a lot of defocus in the resultant $\mathrm{EFI_P}(k,l)$, in all three object regions. From this figure it is clear that $\mathrm{EFI_N}(k,l)$ does not struggle in these regions and it is important to note that instead of there being a reduction in sharpness in $\mathrm{EFI_N}(k,l)$, regions 1-3 are more clearly in-

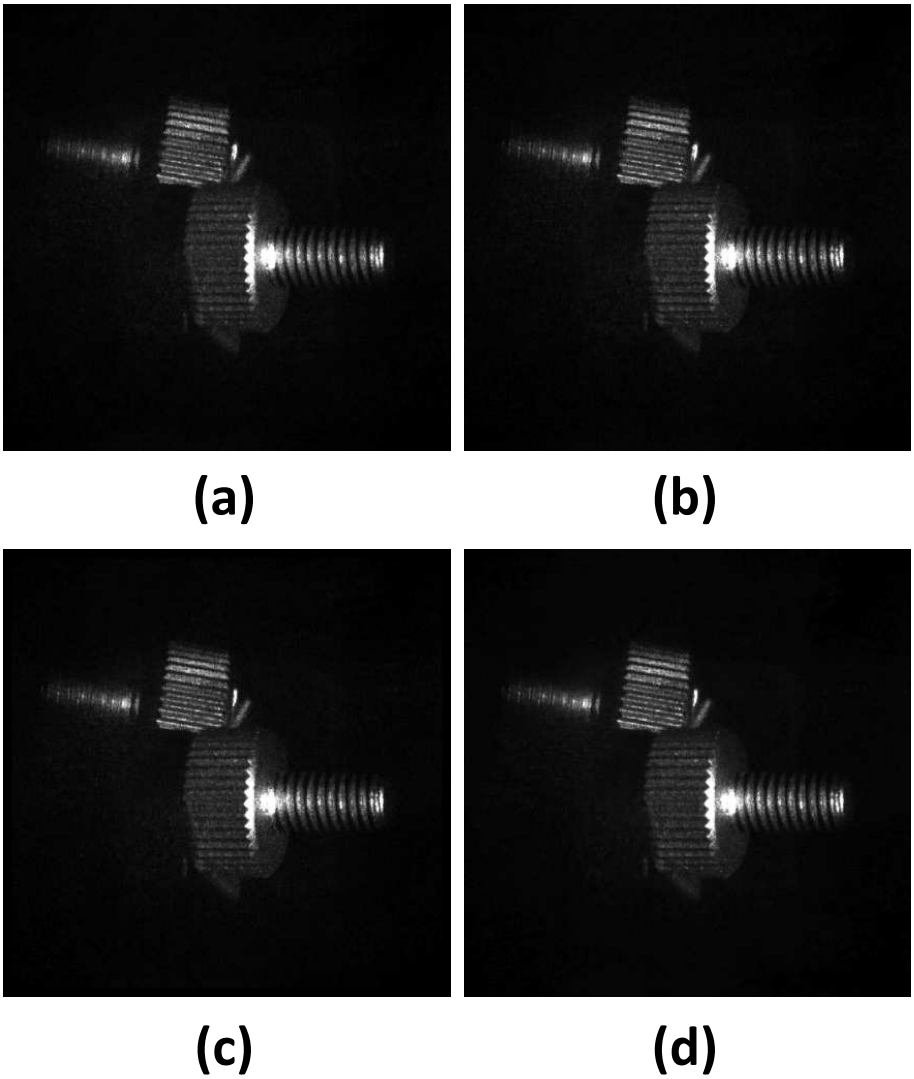

Figure 5.5: Two bolts object EFIs created using the (a) non-overlapping approach and 11 reconstructions, (b) non-overlapping approach and 151 reconstructions, (c) overlapping pointwise approach and 151 reconstructions, and (d) overlapping neighbourhood approach and 151 reconstructions.

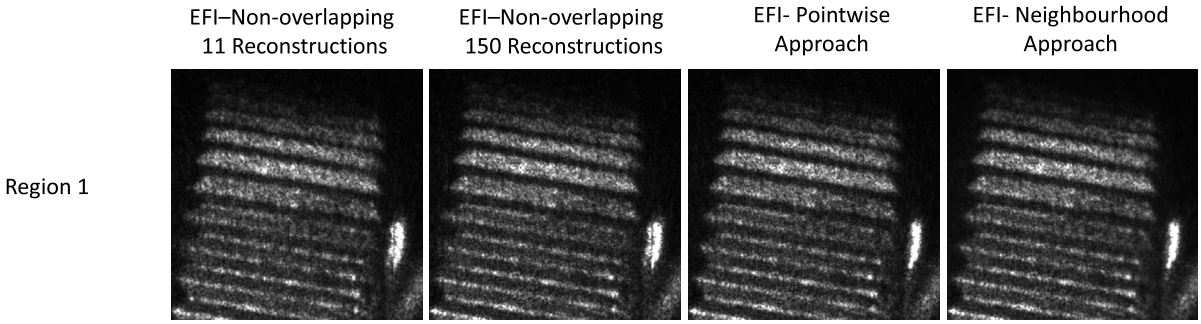

Figure 5.6: Two bolts object DH reconstructions for region 1 and the EFI creation approaches.

focus. This demonstrates that in certain cases an improvement can be made on $\mathrm{EFI}_{\mathrm{P}}(k,l)$ through applying the neighbourhood approach.

5.2.3 EFI examples

To illustrate our techniques effectiveness on low contrast objects we calculated $\mathrm{EFI}_{\mathrm{P}}(k,l)$ and $\mathrm{EFI}_{\mathrm{N}}(k,l)$ for a Lego block object DH, with a depth-of-focus of 11mm. In Fig. 5.8 a front focal plane and back focal plane reconstruction are shown alongside $\mathrm{EFI}_{\mathrm{P}}(k,l)$ and $\mathrm{EFI}_{\mathrm{N}}(k,l)$. We identified two object regions: the back Lego block, region 1, and the front Lego block, region 2, both with the word "Lego" inscribed. In these reconstructions the word "Lego" is only legible in one of the reconstructions, region 2 and region 1 in the front focal and back focal plane respectively. However, in $\mathrm{EFI}_{\mathrm{P}}(k,l)$ and $\mathrm{EFI}_{\mathrm{N}}(k,l)$ the word "Lego" is legible in both region 1 and region 2.

To demonstrate the general applicability of EFI process we display $\mathrm{EFI}_{\mathrm{P}}(k,l)$ from three more of our DHs alongside front and back focal plane reconstructions in:

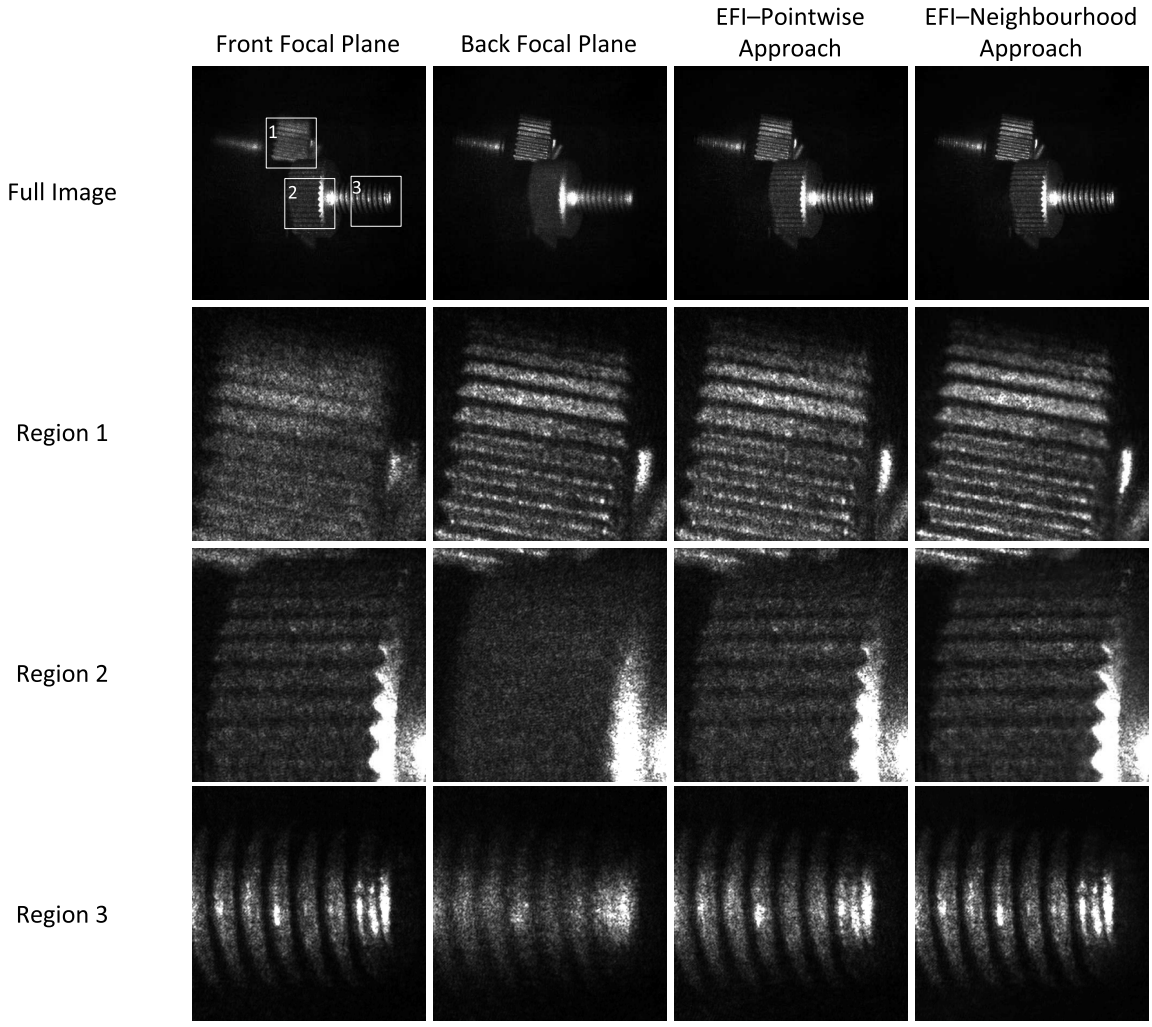

Figure 5.7: Two bolts object DH reconstructions for pointwise approach compared to neighbourhood approach using a reconstruction interval of 5mm.

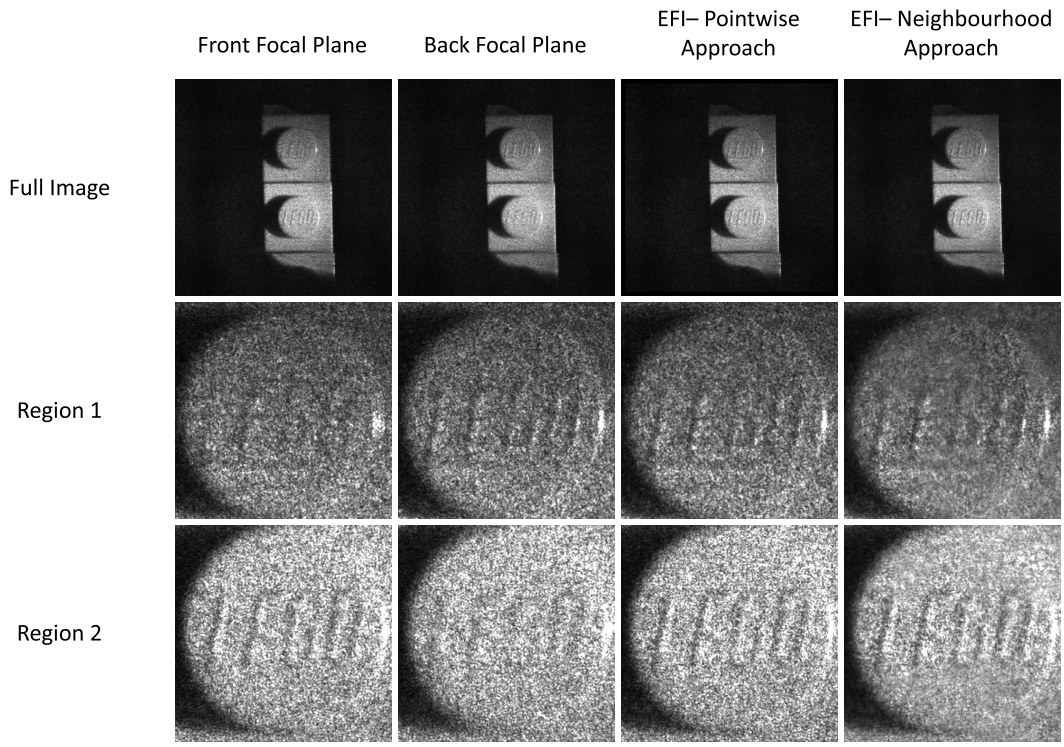

Figure 5.8: Lego block object DH, reconstructions and the overlapping approach EFIs.

Figure 5.9: Hairs object DH using the $D_1(k, l)$ from Fig. 3.17

Figure 5.10: Large bolt object DH using the $D_{0.5}(k, l)$ from Fig. 3.18

Figure 5.11: Bolts object DH using the $D_{0.5}(k, l)$ from Fig. 3.23

5.3 Discussion

We have detailed a novel method for creating an image where all objects are in-focus, an EFI, out of volumes of digital holographic reconstructions. Using DHs of real-world three-dimensional macroscopic objects we have experimentally verified our technique. Multiple approaches for creating EFIs have been described along with their disadvantages and advantages. The non-overlapping DFF algorithm is relatively fast but there is a significant loss of resolution. Our overlapping DFF algorithm is computationally expensive but has the advantages of high resolution and, if required, error suppression. We have successfully created EFIs for scenes containing multiple and single objects and containing low and high contrast objects and have demonstrated an increase to the depth-of-focus of our system from 0.8mm to 56mm.

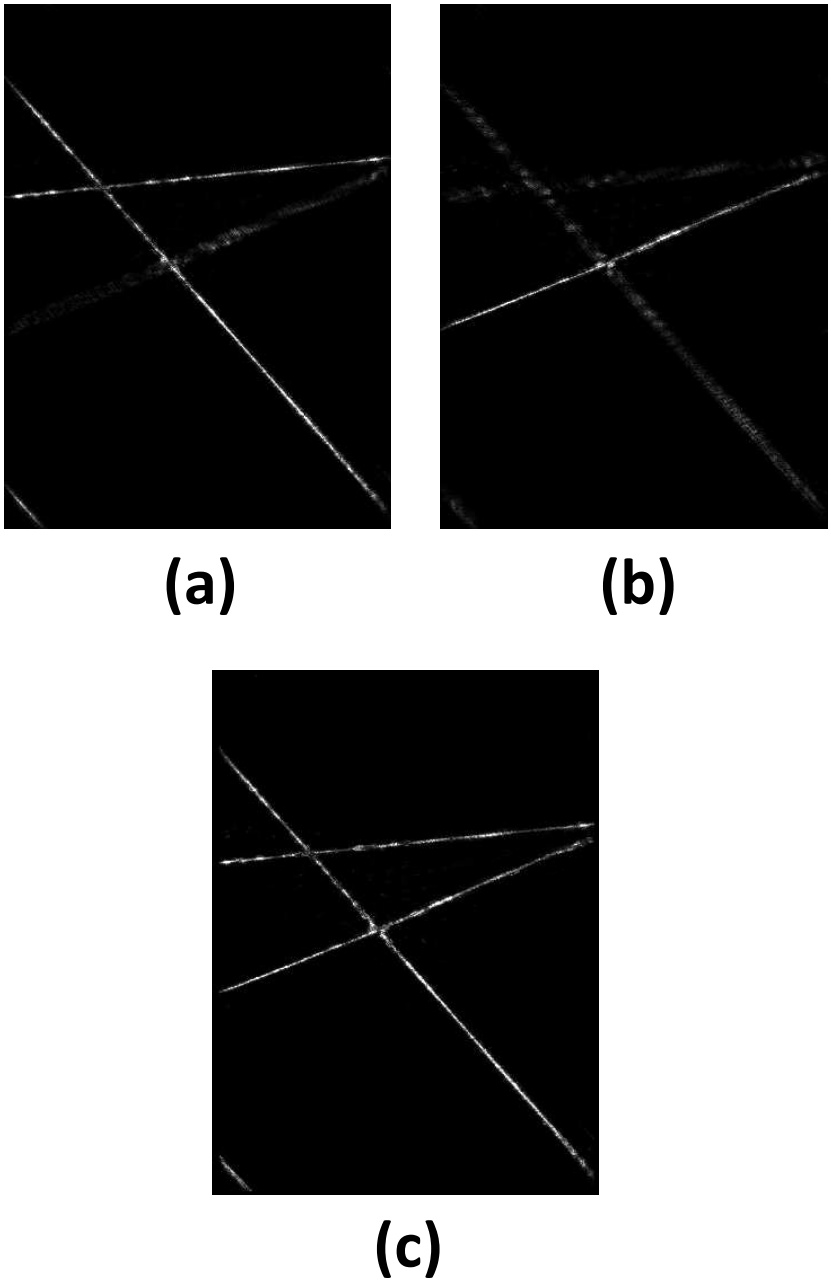

Figure 5.9: Hairs object DH: (a) front focal plane reconstruction, (b) back focal plane reconstruction and (c) EFI_P.

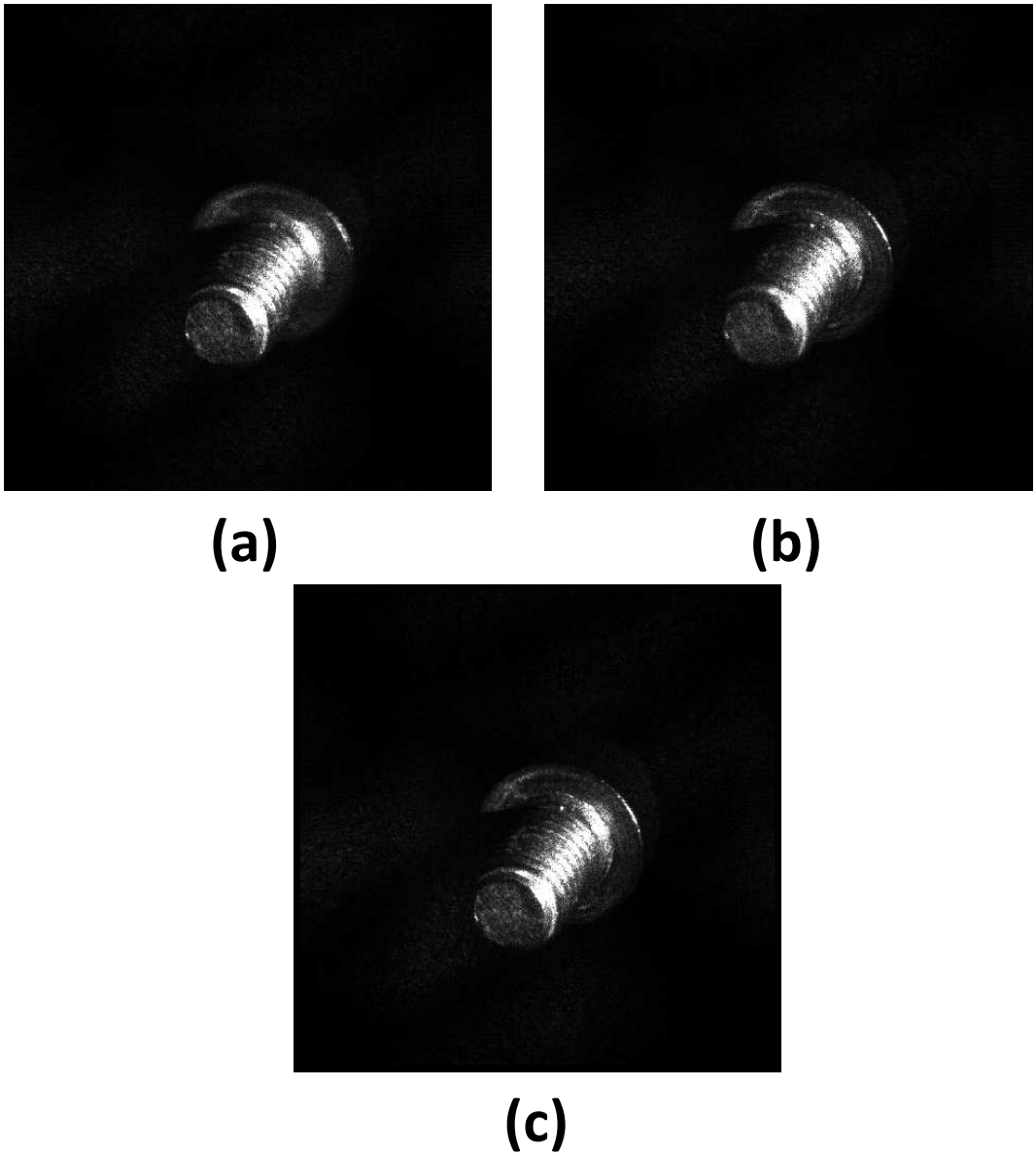

Figure 5.10: Large bolt object DH: (a) front focal plane reconstruction, (b) back focal plane reconstruction and (c) EFI_P.

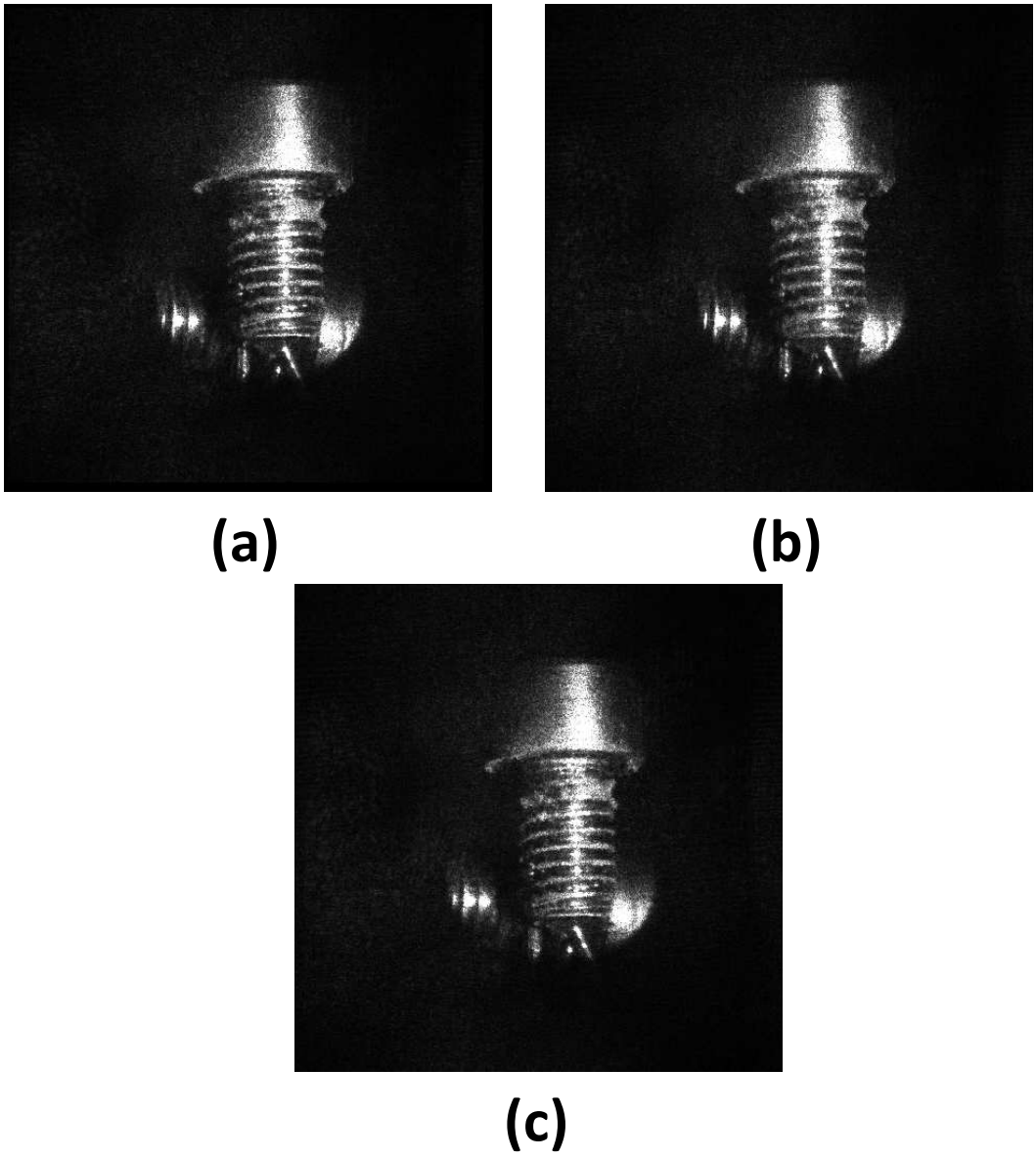

Figure 5.11: Bolts object DH: (a) front focal plane reconstruction, (b) back focal plane reconstruction and (c) EFI_P.

Chapter 6

Twin-image removal

The quality of numerical reconstructions from digitally recorded in-line holograms can be significantly improved by successfully removing the unwanted twin-image. We have developed a novel three stage solution which given an in-line digital hologram as input only requires a single manual step. In this chapter we detail how to calculate the spatial extent of the wanted twin-image at the unwanted twin-images focal plane. We also detail a segmentation algorithm and provide experimental results of in-line DHs free of the twin-image. We have also implemented this algorithm using stream programming allowing us to calculate reconstructions of size 8192×8192 in 3.4 seconds and a 2048×2048 sized DH free of the twin-image in under 9 seconds.

In our twin-image removal algorithm we employ both the DFRT and the PTF reconstruction methods. We use Eqn. (A.23) in the autofocus process and Eqn. (A.32) in the reconstruction and segmentation process. This is due to the fact that Eqn. (A.23) is not reciprocal and therefore we cannot

use it in our segmentation algorithm to propagate to the in-focus unwanted twin-image plane and then back to the original hologram plane. However, if we were to employ Eqn. (A.32) in our autofocus algorithm we would need to pad a hologram $H(x, y)$ with zeros, to guarantee no wrapping of the object data in the reconstruction, which would increase the computation time of our algorithm. To combat this we use Eqn. (A.23) which allows us to reconstruct $H(x, y)$ with a larger field of view than a reconstruction using Eqn. (A.32) with the same number of samples, which in turn significantly decreases the computation time.

6.1 Spatial extent of the object signal

When the distance to the unwanted twin-image plane has been correctly identified, we need to calculate the amount of padding required for Eqn. A.32 to ensure that no wrapping of the wanted twin-image in the reconstruction. The subsequent analysis of the spatial extent of the wanted twin-image is carried out for an in-line setup, but can easily be extended to an off-axis setup [XMA00]. We use Eqn. A.32 to numerically propagate our DHs [Kre05] in this section of the twin-image removal process. This is a lossless transform and ensures that the energy of the object signal is preserved after propagation. Due to its use of the discrete Fourier transform with finite support and the conservation of energy the object signal will be wrapped within the reconstruction window. This wrapping occurs if the reconstruction window is not large enough to contain the entire spatial support of the object. Therefore, we have to pad the DH (in the camera plane) with zeros to ensure that

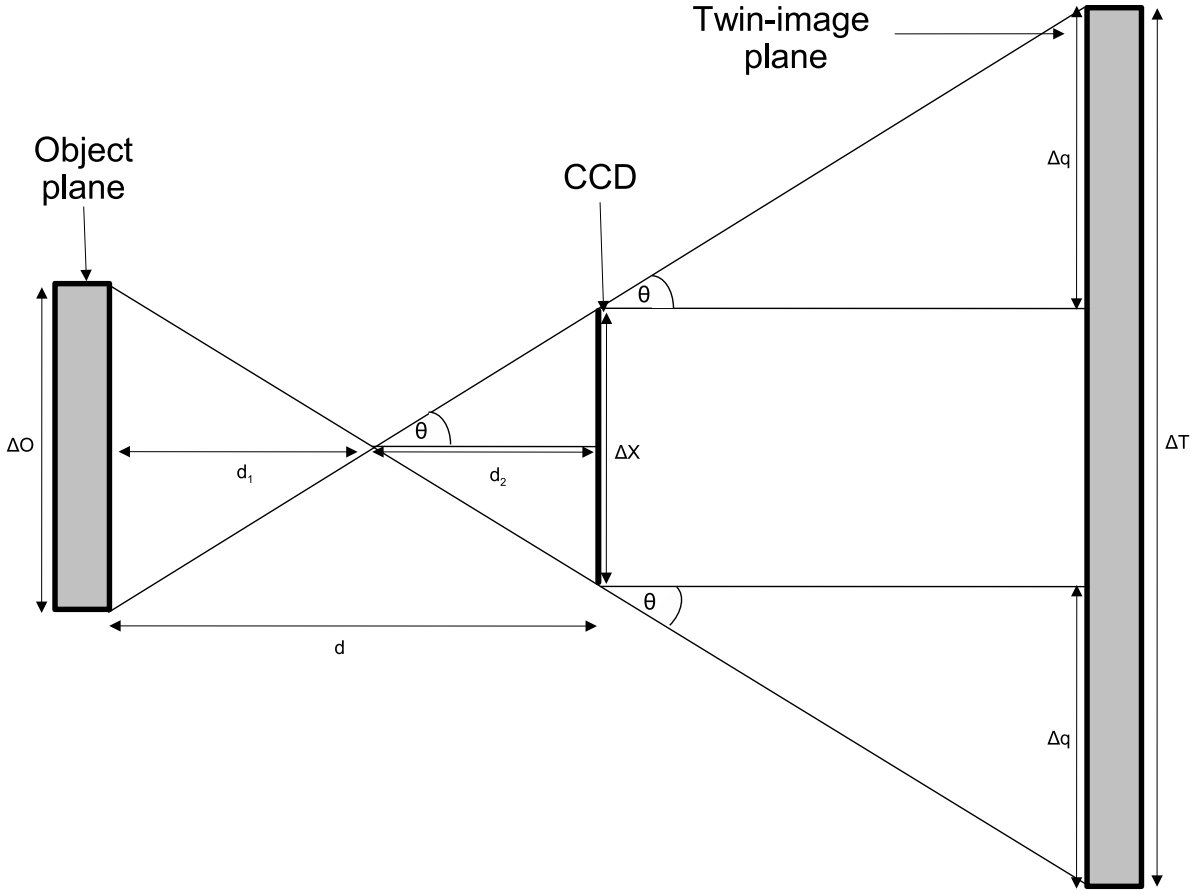

Figure 6.1: Spatial extent of object signal in unwanted twin-image plane.

the reconstruction window is at least as large as the spatial extent of the object signal in the reconstructions plane. If we did not pad, it is likely that some of the object signal will be wrapped and therefore removed in the segmentation process. In this section, we detail how to determine the size of the out-of-focus object signal in the unwanted twin-image plane. Our analysis is limited to 1D for simplicity of representation with extension to 2D being straight forward.

In Fig. 6.1, θ is the maximum interference angle allowed between the reference wave direction and the object wave direction, for in-line digital holography, to avoid aliasing [Onu00]. The spatial extent of ΔT is dependent on the maximum lateral size of the object, the maximum lateral size of the CCD and its distance from the CCD: ΔO, ΔX and d respectively as shown in Fig. 6.1. It can be seen from the figure that this quantity can be calculated with

$$\Delta T = \Delta X + 2\Delta q. \tag{6.1}$$

This equation necessitates we first calculate Δq, which can be calculated from

$$\Delta q = \tan\theta \times d, \tag{6.2}$$

where, from Fig. 6.1,

$$d = d_1 + d_2. \tag{6.3}$$

To find d we first need to find d_1 and d_2 which can be represented in terms of θ with

$$\tan\theta = \frac{\Delta X/2}{d_2} = \frac{\Delta O/2}{d_1}. \tag{6.4}$$

From this equation we can easily describe d_1 and d_2 as

$$d_1 = \frac{\Delta O}{2\tan\theta} \quad \text{and} \quad d_2 = \frac{\Delta X}{\Delta O} d_1 \tag{6.5}$$

and substituting these values into Eqn. 6.3 we obtain

$$\begin{aligned} d &= d_1 + \frac{\Delta X}{\Delta O} d_1 && (6.6) \\ &= \frac{\Delta O + \Delta X}{2\tan\theta}. && (6.7) \end{aligned}$$

Now that we have a description of d we can find Δq by substituting d into Eqn. 6.2

$$\begin{aligned} \Delta q &= \tan\theta \times \frac{\Delta O + \Delta X}{2\tan\theta}, && (6.8) \\ \Delta q &= \frac{\Delta O + \Delta X}{2}. && (6.9) \end{aligned}$$

With this suitable definition of Δq, we can define ΔT in terms of ΔX and ΔO by substituting Δq into Eqn. 6.1

$$\Delta T = 2\Delta X + \Delta O. \tag{6.10}$$

Given ΔO and N_x, the number of pixels in the CCD, and Eqn. 6.10 we can calculate the total number of samples required at the hologram plane, in one-dimension, with

$$N_H = \left\lceil \frac{\Delta T}{\delta \xi} \right\rceil. \tag{6.11}$$

Padding up to this amount guarantees that after propagation to the un-

wanted twin-image plane the object signal will not be wrapped within the reconstruction window. This equation relies on knowing ΔO which is unknown. However, assuming that the hologram was recorded in adherence to the sampling theorem if we can calculate the distance d the object was positioned away from the CCD, with Alg. 3.1, we can calculate the maximum size of ΔO at d by rewriting Eqn. (2.14) as

$$\Delta O = \frac{d\lambda}{\delta\xi} - N_x\delta\xi. \tag{6.12}$$

If the number of pixels in the camera is different in the x and y dimensions, a different N_H can be calculated for the amount of padding required in the y dimension. Having computed N_H using Eqn. 6.11 we round up to the nearest power of 2. This is done to accomodate the use of the fast Fourier transform which is more efficiently computed when a matrix whose size is a power of 2 is input. We note that the spatial extent of the spread out, out-of-focus, object signal in the unwanted twin-image plane can be calculated using only the camera parameters, the wavelength of light used and the distance the object is positioned away from the CCD.

6.2 Automated removal

Our twin-image removal algorithm is a three stage process as displayed in Fig. 6.2. In the first stage we reconstruct the unwanted twin-image, this process is fully automated. The second step consists of segmenting the unwanted twin-image and requires one manual user intervention, the choice of

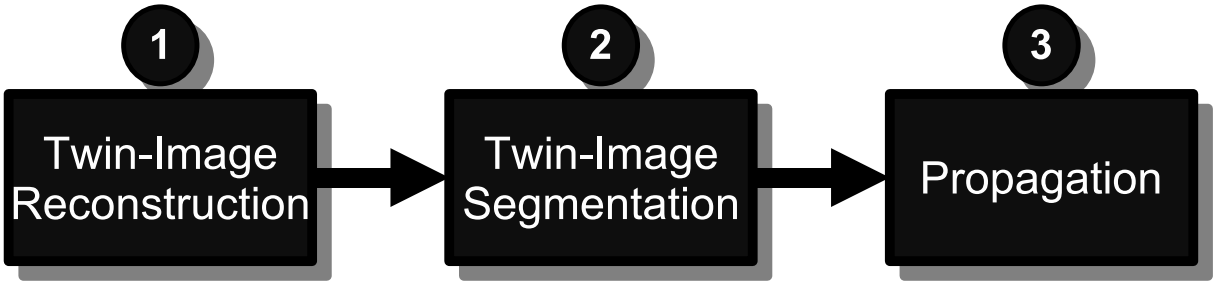

Figure 6.2: Algorithm for removing the unwanted twin-image.

threshold value. The final stage is the propagation to the hologram plane and extraction of the $M \times N$ complex data. We now describe these three stages in detail.

Stage 1: Stage 1 combines two steps as shown in Fig. 6.3. The first step, (a), takes our original hologram $H^{DC}(x, y)$, of size $M \times N$, and automatically determines the focal plane of the twin-image using the algorithm outlined in Chapter 3.2. The second part of this process requires the calculation of the total number of samples required in the hologram plane before propagation to the unwanted twin-image plane; N_H as given by Eqn. 6.11. Padding to N_H, we reconstruct using Eqn. A.32 resulting in an in-focus reconstruction, $R^T(x, y)$, which we can segment to remove the unwanted twin-image.

Stage 2: This stage consists of two steps, (a) calculation of the segmentation mask, SMask(x, y), and (b) sementation of the unwanted twin-image. In the first step, as shown in Fig. 6.4(a), we calculate a focus map, $V_z(x, y)$, from the intensity of $R^T(x, y)$.This focus map is calculated using Eqn. (3.7) and a block size of 81×81 and where z is the distance returned from the autofocus in Stage 1. $V_z(x, y)$ is then transformed into SMask(x, y) using Eqn. (4.1) where $V_z(x, y)$ is input in place of $V_{\max}(x, y)$. The mask is created

as follows; pixels whose values are above the threshold are labelled as object and given the value of zero, and pixels whose values are below the threshold are labelled as background and given the value of one. It should be noted that a more accurate segmentation mask could be calculated using multiple depths but in the interests of speed we calculate a segmentation mask using only one reconstruction. We then calculate the segmented twin-image, as shown in Fig. 6.4(b), with $\mathrm{R}^S(x,y)$ =$\mathrm{R}^T(x,y)$·SMask(x,y) where $\cdot$ means elementwise product.

Stage 3: Stage 3 is displayed in Fig. 6.5. A hologram $H^S(x,y)$ is calculated through propagation of $R^S(x,y)$, which is free of the unwanted twin-image, by $-z$ the negative of the distance calculated in Stage 1. We then take the centre $M \times N$ samples, the original hologram size before padding, from $H^S(x,y)$ and store it in $H(x,y)$, which is our new hologram free of the unwanted twin.

We verified our automated approach with the two bolts object DH, as shown in Figure 6.6 and 6.7. The two bolts object was positioned approximately 355mm away from the camera and the maximum lateral size of approximately 20mm. Figure 6.6 shows the results for the two bolt object DH. In Fig. 6.6 (a) and (b) reconstructions of the original DH and the DH after DC-term suppression are shown. The results after twin-image removal with our approach, and through recording of a four-frame PSI hologram are shown in Fig. 6.6(c-d). Magnified reconstructions centred on the objects are displayed in Fig. 6.7, where a numerical reconstruction prior to twin-image removal is compared to the two outlined methods. It is evident from the

figures that our automated approach is comparable to the PSI approach. We have the distinct advantage over PSI of needing only a single capture allowing for the recording of dynamic scenes. We note that the resultant reconstructions still contain speckle and that if required speckle reduction algorithms can be applied [MHM+07]. We also verified this technique with another DH containing a low-contrast Lego block. This object was positioned approximately 300mm away from the CCD and the object has a maximum lateral size of approximately 11mm. In Fig. 6.8(a-b) we display reconstructions of the original DH prior to any processing and a reconstruction of the DH after DC-term removal. In parts (c-d) of Fig. 6.8 we display the results of the different twin-image removal approachs. We provide magnified reconstructions centred on the Lego object in Fig. 6.9.

6.3 Implementation

The autofocus algorithm and the three stages in the twin-image removal process have been implemented using our groups framework for digital hologram processing on programmable graphics hardware [APH+09], which has been shown to render images from DHs far more efficiently than traditional CPU-based methods. Considering the three stages described in the previous section; the first and third involve multiple propagations using the discrete Fresnel transform and can be implemented using the direct and convolution methods for large holograms as described in [APH+09]. For part (a) of Stage 1, autofocus, the propagation has been implemented using the direct method and a non padded hologram as we are only interested in the computed in-

tensity images for our calculation at this moment. For part (b) of Stage 1 and in Stage 3, we are however working on the hologram distribution and will thus need to pad the hologram and use the convolution method.

Stage 1 (a), autofocus, and Stage 2, segmentation, contain variance calculations, which may not be considered straightforward to implement on graphics hardware, due to the multiple summations needed. The key to implementing this in our framework is to observe that Eqn. 3.1 can be rewritten as

$$V(k,l) = \left[\frac{1}{n^2} \sum_{x=k-\lfloor \frac{n-1}{2} \rfloor}^{k+\lceil \frac{n-1}{2} \rceil} \sum_{y=l-\lfloor \frac{n-1}{2} \rfloor}^{l+\lceil \frac{n-1}{2} \rceil} |R^{\mathrm{TI}}(x,y)|^4 \right] - \mu^2. \tag{6.13}$$

This formulation of the variance function consists of the difference between two sums over the same block area, the mean squared intensities, in brackets, and the squared mean intensities, μ^2. We thus divide Stage 2 into two steps. First, two summed area tables [Cro84] are computed, one for each sum in the equation. Second, the variance for a specific location is computed as the difference of the appropriate block areas in the two tables. This allows the variance in each position to be computed using only two lookups and a subtraction which is very efficient. Using an Nvidia GeForce 8800GTX with 768MB of RAM the full three stages is executed in under 9 seconds for a 2048×2032 hologram padded to the needed 8192×8192 samples. The detailed times are shown in Table 6.1.

Table 6.1: Twin-image removal computation time (seconds)

Process	GPU time
Pixel Resolution	8192×8192
Stage 1 a)	0.5
Stage 1 b)	3.4
Stage 2	1.59
Stage 3	3.4
Total	8.4

6.4 Processing of interferograms

Our twin-image removal process now provides us with in-line DHs free of the twin-image and capable of being used as input to our DHIP algorithms. This gives us the opportunity to verify our DHIP algorithms. We first select our two bolts object DH and apply DFF to it with the following parameters:

$z_{\text{min}} = 345\text{mm}$

$z_{\text{step}} = 0.2\text{mm}$

$z_{\text{max}} = 380\text{mm}$

$n \times n = 81 \times 81$

$M \times N = 2048 \times 2048.$

Our background segmentation process is applied with a threshold of $\tau = 0.11$ and the resulting $\text{I}_{355}(k,l)$, $\text{D}_{0.2}(k,l)$, $\text{SMask}(k,l)$ and $\text{DMap}_{0.2}(k,l)$ are displayed in Fig. 6.10. Using the resultant $\text{DMap}_{0.2}(k,l)$ we can segment the

reconstructions from this DH into two regions, inputting $s = 2$ with the results in Fig. 6.11, and into four regions, using $s = 4$ displayed in Fig. 6.12. We demonstrate the results of our overlapping EFI creation algorithms in Fig. 6.14. We show a direct comparison of the results from a single interferogram and a PSI DH in Fig. 6.13.

For completeness we also apply our algorithms to a second low-contrast DH after twin-image removal, the lego block object. We input the following parameters to DFF and background segmentation:

$$z_{\text{min}} = 290\text{mm}$$

$$z_{\text{step}} = 0.5\text{mm}$$

$$z_{\text{max}} = 310\text{mm}$$

$$n \times n = 81 \times 81$$

$$M \times N = 2048 \times 2048$$

$$\tau = 0.14.$$

This returns $\text{D}_{0.5}(k, l)$, $\text{SMask}(k, l)$ and $\text{DMap}_{0.5}(k, l)$ which are shown in Fig. 6.15. Taking $\text{DMap}_{0.5}(k, l)$ and $s = 3$ as input to our depth segmentation algorithm we create $\text{DMask}(k, l)$ with three object regions which is shown in Fig. 6.16. A direct comparison of the results from DFF applied to a single interferogram and a PSI DH are shown in Fig. 6.17. Finally we create $\text{EFI}_{\text{P}}(k, l)$ and $\text{EFI}_{\text{N}}(k, l)$ which are compared to the focused reconstructions in Fig. 6.18. For both these objects these results are comparable

to those achieved using PSI holograms and demonstrates that our algorithms are applicable to single capture in-line DHs.

6.5 Discussion

We have developed a twin-image process for in-line digital holography which requires the recording of only one hologram and no modification of the experimental setup. This allows for the recording of dynamic scenes unlike other in-line alternatives such as PSI. The implementation of our algorithm on a GPU significantly reduces the computation time to 9 seconds for an input 2048×2048 sized digital hologram. We have discussed the spatial extent of the object signal as a function of distance. The derived equations lets us determine the correct padding in the twin-image plane to avoid signal wrapping. We have used these two novel contributions which are fully automated to create a semi-automated twin-image removal algorithm based on the segmentation of the unwanted twin-image at its in-focus plane. The only element of this process which is not automated is the thresholding required to create the segmentation mask. However, we have experimentally found that for our DHs the threshold value falls within a small range of a seed value of $0.1 - 0.3$. We are hopefull that we will be able to fully automate the last step of the method. In the future we will investigate the removal of the unwanted twin-image in cases where the depth-of-focus of the scene is too large to be segmented using a single plane. We intend to extend the work by modifying our algorithm to include our depth segmentation approach which will remove the unwanted twin-image at multiple planes increasing the approaches

accuracy.

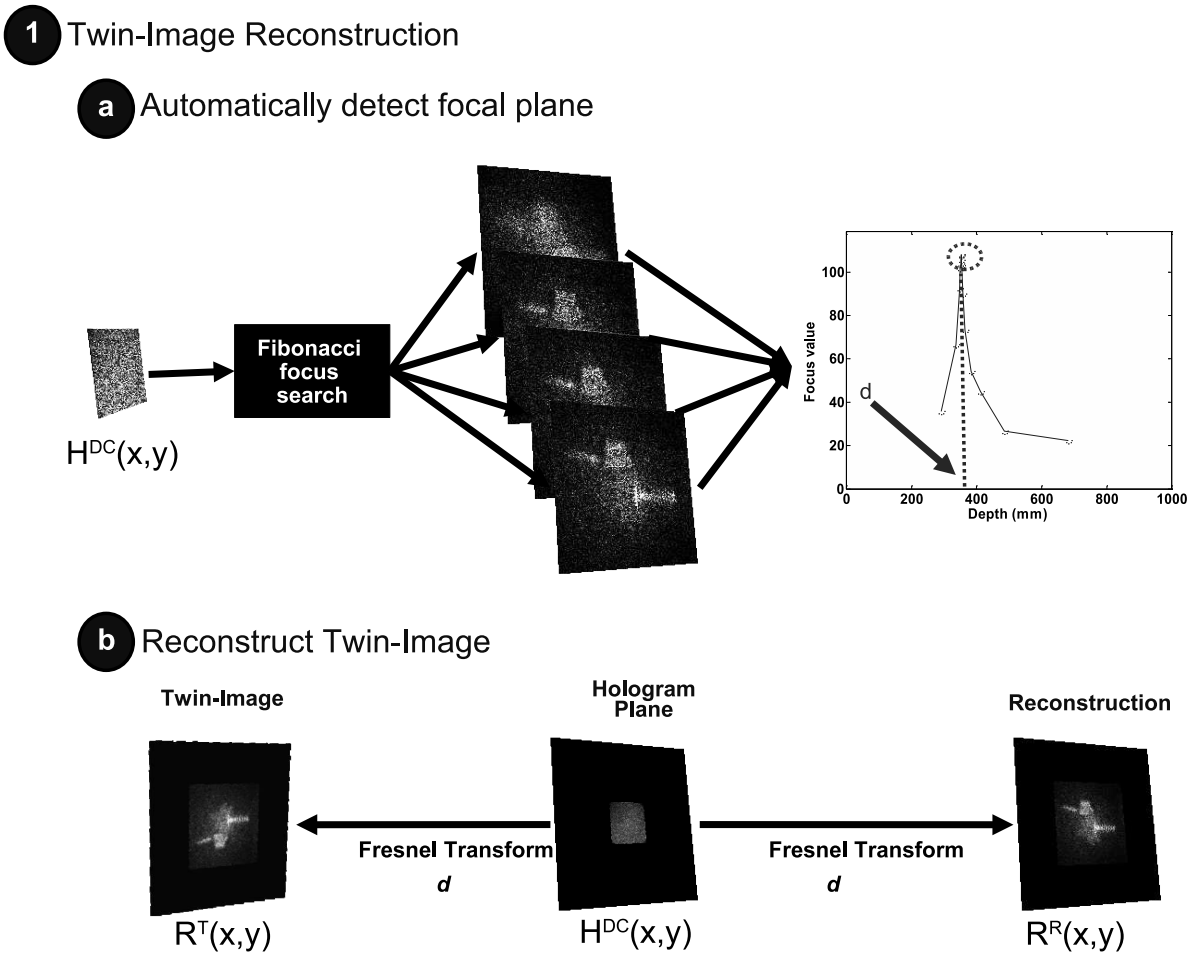

Figure 6.3: Algorithm Stage 1: Twin-image reconstruction, (a) autofocus and (b) numerical reconstruction.

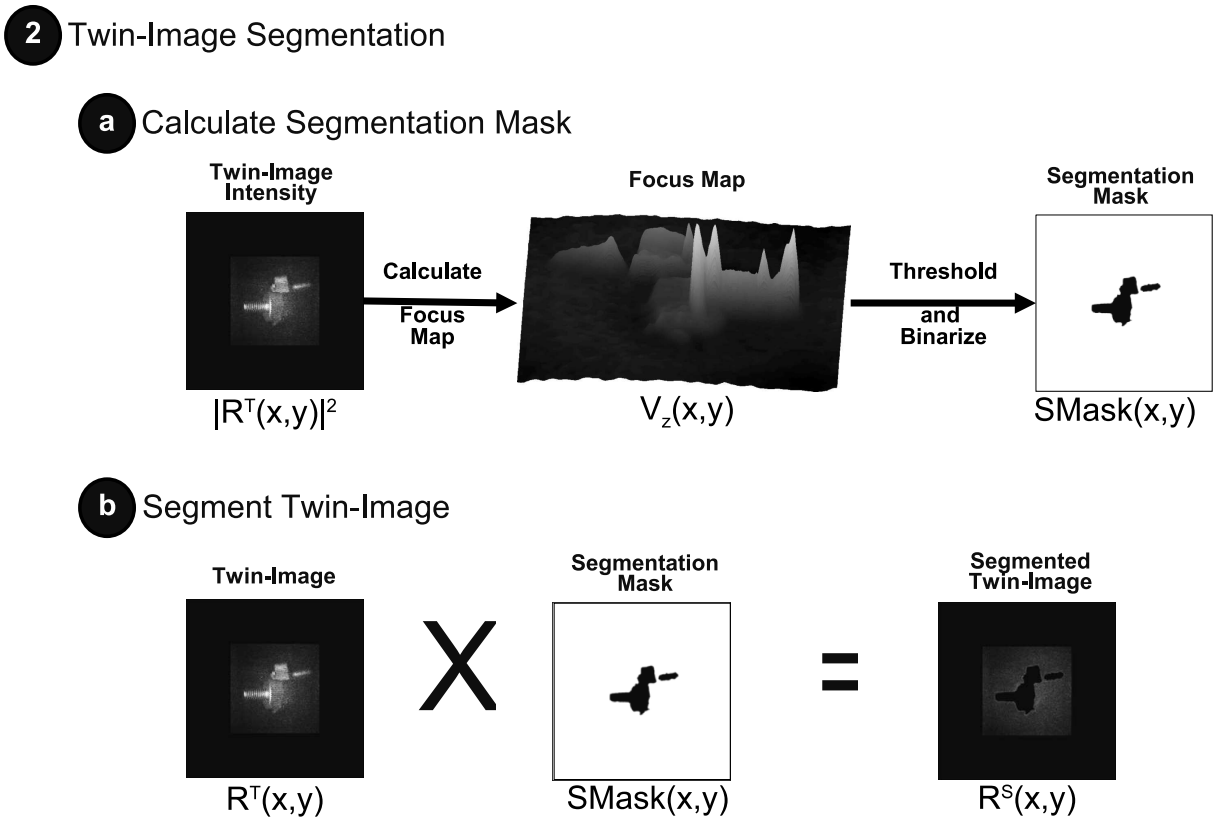

Figure 6.4: Algorithm Stage 2: Twin-Image Segmentation, (a) calculate segmentation mask and (b) segment twin-image.

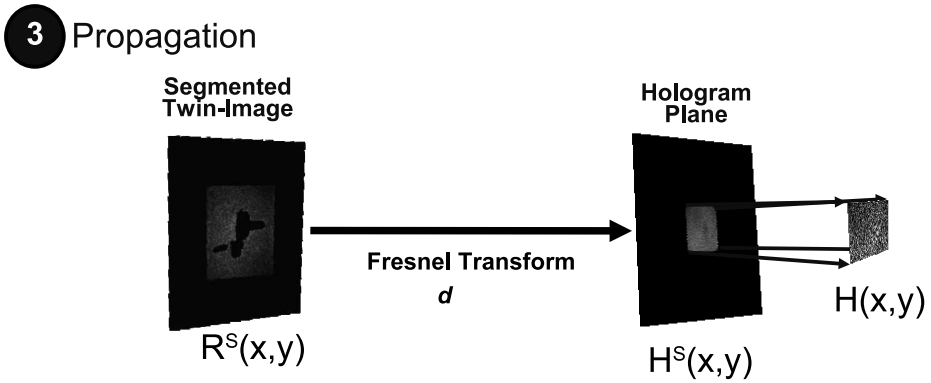

Figure 6.5: Algorithm Stage 3: Propagate the segmented twin-image to the hologram plane.

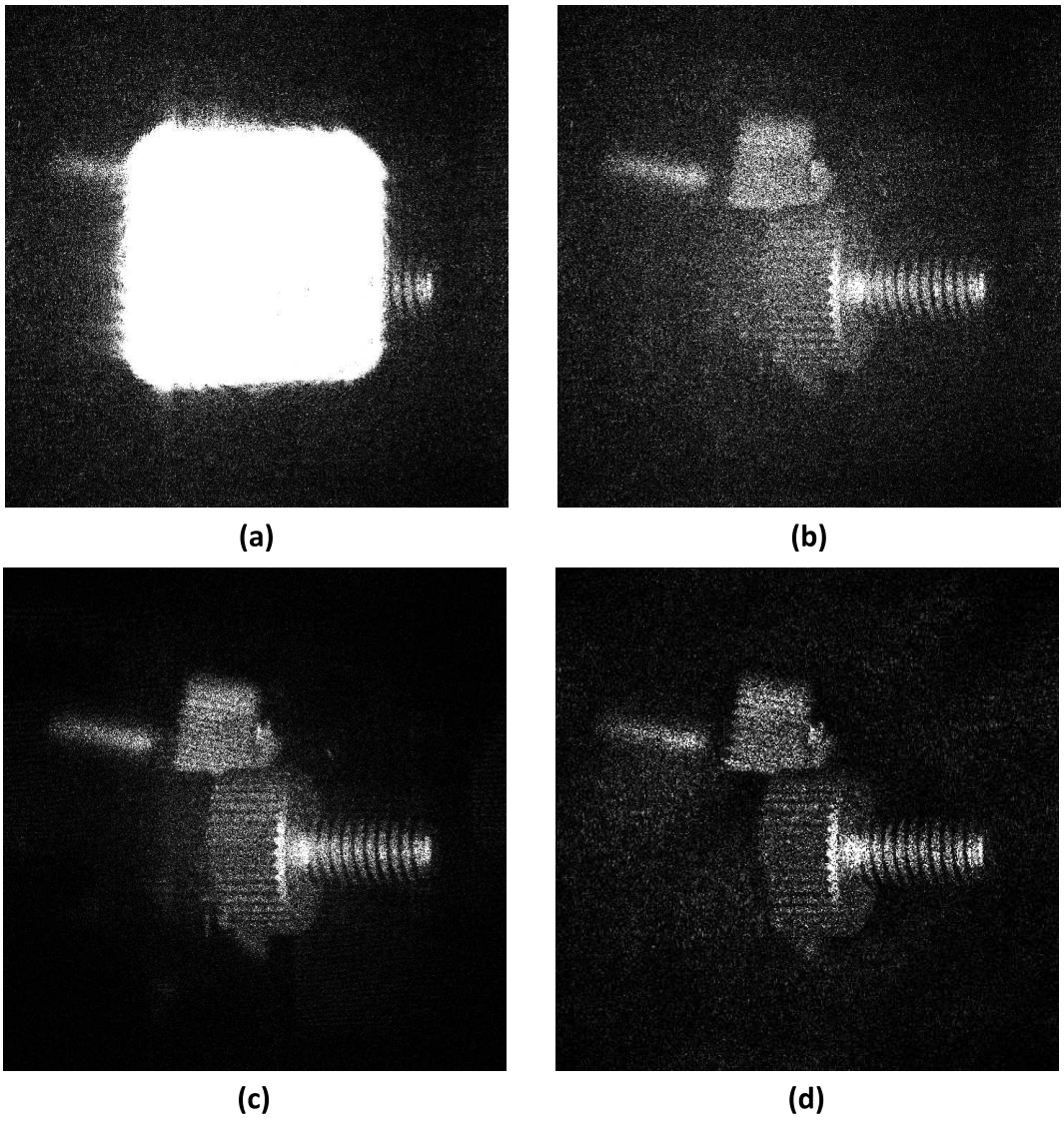

Figure 6.6: Numerical reconstructions of two bolts hologram, reconstruction of hologram after(a) no processing, (b) DC-term suppression, (c) DC-term suppression and automated twin-image removal and (d) reconstuction of PSI hologram.

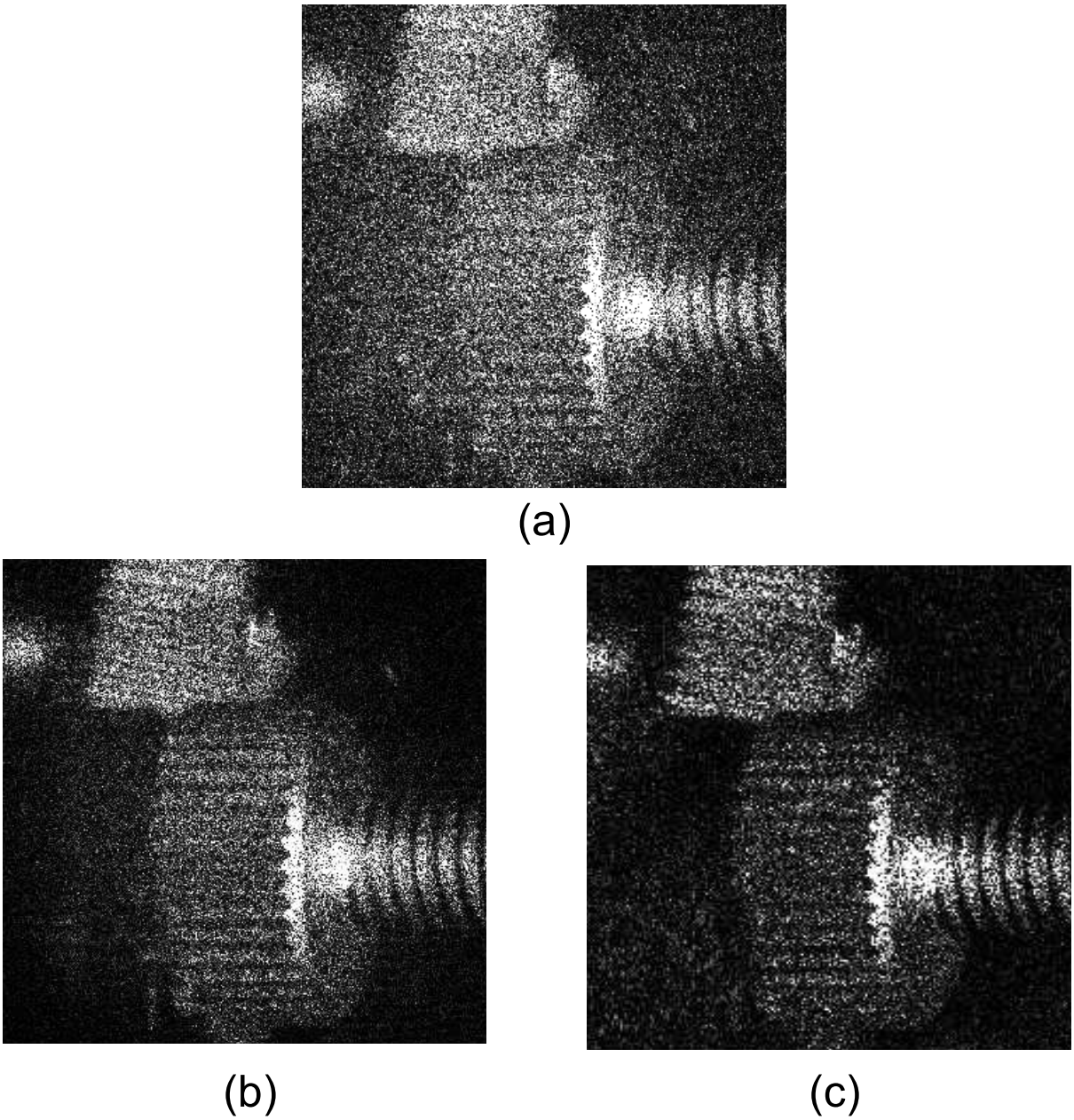

Figure 6.7: Zoomed in numerical reconstructions of two bolts hologram, reconstruction of hologram after (a) DC-term suppression, (b) DC-term suppression and automated twin-image removal and (c) reconstuction of PSI hologram.

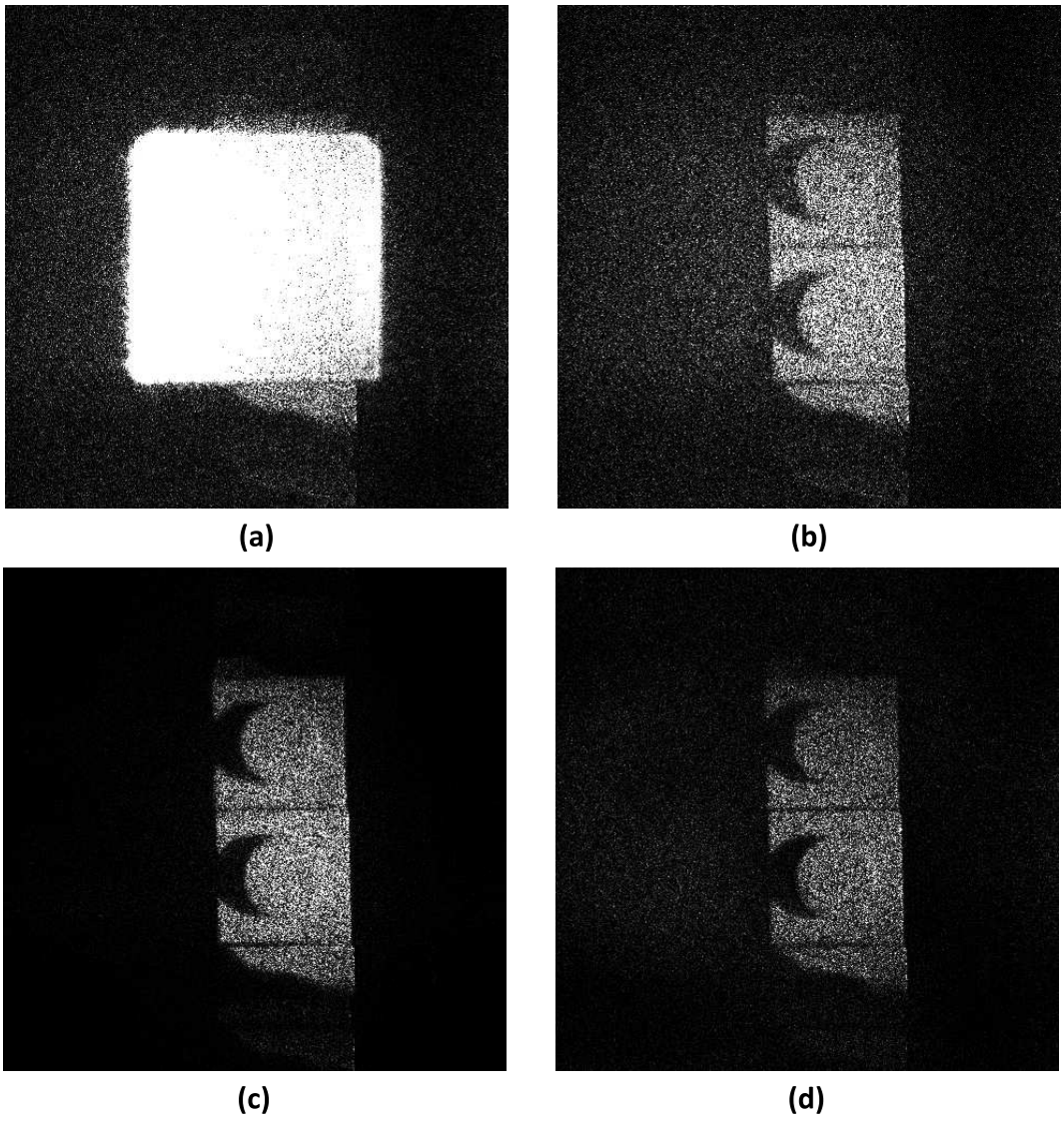

Figure 6.8: Numerical reconstructions of Lego hologram, reconstruction of hologram after(a) no processing, (b) DC-term suppression, (c) DC-term suppression and automated twin-image removal and (d) reconstuction of PSI hologram.

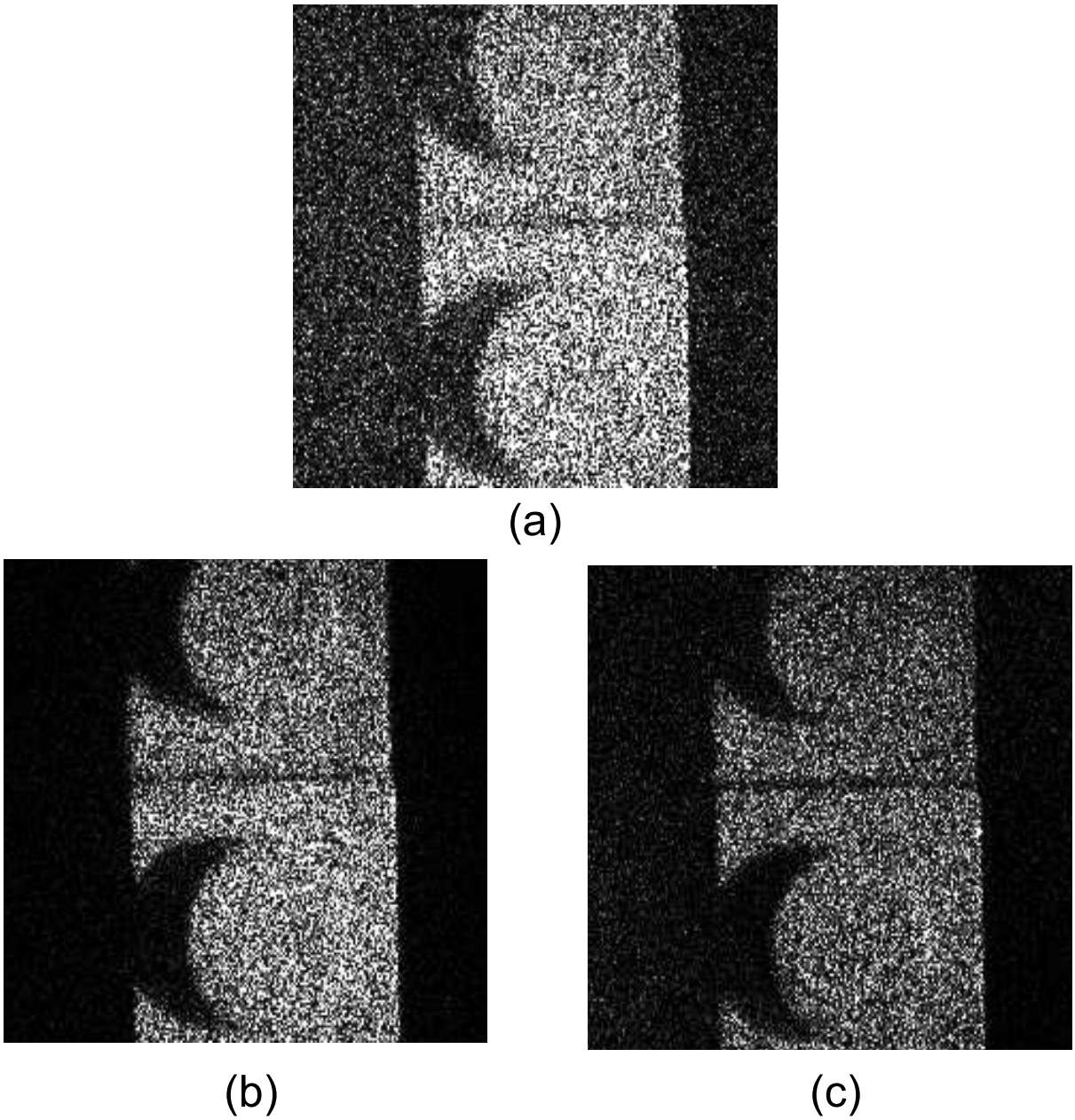

Figure 6.9: Zoomed in numerical reconstructions of screws hologram, reconstruction of hologram after (a) DC-term suppression, (b) DC-term suppression and automated twin-image removal and (c) reconstuction of PSI hologram.

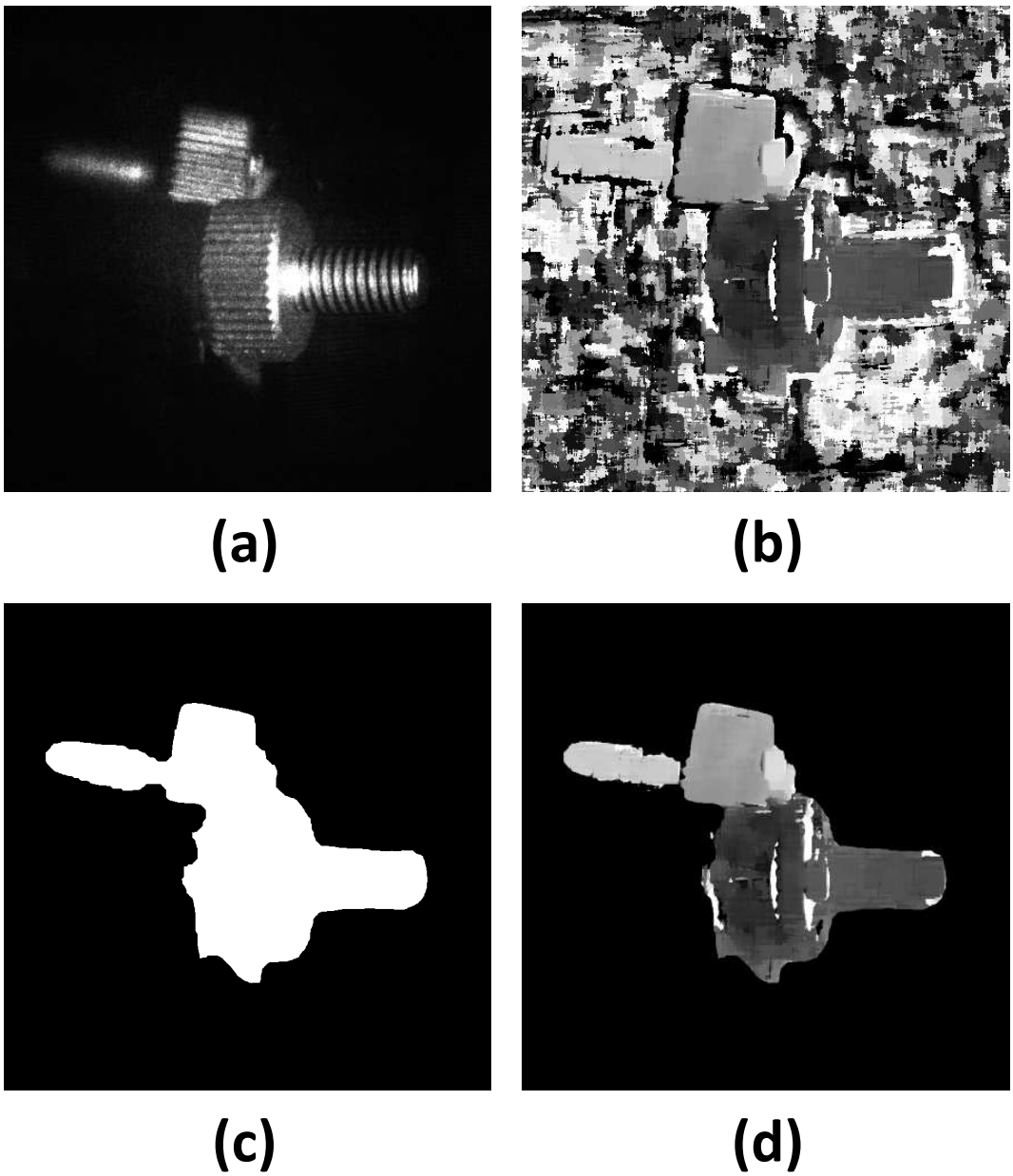

Figure 6.10: Two bolts object single interferogram, (a) numerical reconstruction, (b) depth map, (c) segmentation mask and (d) segmented depth map.

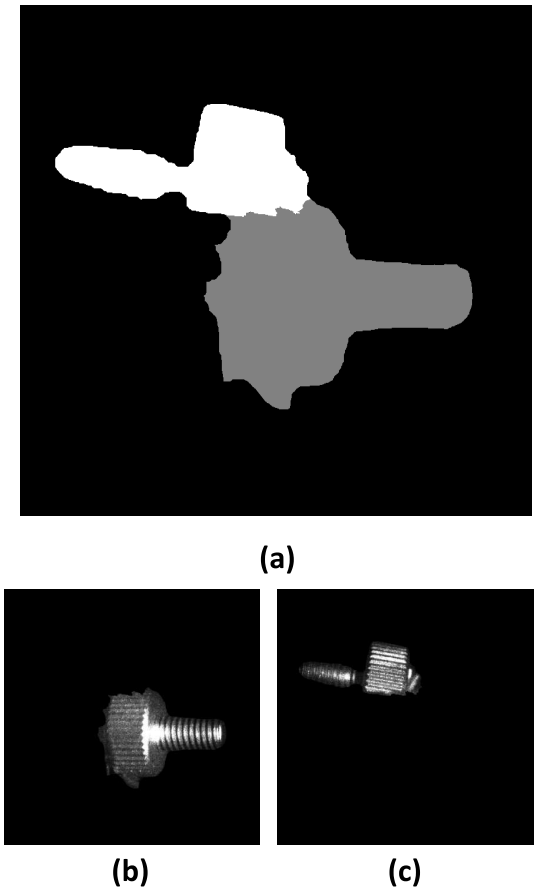

Figure 6.11: Two bolts object single interferogram segmented into two regions: (a) depth segmentation mask, (b) in-focus reconstruction of segment 1, (c) in-focus reconstruction of segment 2.

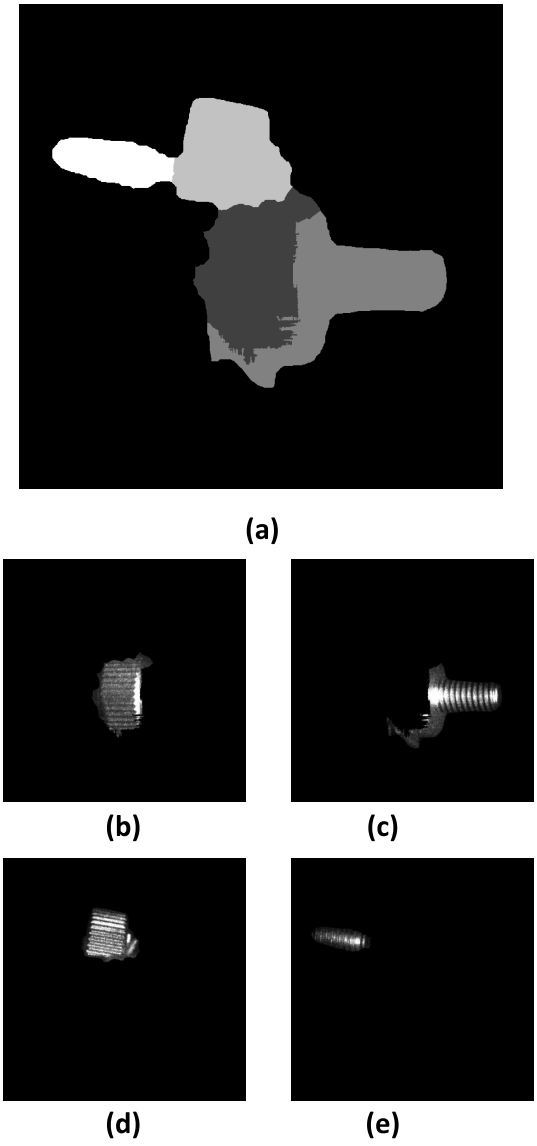

Figure 6.12: Two bolts object single interferogram segmented into two regions: (a) depth segmentation mask, (b) in-focus reconstruction of segment 1, (c) in-focus reconstruction of segment 2, (d) in-focus reconstruction of segment 2 and (e) in-focus reconstruction of segment 2.

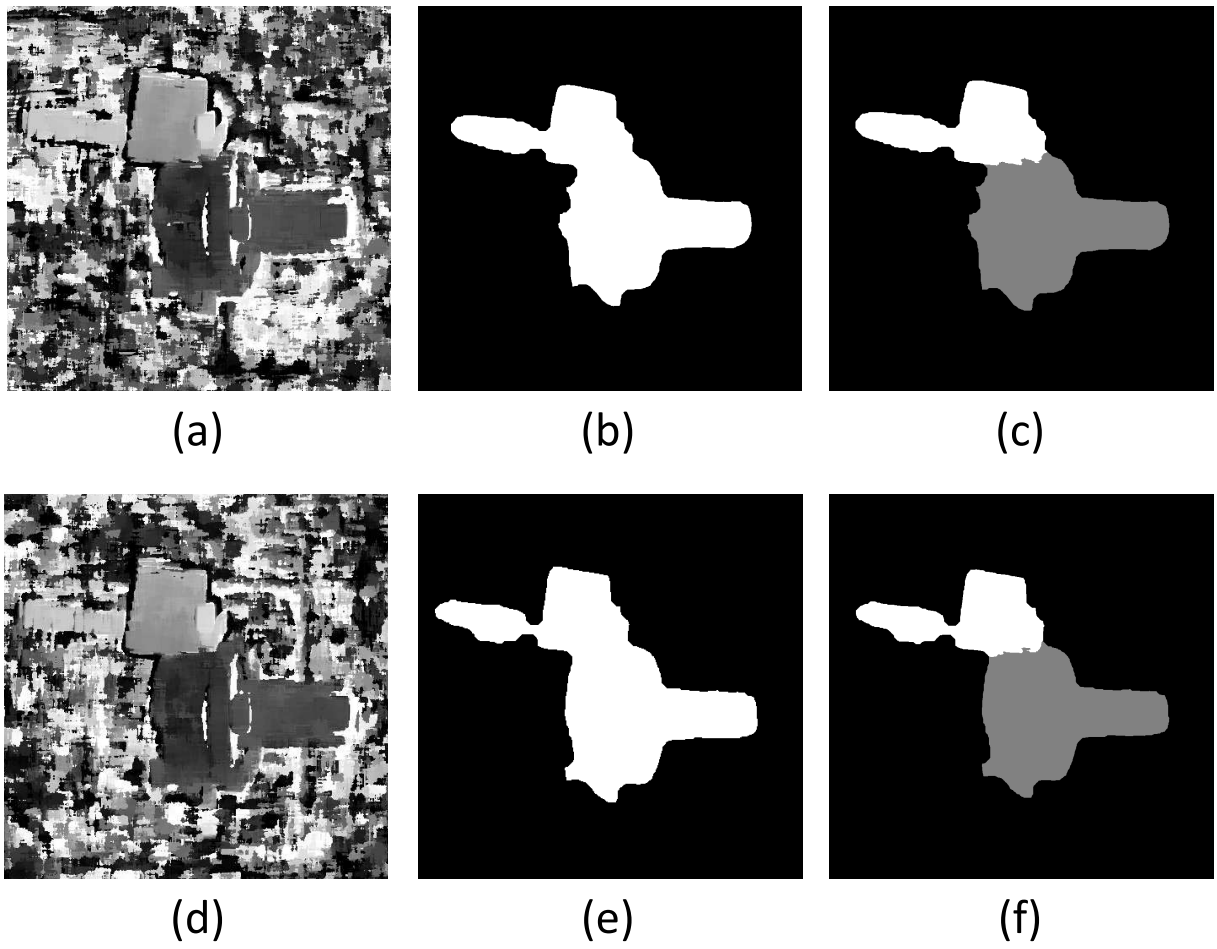

Figure 6.13: Two bolts object DH: (a) depth map, (b) segmentation mask, (c) depth segmentation mask for single inteferogram and (d) depth map, (e) segmentation mask, (f) depth segmentation mask for PSI DH.

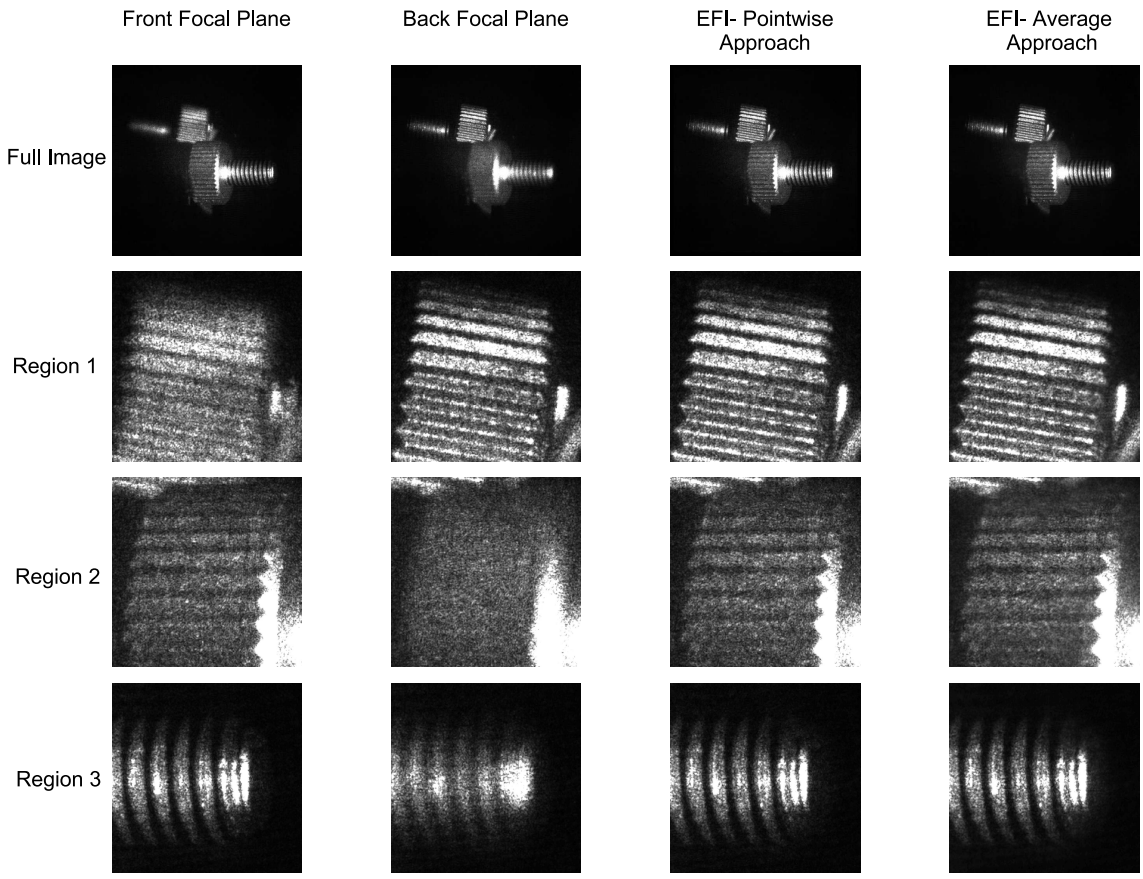

Figure 6.14: Two bolts block object single interferogram, reconstructions and the overlapping approach EFIs.

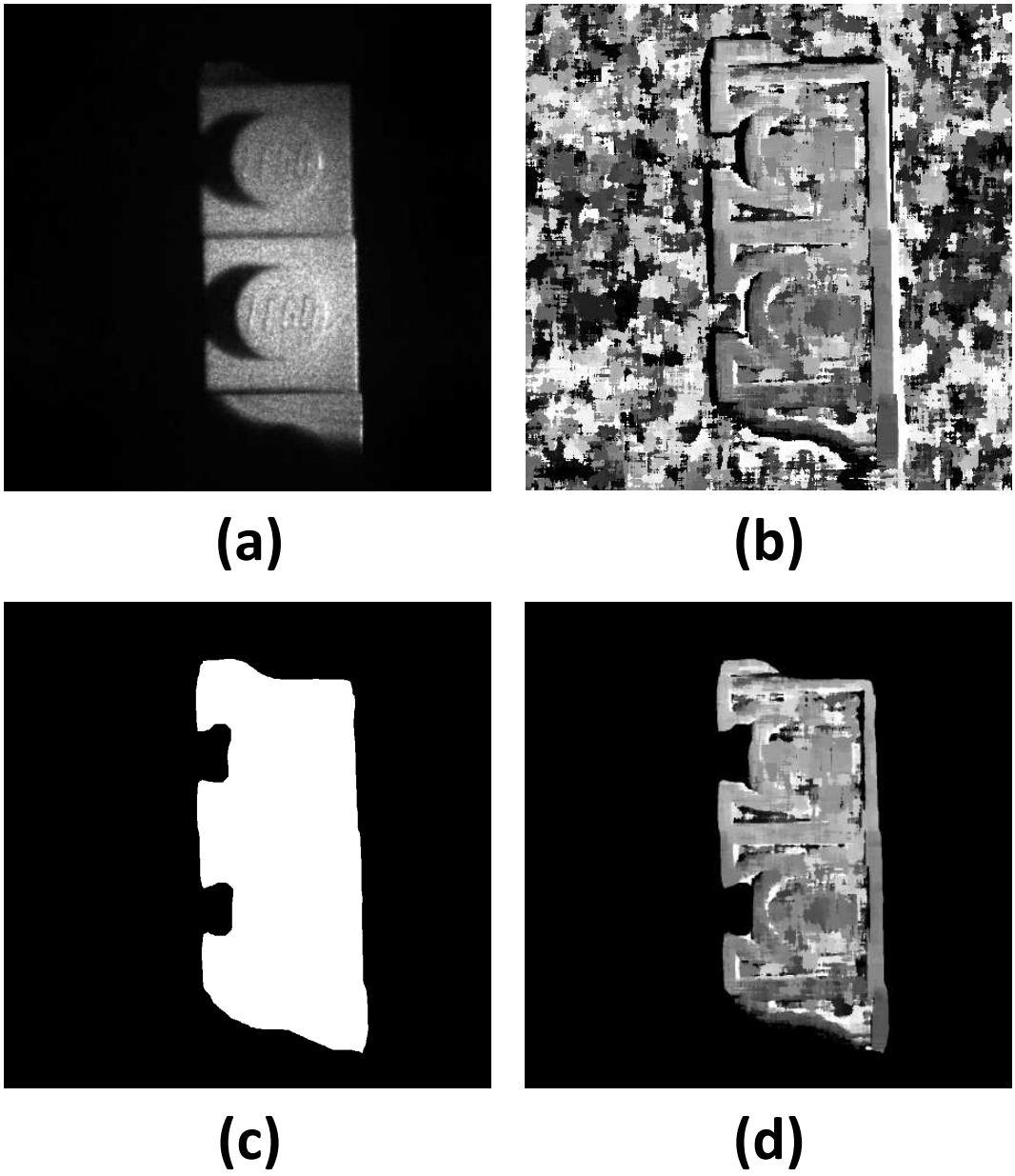

Figure 6.15: Lego block object single interferogram, (a) numerical reconstruction, (b) depth map, (c) segmentation mask and (d) segmented depth map.

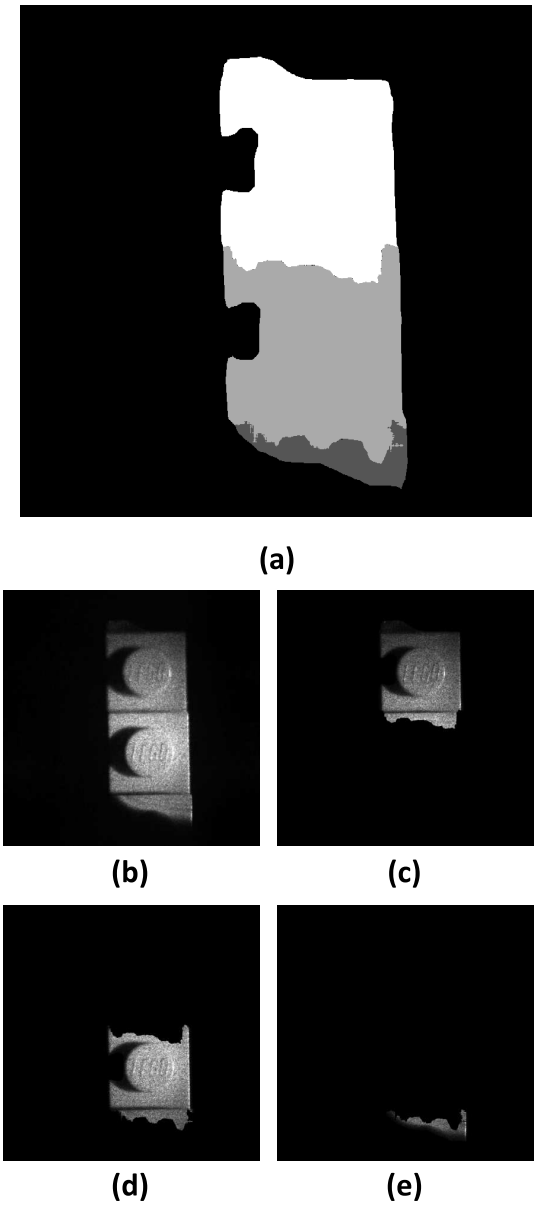

Figure 6.16: Lego object single interferogram segmented into three regions: (a) depth segmentation mask, (b) in-focus reconstruction of full object, (c) in-focus reconstruction of segment 1, (d) in-focus reconstruction of segment 2, (e) in-focus reconstruction of segment 3.

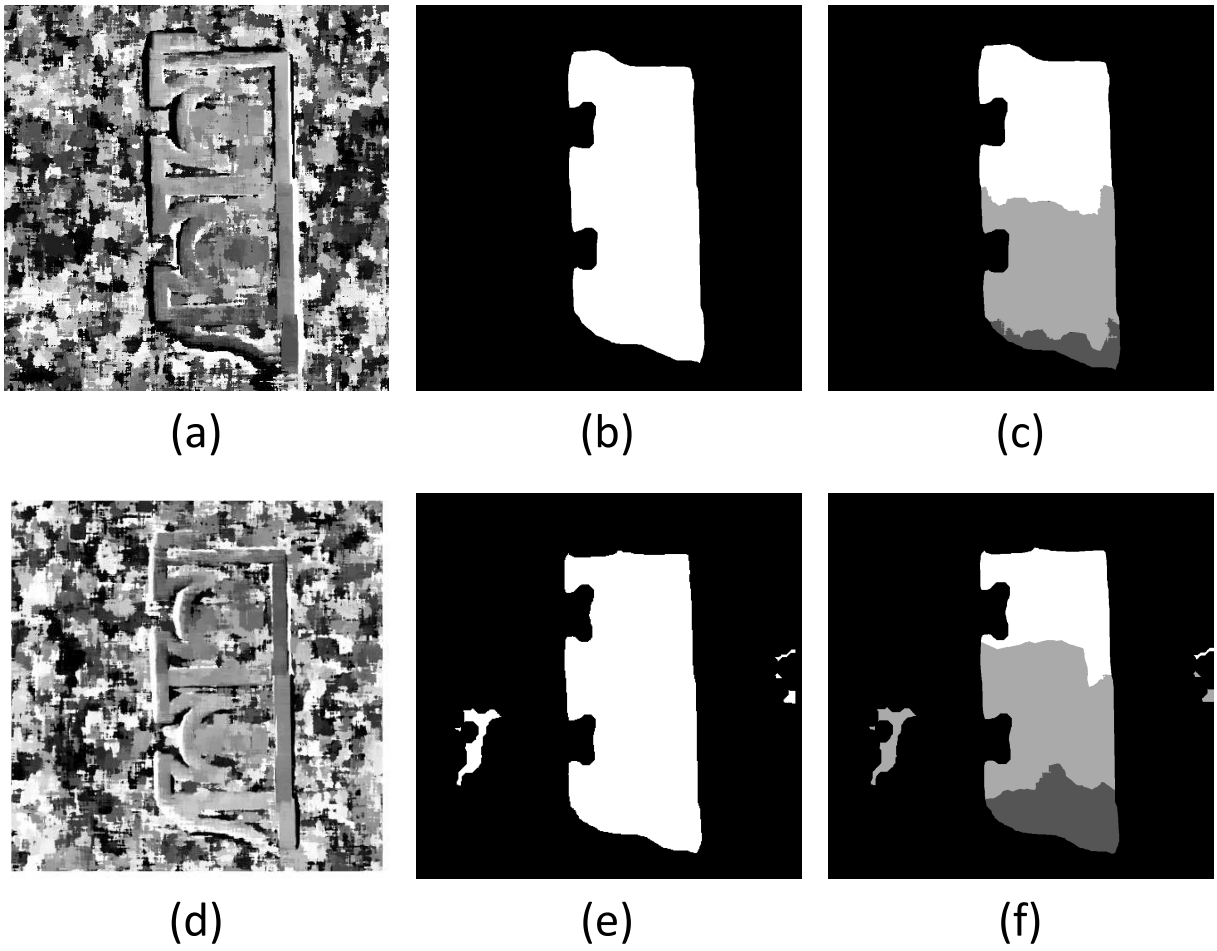

Figure 6.17: Lego object DH: (a) depth map, (b) segmentation mask, (c) depth segmentation mask for single inteferogram and (d) depth map, (e) segmentation mask, (f) depth segmentation mask for PSI DH.

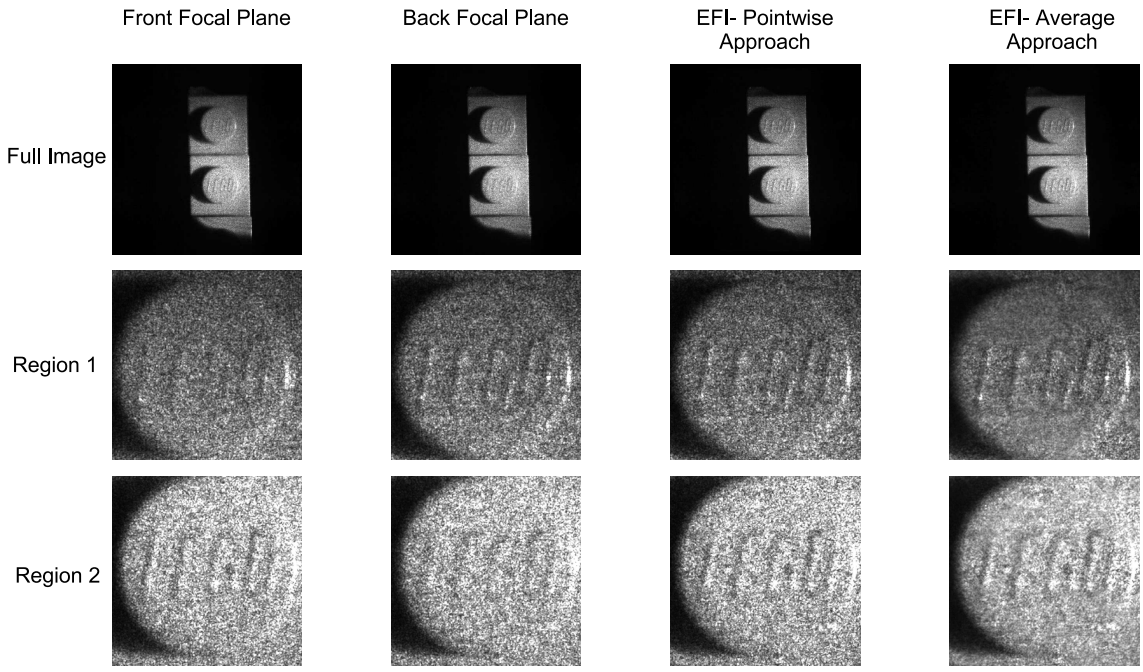

Figure 6.18: Lego block object single interferogram, reconstructions and the overlapping approach EFIs.

Chapter 7

Conclusions

This thesis details the authors' contributions to the field of DHIP. A review of the relevant work carried out in the fields of digital holography and DHIP has been presented. We introduced the three stages of digital holography: recording, noise removal and reconstructing. These were discussed in detail with particular emphasis on highlighting the advantages and limitations of the different recording architectures and reconstruction methods. This concluded our discussion of the most relevant and important background information required to understand our work. We then proceed to present and examine our four contributions to the field of DHIP: focus detection algorithms, segmentation algorithms, extended focused imaging and twin-image removal

7.1 Focus detection algorithms

The estimation of the focal plane of an object or object region is required for many applications in digital holography such as object recognition, object tracking, depth estimation and segmentation. In Chapter 3 we showed that the focal plane of an object encoded in a DH can be recovered by applying a focus measure to the intensity information from a digital holographic reconstruction. Using this information we have developed and discussed a novel autofocus algorithm which given a DH and a search range accurately determines the focal plane of a the digital hologram. We developed an optimised termination condition for digital holography based on the depth-of-focus of the reconstruction function used and employed variance as our focus measure. Our algorithm was successfully applied to two of our single-capture DHs, these holograms were selected as one contained a high-contrast and high-textured object while the other contained a low-contrast and low-textured object. This demonstrated our algorithms applicability to DHs containing macroscopic objects. However, our autofocus algorithm can be used with any focus measure or reconstruction function making it applicable to all forms of digital holography.

Our second contribution to focus detection is our DFF algorithm which estimates the depth of regions in a DH. It returns a depth map and maximum focus map which are used in all the other contributions in the thesis. The algorithm requires a number of parameters to be input and we discussed the impact of the four key ones in detail: block size, overlapping or non-overlapping, speckle reduction and reconstruction interval. We noted that the choice of

block size is reliant on the desired trade-off between the estimation of the depth of local features or the global shape of the object and can have a significant impact on our other algorithms, in particular segmentation. Again the decision to employ the overlapping or non-overlapping algorithm comes down to a trade-off decision: resolution or speed. The non-overlapping algorithm is significantly faster but the low-resolution of the depth map and maximum focus map inhibit their use in the segmentation algorithms. Speckle reduction is an optional step, it is applied before a reconstruction is processed with the focus measure. We maintain that in macroscopic digital holography, speckle is a noise source in the estimation of depth. We verified this by comparing depth maps created with and without speckle reduction. In both the overlapping and non-overlapping case, the noise in the depth map was less when speckle reduction was applied. Finally we demonstrated that selecting the reconstruction interval based on the depth-of-focus of the reconstruction function results in the qualitatively best depth maps. We provided examples of depth maps of multiple DHs containing different textured and contrasted objects.

7.2 Segmentation algorithms

Segmentation is an integral part of most object recognition, counting and tracking applications. Our background segmentation algorithm requires a focus map and a threshold value to decide what parts of the reconstruction are background and what parts are object. We found that a high variance in the focus map corresponds to an object region while a low variance equates

to a background region. The threshold selection is manual as it depends on the intensity and contrast of the object encoded in the DH, although we have found that it lies between 0.1 and 0.3 for DHs recorded with our experimental setup. The accuracy of the segmentation mask can be improved upon through the use of the erosion operator. By comparing the output segmentation masks to ground-truth data we quantitatively determined the best block size for background segmentation and also show that for all block sizes thresholding the multi-reconstruction maximum focus map outperforms thresholding a single-reconstruction focus map. Our segmentation was applied to multiple DHs demonstrating its general applicability.

If the objects in a DH are not spatially separated, a method for differentiating between them after the background has been removed is needed. Using a depth map and a segmentation mask we have developed a depth segmentation algorithm. The desired number of segments in the scene is input and we manually select the largest modes from the histogram of the depth map. Each mode is assigned an index and the pixels belonging to that mode are assigned the modes index. Any remaining unlabeled pixels are then assigned an index based on their proximity to each segments boundary. We have one optional step which we have developed to suppress error. Any continuous regions whose area is below a reasonable threshold are unlabeled and are then reassigned to the segment they are closest to. We show again that selecting the correct reconstruction interval is important and that selecting a reconstruction interval below the depth-of-focus of the reconstruction function has no benefit. Depth segmentation is demonstrated on multiple different DHs.

7.3 Extended focused imaging

Digital holographic reconstructions have a limited depth-of-focus. DHs where the depth of the object(s) is a factor greater than the depth-of-focus of the reconstruction leads to object regions appearing blurred and out-of-focus. We have developed three approaches for creating an image where all object regions are in-focus. The first approach uses a low-resolution non-overlapping depth map and creates an EFI in a relatively fast time. The use of a low-resolution non-overlapping depth map makes this approach prone to some error. Secondly, our pointwise approach employs the high-resolution overlapping depth map to create an EFI which is less prone to error but in a significantly slower time. Finally, we developed the neighbourhood approach which uses a high-resolution overlapping depth map and through a neigbourhood averaging operation suppresses error and can create an EFI where object regions appear sharper. The choice of neighbourhood is directly linked to the block size input to DFF. In the DFF algorithm an $n \times n$ block is transformed into an individual depth value. We can then reverse this transformation in the EFI process to average pixel intensity values and suppress error. We demonstrated our EFI algorithm on multiple DHs with the most significant result being an increase in DOF from 0.5mm to 56mm.

7.4 Twin-image removal

The single biggest issue with in-line DHs is the presence of the twin-image. It has a serious corruptive effect on the reconstruction quality. PSI is a

technique which removes the unwanted twin from the DH but requires the recording of multiple DHs. This forces the object to be static during recording. We have developed a method for removing the unwanted twin from a single capture DH allowing one to record dynamic objects using in-line digital holography. Our method removes the complex distribution of the unwanted twin when it is contained within the fewest pixels, at its focal plane. This requires us to do three things: find its focal plane, pad the DH to ensure that none of the wanted twins information is wrapped in the area marked for removal and remove the unwanted twin through segmentation. We apply our autofocus algorithm to find the focal plane of the unwanted twin. We derived the equations required to determine the number of samples required in the hologram plane to ensure that the object signal is not wrapped within the reconstruction window and we employ our background segmentation algorithm to remove the unwanted twin. For speed we segment using a single reconstruction but intend to examine whether segmenting using the maximum focus map and subsequently using a depth segmentation mask to segment the unwanted twin in multiple planes results in a higher quality DH. We believe that our twin-image removal approach is generally applicable and is not restricted by the wavelength of the light used to record the hologram. We also applied our DFF, segmentation and EFI algorithms to two single capture DHs which had the unwanted twin-image removed. The results were comparable to those achieved with PSI DHs. This summarises the contributions in this thesis. In the following chapter we detail future work.

Chapter 8

Work in progress

In this chapter, we present some of the research directions that are enabled by the work in this thesis. This includes novel ideas, extensions to the work outlined in this thesis and improvements to current algorithms.

Fast DFF using Fibonacci search

We use a simple linear search in our DFF algorithm to find the depth of an object region. The Fibonacci search is a more efficient option for searching but implementing it in a block processing algorithm is not trivial. We intend to investigate if it is feasible to re-write our DFF algorithm to use the Fibonacci search.

Twin-image removal using depth segmentation

To date we segment the twin-image in one plane and then remove it. What if the twin-image has a large depth of field, i.e the scene has

two objects in it separated by 40mm? We will try and develop code which replaces the single plane segmentation currently employed with our multi-plane DFF segmentation. This will allow us to create a depth segmentation mask and segment different objects in different planes.

Detection of focal plane for unwrapping phase in DHM

To successfully unwrap phase in DHM, you need to be at the in-focal plane of the object. However, if there are multiple objects which are again separated in space it may be necessary to unwrap their phase values in different planes. Using DFF and the autofocus code it should be achievable to automatically determine what planes to unwrap and what values belong to which plane.

Depth map error compensation through focus plot analysis and correction

Currently depth is estimated as the depth which returns the largest focus value. However, it has been shown that this can return incorrect depth estimates. By analysing a focus plot, we can extract the locations of all the peaks. We can then extract their heights and widths. It is expected that focus plots should have a relative large height with a narrow width. With this in mind we expect to "correct" the estimation of depth values for object regions.

Automated depth segmentation

Our depth segmentation algorithm takes in as input the number of segments required and also requires the manual selection of the modes from the histogram of the depth map. We expect to be able to automate this using two methods. Firstly, using our peak analysis which we are developing, we expect to be able to determine the number of peaks in the histogram, their relative width and height. With this information we should be able to convert this information into "modes" and automate the depth segmentation process.

Using DFF for hologram edge detection

Focus metrics in image processing are based on the identification of sharpness in images or image blocks. The metric we employ is similar to finding the block with the highest spatial frequency in the Fourier domain. Therefore, in-focus blocks containing edges will return a higher value than in-focus blocks containing curved surfaces due to a larger quantity of high frequency content in the block. This knowledge can be used to edge detect a reconstruction volume. The reconstruction volume is the set of reconstructions from a single perspective of a DH used to create the depth map. By thresholding the maximum variance map using two values α, β where $0 > \alpha < \beta \leq 1$ we can identify edges. If we select $\beta = 1$ and an α separated by a small amount we can find the strongest edges. Through reducing α and β by a uniform amount we can "scan" the maximum variance map for weaker edges

until we can identify no more edges. Combining the identified weaker and stronger edges we can create an edge map of the reconstruction volume. By pointwise multiplication of the binary edge map with our depth map we can create a edge map in 2.5D. The algorithm will also use thresholding to moderate the strength of the edges in the outputted edge map.

Multi-resolution depth maps

By calculating depths maps of the same DH using multiple different block sizes we have information about the focus of large and small regions in the DH. Larger block sizes create depth maps that contain information about the gross structure of the scene with low error, while smaller block sizes can give us fine object detail but contain large amounts of error. We intend to investigate a method for combining depth maps of the same DH created using different block sizes to increase the accuracy of our depth maps. This work would then be used to speed up DFF by first creating low resolution depth maps. Then sections of the depth map could be refined. The decision on which sections should be refined could be made based on the maximum variance of these sections.

Appendix A

Mathematics preliminaries

In this section we discuss preliminary mathematics that are important to the work in this thesis. We begin by introducing convolution, the Fourier transform and sampling. Undersampling is then briefly demonstrated and the Fresnel transform and two of it's discretisations are introduced.

A.1 Convolution

The application of a filter to a signal is called convolution. In one-dimension it can be defined in the spatial domain as

$$g(x) = \int_{-\infty}^{\infty} m(\tau)n(x-\tau)d\tau \tag{A.1}$$

where $m(x)$ is the input signal, $n(x)$ is the filter and $g(x)$ is the convolution of n with m. This equation is more commonly written as

$$g = m * n. \tag{A.2}$$

where $*$ denotes convolution. The three main properties of convolution are that it is symmetric

$$(m * n) = (n * m), \tag{A.3}$$

that it is associative

$$(g * (m * n)) = ((g * m) * n), \tag{A.4}$$

and that it is distributive

$$g * (m + n) = (g * m) + (g * n). \tag{A.5}$$

These properties are true for both one- and two-dimensional convolution. We have introduced convolution because it is integral to sampling, but before we can move onto sampling we need to describe the Fourier transform.

A.2 1D Fourier Transform

The Fourier transform is a transformation that maps a complex-valued input signal, $m(x)$, from the spatial domain to the spatial frequency domain. In

one-dimension it is defined as

$$F(m(x)) = M(k) = \int_{-\infty}^{\infty} m(x) \exp^{-i2\pi kx}\, dx. \tag{A.6}$$

This transform is complex valued and is also lossless, which means that the original signal $f(x)$ can be recovered using the inverse Fourier transform

$$F^{-1}(M(k)) = m(x) = \frac{1}{2\pi} \int_{-\infty}^{\infty} M(k) \exp^{i2\pi kx}\, dk. \tag{A.7}$$

The Fourier transform has a number of properties and amongst these are two that are useful for this thesis, linearity

$$F(am(x) + bn(x)) = aF(m(x)) + bF(n(x)) = aM(k) + bN(k), \tag{A.8}$$

and the convolution theorem

$$m(x) * n(x) = F^{-1}(M(k) \times N(k)), \tag{A.9}$$

$$m \times n = F^{-1}(M(k) * N(k). \tag{A.10}$$

The convolution theorem is very useful as it equates multiplication in the Fourier domain with convolution in the spatial domain and vice-versa. This theorem is especially helpful in sampling.

A.3 Sampling

A sampled signal, m_s, is described as the product of the original signal, $m(x)$, with a shah function, $s_{x_0}(x)$

$$m_s(x) = m(x) \times s_{x_0}(x), \tag{A.11}$$

where the shah function is a train of delta functions with the distance between the delta functions being spaced by x_0

$$s_{x_0}(x) = \sum_{n=-\infty}^{\infty} \delta(x - nx_0). \tag{A.12}$$

The convolution theorem allows Eq. (A.11) to be rewritten as the convolution of the Fourier transform of the original signal with the Fourier transform of the shah function

$$M_s(k) = M(k) * S_{x_0}(k), \tag{A.13}$$

$$m_s(x) = F^{-1}(M(k) * S_{x_0}(k)). \tag{A.14}$$

It is important to note that the convolution of a signal with a delta function shifts the signal

$$m(x) * \delta(x - a) = m(x - a). \tag{A.15}$$

Now considering a shah function is a train of delta functions, this means that $M_s(k)$ is the sum of an infinite set of shifted versions of the Fourier transforms of the original signal $m(x)$. To be able to correctly reconstruct the

original signal, for $m_s(x)$ to be representative of $m(x)$, these shifted versions or " Fourier copies" must not overlap. If they do overlap, the signal can not be recovered correctly and errors such as aliasing occur. The distance between the centres of these copies in the Fourier domain is controlled by the sampling rate of $m(x)$, the x_0 in $s_{x_0}(x)$, and is $\frac{1}{x_0}$ which is known as the sampling frequency. Claude Shannon discovered in 1949 that

"A signal can be reconstructed from its samples without loss of information, if the original signal has no frequencies above $\frac{1}{2}$ the sampling frequency."

This theorem states that the maximum frequency in $M(k)$ must be less than or equal to half the sampling frequency or

$$\max(M(k)) \leq \frac{1}{2x_0}. \tag{A.16}$$

To demonstrate the effect of sampling and of undersampling we create some simple examples. In the first example we calculate a discrete cosine wave with a period of 16

$$\cos(2\pi * 16 * x) \tag{A.17}$$

where the range is always $-0.5 < x < 0.5$ but with three different sampling frequencies. We know that the Fourier transform of this wave is 2 peaks located a distance of ± 16 (the period) from the centre of the x-axis, and this is what we need to be able to extract from the Fourier domain to reconstruct the signal. We calculate the discrete Fourier transform (DFT) on the three

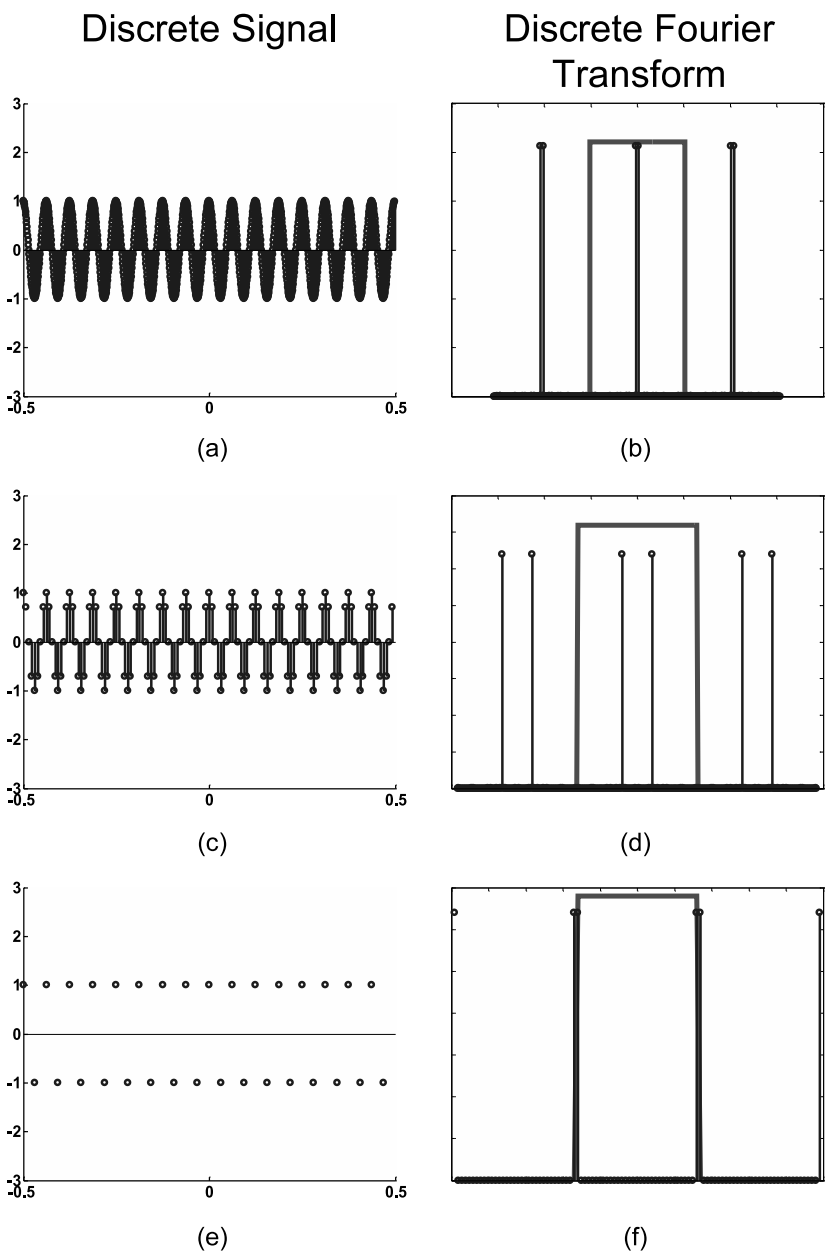

Figure A.1: Sampling a cosine wave, sampled (a) 1024 times, (c) 128 times, (e) 32 times and their DFT's (b),(d),(f) respectively.

signals to visually demonstrate the effect of different sampling frequencies. The DFT in one-dimension can be calculated by

$$M(k) = \sum_{\infty}^{n=-\infty} m(nx_0)e^{-i2\pi knx_0}. \tag{A.18}$$

The results are shown in Fig. A.1 where in part (a) of this figure we sample the cosine wave at 64 samples per period or a sampling frequency of $\frac{1}{x_0} = 1024$ and with the maximum frequency in this signal being 16, this is a well sampled signal. This is apparent from Fig. A.1(b), the DFT of the signal, where the "Fourier copies" have been separated by $\frac{1}{x_0}$ and it is easy to extract one of the "Fourier copies" with multiplication of $M_s(k)$ by a rect function such as

$$R(k) = x_0 Rect(kx_0) = \begin{cases} x_0, & \text{if } |k| < \frac{1}{2x_0} \\ 0, & \text{otherwise.} \end{cases} \tag{A.19}$$

The calculated rect function for each of the three sampled signals is highlighted in Fig. A.1(b),(d) and (f). In Fig. A.1(c) we sample the cosine wave at 8 samples per period or a sampling frequency of 128 which is again a well sampled signal. Figure A.1(d) demonstrates that the three "Fourier copies" are well separated, a distance of 128 between their centres, and that through $M_s(k) \times R(k)$ we can extract the signal. In the final row of the figure we sample the cosine wave at 2 samples per period, as shown in Fig. A.1(e), this is a sampling frequency of 32 and is the twice the maximum frequency in the signal which is the lowest sampling frequency as in this case $\text{Max}(M_s(k)) = \frac{1}{2x_0}$. This is apparent from Fig. A.1(f) where the "Fourier copies" are as close as

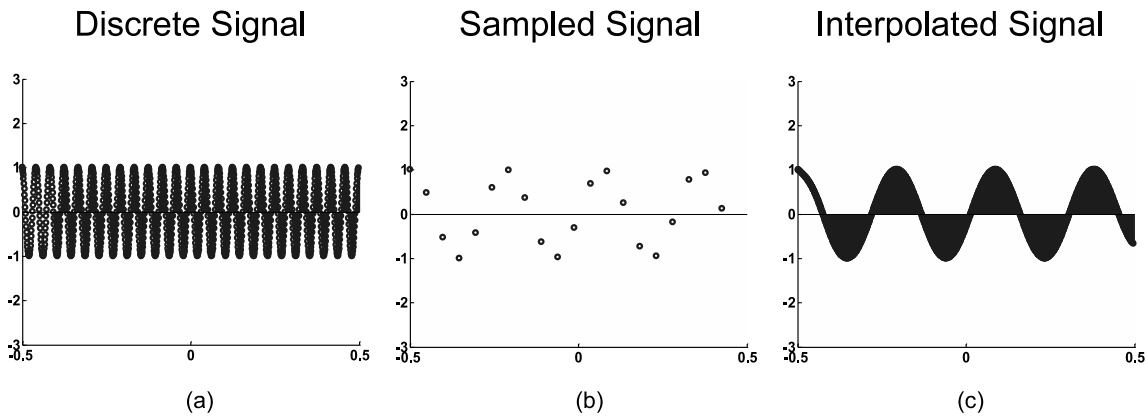

Figure A.2: Undersampling a cosine wave, the cosine wave with a period of 24 sampled (a) 1024 times, (b) 20 times and the signal displayed in (b) interpolated to 1024 samples.

they can get without overlapping and the rect function can just extract one individual copy. Due to the limitations of using discrete systems to model the effects of discretising a continuous signal we cannot demonstrate the effects of undersampling in the Fourier domain.

In Fig. A.2 we attempt to demonstrate some of the effects of undersampling by using interpolation. In the Fig. A.2(a) we have computed a discrete cosine wave with a period of 24 over a range of $-0.5 < x < 0.5$ with 1024 samples. This means the maximum frequency of this signal is 24. We then sampled this signal at a sampling frequency of 20, as displayed in Fig. A.2(b), which means that we are sampling at less than half the rate required. By interpolating the signal back to the original number of samples, 1024, we can see the impact of the undersampling, in Fig. A.2(c). The period of the wave has changed from 24 to 4 and it has changed from a cosine wave to a sine wave. This is an extreme example but undersampling can have dramatic

effects to the output sampled signal.

A.4 2D Fourier Transform

In this thesis we are working with two-dimensional signals, and so need the two-dimensional (2D) Fourier transform. In the continuous case it is described by

$$F(m(x,y)) = M(k,l) = \int\int_{-\infty}^{\infty} g(x,y) \exp\left[-i2\pi(kx+ly)\right], \tag{A.20}$$

and in the discrete case it is described by

$$F(k,l) = \sum_{m=0}^{M-1}\sum_{n=0}^{N-1} I(m,n) \exp\left[-\frac{2\pi ikm}{M}\right] \exp\left[-\frac{2\pi iln}{N}\right] \tag{A.21}$$
$$k = 0, ..., M-1 \quad l = 0, ..., N-1.$$

We primarily use the 2D DFT in the propagation of wavefronts, a subject dealt with in detail in Chapter 2, and to compare the function of variance to the DFT as a focus measure, as described in Chapter 3.

A.5 Numerical Propagation

The Fresnel transform is a transformation that maps a complex wavefront representing an optical wavefront from one spatial plane to another as displayed in Fig. A.3. In this figure we have an illuminated aperture located in the $(\epsilon, \eta, z = 0)$ plane. The Fresnel transform is used to calculate the

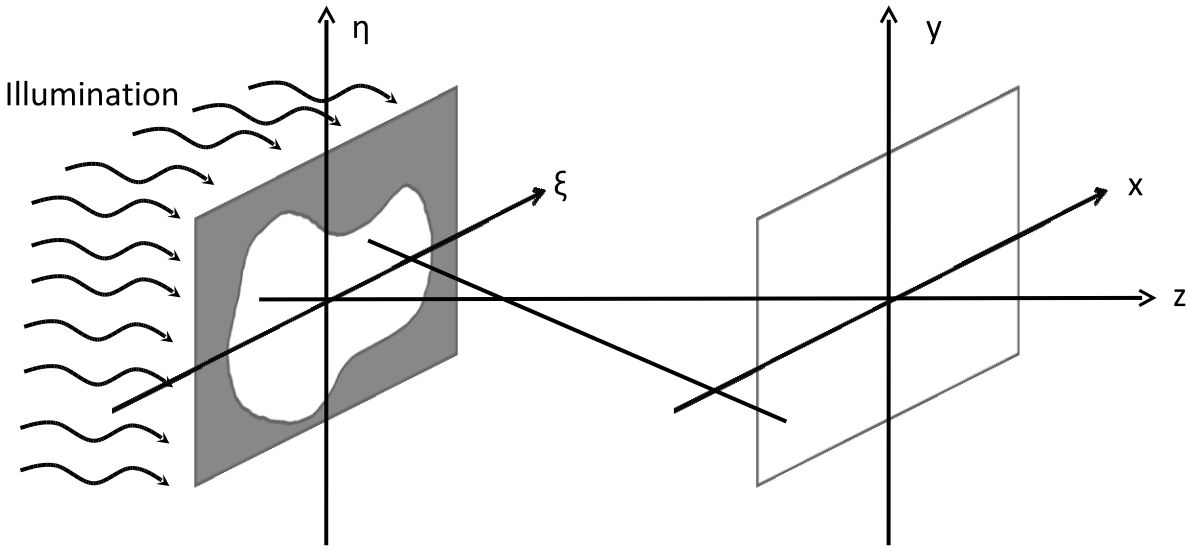

Figure A.3: Geometry for the Fresnel approximation, from Kreis "Handbook of holographic interferometry" 2005 [Kre05].

diffracted field in the (x, y, z) plane with

$$U_z(x,y) = \frac{\exp^{i\frac{\pi}{\lambda z}(x^2+y^2)}}{i\lambda z} \int\int_{\infty}^{-\infty} H_0(\epsilon,\eta) \exp\left[j\frac{\pi}{\lambda z}(\epsilon^2+\eta^2)\right] \exp\left[-j\frac{2\pi}{\lambda z}(x\epsilon+y\eta)\right]. \tag{A.22}$$

We have implemented and applied two discretisations of the Fresnel transform to carry out the work in this thesis, the discrete Fresnel transform and the propagation transfer function.

The discrete Fresnel transform (DFRT) can be calculated directly by

$$U_z(m'\delta\xi', n'\delta\eta') = \exp\left[-\frac{i\pi}{\lambda d}\left(m'^2\delta\xi'^2 + n'^2\delta\eta'^2\right)\right] \times \sum_{m=0}^{N_x-1}\sum_{n=0}^{N_y-1} H(m\delta\xi, n\delta\eta) \times \exp\left[-\frac{i\pi}{\lambda d}\left(m^2\delta\xi^2 + n^2\delta\eta^2\right)\right] \times \exp\left[-i2\pi\left(\frac{m'm}{N_x} + \frac{n'n}{N_y}\right)\right] \tag{A.23}$$

where (m, n) and (m', n') are the discrete coordinates in the CCD plane and image plane respectively and $(\delta\xi, \delta\eta)$ and $(\delta\xi', \delta\eta')$ are the spatial resolutions at the CCD plane and the image plane respectively. N_x and N_y are the number of samples in the horizontal and vertical directions and λ is the wavelength of the light. After propagation by the DFRT the spatial resolution at the image plane is a function of the CCD parameters, the wavelength of the light (λ) and the distance (d) from the object to the CCD. The DFRT is based on the use of the DFT, and makes the assumption that the following two exponents are equivalent,

$$\exp\left(\frac{j2\pi nm}{N_x}\right) = \exp\left(\frac{j2\pi n\delta\xi m\delta\xi'}{\lambda z}\right). \tag{A.24}$$

If we are to find out what the spatial resolution will be at the image plane $z$mm away from the CCD we need to resolve this equation with respect to

$\delta\xi'$ by

$$\frac{j2\pi nm}{N_x} = \frac{j2\pi n\delta\xi m\delta\xi'}{\lambda z} \tag{A.25}$$

$$\frac{1}{N_x} = \frac{\delta\xi\delta\xi'}{\lambda z} \tag{A.26}$$

$$\frac{\lambda z}{N_x} = \delta\xi\delta\xi' \tag{A.27}$$

$$\frac{\lambda z}{N_x\delta\xi} = \delta\xi' \tag{A.28}$$

$$\delta\xi' = \frac{\lambda z}{N_x\delta\xi}. \tag{A.29}$$

The spatial resolution in the y-direction is calculated by

$$\delta\eta' = \frac{\lambda z}{N_y\delta\eta}. \tag{A.30}$$

This means that $(\delta\xi', \delta\eta')$ changes with the reconstruction distance which in turn means that Eq. (A.23) is not reciprocal. The focal range for a reconstruction using Eqn. (A.23) is in the range $[\text{dof}_d^i, \text{dof}_d^j]$ where dof_d^i and dof_d^j are defined by [Kre05]:

$$\text{dof}_d^i = d\left(\frac{1}{1+\frac{d\lambda}{N^2\delta\xi^2}}\right), \quad \text{dof}_d^j = d\left(\frac{1}{1-\frac{d\lambda}{N^2\delta\xi^2}}\right), \tag{A.31}$$

where λ is the wavelength of the light, d is the propagation distance, N is the number of pixels in the CCD and $\delta\xi$ is the spatial resolution in the CCD plane. These are the parameters that determine the depth-of-focus of the reconstructed images.

An alternative to the discretisation of the Fresnel transform is the prop-

agation transfer function (PTF) defined by [Kre05, FNM+06]

$$U_z(m'\delta\xi', n'\delta\eta') = \mathcal{F}^{-1}\left[\mathcal{F}\left(H(m\delta\xi, n\delta\eta)\right) \times \exp\left[-i\lambda\pi d\left(\frac{u}{(\delta\xi N_x)^2} + \frac{v}{(\delta\eta N_y)^2}\right)\right]\right] \tag{A.32}$$

where $\mathcal{F}$ is the fast Fourier transform and u and v are the discrete spatial frequencies. With this function the spatial resolution in the object plane is the same as the spatial resolution in the CCD plane, $\delta\xi = \delta\xi'$. Another relevant property is the focal range for a reconstruction using this Fresnel discretisation which we define in the range of $[\mathrm{dof}_d^i, \mathrm{dof}_d^j]$ [Kre05]

$$\mathrm{dof}_d^i = d\left(\frac{N}{N+1}\right), \qquad \mathrm{dof}_d^j = d\left(\frac{N}{N-1}\right), \tag{A.33}$$

Unlike the DFRT, this function is reciprocal so that if one propagates from $H(x, y)$ a distance of 300mm to $U_{300}(x, y)$ and then from $U_{300}(x, y)$ a distance of -300mm to $H'(x, y)$, one has the same complex distribution that was started with i.e. $H(x, y) = H'(x, y)$. The advantages and disadvantages of using these two discretisations is discussed in Chapter 2.3

Bibliography

[ACN+05] D. Alfieri, G. Coppola, S. D. Nicola, P. Ferraro, A. Finizio, G. Pierattini, and B. Javidi. Method for superposing reconstructed images from digital holograms of the same object recorded at different distance and wavelength. *Optics Communications*, 260:113–116, 2005.

[ACYD08] M. Antkowiak, N. Callens, C. Yourassowsky, and F. Dubois. Extended focused imaging of a microparticle field with digital holographic microscopy. *Optics Letters*, 33:1626–1628, 2008.

[AMHN08] L. Ahrenberg, C.P. McElhinney, B.M. Hennelly, and T.J. Naughton. Parallel approaches to reconstruction and noise reduction in digital holography. *ICO Topical Meeting on Optoinformatics/Information Photonics, St. Petersburg*, 2008.

[APH+09] L. Ahrenberg, A.J. Page, B.M. Hennelly, J.B. McDonald, and T.J. Naughton. Using commodity graphics hardware for real-time digital hologram view reconstruction. *Journal of Display Technology*, 5, 2009.

[ARS05] J.F. Arocena, T.A. Rothwell, and M.R.A. Shegelski. Iterative reconstruction of in-line electron holograms. *Micron*, 36:23–30, 2005.

[Bat00] C.F. Batten. Autofocusing and astigmatism correction in the scanning electron microscope. Master's thesis, University of Cambridge, 2000.

[BFRJ04] N. Bertaux, Y. Frauel, P. Réfrégier, and B. Javidi. Speckle removal using a maximum-likelihood technique with isoline gray-level regularization. *Journal of the Optical Society of America: A*, 21:2283–2291, 2004.

[BHG+74] J.H. Bruning, D.R. Herriott, J.E. Gallagher, D.P. Rosenfeld, A.D. White, and D.J. Brangaccio. Digital wavefront measuring interferometer for testing optical surfaces and lenses. *Applied Optics*, 13:2693–2703, 1974.

[BL66] B.R. Brown and A.W. Lohmann. Complex spatial filtering with binary masks. *Applied Optics*, 5:967–969, 1966.

[BL68] O. Bryngdahl and A. Lohmann. Single-sideband holography. *Journal of the Optical Society of America*, 58:620–624, 1968.

[BOKJ06] T. Baumbach, W. Osten, C. Kopylow, and W. Jüptner. Remote metrology by comparitive digital holography. *Applied Optics*, 45:925–934, 2006.

[Bov93] V.M. Bove. Entropy-based depth from focus. *Journal of the Optical Society of America: A*, 10:561–566, 1993.

[BR51] W.L. Bragg and G.L. Roger. Elimination of the unwanted image in diffraction microscopy. *Nature (London)*, 167:190–191, 1951.

[BSS05] A. Bartesaghi, G. Sapiro, and S. Subramaniam. An energy-based three-dimensional segmentation approach for quantitative interpretation of electron tomograms. *IEEE Transactions on Image Processing*, 14:1314–1323, 2005.

[BW07] N. Burns and J. Watson. Data extraction from underwater holograms of marine organisms. *Proc. IEEE*, page 1, 2007.

[Cau79] H.J. Caulfield. *Handbook of Optical Holography.* Academic Press, New York, 1979.

[CBD99] E. Cuche, F. Bevilacqua, and C. Depeursinge. Digital holography for quantitative phase-contrast imaging. *Optics Letters*, 24:291–293, 1999.

[CCD+02] T. Colomb, E. Cuche, P. Dahlgen, A. Marian, F. Montfort, C. Depeursinge, P. Marquet, and P. Magistretti. 3D imaging of surfaces and cells by numerical reconstruction of wavefronts in digital holography applied to transmission and reflection microscopy. *Proc. IEEE - International Symposium on Biomedical Imaging*, pages 773–776, 2002.

[CLKC07] G.-L. Chen, C.-Y. Lin, M.-K. Kuo, and C.-C. Chang. Numerical suppression of zero-order image in digital holography. *Optics Express*, 15:8851–8856, 2007.

[CMD99] E. Cuche, P. Marquet, and C. Depeursinge. Simultaneous amplitude-contrast and quantitative phase-contrast microscopy by numerical reconstruction of fresnel off-axis holograms. *Applied Optics*, 38:6994–7001, 1999.

[CMD00] E. Cuche, P. Marquet, and C. Depeursinge. Spatial filtering for zero-order and twin-image elimination in digital off-axis holography. *Applied Optics*, 39:4070–4075, 2000.

[Cro84] F.C. Crow. Summed-area tables for texture mapping. *SIGGRAPH Computer Graphics*, 18:207–212, 1984.

[DFFD05] L. Denis, C. Fournier, T. Fournel, and C. Ducottet. Twin-image noise reduction by phase retrieval in in-line digital holography. *Proc. SPIE*, 5914:59140J–1, 2005.

[DJ06] M. DaneshPanah and B. Javidi. Segmentation of 3d holographic images using bivariate jointly distributed region snake. *Optics Express*, 14:5143–5153, 2006.

[DJ07] C.M. Do and B. Javidi. Multifocus holographic 3-d image fusion using independent component analysis. *Journal of Display Technology*, 3:326–332, 2007.

[DJT66] J.B. DeVelis, G.B. Parrent Jr., and B.J. Thompson. Image reconstruction with fraunhofer holograms. *Journal of the Optical Society of America*, 56:423–427, 1966.

[DMS03] N. Demoli, J. Mestrovic, and I. Sovica. Subtraction digital holography. *Applied Optics*, 42:798–804, 2003.

[DS06a] E. Darakis and J.J. Soraghan. Compression of interference patterns with application to phase-shifting digital holography. *Applied Optics*, 45:2437–2433, 2006.

[DS06b] E. Darakis and J.J. Soraghan. Use of fresnelets for phase-shifting digital hologram compression. *IEEE Transactions on Image Processing*, 15:3804–3811, 2006.

[DS07] E. Darakis and J.J. Soraghan. Reconstruction domain compression of phase-shifting digital holograms. *Applied Optics*, 46:351–356, 2007.

[DSCY06] F. Dubois, C. Schockaert, N. Callens, and C. Yourassowsky. Focus plane detection criteria in digital holography microscopy. *Optics Express*, 14:5895–5908, 2006.

[DW88] T. Darrell and K. Wohn. Pyramid based depth from focus. *IEEE Computer Society Conference on Computer Vision and Pattern Recognition*, pages 504–509, 1988.

[EL91] J. Ens and P. Lawrence. An investigation of methods for determining depth from focus. *IEEE Computer Society Conference*

on Computer Vision and Pattern Recognition, pages 600–606, 1991.

[EL93] J. Ens and P. Lawrence. An investigation of methods for determining depth from focus. *IEEE Transactions on Pattern Analysis and Machine Intelligence*, 15:97–108, 1993.

[Faw06] T. Fawcett. An introduction to roc analysis. *Pattern Recognition Letters*, 27:861–874, 2006.

[FCA+04] P. Ferraro, G. Coppola, D. Alfieri, S. D. Nicola, A. Finizio, and G. Pierattinni. Controlling images parameters in the reconstruction process of digital holograms. *IEEE Journal of Selected Topics in Quantum Electronics*, 16:829–839, 2004.

[FCN+03] P. Ferraro, G. Coppola, S. D. Nicola, A. Finizio, and G. Peirattini. Digital holographic microscope with automatic focus tracking by detecting sample displacement in real time. *Optics Letters*, 28:1257–1259, 2003.

[Fer60] D. Ferguson. Fibonaccian searching. *Communications of the ACM*, 3:648, 1960.

[FGA+05] P. Ferraro, S. Grilli, D. Alfieri, S. D. Nicola, A. Finizio, G. Pierattini, B. Javidi, and and V. Striano G. Coppola. Extended focused image in microscopy by digital holography. *Optics Express*, 13:6738–6749, 2005.

[Fie78] J.R. Fienup. Reconstruction of an object from the modulus of its fourier transform. *Optics Letters*, 3:27–29, 1978.

[Fie97] J.R. Fienup. Invariant error metrics for image reconstruction. *Applied Optics*, 36:8352–8357, 1997.

[FNC+04] P. Ferraro, S. D. Nicola, G. Coppola, A. Finizio, D. Alfieri, and G. Pierattini. Controlling image size as a function of distance and wavelength in fresnel-transform reconstruction of digital holograms. *Optics Letters*, 29:854–856, 2004.

[FNM+06] Y. Frauel, T.J. Naughton, O. Matoba, E. Tajahuerce, and B. Javidi. Three-dimensional imaging and processing using computational holographic imaging. *Proceedings of the IEEE, Special Issue on 3-D Technologies for Imaging and Display*, 94:636–653, March 2006.

[FP03] D.A. Forsyth and J. Ponce. *Computer Vision: A Modern Approach*. Prentice Hall, third edition, 2003.

[FPO07] Y. Fu, G. Pedrini, and W. Osten. Vibration measurement by temporal fourier analyses of a digital hologram sequence. *Applied Optics*, 46:5719–5727, 2007.

[FTHH07] S. Frey, A. Thelen, S. Hirsch, and P. Hering. Generation of digital textured surface models from hologram recordings. *Applied Optics*, 46:1986–1993, 2007.

[Gab48] D. Gabor. A new microscope principle. *Nature (London)*, 161:77–79, 1948.

[GK89] J. Gillespie and R. King. The use of self entropy as a focus measure in digital holography. *Pattern Recognition Letters*, 9:19–25, 1989.

[GL67] J.W. Goodman and R.W. Lawrence. Digital image formation from electronically detected holograms. *Applied Physics Letters*, 11:777–778, 1967.

[GMH+08] U. Gopinathan, D.S. Monaghan, B.M. Hennelly, C.P. McElhinney, D.P. Kelly, J.B. McDonald, T.J. Naughton, and J.T. Sheridan. A projection system for real world three-dimensional objects using spatial light modulators. *Journal of Display Technology*, 4(2):254–261, June 2008.

[Goo05] J. Goodman. *Introduction to Fourier Optics*. Roberts and Company, Englewood, Colorado, 2005.

[GS72] R.W. Gerchberg and W.O. Saxton. A practical algorithm for the determination of phase from image and diffraction plane pictures. *Optik*, 35:227–246, 1972.

[GS04] M. Gustafsson and M. Sebesta. Refractometry of microscopic objects with digital holography. *Applied Optics*, 43:4796–4801, 2004.

[GSFP05] J. Garcia-Sucerquia, J.A.J. Famirez, and D.V. Prieto. Reduction of speckle noise in digital holography by using digital image processing. *Optik*, 116:44–48, 2005.

[Har02] P. Hariharan. *Basics of Holography*. Cambridge University Press, 2002.

[HFS03] M Hernandez, A.F. Frangi, and G. Sapiro. Three-dimensional segmentation of brain aneurysms in cta using non-parametric region-based information and implicit deformable models: Method and evaluation. *MICCAI*, 2879:594–602, 2003.

[HJ07] W. Huang and X. Jing. Evaluation of focus measures in multi-focus image fusion. *Pattern Recognition Letters*, 28:493–500, 2007.

[HK84] G. Häusler and E. Körner. Simple focusing criterion. *Applied Optics*, 23:2468–2469, 1984.

[HL80] G. Haussmann and W. Lauterborn. Determination of size and position of fast moving gas bubbles in liquids by digital 3-d image processing of hologram reconstructions. *Applied Optics*, 19:3529–3535, 1980.

[HLR+00] P.R. Hobson, R.S. Lampitt, A. Rogerson, J. Watson, X. Fang, and E.P. Krantz. Three-dimensional spatial coordinates of individual plankton determined using underwater hologrammetry. *Limnology and Oceanography*, 45:1167–1174, 2000.

[HMF+06] B.M. Hennelly, C.P. McElhinney, Y. Frauel, T.J. Naughton, and J.B. McDonald. Superposition of digital holograms. *Information Optics: 5th International Workshop, Toledo*, pages 281–289, 5^{th}-7^{th} June 2006.

[HMM+06] B.M. Hennelly, J. Maycock, C.P. McElhinney, T.J. Naughton, J.B. McDonald, and B. Javidi. Analysis of partially occluded objects encoded in digital holograms using the wigner distribution function. *Proc. SPIE Optics and Photonics, San Diego*, 6311, 30^{th} August - 1^{st} September 2006.

[HNM06] B.M. Hennelly, T.J. Naughton, and J.B. McDonald. Wigner distribution function and digital holography. *Proc. SPIE*, 6311:63110L, 2006.

[HS05] B.M. Hennelly and J.T. Sheridan. Fast numerical algorithm for the linear canonical transform. *Journal of the Optical Society of America: A*, 22:928–937, 2005.

[JFH+05] B. Javidi, P. Ferraro, S.H. Hong, S. D. Nicola, A. Finizio, D. Alfieri, and G. Pierattini. Three-dimensional fusion by use of multiwavelength digital holography. *Optics Letters*, 30:144–146, 2005.

[JH08] S.J. Jeong and C.K. Hong. Pixel-size-maintained image reconstruction of digital holograms on arbitrarily titled planes by the angular spectrum method. *Applied Optics*, 47:3064–3071, 2008.

[JK05] B. Javidi and D. Kim. Three-dimensional-object recognition by use of single-exposure on-axis digital holography. *Optics Letters*, 30:236–238, 2005.

[JMYC05] B. Javidi, I. Moon, S. Yeom, and E. Carapezza. Three-dimensional imaging and recognition of microorganism using single-exposure on-line (seol) digital holography. *Optics Express*, 13:4492–4506, 2005.

[JT00] B. Javidi and E. Tajahuerce. Three-dimensional object recognition by use of digital holography. *Optics Letters*, 25:610–612, 2000.

[JYMD06] B. Javidi, S. Yeom, I. Moon, and M. Daneshpanah. Real-time automated 3d sensing, detection and recognition of dynamic biological micro-organic events. *Optics Express*, 14:3806–3829, 2006.

[KAJ97] T.M. Kreis, M. Adams, and W.P.O. Jüptner. Methods of digital holography: a comparison. *Proc. SPIE Optical Inspection and Micromeasurements II*, 3098:224–233, 1997.

[KFZv06] J. Kautsky, J. Flusser, B. Zitová, and S. vSimberová. A new wavelet-based measure of image focus. *Pattern Recognition Letters*, 27:1431–1439, 2006.

[KHMN08] D.P. Kelly, B.M. Hennelly, C.P. McElhinney, and T.J. Naughton. A practical guide to digital holography and gener-

alized sampling. *Proc. SPIE Optics and Photonics, San Diego*, 7072:707215, 30^{th} August - 1^{st} September 2008.

[KJ97] T.M. Kreis and W.P.O. Jüptner. Suppression of the dc term in digital holography. *Optical Engineering*, 36:2357–2360, 1997.

[KJ04] D. Kim and B. Javidi. Distortion-tolerant 3-d object recognition by using single exposure on-axis digital holograph. *Optics Express*, 12:5539–5548, 2004.

[KK02] P. Korecki and J. Korecki. γ-ray holography three-dimensional imaging of a local atomic structure. *Hyperfine Interact.*, 144:85–92, 2002.

[KOKL03] E. Kolenovic, W. Osten, R. Klattenhoff, and S. Lai. Miniaturized digital holography sensor for distal three-dimensional endoscopy. *Applied Optics*, 42:5167–5172, 2003.

[Kre05] T. Kreis. *Handbook of Holographic Interferometry.* WILEY-VCH GmbH and Co.KGaA, Weinheim, first edition, 2005.

[LBV99] S. Lai, B.Kemper, and G. V.Bally. Off-axis reconstruction of in-line holograms for twin-image elimination. *Optics Communications*, 169:37–43, 1999.

[LF07] T. Latychevskaia and H.-W. Fink. Solution to the twin-image problem in holography. *Physics Review Letters*, 98:233901–1–233901–4, 2007.

[LKB08] P. Langehanenberg, B. Kemperand, and G.V. Bally. Autofocusing in digital holographic phase contrast microscopy on pure phase objects for life cell imaging. *Applied Optics*, 47:D179–D182, 2008.

[LKN00] S. Lai, B. King, and M.A. Neifeld. Wave front reconstruction by means of phase-shifting digital in-line holography. *Optics Communications*, 173:155–160, 2000.

[LS87] G. Liu and P.D. Scott. Phase retrieval and twin-image elimination for in-line fresnel holograms. *Journal of the Optical Society of America: A*, 4:159–165, 1987.

[LU62] E.N. Leith and J. Upatnieks. New techniques in wavefront reconstruction. *Journal of the Optical Society of America: A*, 51:1469–1473, 1962.

[LU63] E.N. Leith and J. Upatnieks. Wavefront reconstruction with continuous-tone objects. *Journal of the Optical Society of America*, 53:1377–1381, 1963.

[LU64] E.N. Leith and J. Upatnieks. Wavefront reconstruction with diffused illumination and three-dimensional objects. *Journal of the Optical Society of America*, 54:1295–1301, 1964.

[LU04] M. Liebling and M. Unser. Autofocus for digital fresnel holograms by use of a fresnelet-sparsity criterion. *Journal of the Optical Society of America: A*, 21:2424–2430, 2004.

[Luc97] M. Lucente. Interactive three-dimensional holographic displays: seeing the future in depth. *SIGGRAPH Computer Graphics*, 31:63–67, 1997.

[MAK04] E. Malkiel, J.N. Abras, and J. Katz. Automated scanning and measurement of particle distributions within a holographic reconstructed volume. *Measurement Science and Technology*, 15:601–612, 2004.

[MB74] R.A. Muller and A. Buffington. Real-time correction of atmospherically degraded telescope images through image sharpening. *Journal of the Optical Society of America*, 64:1200–1210, 1974.

[MBA79] K.H.S. Marie, J.C. Bennett, and A.P. Anderson. Digital processing technique for suppressing the interfering outputs in the image from an inline hologram. *Electronics Letters*, 15:241–243, 1979.

[MHA+08] C.P. McElhinney, B.M. Hennelly, L. Ahrenberg, J. Maycock, T. Kreis, J. McDonald, and T.J. Naughton. Automated twin-image removal from in-line digital holograms. *Euro American Workshop on Information Optics, Annecy, France*, 1^{st}-5^{th} June 2008.

[MHAN08] C.P. McElhinney, B.M. Hennelly, L. Ahrenberg, and T.j. Naughton. Twin-image reduction via segmented removal of

the twin-image. *Proc. SPIE Optics and Photonics, San Diego*, 2008.

[MHAN09] C.P. McElhinney, B.H. Hennelly, L. Ahrenberg, and T.J. Naughton. Rapid twin-image removal through inverse aperture segmentation in inline digital holograms. *in preparation for Optics Letters*, 2009.

[MHBN08] C.P. McElhinney, B.M. Hennelly, B.Javidi, and T.J. Naughton. *Extraction of three-dimensional information from reconstructions of in-line digital holograms*. Springer, September 2008.

[MHM+07] J. Maycock, B.M. Hennelly, J.B. McDonald, T.J. Naughton, Y. Frauel, A. Castro, and B. Javidi. Reduction of speckle in digital holography by discrete fourier filtering. *Journal of the Optical Society of America: A*, 24:1617–1622, 2007.

[MHMN07] C.P. McElhinney, B.M. Hennelly, J.B. McDonald, and T.J. Naughton. Segmentation of macroscopic objects from digital holograms using focus and shape information. *Proc. Photonics Ireland, Galway*, 24^{rd}-26^{th} September 2007.

[MHMN08] C.P. McElhinney, B.M. Hennelly, J.B. McDonald, and T.J. Naughton. Segmentation of macroscopic object digital holographic reconstructions using extracted depth information. *Proc. SPIE Photonics Europe, Strasbourg*, 7000, 7^{th}-11^{th} April 2008.

[MHMN09] C.P. McElhinney, B.H. Hennelly, J.B. McDonald, and T.J. Naughton. Multiple object segmentation in macroscopic three-dimensional scenes from a single perspective using digital holography. *in preparation for Applied Optics*, 2009.

[MHN07] C.P. McElhinney, B.M. Hennelly, and T.J. Naughton. Image processing of real-world three-dimensional object sensed with digital holography. *Advanced Laser Technologies - ALT'07, Levi, Finland*, 3^{rd}-7^{th} September 2007.

[MHN08a] C.P. McElhinney, B.M. Hennelly, and T.J. Naughton. Extended focused imaging for digital holograms of macroscopic three-dimensional objects. *Applied Optics*, 47(19):D71–D79, July 2008.

[MHN08b] C.P. McElhinney, B.M. Hennelly, and T.J. Naughton. Focused image creation algorithms for digital holograms of macroscopic three-dimensional objects. *Digital Holography and Three-Dimensional Imagin, Tampa Bay*, 17^{th}-19^{th} March 2008.

[MHN08c] C.P. McElhinney, B.M. Hennelly, and T.J. Naughton. Focused image creation approaches for macroscopic objects encoded in digital holograms. *Proc. SPIE Photonics Europe, Strasbourg*, 6994, 7^{th}-11^{th} April 2008.

[MHNY06] O. Matoba, K. Hosoi, K. Nitta, and T. Yoshimura. Fast acquisition system for digital holograms and image processing

for three-dimensional display and data manipulation. *Applied Optics*, 46:8945–8950, 2006.

[MMC+07a] C.P. McElhinney, J.B. McDonald, A. Castro, Y. Frauel, B. Javidi, and T.J. Naughton. Depth-independent segmentation of three-dimensional objects encoded in single perspectives of digital holograms. *Optics Letters*, 32(10):1229–1231, April 2007.

[MMC+07b] C.P. McElhinney, J.B. McDonald, A. Castro, Y. Frauel, B. Javidi, and T.J. Naughton. Segmentation of three-dimensional objects from background in digital holograms. *Proc. IMVIP, Maynooth*, 5^{rd}-7^{th} September 2007.

[MMH+06a] J. Maycock, C.P. McElhinney, B.M. Hennelly, T.J. Naughton, J.B. McDonald, and B. Javidi. Reconstruction of partially occluded objects encoded in three-dimensional scenes by using digital holograms. *Applied Optics*, 45(13):2975–2985, May 2006.

[MMH+06b] J. Maycock, C.P. McElhinney, B.M. Hennelly, T.J. Naughton, J.B. McDonald, and B. Javidi. Reconstruction of partially occluded objects using digital holograms. *Proc. SPIE Photonics Europe, Strasbourg*, 6187, 3^{rd}-7^{th} April 2006.

[MMH+06c] C.P. McElhinney, J. Maycock, B.M. Hennelly, T.J. Naughton, J.B. McDonald, and B. Javidi. Extraction and reconstruction of shape information from a digital hologram of three-dimensional

objects. *Proc. of IMVIP, Dublin*, pages 76–83, 30^{rd} August -1^{st} September 2006.

[MMH+06d] C.P. McElhinney, J. Maycock, B.M. Hennelly, T.J. Naughton, J.B. McDonald, and B. Javidi. Extraction of shape information from three-dimensional objects encoded in a digital hologram. *ICO Topical Meeting on Optoinformatics/Information Photonics, St. Petersburg*, 4^{th} -7^{th} September 2006.

[MMH+09] C.P. McElhinney, J. Maycock, B.H. Hennelly, L. Ahrenberg, T. Kreis, and T.J. Naughton. Automated detection and subsequent removal of the twin-image through digital processing for in-line digital holography. *in preparation for Applied Optics*, 2009.

[MMHN08] K.M. Molony, C.P. McElhinney, B.M. Hennelly, and T.J. Naughton. Segmentation of three-dimensional scenes encoded in digital holograms. *Proc. SPIE Optics and Photonics, San Diego*, 2008.

[MMM+05a] J. Maycock, C.P. McElhinney, J.B. McDonald, T.J. Naughton, and B. Javidi. Independent component analysis applied to digital holograms of three-dimensional objects. *Proc. SPIE Optics and Photonics, San Diego*, 5908, 31^{st}-4^{th} August 2005.

[MMM+05b] C.P. McElhinney, J. Maycock, J.B. McDonald, T.J. Naughton, and B. Javidi. Three-dimensional scene reconstruction using

digital holography. *Proc. Opto-Ireland, Dublin*, 5823:48–57, 4^{th}-6^{th} April 2005.

[MMM+06] J. Maycock, C.P. McElhinney, J.B. McDonald, T.J. Naughton, B.M. Hennelly, and B. Javidi. Speckle reduction in digital holography using independent component analysis. *Proc. SPIE Photonics Europe, Strasbourg*, 6187, 3^{rd}-7^{th} April 2006.

[MMN+05] C.P. McElhinney, J. Maycock, T.J. Naughton, J.B. McDonald, and B. Javidi. Extraction of three-dimensional shape information from a digital hologram. *Proc. SPIE Optics and Photonics, San Diego*, 5908, 31^{st}-4^{th} August 2005.

[MMS+05] J. Maycock, C.P. McElhinney, A.E. Shortt, T.J. Naughton, J.B. McDonald, B.M. Hennelly, U. Gopinathan, D.S. Monaghan, J.T. Sheridan, and B. Javidi. Holographic image processing of three-dimensional objects. *Proc. SPIE Optics East, Boston*, 4471, 23^{rd}-26^{th} October 2005.

[MNF+02] O. Matoba, T.J. Naughton, Y. Frauel, N. Bertaux, and B. Javidi. Real-time three-dimensional object reconstruction by use of a phase-encoded digital hologram. *Applied Optics*, 41:6187–6192, 2002.

[MR94] V. Murino and C.S. Regazzoni. Visual surveillance by depth from focus. *IEEE International Conference on Industrial Electronics, Control and Instrumentation*, 2:998–1002, 1994.

[MSNJ04a] C.P. McElhinney, A.E. Shortt, T.J. Naughton, and B. Javidi. Blockwise discrete fourier transform analysis of digital hologram data of three-dimensional objects. *Proc. of SPIE Optics and Photonics, Colorado*, 5557:62–69, 2^{nd}-6^{th} August 2004.

[MSNJ04b] C.P. McElhinney, A.E. Shortt, T.J. Naughton, and B. Javidi. Discrete fourier transform quantisation tables for digital holograms of three-dimensional objects. *Proc. of IMVIP, Dublin*, 1^{st}-3^{rd} September 2004.

[MWLJ04] L. Ma, H. Wang, Y. Li, and H. Jin. Numerical reconstruction of digital hologram for three-dimensional shape measurement. *Journal of Optics A*, 6:396–400, 2004.

[MY00] S. Murata and N. Yasuda. Potential of digital holography in particle measurement. *Optics and Laser Technology*, 32:567–574, 2000.

[MY05] G.A. Mills and I. Yamaguchi. Effects of quantization in phase-shifting digital holography. *Applied Optics*, 44:1216–1225, 2005.

[MYlK05] C. Mann, L. Yu, C. lo, and M. Kim. High-resolution quantitative phase-contrast microscopy by digital holography. *Optics Express*, 13:8693–8698, 2005.

[NATG96] I.R. Nourbaksh, D. Andre, C. Tomasi, and M.R. Genesereth. Obstacle avoidance via depth from focus. *Proceedings of*

the ARPA Image Understanding Workshop, pages 1339–1344, 1996.

[NATG97] I.R. Nourbaksh, D. Andre, C. Tomasi, and M.R. Genesereth. Mobile robot obstacle avoidance via depth from focus. *Robotics and Autonomous Systems*, 22:151–158, 1997.

[Nay92] S.K. Nayar. Shape-from-focus. *IEEE International Conference on Computer Vision and Pattern Recognition*, 1992:302–308, 1992.

[NFJT02] T.J. Naughton, Y. Frauel, B. Javidi, and E. Tajaheurce. Compression of digital holograms for three-dimensional object reconstuction and recognition. *Applied Optics*, 41:4124–4132, 2002.

[NJ04] T.J. Naughton and B. Javidi. Compression of encrypted three-dimensional objects using digital holography. *Optical Engineering*, 43:2233–2238, 2004.

[NMJ03] T.J Naughton, J.B. McDonald, and B. Javidi. Efficient compression of Fresnel fields for Internet transmission of three-dimensional images. *Applied Optics*, 42:4758–4764, 2003.

[NN90] S.K. Nayar and Y. Nakagawa. Shape from focus: An effective approach for rough surfaces. *IEEE International Conference on Robotics and Automatio*, 2:218–225, 1990.

[OBu02] W. Osten, T. Baumbach, and W. üptner. Comparative digital holography. *Optics Letters*, 27:1764–1766, 2002.

[Onu00] L. Onural. Sampling of the diffraction field. *Applied Optics*, 39:5929–5935, 2000.

[OO92] L. Onural and M.T. Özgen. Extraction of three-dimensional object-location information directly from in-line holograms using wigner analysis. *Journal of the Optical Society of America: A*, 9:252–260, 1992.

[OS87] L. Onural and P.D. Scott. Digital decoding of in-line holograms. *Optical Engineering.*, 26:1124–1132, 1987.

[PFFT98] G. Pedrini, P. Fröning, H. Fessler, and H.J. Tiziani. In-line digital holographic interferometry. *Applied Optics*, 37:6262–6269, 1998.

[PFTS99] G. Pedrini, P. Froning, H. Tiziani, and F. Santoyo. Shape measurement of microscopic structures using digital holograms. *Optics Communications*, 264:257–268, 1999.

[PK83] R.J. Pieper and A. Korpel. Image processing for extended depth of field. *Applied Optics*, 22:1449–1453, 1983.

[PKI+00] T-C. Poon, T. Kim, G. Indebetouw, B.W. Schilling, M.H. Wu, K. Shinoda, and Y. Suzuki. Twin-image elimination experiments for three-dimensional images in optical scanning holography. *Optics Letters*, 25:215–217, 2000.

[PL08] P. Picart and J. Leval. General theoretical formulation of image formation in digital fresnel holography. *Journal of the Optical Society of America: A*, 25:1744–1761, 2008.

[PST99] G. Pedrini, S. Schedin, and H.J. Tiziani. Lensless digital-holographic interferometry for the measurement of large objects. *Optics Communications*, 171:29–36, 1999.

[SC95] M. Subbarao and T. Choi. Accurate recovery of three-dimensional shape from image focus. *IEEE Transactions on Pattern Analysis and Machine Intelligence*, pages 266–274, 1995.

[Sch94] U. Schnars. Direct phase determination in hologram interferometry with use of digitally recorded holograms. *Jounral of the Optical Society of America: A*, 11:2011–2015, 1994.

[SCK07] Y-H. Seo, H-J. Choi, and D-W. Kim. 3d scanning-based compression technique for digital hologram video. *Signal Processing: Image communication*, 22:144–156, 2007.

[SCN93] M. Subbarao, T. Choi, and A. Nikzad. Focusing techniques. *Optical Engineering*, 32:2824–2836, 1993.

[SCS05] C. Slinger, C. Cameron, and M. Stanley. Computer-generated holography as a generic display technology. *IEEE Computer Magazine*, 38:46–53, 2005.

[Sho06] A. Shortt. *Compression of digital hologram of three-dimensional objects*. PhD thesis, National University of Ireland, Maynooth., 2006.

[SJ94] U. Schnars and W.P.O Jüptner. Direct recording of holograms by a ccd target and numerical reconstruction. *Applied Optics*, 33:179–181, 1994.

[SJ04a] U. Schnars and W. Jüptner. *Digital Holography: Digital Hologram Recording, Numerical Reconstruction, and Related Techniques*. Springer, Berlin, 2004.

[SJ04b] A. Stern and B. Javidi. Sampling in the light of wigner distribution. *Jounral of the Optical Society of America: A*, 21:360–366, 2004.

[SNJ06a] A.E. Shortt, T.J. Naughton, and B. Javidi. A companding approach for nonuniform quantization of digital holograms of three-dimensional objects. *Optics Express*, 14:5129–5134, 2006.

[SNJ06b] A.E. Shortt, T.J. Naughton, and B. Javidi. Compression of digital holograms of three-dimensional objects using wavelets. *Optics Express*, 14:2625–2630, 2006.

[SNJ06c] A.E. Shortt, T.J. Naughton, and B. Javidi. Compression of optically encrypted digital holograms using artificial neural networks. *Journal of Display Technology*, 2:401–410, 2006.

[SNJ07] A.E. Shortt, T.J. Naughton, and B. Javidi. Histogram approaches for lossy compression of digital holograms of three-dimensional objects. *Proceeding of IEEE, Transactions on Image Processing*, 16:1548, 2007.

[ST98] M. Subbarao and J.K. Tyan. Selecting the optimal focus measure for autofocusing and depth-from-focus. *Proc. IEEE Transactions on Pattern Analysis and Machine Intelligence*, 20:864–870, 1998.

[TBG+05] A. Thelen, J. Bongartz, D. Giel, S. Frey, and P. Hering. Iterative focus detection in hologram tomography. *Journal of the Optical Society of America: A*, 22:1176–1180, 2005.

[TBPN00] J.B. Tiller, A. Barty, D. Paganin, and K.A. Nugent. The holographic twin-image problem: a deterministic phase solution. *Optics Communications*, 183:7–14, 2000.

[Tea83] M.R. Teague. Deterministic phase retrieval: a green's function solution. *Journal of the Optical Society of America*, 73:1434–1441, 1983.

[TF96] M. Tegze and J. Faigel. X-ray holography with atomic resolution. *Nature (London)*, 380:49–51, 1996.

[TIY08] M.L. Tachiki, M. Itoh, and T. Yatagai. Simultaneous depth determination of multiple objects by focus analysis in digital holography. *Applied Optics*, 47:D144–D153, 2008.

[TKN04] K. Takahashi, A. Kubota, and T. Naemura. A focus measure for light field rendering. *IEEE International Conference on Image Processing*, 4:2475–2478, 2004.

[TKO99] Y. Takari, H. Kawai, and H. Ohzu. Hybrid holographic microscopy free of conjugate and zero-order images. *Applied Optics*, 38:4990–4996, 1999.

[TWZ67] B.J. Thompson, J.H. Ward, and W.R. Zinky. Application of hologram techniques for particle size analysis. *Applied Optics*, 6:519–526, 1967.

[Wat04] J. Watson. The development of a subsea holographic camera for the imaging and analysis of marine organisms. *Proc. SPIE*, 5477:366, 2004.

[WOS00] C. Wagner, W. Osten, and S. Seebacher. Direct shape measurement by digital wavefront reconstruction and multiwavelength contouring. *Optical Engineering*, 39:79–85, 2000.

[XMA00] L. Xu, J. Miao, and A. Asundi. Properties of digital holography based on in-line configuration. *Optical Engineering*, 39:3214–3219, 2000.

[XPMA01] L. Xu, X. Peng, J. Miao, and A. Asundi. Studies of digital microscopic holography with applications to microstructure testing. *Applied Optics*, 40:5046–5051, 2001.

[YFB02] R. Yin, P.J. Flynn, and S.L. Broschat. Position-dependent defocus processing for acoustic holography images. *International Journal of Imaging Systems and Technology*, 12:101–111, 2002.

[YK08] Y. Yang and B-S. Kang. Experimental validation for the determination of particle positions by the correlation corefficient method in digital particle holography. *Applied Optics*, 47:5953–5960, 2008.

[YM80] L.P. Yaroslavskii and N.S. Merzlyakov. *Methods of Digital Holography*. Consultants Bureau, New York, 1980. Translated from Russian by Dave Parsons.

[YYMY06] I. Yamaguchi, K. Yamamoto, G.A. Mills, and M. Yokota. Image reconstruction only by phase data in phase-shifting digital holography. *Applied Optics*, 45:975–983, 2006.

[YZ97] I. Yamaguchi and T. Zhang. Phase-shifting digital holography. *Optics Letters*, 22:1268–1270, 1997.

[ZC05] S. Zhang and M. Chen. Preprocessing and compression of digital holographic images. *Proc. SPIE*, 5909:655, 2005.

[ZLG04] Y. Zhang, Q. L, and B. Ge. Elimination of zero-order diffraction in digital off-axis holography. *Optics Communications*, 240:261–267, 2004.

[ZPOT03] Y. Zhang, G. Pedrini, W. Osten, and H. Tiziani. Whole optical wave field reconstruction from double or multi in-line holo-

grams by phase retrieval algorithm. *Optics Express*, 11:3234–3241, 2003.